

Physical Modeling of Electrical Conduction in Printed Circuit Board Insulation

by
Vasanth Sarathy

Submitted to the Department of Electrical Engineering and Computer Science
on August 18, 2005, in partial fulfillment of the
requirements for the degree of
Master of Science

Abstract

This thesis is concerned with understanding the degradation of electrical and electronic components in automobiles due to environmental effects. A special emphasis is placed on understanding the physical processes underlying the degradation, so that accelerated reliability tests can be specified with increased confidence of their validity. As a first case, printed circuit board (PCB) insulation was selected as a target for investigation. With an increase in the electronics and circuit miniaturization coupled with an increase in voltage in 42 volt as well as hybrid vehicles, PCB reliability has become an important issue. We first provide a broad presentation of insulation degradation theory as well as electrical conduction theory according to existing literature and then narrow our focus towards printed circuit board insulation. We develop a novel first-order mathematical model to describe electrical currents in printed circuit board insulation as a function of temperature, relative humidity, absorbed moisture content, voltage and geometrical characteristics. This model was developed from a series of experiments that were carefully performed under controlled laboratory conditions. In addition to describing the experimental procedure and results, we also explain the details of the experimental setup and measurement instrumentation. Furthermore, we present an intuitive physical explanations for some observations and model responses.

Thesis Supervisor: Dr. Thomas A. Keim
Title: Principal Research Engineer

Thesis Supervisor: Dr. Chathan M. Cooke
Title: Principal Research Engineer

Acknowledgements

I would firstly like to thank Dr. Tom Keim, my research advisor and mentor, for his constant support of my work and expertise in more areas than I can imagine. With his deep insight and quick wit, my graduate school experience has been greatly enriched. I would also like to thank Dr. Chat Cooke, my research advisor, whose extensive experience in the area of insulation research was instrumental in guiding this experimentally based research project.

Of course, I would not be where I am today without the love, support and encouragement from Amma (my Mom), Appa (my Dad) and Arun Anna (my Brother, Arun). I am eternally indebted to them for teaching me right from wrong and appreciating the value of good character paramount to any academic qualifications.

I would like to thank many people at the Laboratory for Electromagnetic and Electronic Systems (LEES) here at MIT for assisting me in more ways than one, especially Vivian and Wayne. I appreciate gaining the friendship and trust of some of the nicest and smartest people in the world – Abhi, Akshay, Brandon, Beth, Keith, Laura, Rupam, Shubham and Tushar. I am also thankful for the valuable life lessons I have learned through my collegiate experience and my friends at Arkansas including Bala, Khaled, Lyle, Milos and Sheldon.

Support for this research was provided by the Massachusetts Institute of Technology Department of Electrical Engineering and Computer Science and the MIT/Industry Consortium on Advanced Automotive Electrical/Electronic Components and Systems.

Contents

1	Introduction	25
1.1	Introduction	25
1.2	Automotive Electronics: The Printed Circuit Board	27
1.3	The Study of Electrical Conduction	28
1.4	Current Literature on Reliability Measurement	30
1.5	Our Approach	34
1.6	Thesis Goals	35
1.7	Thesis Organization	35
I	Theory	37
2	Theoretical Overview	39
2.1	Introduction	39
2.2	Organization of Research	40
2.3	Probabilistic Failure Models	44
2.4	Insulation Breakdown Models	47
2.5	Aging and Degradation Models	49
3	Chemical and Physical Properties	51
3.1	Introduction	51
3.2	Morphology of Printed Circuit Board Insulation	51
3.2.1	The Resin System	52
3.2.2	The Reinforcement	54
3.2.3	The Conductive Material	55

Contents

3.2.4	FR-4	55
3.3	Moisture Diffusion Theory	56
3.4	Diffusion Mathematics	58
3.4.1	Square-root Relationship	59
3.5	Numerical Values of the Diffusion Coefficient	60
3.6	Gravimetric Method and Diffusion Approximations	61
3.7	Non-Fickian Diffusion	62
3.7.1	Berens and Hopfenberg Absorption Model	63
3.7.2	Dual Mode Sorption Theory	65
3.8	Reversibility, Repeatability and Desorption	65
3.9	Experimental Methods	67
3.9.1	Pre-conditioning	67
3.9.2	Absorption and Desorption Profiles	68
3.10	Interfacial Damage due to Moisture	69
4	Electrical Conduction	71
4.1	Introduction	71
4.2	Electrical Conductivity	72
4.3	Electronic Steady State Conduction	73
4.3.1	Energy Band Theory	74
4.3.2	Charge Carrier Generation, Transport and Traps	75
4.3.3	Ohmic Conduction (Low Field)	76
4.3.4	High Field Conduction Mechanisms	76
4.3.4.1	Electron Injection	77
4.3.4.2	Steady State Conduction	77
4.3.5	Shortfall of Band Theory in Polymers	79
4.4	Ionic Steady State Conduction	80
4.4.1	Intrinsic Ionic Conduction	81
4.4.2	Extrinsic Ionic Conduction	81
4.4.3	Ionic Hopping Model	82

4.4.4	Activation Energy, Random Barriers and Percolation	85
4.4.4.1	Percolation Theory	87
4.5	Transient Conduction Mechanisms	89
4.6	Surface Conduction and Interfacial Effects	92
4.7	Role of Water	93
II	Experiment	95
5	Design of the Test Sample	97
5.1	Introduction	97
5.2	First Generation Test Sample	99
5.2.1	The Pattern Dimensions	101
5.2.2	Motivation to Redesign The Test Sample	103
5.3	Second Generation Test Sample	105
6	The Measurement System	109
6.1	Introduction	109
6.2	Low-Current Measurement Instrumentation	109
6.2.1	The Electrometer	110
6.2.2	The Logarithmic Amplifier	110
6.3	Chambers and Measurement of Environmental Conditions	116
6.4	Automated Data Acquisition System	117
6.4.1	A/D Converter and Serial Interfacing	117
6.4.2	GPIB	118
6.4.3	Direct Serial Interface	118
6.4.4	LABVIEW® Graphical User Interface	119
6.5	Miscellaneous Cables and Connectors	120
6.6	System Calibration and Performance	120
6.7	Weight Measurement Methodology and Instrumentation	125
6.8	Thickness Measurement Methodology and Instrumentation	126

7	Extraneous Effects and Disturbances at Very Low Currents	129
7.1	Introduction	129
7.2	Internal Sources of Disturbance	130
7.2.1	Alternative Leakage Paths	130
7.2.2	Ground Loops	133
7.2.3	Capacitive Coupling	135
7.2.4	Channel Crosstalk	135
7.3	External Sources of Disturbance	136
7.3.1	Random Noise Elimination through Averaged Down Sampling	136
7.3.2	ESI	139
7.3.3	EMI and RFI	139
7.3.4	Cable Interference	139
III	Analysis	141
8	Preliminary Experimental Results	143
8.1	Introduction	143
8.2	Naming Conventions	143
8.3	Preliminary Experiments on First Generation Samples	144
8.3.1	Faraday Cage Tests	144
8.3.1.1	As Arrived Condition	147
8.3.1.2	Oven Baked Tests	149
8.3.1.3	Water Soaked Tests	151
8.3.1.4	Comparison between Boards	153
8.3.2	Environment Chamber Tests	158
8.3.3	Generation Conclusions from First Generation Samples	163
8.4	Preliminary Experiments on Second Generation Samples	163
8.4.1	Initial Polarization Tests (CB0 and CB1)	163
8.4.2	Initial Thermal and Moisture Sensitivity Tests	166
8.4.3	Wide-Range Thermal and Moisture Sensitivity Tests	168

8.4.4	Size-Scaling Effects Tests	172
8.4.5	Voltage Sensitivity Tests	173
8.4.6	General Conclusions from Second Generation Samples	174
9	The Hygrothermal Test Plan	175
9.1	Introduction and General Overview	175
9.2	Hygrothermal Experimental Scheme	176
9.2.1	Modified Conduction Tests	176
9.3	Weight Change Results	178
9.3.1	Net Weight Gain	181
9.3.2	Weight Change during Modified Conduction Test	181
9.4	Thickness Change Results	182
9.5	Moisture Diffusion Characteristics	185
9.5.1	Fickian Approximations	185
9.5.2	Theoretical Concentration-Distance Estimates	193
9.6	Electrical Steady State Conduction	198
9.6.1	General Observations	198
9.6.2	Quasi-Steady State Currents	202
9.6.2.1	The Exponential Dependence of I_{QSS} on Moisture	202
9.6.3	Activation Energy	207
9.6.3.1	The Dependence of E_A on Moisture	208
9.7	Mathematical Model for Steady State Conduction	209
9.7.1	Absorbed Moisture Density $\tilde{\rho}$	209
9.7.2	Exposure Rate \tilde{r}	209
9.7.3	Simplified First-Order Models	210
9.7.3.1	Mass-Based Model (MBM)	210
9.7.3.2	Exposure-Based Model (EBM)	211
9.7.4	Arrhenius Fit and Parameter Estimation	211
9.7.4.1	Estimated α Values for the Exposure-Based Model	218
9.7.4.2	Estimated α Values for the Mass-Based Model	220

Contents

9.7.4.3	Estimated δ Values for Either Model	222
9.7.4.4	Summary of α and δ Observations	222
9.7.5	Performance of First-Order Model	224
9.7.6	Adjustments for Geometric Scaling	228
9.7.6.1	Depth of Penetration Estimate Based on Dielectric Gap . .	229
9.7.6.2	Depth of Penetration Estimate Based on Conductor Trace Width	230
9.7.6.3	Geometric Scaling for the Volume Pattern	232
9.7.7	Universal Scaled First-Order Model for Surface and Bulk Conduction	233
9.7.7.1	Surface Conduction	233
9.7.7.2	Volume (Bulk) Conduction	233
9.7.8	Effects of Aging	234
9.7.9	Limitations of the First-Order Model	234
9.8	Electrical Transient Conduction	237
9.9	Visual Observations about Second Generation Test Samples	239
10	Conclusions	243
10.1	Introduction	243
10.2	Summary and Major Conclusions	243
10.3	Evaluation of Thesis Objectives and Contributions	245
10.4	Future Work	246
IV	Appendices	249
A	Geometric Calculations of Test Samples	251
A.1	Geometric Considerations and Active Area Calculations	251
A.1.1	Comb Pattern	251
A.1.2	Comb Pattern with Dimples	253
A.1.3	Square Pattern (First generation boards)	254
A.1.4	Circular Disc Pattern (Second generation boards)	255

A.1.5	Active Areas of all the Patterns	255
B	Solutions to Fick’s Law	257
B.1	Method of Reflection and Superposition	257
B.2	Method of Separation of Variables	258
B.3	The Laplace Transform	261
B.3.1	Plane Sheet of Finite Thickness	262
B.4	Other Solutions	263
B.4.1	Surface Evaporation	264
C	Additional Plots	265
C.1	Moisture Desorption Data	265
D	MATLAB Code	271
D.1	ADAQ Data Extracter	271
D.2	Data Interpolation and Smoothing	273
D.3	Moisture Absorption Curve Fitting	275
D.4	Moisture Desorption Curve Fitting	278
D.5	Solution to Fick’s Diffusion Law	281
E	LABVIEW Code	283

List of Figures

1.1	Typical Automotive Under-Hood Operating Environments [41]	26
1.2	Impact of Charge on Conduction in Insulating Systems	28
1.3	Factors Affecting Conduction During the Service Life of PCBs	29
1.4	IPC-B-25A Multipurpose One-sided Test Pattern	33
2.1	Research Framework for Accelerated Reliability Test Development	41
3.1	Three-membered epoxide ring	52
3.2	Bisphenol A	52
3.3	Difunctional epoxy resin	52
3.4	Brominated difunctional epoxy resin	53
3.5	Diamine compound	53
3.6	Variation of Moisture Diffusion with Temperature for Similar Materials	61
3.7	Comparison between Fickian and Non-Fickian absorption	63
3.8	Theoretical Absorption Curves from Shao [51]	64
3.9	Atomic Force Microscope Image of Glass-Epoxy Debonding (Courtesy: NIST) [58]	70
4.1	Cubic Crystal Structure with a vacancy in the center instead of a Cation (Adapted from [18])	83
4.2	Mechanism of Ionic Hopping over a Potential Barrier	86
4.3	Comparison between Dipolar and Charge Transport Power Law Relations	90
5.1	Dominant Conduction Paths	98
5.2	The Test Coupon Design	99
5.3	The Test Coupon Design	100
5.4	Dimensions of the Comb Pattern	101
5.5	Dimensions of the Comb Pattern with Triangular Dimples	101

List of Figures

5.6	Dimensions of the Filled Square Pattern	102
5.7	2nd Generation Board	105
5.8	2nd Generation Board	106
6.1	Basic Test Circuit	110
6.2	Simplified circuit of the LogAmp IC	111
6.3	Overall Circuit	113
6.4	Performance of the Logarithmic Amplifier with Positive Input Current . . .	114
6.5	Performance of the Logarithmic Amplifier with Negative Input Current . .	115
6.6	Constant Current Addition of 5pA	116
6.7	Full Block Diagram of the Automated Data Acquisition System	118
6.8	Automated Data Acquisition System GUI Screenshot	119
6.9	System Calibration	122
6.10	System Calibration	123
6.11	Temperature Oscillation in the Chamber during System Calibration Tests .	123
6.12	Relative Humidity Oscillation in the Chamber during System Calibration Tests	124
6.13	Thickness Measurement Stand Drawing	126
6.14	Locations for Thickness Measurements	127
7.1	Sensitivity of Current without Silver Guard Rings	131
7.2	Sensitivity of Current with Silver Guard Rings	132
7.3	DC error in data	134
7.4	DC error has been corrected in data	134
7.5	Crosstalk between Nearby Channels	135
7.6	Crosstalk between channels has been eliminated	136
7.7	Random Noise	138
7.8	Averaged Down Sampled and Scaled Output	138
8.1	Schematic of the Test Setup	146
8.2	“As Arrived” Current Measurements during Charging	147
8.3	“As Arrived” Current Measurements during Discharging	148
8.4	“Oven Baked” Current Measurements during Charging	149

8.5	“Oven Baked” Current Measurements during Discharging	150
8.6	“Water Soaked” Current Measurements during Charging	151
8.7	“Water Soaked” Current Measurements during Discharging	152
8.8	“Small Pattern” Current Measurements during Charging	153
8.9	“Small Pattern” Current Measurements during Discharging	154
8.10	“Large Pattern” Current Measurements during Charging	155
8.11	“Large Pattern” Current Measurements during Discharging	156
8.12	“Square Pattern (Volume)” Current Measurements during Charging	156
8.13	“Square Pattern (Volume)” Current Measurements during Discharging	157
8.14	Acclimatization Profile for the Environment Chamber Tests	158
8.15	Leakage Currents: Small Pattern [1st generation board]	160
8.16	Leakage Currents: Large Pattern [1st generation board]	161
8.17	Leakage Currents: Bulk (Volume) Pattern [1st generation board]	162
8.18	Leakage Currents: All Patterns at 85°C and 85% RH [CB0]	164
8.19	Leakage Currents: All Patterns at 85°C and 85% RH and conditioned [CB1]	165
8.20	Sensitivity of Leakage Current in CB1	167
8.21	Leakage Currents in the Small Pattern in CB1	169
8.22	Leakage Currents in the Large Pattern in CB1	170
8.23	Leakage Currents in the Volume Pattern in CB1	171
8.24	Leakage Currents in the Small Patterns and their Parallel Combination at low RH in CB1	172
8.25	Leakage Currents in CB1 (Low RH) at 20V	173
9.1	Hygrothermal-Conduction Experimental Scheme	176
9.2	Modified Conduction Test	177
9.3	Aging History of the Witness Boards	178
9.4	Aging History of the Conduction Boards	179
9.5	Thickness History of WB1 and CB2	183
9.6	Thickness History of WB2 and CB3	184
9.7	Non-Least Squares Fit of Moisture Absorption Data for WB1	186
9.8	Non-Least Squares Fit of Moisture Absorption Data for WB2	187

List of Figures

9.9	Non-Least Squares Fit of Moisture Absorption Data for CB1	188
9.10	Non-Least Squares Fit of Moisture Absorption Data for CB2	189
9.11	Non-Least Squares Fit of Moisture Absorption Data for CB3	190
9.12	Concentration-Distance Curves at 50°C/50% RH	194
9.13	Concentration-Distance Curves at 85°C/50% RH	195
9.14	Concentration-Distance Curves at 50°C/85% RH	196
9.15	Concentration-Distance Curves at 85°C/85% RH	197
9.16	Hygrothermal Leakage Conduction in CB1	199
9.17	Hygrothermal Leakage Conduction in CB2	200
9.18	Hygrothermal Leakage Conduction in CB3	201
9.19	Quasi-Steady State Currents measured at 85°C plotted versus actual water vapor density	204
9.20	Quasi-Steady State Currents measured at 85°C plotted versus relative humidity	205
9.21	Quasi-Steady State Currents measured at 85°C plotted versus net weight gain	206
9.22	Activation Energies measured in eV plotted versus net weight gain	208
9.23	CB1 (85°C/85% RH)	212
9.24	CB2 (50°C/50% RH)	213
9.25	CB2 (50°C/85% RH)	214
9.26	CB3 (50°C/50% RH)	215
9.27	CB3 (85°C/50% RH)	216
9.28	CB3 (85°C/85% RH)	217
9.29	Estimated α Values for the Exposure-Based Model	219
9.30	Estimated α Values for the Mass-Based Model	221
9.31	Performance of the First-Order Model on CB3 (50°C/50%)	225
9.32	Performance of the First-Order Model on CB3 (85°C/50%)	226
9.33	Performance of the First-Order Model on CB3 (85°C/85%)	227
9.34	Cross Section of the Test Sample with Marked Dimensions	229
9.35	Performance of Model on CB1 (85°C/85% RH)	235
9.36	Transient (Absorption) Currents when a step voltage of 100V is applied . .	237
9.37	Witness Board (WB1)	239

9.38 Witness Board (WB2)	240
9.39 Conduction Board (CB1)	240
9.40 Conduction Board (CB2)	241
9.41 Conduction Board (CB3)	241
A.1 Dimensions of the Comb Pattern	251
A.2 Dimensions of the Comb Pattern with Triangular Dimples	252
A.3 Dimensions of the Filled Square Pattern	252
B.1 Concentration-distance curves for an instantaneous plane source	258
B.2 Concentration-distance curves for a plane sheet of initial surface concentration C_0 at $x = l$	263
C.1 Non-Least Squares Fit of Moisture Desorption Data for WB1	265
C.2 Non-Least Squares Fit of Moisture Desorption Data for WB2	266
C.3 Non-Least Squares Fit of Moisture Desorption Data for CB1	267
C.4 Non-Least Squares Fit of Moisture Desorption Data for CB2	268
C.5 Non-Least Squares Fit of Moisture Desorption Data for CB3	269

List of Tables

3.1	Chemical Composition of E-Glass	54
5.1	Dimensions (in mils) of the Patterns on the First Generation Sample	102
5.2	Dimensions (in mils) of the Patterns on the Second Generation Sample . . .	107
8.1	Naming Convention for the Second Generation Test Samples	144
8.2	Board Characteristics	145
9.1	Dry Weight (g) and the Net Weight Gain (g) after each Conditioning Cycle	181
9.2	Net Weight Change During the Modified Conduction Test	182
9.3	Calculated Values of the Diffusion Coefficient and Saturation Moisture during Absorption	191
9.4	Calculated Values of the Diffusion Coefficient and Saturation Moisture during Desorption	192
9.5	Calculated Values of Quasi-Steady State (QSS) Current (A)	203
9.6	Calculated Values of the Activation Energy (eV)	207
9.7	Calculated Values of $\alpha_{\bar{\tau}}$ for the Small Pattern	218
9.8	Calculated Values of $\alpha_{\bar{\tau}}$ for the Large Pattern	218
9.9	Calculated Values of $\alpha_{\bar{\tau}}$ for the Volume Pattern	218
9.10	Calculated Values of $\alpha_{\bar{\rho}}$ for the Small Pattern (mm^3/g)	220
9.11	Calculated Values of $\alpha_{\bar{\rho}}$ for the Large Pattern (mm^3/g)	220
9.12	Calculated Values of $\alpha_{\bar{\rho}}$ for the Volume Pattern (mm^3/g)	220
9.13	Calculated Values of δ for the Small Pattern (eV) along with $E_{A,dry}$	222
9.14	Calculated Values of δ for the Large Pattern (eV) along with $E_{A,dry}$	222
9.15	Calculated Values of δ for the Volume Pattern (eV) along with $E_{A,dry}$	222
9.16	Average Values of α for Each Pattern	224
9.17	Average Values of δ for Each Pattern	224

List of Tables

9.18	Pattern Dimensions with the $\epsilon = g$	230
9.19	Pattern Dimensions	231
9.20	Ratio of Small QSS Current to Large QSS Current	232
9.21	The Least Squares Fitted Parameters for the Universal Curie-Von Schweidler Power Law and the Jonscher Low Frequency Dispersion Power Law	238
A.1	Active Lengths and Active Areas of all the Patterns on the First Generation Sample	255
A.2	Active Lengths and Active Areas of all the Patterns on the Second Generation Sample	256

Introduction

1.1 Introduction

RECENT years have seen a big increase in technical advances in automobiles. The direction of these advances has been toward including more and more electronics. Due to the resulting increase in electrical loads, the automotive electrical systems are moving towards higher power requirements. To meet this new requirement, the automotive industry established a new 42V standard that will eventually replace the 14V system. The mission of the MIT/Industry Consortium on Advanced Automotive Electrical/Electronic Components and Systems based in the Laboratory for Electromagnetic and Electronic Systems at MIT has been to improve the performance of automobiles using innovative and advanced electrical technologies. Many of the innovations significantly increase fuel economy, and some involve the replacement of automotive mechanical systems with electrical. Also, there has been a lot of focus on miniaturization of circuits so that more electronics can be incorporated into the vehicle without modifying the overall architecture too much.

In aircraft and space vehicles, adverse effects of failures in most electrical and electronic components can be kept in check through redundancy. However, the low costs required for high volume automobile manufacturing severely restrict the use of redundancy of components in road vehicles. Therefore, the components and wiring have to display a high degree of reliability against failure. Failures do occur and understanding when and how they can occur is central in ensuring this reliability.

Now, the average run time during the life of a typical automobile is usually much less than 50% and the run time of most electronic circuits in these automobiles is a much smaller fraction of this run time. Therefore, it is plausible that failure in most of these circuits results from environmental and ambient stresses, and not necessarily usage.

In fact electronic circuits face harsh environmental and operating conditions during their average lifetime. For example, Figure 1.1 illustrates the adverse temperatures that the automotive circuits experience under the hood of a typical automobile.

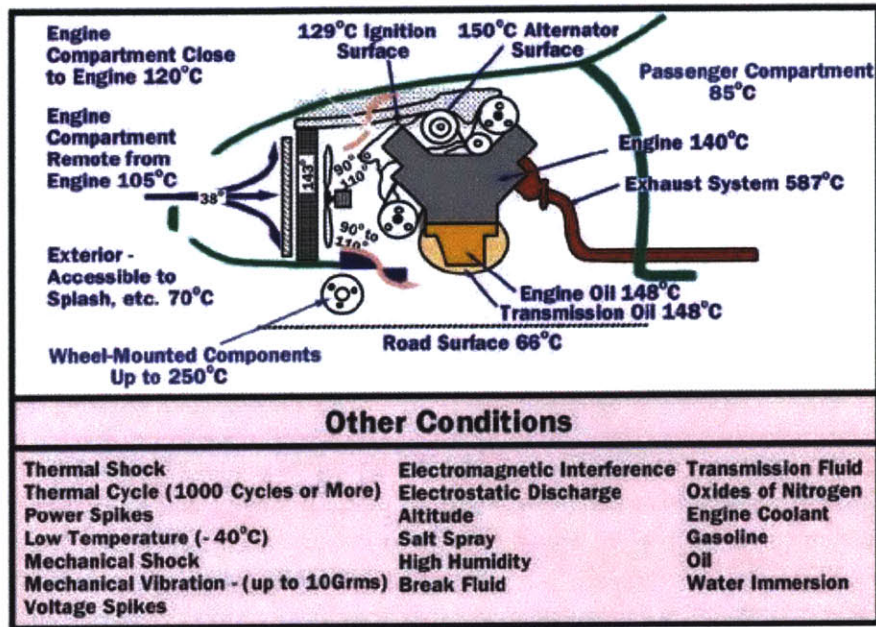


Figure 1.1: Typical Automotive Under-Hood Operating Environments [41]

In addition to temperature, they are subject to other stresses such as humidity, salt spray etc.

Therefore, the advances in the automotive electrical system coupled with the knowledge of possible failure mechanisms warrant the development of a test that accelerates certain causes and catalysts in the failure process and determines the reliability of a particular component. The acceleration of such processes is extremely important because most degradation mechanisms can take many years to manifest in real automotive environments.

To be able to develop such an accelerated test, there is a need for a robust model that not only explains how various environmental factors can affect the insulation in electronics but also be able to predict certain degradation phenomena.

Due to the constant development and change in automotive electrical systems, such an accelerated testing scheme should be scalable for many applications.

1.2 Automotive Electronics: The Printed Circuit Board

One of the many factors contributing to automotive electrical system reliability is the reliability of circuits built on printed circuit boards (PCBs). Briefly, a printed circuit board is made up of an insulating bulk base material on which copper traces (very thin wires) are printed in specific patterns to make a desired circuit. All manner of electrical components are attached to a PCB to produce a functioning circuit. A brief description of the morphology of typical insulating materials is presented in the Theory section of this thesis. A more detailed description of the chemical composition of PCBs, the method of manufacture and various properties can be found in [11].

PCBs are well represented in automotive electrical systems and are therefore a good choice for a starting case. They can be increasingly found in a variety of applications such as the automotive electronic control unit (ECU), airbag deployment controlling circuits, power electronic circuitry to improve the efficiency of alternators and with the advent of X-by-wire components, PCBs will be a major constituent of future vehicles.

Shown here is a glimpse of a other applications for PCBs in automobiles:

- Engine Control Modules.
- Power Train and Transmission Control Modules.
- Collision Warning Systems.
- Vehicle Stability Control Systems.
- Heating/Ventilation/Air Conditioning Controls.
- Suspension Controllers.
- Ignition Electronics.

In addition to the automotive industry, PCBs are widely used in many other industries. In the oilfield services industry, electronic circuitry on PCBs are exposed to extreme conditions of temperatures and humidity beneath the surface of the earth and therefore a good degradation model can be useful for many such applications.

1.3 The Study of Electrical Conduction

It can be hypothesized that electrical conduction as a result of electrochemical reaction is a primary cause for insulator degradation. To be able to effectively study degradation, an appropriate metric might be current. Since degradation is an accumulation of damage over time, charge (Q) (integral of current over time) can also be a major indicator. Charge also gives us an idea of the amount of material that might have been transported through the insulator (by Faraday's Law) from one metal electrode to the other.

As stated earlier, degradation is believed to be caused by conduction in the insulators. But how is this conduction affected? We know that current (I) is given by the rate of change of charge (Q).

$$I = \frac{d}{dt}Q \quad (1.1)$$

This means that we can change conduction by changing charge or the time it takes to travel through the insulator. There are three simple ways this current can be increased as shown in Figure 1.2:

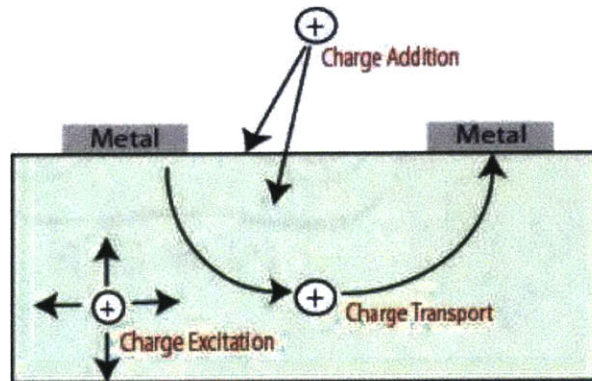


Figure 1.2: Impact of Charge on Conduction in Insulating Systems

- *Addition of charge carriers* from the external environment or from the metal.
- *Excitation of charges carriers* resulting in faster moving charges and therefore smaller transit time therefore higher currents.
- *Better pathways for charge transport* consider how these charges move in the material

and reduction of the physical barriers that impede this movement and increase transit time.

Conduction in many insulators and automotive PCBs in particular, is influenced by many different factors as mentioned in Section 1.1. Figure 1.3 highlights a few of those factors.

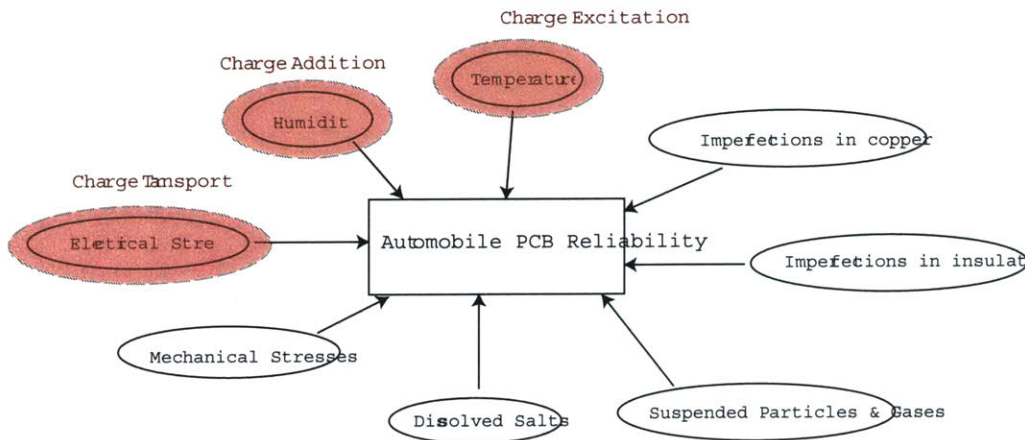


Figure 1.3: Factors Affecting Conduction During the Service Life of PCBs

These factors contribute by influencing conduction through the three methods of addition, excitation and transport of charge carriers. We have considered three of the many factors indicated by the shading. Depending on the details of any particular duty, one of the other factors in Figure 1.3 may be the most important consideration in that case, but the highlighted combination of factors is known to produce life-limiting changes in many important cases. This, therefore presents a useful starting point.

Humidity adds charges to the system, temperature excites these charges and electrical stresses (voltages) facilitate the movement of these charges through the insulator. Additionally, temperature could also modify the structure of the insulator and thereby create less resistant pathways for charges to flow.

In order to study conduction and eventually degradation in PCBs, we have to measure currents on the surface and through the volume. Additionally, we would like to study which parts of the insulator suffer a concentration of stresses.

1.4 Current Literature on Reliability Measurement

In the introduction, the need for an accelerated reliability test, linked to a strong theoretical understanding of insulation degradation is described. However, at this point it is important to review some previous work in theory and established reliability tests that are currently being used. A search into insulation degradation and reliability in PCBs will produce numerous matches that showcase the extensive work that is being undertaken by various universities and industrial entities. However, some commonalities do exist in this body of literature and I will point out some of them.

At the root of many industrial tests lies the IPC-TM-650 Test Methods Manual. IPC - Association Connecting Electronics Industries is a member-driven organization and leading source for industry standards. This manual (TM-650) contains industry approved test techniques and procedures for chemical, mechanical, electrical, and environmental tests on all forms of printed boards and connectors. It establishes uniform methods for testing electronic and electrical parts including basic environmental, physical and electrical tests. These tests were developed to support IPC standards and specifications. Shown below is a summary of some of the IPC-TM-650 methods manual's electrical and environmental tests: This summary is presented without discussion or elaboration, simply to demonstrate that there are many test protocols, containing many similarities but each emphasizing a slightly different aspect of performance.

IPC Test Methods (IPC-TM-650) Method 2.5.27

Surface Insulation Resistance (SIR) of Raw Printed Wiring Board Material.

Being evaluated	SIR of PWB materials after conditioning
Test Conditions	50C - 24hrs, measure (500V charge, measure after 1 min.), conditioning cycle of MIL STD-202 (150C - 2hrs), measure
Tested On	IPC-B25 test board, 25 mil spacing

IPC Test Methods (IPC-TM-650) Method 2.6.3.1

Moisture and Insulation Resistance (IR), Polymer Solder Masks and Conformal Coatings.

Being evaluated	Moisture and IR
Test Conditions	Class T: 65C, 90% RH, no bias voltage, 24 hrs Class H: 25-65C, 90% RH, 50V DC bias, 6 2/3 days, 100V polarization
Tested On	IPC-B25-B or E for compliance testing

1.4 Current Literature on Reliability Measurement

IPC Test Methods (IPC-TM-650) Method 2.6.3.2

Moisture and Insulation Resistance, Flexible Base Dielectric.

Being evaluated	Moisture and IR
Test Conditions	50C, no added humidity - 24 hrs Initial IR - 500V polarization Classes 1 and 2: 35C, 90% RH, 4 days, no bias voltage Class 3: 25-65C, 90-98% RH, 6 2/3 days cycling (20) 100V bias recovery: 23C, 50% RH, 2-24 hrs Final IR ambient - 500V polarization
Tested On	Bellcore SIR coupon - 25 mil lines, 50 mil spaces

IPC Test Methods (IPC-TM-650) Method 2.6.3.3

Surface Insulation Resistance, Fluxes.

Being evaluated	Moisture and IR of liquid fluxes
Test Conditions	Class 3: 85C, 85% RH, 7 days, 45-50V polarization, 100V test (reversed polarity), 50 bias
Tested On	IPC B-25 comb pattern

IPC Test Methods (IPC-TM-650) Method 2.6.13

Assessment of Susceptibility to Metallic Dendritic Growth: Uncoated Printed Wiring.

Being evaluated	Effect of ionic residues and condensed moisture on the growth of electrochemical dendritic structures
Test Conditions	15 V, water drop, ambient temperature, current limiting re- sistor
Tested On	Military "Y" pattern, parallel conductors with a spacing 15- 30 mils

IPC Test Methods (IPC-TM-650) Method 2.6.14

Resistance to Electrochemical Migration, Polymer Solder Mask.

Being evaluated	Resistance of Polymeric solder mask to electrochemical mi- gration
Test Conditions	Class T: 85C, 90% RH, 500 hrs, 10V bias Class H: 85C, 85% RH, 168 hrs
Tested On	IPC-B25A

Introduction

In addition to the IPC based standards and methods, there are other industrial standards that have been developed. A brief description of some of this work is shown below:

Dupont Electromigration Test

Being evaluated	Electromigration in the presence of a water drop.
Test Conditions	Ambient temperature, 6.5V, 6-8 micro amps
Tested On	IPC-B25A

Siemens-Stromberg-Carlson Electromigration Test

Being evaluated	Electromigration resistance of coatings, masks, adhesives etc.
Test Conditions	85C, 90% RH, 500 hrs, non-condensing atmosphere 10V bias, 100V test voltage (same polarity), 1M Ω resistor
Tested On	IPC-B25B patterns (coated)

Unisys Electromigration Test

Being evaluated	Electromigration on any surface.
Test Conditions	125F, 95% RH, 20 hours, 250V
Tested On	5000 Å copper over 400 Å chromium on glass, 10 mil lines, 50 mil spacing

Bellcore TR-NWT-000078, Method 12.1.5 "Electromigration Resistance"

Being evaluated	Compliance of fluxes, pastes, coatings with respect to electromigration.
Test Conditions	85C, 85% RH, 500 hrs, 1M Ω limiting resistor, 96 hr stabilization at 85C, 85% RH - no bias Measure SIR - test voltage 45-100V then 10V bias for the remainder of the test.
Tested On	IPC-B25B or E

The IPC tests are designed as universal tests on a specified standard printed circuit board material regardless of the final use. Most printed circuit boards in automobiles use standardized insulation material and therefore could possibly be studied using these tests.

However, it is clear from the above examples that there are numerous and sometimes overlapping standards and tests. Most of these tests are obtained from contributions from

industry members to the standardizing organization. Many such industry-based standards consist mainly of a pass/fail criterion where a certain threshold is set and the performance of a product is defined by whether it is above or below the threshold. Also, the determination of acceleration and test environmental conditions are quite arbitrary and not clearly justified. This has been working acceptably well in the automotive industry so far because there are available physical samples of automotive parts that have been on the road for many years. Many standards have been developed on the basis of the performance of weathered samples. However, with the possibility of 42 volt systems or 288 volt systems in the case of hybrids, such samples do not exist for the new systems. These tests developed for lower voltage systems might not scale easily and therefore may not display the same degradation physics at higher electrical stresses. Therefore there is a strong need for better accelerated testing methods that have some theoretical backing.

Additionally, it was noticed that the test sample is different for many of the tests. The most common one used is the IPC-B-25A sample. The IPC-B-25A is a multipurpose test board with six different test patterns. Figure 1.4 shows all these patterns.

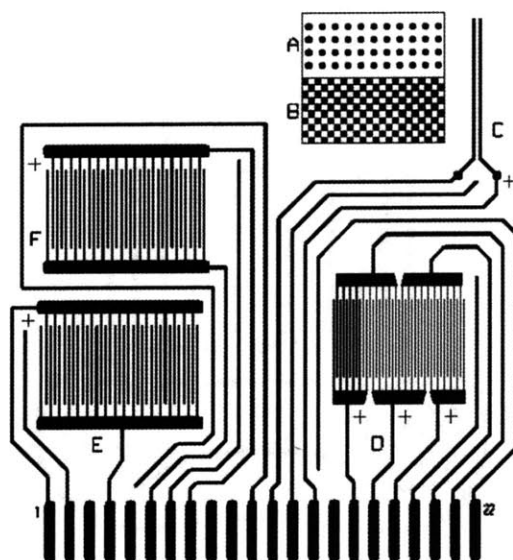


Figure 1.4: IPC-B-25A Multipurpose One-sided Test Pattern

In addition to the industrial standards such as IPC, there are numerous publications in different journals that describe degradation models and mechanisms and the development of interesting techniques to detect and analyze failure modes. For example, work has been done by Harsanyi[26] to study and present many different processes in electrochemical migration. Amla[7], Ready[46] and Navarro[42] have contributed to the understanding of

Introduction

Conductive Anodic Filaments¹. Simultaneously, Chan[10], El-Kishky[24], Jachim[27] and Sarkar[48] have explored the topic of surface insulation resistance.

Also, there have been many publications that record insulation degradation in terms of mean time to failure (MTTF). The probabilistic behavior of this estimator is determined by running many experiments on many different samples. The problems with running many experiments are evident. The benefit is that we can come to understand the characteristics of a whole class of samples without worrying too much about individual anomalies.

After reviewing these and many other publicly available research reports, there seem to be many common patterns. First, many researchers have studied the behavior of surface insulation resistance. But the methodology is far from universal. There have been different voltages used for the aging interval (bias voltage) and different voltages used for measurement (test voltage). Also, most of the measurements have been taken periodically either once per day or at most once per hour.

The approach presented in our research is quite different from previous work in many respects including those mentioned above.

1.5 Our Approach

Our approach will differ from existing work in that far more frequent measurements will be made. With the help of a robust data acquisition system, we can take measurements every minute, second, or millisecond depending on the test being performed.

Also, since we are measuring leakage currents, we take measurements during the test. One obvious advantage of measuring currents at a higher frequency and during the experiment is that we may capture transient events which precede total circuit breakdown. Additionally, we will be applying the same voltage for biasing and testing. Also, we will have a more accurate idea of the total charge being transferred by integrating current over time. We can then determine the total mass of material that might have been transported using Faraday's Law. These are some of the many different techniques this research is attempting. Later chapters in this thesis will illustrate the various techniques and challenges.

¹Copper corrosion byproducts that emanate from the anode and grow subsurface toward the cathode.

1.6 Thesis Goals

The goals of this thesis are: 1) To build and automate an experimental test setup, 2) To design and build a test PCB with specifically chosen patterns to test different conduction mechanisms, 3) To design and run experiments with varying temperatures, humidities and voltages, and 4) To identify a likely model to explain electrical conduction in PCB insulation.

1.7 Thesis Organization

This thesis is divided into 3 major parts. Part 1 includes chapters 2, 3 and 4 where a theoretical background is presented. Here, the reader can become more familiar with the exact scope of this work, refresh some fundamental principles and become acquainted with some current research in the field of insulation degradation and leakage conduction. Part 2 includes chapters 5, 6 and 7 where the entirety of the experimental setup is discussed. This includes a detailed look at the test samples, measurement devices and interference reduction techniques. Part 3 includes chapters 8 and 9 and presents a procedural summary of all the experiments performed and results accompanied by discussions and interpretations. Chapter 10 concludes and summarizes the work with some suggestions for possible future directions.

Part I

Theory

Theoretical Overview

THIS chapter establishes an overall framework for research in the area of insulation degradation and accelerated test specification accompanied by a fairly comprehensive literature survey. The scope of our research work will then be carved out from this framework. The specific topic of conduction is addressed in Chapter 4.

2.1 Introduction

Chapter 1 briefly outlined the various accelerated tests used in the industry. It was observed that these tests were not based on any physical theory, instead on a group of statistical measurements of failure and on the experience gained from decades of observation and postmortem analyses. The accelerated environmental conditions were chosen quite arbitrarily and might not be representative of the actual physical processes that occur within the insulation prior to failure. In one testing method, samples were placed in specified accelerated conditions and as soon as electrical failure was observed, time to failure was recorded. In an another method, samples were placed in an environment for a fixed period of time and then certain measurements were made that determined if it either passed or failed its reliability assessment. There could have been many different physical processes that might have caused failure in either method and therefore these testing methods give us no indication of the cause of failure. Without an understanding of the cause of failure, parts often fail even when they might otherwise pass these tests.

To perform an accelerated test is to modify and scale certain test variables that “might influence parts in real world use” so as to speed up physical processes causing degradation and failure. In this way one might be able to predict how the part might perform in regular use. However, one must ensure that scaling some of the environmental or electrical variables does not engage physical processes that would otherwise not occur. This problem becomes evident when certain parts that might function well in regular use fail the accelerated test. For example, if we apply test voltages and temperatures that are too high then the physics of failure is very different from the failure modes in typical service conditions and consequently the part fails the accelerated test even though it may have worked well in service.

Appropriate scaling of test variables plays a crucial role in specifying future accelerated tests when automotive electrical systems will operate at higher voltages. Parts that might be adequately tested and passed by older accelerated tests are not guaranteed to perform at these higher voltages. More importantly, we will not have decades of knowledge gained from failed parts to compare and fine tune our testing methods.

To address these concerns we have to develop a body of theoretical and experimental work that helps reveal some of the fundamental physical mechanisms that constitute these failure processes. Starting with the assumption that electrical conduction is one of the causes for electrical degradation and aging, we will seek an intuitive physical model to describe the behavior of electrical currents in PCB insulators in different environmental and electrical conditions.

2.2 Organization of Research

In developing such a body of theoretical work in the area of accelerated testing and insulation degradation, it becomes very obvious very quickly that there is an overwhelming amount of published literature representing a broad area of sub-topics ranging from the purely theoretical to the purely experimental. In addition, plenty of work has been done on a wide array of materials and accelerated tests have been specified for different uses depending on the service application of the material. A “good coverage” of all this literature, let alone an exhaustive one is lacking and developing such a summary can be quite a challenge. Shown in the discussion below is an attempt to present relevant and well cited literature in the context of designing an accelerated test and understanding insulation degradation.

With the previously stated notion that electrical conduction is a major cause as well as a good indicator of degradation we will focus our interests on understanding conduction behavior. Other physical and chemical factors influencing degradation and consequent breakdown serve to strengthen the understanding of electrical leakage currents and therefore we will study them in that context. This will help in reducing our research scope in this broad and extensively studied field.

Shown in Figure 2.1 is a framework for the different relevant approaches to characterizing and building an accelerated test.

Accelerated reliability tests for simulating (in compressed time) the performance of a material in service conditions are usually specified in a macroscopic framework. Studies falling

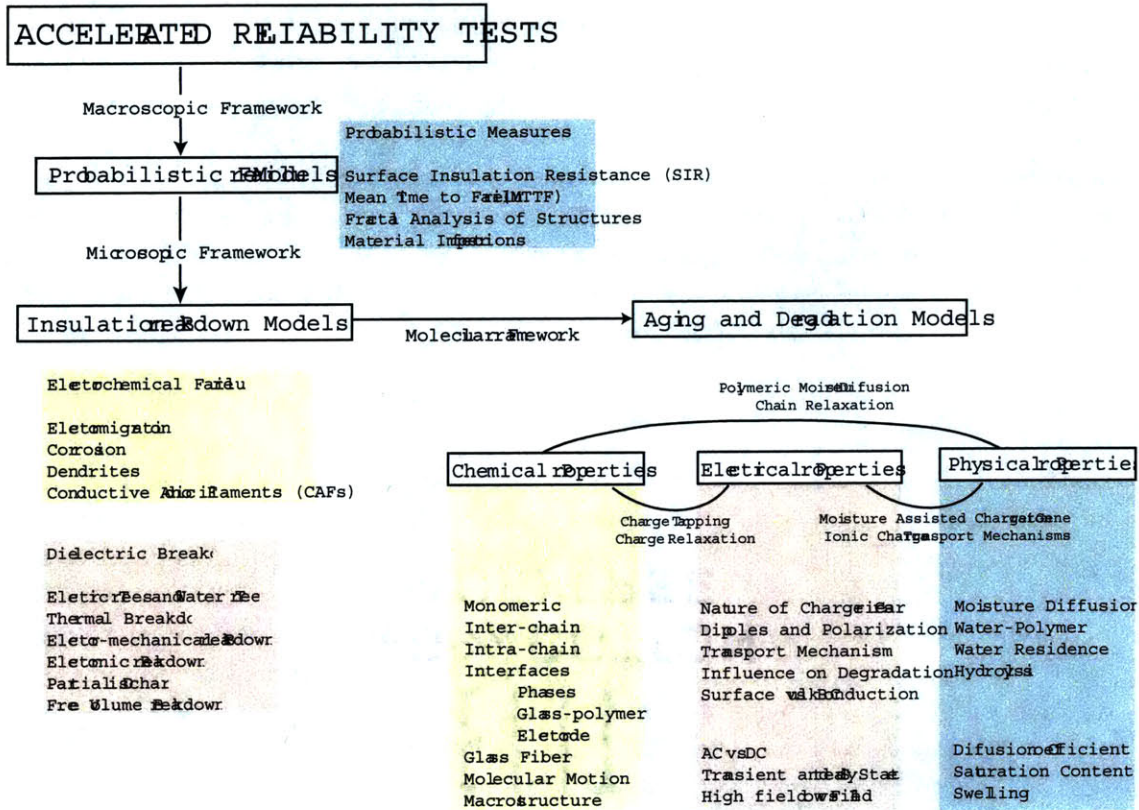


Figure 2.1: Research Framework for Accelerated Reliability Test Development

under the umbrella of a macroscopic framework explore the failure of many parts simultaneously. Statistical distributions are generated for a family of parts and, therefore, group characteristics can be easily derived without worrying about individual anomalies. Extrapolations based on such statistics are used to estimate the working lifetime. The tests typically follow a pass/fail criterion that qualify or disqualify a part based on established group statistics. Acceleration factors are also calculated to determine the amount of scaling the testing variables have to undergo. The advantages of easing automation and design of parts through large scale testing are overshadowed by a number of disadvantages and objections. Without a solid understanding of the physical processes and mechanisms underlying failure, the acceleration factors can be misleading. For example, many accelerated tests use the measure of electrical surface insulation resistance to determine the state of degradation. A lack of understanding of the physical meaning of insulation resistance in heterogenous materials such as PCBs, makes this metric fairly meaningless and the pass/fail criterion inadequate in testing reliability. The choice of testing conditions is also crucial and variations in a sample's history and its predisposition to a specific test variable could affect the test data. The most important objection to a purely macroscopic approach is that

Theoretical Overview

the accelerated tests they specify are not scalable. In other words, if a certain in-service stress variable were to be modified (higher voltages in future automotive systems), then accelerated tests cannot be specified from the available data of all the other samples.

Sometimes such modifications of stress variables can occur during the service life of parts. As pointed out by Dissado [18], long time changes during service alter factors that control reliability and failure modes. Material aging takes place too slowly to influence accelerated tests and hence the in-service quality of insulation can only be fully assessed by means of a thorough investigation of the aging process itself.

Analyzing these shortcomings of the purely probabilistic approach will lead us to a microscopic framework which looks at the origin of failure and degradation in which an understanding is acquired through the study of individual parts. The microscopic framework includes the modeling of breakdown phenomena in insulators. Breakdown by definition is catastrophic, meaning that, it is both an irreversible process as well as a destructive one. There are at least two different classifications of breakdown models. The first classification is electrochemical models which includes phenomena such as electrochemical migration (processes similar to electroplating). These processes are purely electrochemical in nature and only occur in the presence of adequate quantity of bulk electrolytic material. Typical accelerated tests derived from such models include different varieties of “water-drop” tests such as those specified in the Section 1.4. The electrochemical processes can be manifested on the surface as well as in the bulk of the insulation and have their origins from external impurities. The electrochemical breakdown mechanisms can develop without any damage to the insulation itself. For instance, the growth of dendritic structures (metallic ionic species) on the surface between two electrodes is accompanied by failure of the corresponding circuit due to the dendritic bridge. However, after the short circuit, the dendritic residue can be removed from the surface leaving behind an intact insulator.

The other classification of breakdown models is dielectric breakdown mechanisms. These are different from electrochemical models because they involve the breakdown of the insulation in a fundamental sense. There is no particular need for any external impurities, however, such impurities do facilitate the processes. Dielectric breakdown mechanisms include electrical and water treeing, thermal breakdown, electromechanical breakdown, electronic breakdown, partial discharge and free volume breakdown. These mechanisms will be discussed in more detail in Section 2.4. Typical metrics used to analyze breakdown data include insulation resistance, time to failure, time to bridge electrodes, visual analysis and voltage-current and current-time curves.

Since insulation breakdown models involve the study of individual parts, they have to eventually be generalized using some kind of statistical distribution to be useful in large

scale accelerated testing. Also, breakdown itself is a statistically distributed process and thus to be genuinely applicable to real systems the deterministic models must be modified to allow for the possibility of stochastic features in the development of instability.

However, insulation breakdown models may not be as useful as what it can sometimes seem in the literature. Most studies in the past have focussed on understanding one or two individual breakdown mechanisms that they believe are dominant. Even though this approach is important in improving our understanding of the influence of electrical degradation on breakdown characteristics, it does nothing to determine the generation and the origin of this electrical degradation over a period of time. As stated earlier, depending on the typical service life of a piece of insulation, it might be subject to long term modifications that consequently change factors that are crucial in determining dielectric failure statistics and if one or another breakdown mechanism dominates.

Within the molecular framework we have the aging/ degradation model which is primarily the study of the material itself as opposed to a specific failure mechanism as was the case of the insulation breakdown models. Aging is defined as the gradual decay of the capacity of a material to behave as an electrical insulator. While breakdown occurs in very small time scales and at well defined high electric fields, degradation and aging processes occurring in service conditions (where such high fields are non-existent) lead to weakening of insulation over a long period of time ultimately culminating in breakdown. Analysis of most breakdown mechanisms require a strong understanding of the way in which carriers may be injected into insulators from the electrodes and the external environment and subsequently move through the bulk during its regular service life.

Aging models can be divided into three major sub-groups - chemical properties, electrical properties and physical properties. Chemical properties refer to the fundamental chemical make-up of the material. In the case of polymers (epoxy in PCB insulation) this includes monomeric units, inter- and intra-chain characteristics, interfacial properties and molecular motions. In composites (PCB: epoxy+fiberglass), glass fibers and the overall macrostructure of the material is also very important. Electrical properties include the answers to important questions such as the nature of charge carriers, transport mechanisms, and differences between surface and bulk conduction mechanisms. Many industry accelerated tests are performed on samples with surface patterns only and therefore do not account for any bulk breakdown mechanism in the material. Electrical properties can be studied in many different ways such as energizing the samples in both high and low AC and DC fields and analyzing transient and steady state (for DC) currents. Finally, physical properties include the study of external influences such as moisture and other impurities.

As described earlier, automotive PCBs experience conditions of high temperature, high hu-

midity and DC voltages during their lifetimes. Therefore, the interplay between the three groups (chemical, electrical and physical) is crucial. The chemical nature of the material influences the movement and residence of charge carriers. Dipole and charge relaxation phenomena can be highly influenced by the chemical structure of the polymer. The chemical structure can also influence general environmentally driven processes such as moisture diffusion. Polymeric chain relaxations also modify moisture diffusion characteristics to a strong extent. The role of moisture is many-fold. Besides physically modifying the structure and contributing to weight, moisture is actively involved in charge generation either through hydrolysis or through the hydration of ionic species. Thus, in addition to contributing to the polarization of the material, water plays an important role in possible ionic charge transport mechanisms.

A limitation of such an involved scientific study of degradation and aging is the specificity of the problem. In the end, a statistical distribution will be needed to benefit large scale design and manufacturing. However, the development of an appropriate metric or a well informed accelerated factor through a well designed molecular model might eventually enable us to develop better accelerated tests.

The scope of our research and this document is limited to the study of electrical conduction in PCB insulation. This would place us firmly in the lower right hand side of Figure 2.1. Within this field of study, we will further limit ourselves to DC conduction at relatively low fields ($< 10^6$ V/m) and low temperatures (less than glass transition temperature).

In the following sections we will look at relevant literature in each part of the framework presented in Figure 2.1.

2.3 Probabilistic Failure Models

In Section 1.4 we looked at the different accelerated reliability tests specified by industrial standards. It was discussed there that these tests lacked sufficient physical understanding and are therefore not very good at predicting service life except possibly for the narrowly defined circumstances for which the test was developed. In the following, we will discuss some industry accelerated tests and some published literature on macroscopic failure models.

Most accelerated tests use the metric of Surface Insulation Resistance (SIR) as a means to qualify the performance of PCBs. The Institute of Printed Circuits (IPC) explained SIR in its IPC-9201 document [2]. Kinner[32] and Sarkar[48] are a few names among many that have provided a good introduction to SIR and some experimental data of SIR test

cases. There are many drawbacks that plague SIR testing methods. The problems briefly stated included the inability to differentiate true SIR measurement from ionic migration in water and contaminants on the surface. Additional concern was pointed towards the dependance of SIR on biasing and history. Chan [10] discussed some the drawbacks of DC SIR measurement and proposed the use of large AC voltages to enable voltage-based acceleration. The IPC tests and many other SIR based tests fall under the macroscopic framework of probabilistic degradation and failure models.

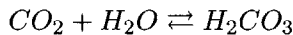
Ricardo plc (a major consultancy serving the auto industry) and one of our sponsors) conducted an analysis of the reliability of automotive electronic control units which are made with PCBs [35]. The purpose of the analysis was to ensure that the design rules on the PCB do not result in electrochemical migration when the board is stressed with voltages. The results of these tests was also believed to guide future testing schemes. The test was based on the IPC-TM-650 manual of standards. The sample was placed in a high temperature and high humidity environment and insulation resistance was measured once per weekday and a resistance below one mega ohm was ascertained to be a failure. An important concern which should be addressed when taking such measurements is the amount of time to wait before actually taking a reading after the application of a voltage. The polarization (transient) currents can be orders of magnitude above steady state currents and could take as much as tens of minutes to settle down. Another important observation made was that surface patterns with ground planes below had much lower currents than surface patterns with no ground planes. This might indicate that the ground plane actually provides an alternative path for current. The observed decrease in current was due to the fact that the bulk material played a dominant role in conduction and therefore some of the current was leaking to the ground plane and hence not measured.

As it was seen in Section 1.4, IPC has many accelerated reliability tests that assess various parameters. One such test of relevance is the Surface Insulation Resistance Test (SIR) - IPC-TM-650-2.5.27 [3]. The test involves the measurement of surface insulation resistance of a PCB after conditioning in a certain environment. The procedure firstly requires the drying of the PCB for 24 hours at $50^{\circ}C$. However, this brings up an important concern of whether the process of moisture desorption has reached equilibrium. If it hasn't equilibrated then we would not have a clear idea about the amount of water in the material and therefore this procedure would not provide a good starting point. The specimens are then subjected to high voltages of 500V followed by conditioning at $150^{\circ}C$. We will see later in this chapter that the physics of conduction and degradation are very different at low and high fields. Additionally, the temperatures used are very close to the glass transition temperature (T_g). The glass transition temperature, typically, signals the onset of molecular chain motions and a shift from the glassy state to the rubbery state of the material. This shift can significantly affect electrical conduction as well as moisture absorption. During their service lives, PCBs

may never undergo such transitions or experience such high voltages. Therefore, such a test might engage failure modes that might never occur. On the application of a voltage, the SIR test requires a settling time of 60 seconds before any resistance measurement. Typical relaxation times observed are on the order of 100s of seconds. Therefore, the specified settling time is far too little. This will become more clear in later chapters when our results are discussed.

Another IPC standard of a similar nature is IPC-TM-650-2.6.3 [3], which specifies a degradation measurement through insulation resistance and visual cues after exposure to high temperature and high relative humidity. The samples are dried for 3 hours at $50^{\circ}C$ before the test. Once again this step suffers from the same drawback discussed earlier of the transient state of hydration. A 100V polarization voltage is applied during the span of the test. Such voltage application could result in the build-up of space charge which can consequently impact the measurement. Another interesting testing condition used is $35^{\circ}C/85\%$ RH for 4 days and $50^{\circ}C/85\%$ for 7 days and temperature cycling of $25^{\circ}C-65^{\circ}C$ and 85% RH for a total of 160 hours. The most glaring inconsistency (which will become obvious through this document) is the choice of number of days for each condition. The authors of this standard have chosen to apply the condition of lower temperature for a much shorter time than the condition of higher temperature. The need for a steady moisture level demands that these conditions and the corresponding times be reversed. This has made evident that the IPC tests have most certainly not given the role of moisture the importance that it deserves.

Additionally, there has been some published literature in accelerated testing and SIR measurements. An early paper by Sbar and Kozakiewicz [49] presented a method of calculation of acceleration factors for temperature and humidity testing. Even though the work suffers from the same shortcomings that all experiments involving SIR suffered, there were some interesting bits of information that might be valuable including the linear variation of isothermal SIR with relative humidity. The work also discussed the formation of conductive species from the reaction of CO_2 and water.



Electrical circuit analogues also fall under the macroscopic framework. Takahashi [56] presented the development of such an equivalent circuit model to describe conduction paths and mechanisms in FR-4 Epoxy/Glass PCBs. It was concluded that there were three major conduction paths including through the epoxy (modest but enhanced by moisture penetration), through the surface (indicative of mobile ionic contaminants) and through the glass/epoxy interface. It was found that interfacial conduction was dependent on moisture

penetration to the glass fibers. These three paths were determined from the impedance spectra on a sample board. Additionally, two major mechanisms were dominant: diffusion-controlled ionic conduction and a purely ohmic conduction. An interesting statement made in this paper was that the author believed that the exposure of samples to a large DC bias after equilibration with a humid environment resulted in a catastrophic failure. This work presents some very important general observations about the difficulty in specifying an accelerated test. However, a generalized circuit model does not provide an adequate physical explanation for the processes leading up to insulation failure.

The importance of interfacial processes was highlighted by Park [43] where it was shown that leakage currents are quantitatively related to the size and extent of the interfacial adhesion damage. Even though the study was limited to the understanding interfacial adhesion damage in dual in-line packages, there are some useful aspects which might be of interest such as the response of the interfacial leakage currents to moisture penetration.

2.4 **Insulation Breakdown Models**

The microscopic framework of insulation breakdown is one of active research. There have been numerous efforts to classify different failure mechanisms for different materials. However, a single general theory of breakdown with the ability to explain failures in all materials including highly disordered polymeric media does not exist. Dissado [18] presented a very good review of some breakdown models. The following is a summary of Dissado's survey.

Breakdown, according to Dissado [18] is the destructive generation of a conducting path in insulators. Most catastrophic processes are electrically driven and ultimately thermal. In the presence of high fields (required for breakdown), instability arises and current rises many orders of magnitude at a constant field. The power dissipated during this time will melt and vaporize the material. Many times there is a positive feedback mechanism between local heating and impact ionization. Deterministic models are categorized according to the processes that are postulated to lead up to catastrophic breakdown as described above. Breakdown can be categorized into "thermal models" where applied power causes heating which leads to increased conductivity due to increased carrier generation and consequently a diverging process; "electrical models" where initiation is caused by locally high fields; "electromechanical models" where electrostatic attraction between the electrodes causes local softening and cracking; and finally "partial discharge models" which involves the ionization of voids causing progressive damage. These different breakdown mechanisms are believed to be either competing with one another where the winning process leads to breakdown the quickest, or in cooperation where various breakdown mechanisms occur at

various stages. Breakdown mechanisms that are cooperative and accumulative can potentially embody stochastic possibilities due to wide spatial and temporal variations. When the mechanisms are in competition, the winning mechanism is highly dependent upon field and operating condition. Imperfections in the insulating systems can enhance degradation processes and bring down the breakdown fields. Also, the electric fields themselves are believed to be widely varying throughout the material and consequently display a distribution of breakdown strengths.

Dissado [18] [17] presented a comprehensive study of various breakdown mechanisms which we have summarized below. Electrical trees are connected channels (hollow tubules) a few microns in diameter with branches of tens of microns long. The walls are not always carbonized and only weakly conducting. Therefore, bridging doesn't always imply a short circuit. They are, therefore, not viewed as a visual aspect of an intrinsic runaway breakdown mechanism, instead they contribute to the cumulative degradation process. Dissado [18] also included a chapter devoted to the study of water trees. Water trees occur at much lower fields than electrical trees. Also, considerable time is required for them to form. Another requirement is the presence of bulk aqueous electrolyte in contact. Most water trees, however, are conducting and can initiate the growth of electrical trees. Partial discharge (PD) was only touched upon in the previous paragraph and requires more attention [18]. Small gas filled voids are quite common in polymeric insulation. These voids have a lower permittivity than the surrounding polymer and hence there is the possibility of field intensification at the boundary walls. The enhanced field can cause ionization and breakdown or discharge within the void. Carriers produced during ionization accelerate across the void and impact the opposite walls causing erosion. Depending on the thickness of the insulation, this process can lead to immediate failure (breakdown) or gradual degradation. PD initiation depends on the gaseous contents, pressure and void characteristics. Due to the inhomogeneity, PD itself is a distributed process. In accelerated conditions, PD quickly leads to the formation of electrical trees which span the insulation and cause breakdown. In service conditions and uniform electric fields, trees do not form immediately, instead defect centers are created that slowly combine to form clusters that are elongated in the direction of the electric field. Breakdown occurs through the weakest link offered by the alignment of these defects.

Having discussed the basics of dielectric breakdown, we will now shift our focus to electrochemical failure models. There has been plenty of work done in this area of electrochemically induced failures and breakdown. Krumbein [33] [34] presents a good tutorial to understanding the phenomena of metallic electromigration as well as various electrolytic models for the electromigration mechanisms. Metallic electromigration is defined as the movement of metallic material, usually through or across a nonmetallic medium under the influence of an applied electric field. The migrating material is usually in the metallic state and not

a corrosion by-product. The mechanism of electromigration is water-dependent and tends to occur whenever the insulator separating the conductors has acquired sufficient moisture to allow for ionic conduction. Some work has also been done by Harsanyi [26], Young [60] and Mouthaan [40] to study and present many different processes and models to describe electrochemical migration. Bhakta [9] presents some accelerated tests to simulate metal migration in hybrid circuits. Statistical distributions such as Weibull plots were used in this study to determine acceleration factors and dominant mechanisms in metal migration. The phenomena of conductive anodic filaments (CAFs) were first noticed when copper filaments were reported to be growing from anodically to cathodically polarized electrodes after the glass-epoxy printed circuitry (with copper conductors) had been subjected to conditions that produced local physical separations of the epoxy resin from the glass fibers. Amla[7], Ready[46] and Navarro[42] have contributed to the understanding of Conductive Anodic Filaments.

We will not be looking anymore into electrochemical models. However, we will be vigilant about the possibility of charge carriers being ionic and hence indicating a strong possibility of an ionic degradation mechanism preceding an electrochemical breakdown mechanism.

2.5 Aging and Degradation Models

Aging is a form of degradation process that impacts and changes the probability of ultimate breakdown over the course of time. Dissado [18] talks about four types of aging processes - physical, chemical, electrical and electromechanical.

As the temperature of the material decreases from high temperatures towards T_g ¹, molecular chain motions decrease. This results in a slow down in the return to equilibrium of mechanical strains and dielectric responses (α relaxation). The time dependent change as a system moves towards thermal equilibrium is what is known as physical aging. It is important to note that physical aging below T_g is almost non-existent. One theory to describe and explain this type of aging mechanism is through the reduction of free volume (The microscopic voids inherent to the material).

According to Dissado [18], chemical aging occurs as a result of the formation of reactive free radicals eventually leading to chain scission and cross-linking. Chemical aging is initiated thermally, through an oxidation process, through ionizing radiation, through mechanical stresses and through hydrolysis.

¹ T_g : Glass Transition Temperature, Temperature above which the material moves from a glassy state to a rubbery state.

Theoretical Overview

Physical and chemical aging processes do not require the application of an electric field and can be easily prevented in service. However, since electrical aging occurs due to service conditions itself, it cannot easily be prevented. DC fields are responsible for dissociation and transport of ionized and ionizable by-products. Electrical aging usually results in breakdown processes such as electrical trees, water trees and partial discharges. Also, mechanically assisted electrical degradation occurs when the breakdown strength is reduced as a result of mechanical stress. Furthermore, defects and traps can trap space charges thereby increasing local fields.

Another important point that can never be stressed enough is the fundamental difference between electrically assisted aging processes and electrical breakdown of insulators. Breakdown mechanisms only occur in the presence of high electric fields. However, aging mechanisms can occur at much lower fields. The slow degradation caused by the aging mechanisms eventually enhance local electric fields and cause breakdown. We are interested in understanding the slow degradation processes that lead to breakdown.

Keeping in mind our primary interest of modeling electrical conduction, we will look at the aging process a little differently. We will attempt to identify the nature of the charge carrier, transport mechanism and external influences on leakage currents. In the upcoming chapters, we will look at the basics of electronic and ionic conduction and look at the various low field and high field conduction mechanisms. However, before we step into the theory of conduction, we will look at chemical and physical properties with particular reference to printed circuit board insulation.

Chemical and Physical Properties

IN this chapter we will look at the chemical and physical properties of polymers, more specifically, of printed circuit board insulation. We will explore the fundamental molecular makeup of the material and then understand the mechanisms of moisture diffusion through it.

3.1 Introduction

While we are interested in understanding electrical conduction, such a study would remain incomplete without the proper knowledge of polymer chemistry. This is because structure and chemical composition of polymers play an influential role in charge carrier generation and charge transport. Additionally, PCB insulation (especially in automotive applications) are exposed to environments with high moisture contents. Therefore, diffusion of atmospheric moisture also needs to be understood since water itself plays many roles in facilitating electrical conduction.

3.2 Morphology of Printed Circuit Board Insulation

The printed circuit boards is a composite structure where the base material consists of three components [11]:

- Resin System (including additives)
- Reinforcement
- Conductive foil.

The most widely used base material is FR4 which is composed of an epoxy resin combined with a woven fiberglass reinforcement. Other base materials include FR-2, FR-3, FR-5,

FR-6, G-10 and CEM-1 through 8. Each of these systems have different resins and/or reinforcements.

3.2.1 The Resin System

Epoxyes are polyethers built up from monomers in which the ether group takes the form of a three-membered ring known as the epoxide ring as shown in Figure 3.1.

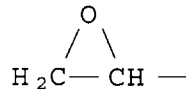


Figure 3.1: Three-membered epoxide ring

While many variations exist, the most common epoxy resin is formed from epichlorohydrin (epoxide ring compound) and bisphenol A (Figure 3.2). These two monomers first form an epoxy prepolymer that retains two terminal epoxide rings. The most common variety of epoxy is difunctional epoxy (Figure 3.3).

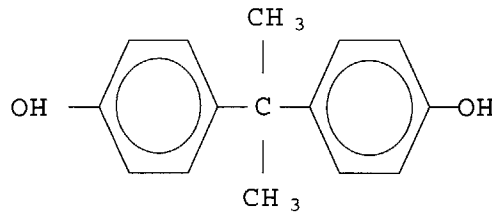


Figure 3.2: Bisphenol A

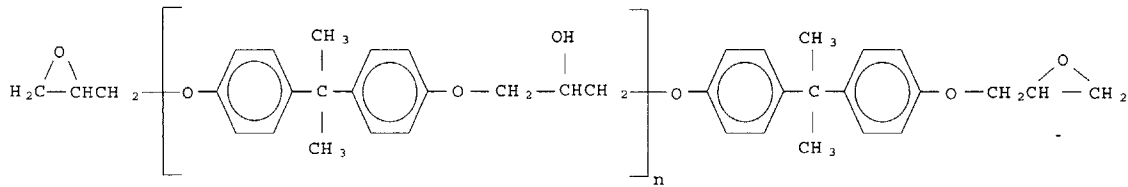


Figure 3.3: Difunctional epoxy resin

In the structure shown in Figure 3.3, n varies from about 2 to 25 repeating units. Depending on their average chain length, the prepolymers vary from dense liquids to solids. Also, in PCBs it is often brominated to make it flame retardant (Figure 3.4).

In a typical epoxy reaction, the prepolymers are further polymerized through the opening of the terminal epoxide rings by amines or anhydrides. This process, called curing, yields complex, thermosetting network polymers in which the repeating units are linked by linear

3.2 Morphology of Printed Circuit Board Insulation

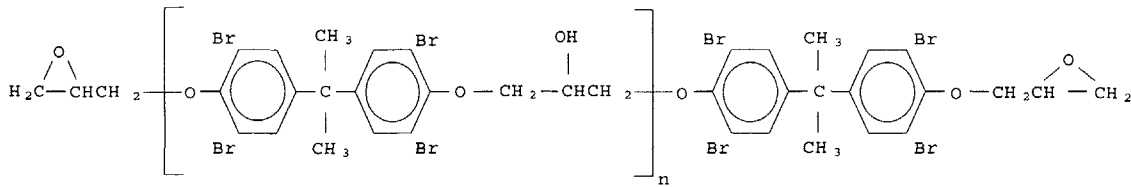


Figure 3.4: Brominated difunctional epoxy resin

ether groups. Diamine compounds are often used and provide four sites for attachments (Figure 3.5). Here, R is usually Bisphenol A and R' is some long chain hydrocarbon.

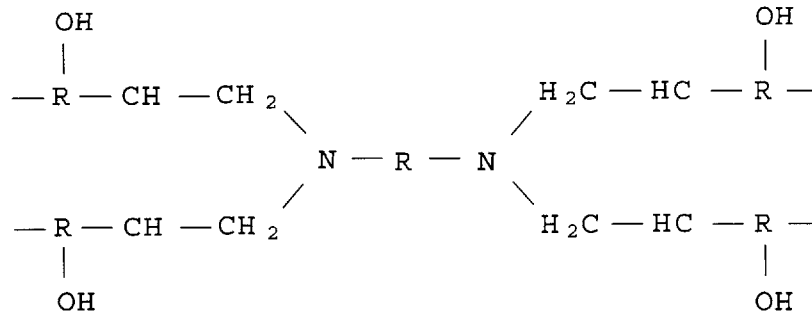


Figure 3.5: Diamine compound

The presence of hydroxyl groups in the repeating polymer component shown in Figure 3.4 makes it evident that these epoxy resins are highly polar molecules. This polarity plays a very important role in electrical conduction by providing sites for water molecules to form hydrogen bonds. Also, because of the high chemical reactivity and potentially large number of epoxide rings, cross-linking in cured epoxies can be very high and an extensive network of connections with high mechanical rigidity is produced.

Additionally, a number of chemical substances are added for different property improvements.

- Flame retardants are of two types - reactive components and additives. Reactive components are flame-retarding chemicals which are reacted into the epoxy itself. They are released only when exposed to heat (Bromine is such an agent). Additive retardants are dispersed in the resin system. When exposed to heat, some of these decompose and liberate water to suppress the heat.
- UV blockers or components that absorb UV light are also added to some resins that by themselves do not absorb UV light. The UV absorption characteristics of base materials are important when it comes to imaging processes once the external circuit image is

formed. This is typically of concern only in relatively thin printed circuit boards. The reason for this is that imaging operations (e.g. forming solder mask pattern) normally use photosensitive polymers applied to both sides of the PCB. These polymers are selectively exposed to UV light in order to form the proper image. Many of these photosensitive masks allow much of the UV light to pass through the film and into the base materials. If the circuit is thin enough and does not sufficiently absorb ultraviolet light, the UV light exposed to the circuit from one side can pass through to the other side, causing unwanted exposure of the mask.

These additive substances can be ionic in nature and therefore contribute to the overall conductivity. We will not discuss the impact of these additives, but it is sufficient to acknowledge them.

3.2.2 The Reinforcement

Materials used for reinforcement include woven fiberglass cloth, paper, glass mat (exhibits a more random orientation as compared to woven fiberglass cloth), non-woven fiberglass etc. In woven fiberglass, various chemical compounds are melted together in certain proportions and then strung into filaments and yarns. These yarns are then woven to make the fiberglass cloth. Shown below in Table 3.1 is the chemical composition of typical electrical grade glass (E-glass).

Component	% in E-glass
Silicone dioxide	52-56
Calcium oxide	16-25
Aluminum oxide	12-16
Boron oxide	5-10
Sodium oxide and Pot. oxide	0-2
Magnesium oxide	0-5
Iron oxide	0.05-0.4
Titanium oxide	0-0.8
Fluorides	0-1

Table 3.1: Chemical Composition of E-Glass

The cloths are coated with finish or coupling agent to improve the bond between the glass filaments and the specific resin used. These finishes also help prevent abrasion and static and help hold the filaments together. The effects of the glass fabric on the base materials are driven by variables such as glass compositions, filament diameters, yarn types, different weave patterns and fabric count (number of parallel and perpendicular yarns).

Fillers are small particles that when added to the resin system, modify the properties of the composite material (e.g. kaolin clay powder, hollow glass spheres etc.). They are very commonly used in many PCB systems.

3.2.3 The Conductive Material

Different copper foil grades are given according to IPC-4562 standard. The foil most commonly used is the standard electrodeposited copper foil. An important aspect of the copper foil is its surface profile. While a rough surface aids in creating strong bonds with the resin system, it might require long etch times which might impact productivity. Subsequently the matte side of the foil is treated with various chemicals to improve foil-to-resin bonds, to prevent thermal degradation of these bonds, to prevent oxidation of the foil during storage and lamination etc. These treatments are sometimes applied to the smooth side of the foil which then results in the low profile surface bonded to the laminate while the rough surface faces out. The advantage of this scheme is that very fine traces can be made in the inner layers and the outer matte surface can adhere better to the photo resist. Other foil types include resistive foils, double-treated copper foil, wrought annealed copper foil etc.

3.2.4 FR-4

We will be primarily concerned with the study of FR-4. However, the specificity of FR-4 and its constituents ends with the above definition and is not restricted to one specific combination of resins, reinforcements and other chemicals. On the contrary there are many different types of printed circuit boards that fit the category of FR-4. The IPC 4101A standard (“Specification for Base Materials for Rigid and Multilayer Printed Boards”) details 15 different formulations of printed circuit board base materials that fall under the FR-4 name. In addition to the IPC, other standardizing organizations such as NEMA (National Electrical Manufacturers Association) also have their own FR-4 based printed circuit board specifications. Many printed circuit board manufacturers make FR-4 similar to an IPC or NEMA standard but might include some other additives and fillers. Resin systems can include resins other than simple epoxies which might be some blends. Catalysts used for the copper plating process (e.g. kaolin clay coated with palladium) are used as a fillers in these laminates.

The reasons for such a diverse range of base materials are many. PCBs have a wide range of applications in many fields and therefore there exists an array of different desired properties. Hence, PCBs with the same FR-4 name may have different electrical characteristics, mechanical and thermal strengths, and different resistances to moisture and chemicals.

This diversity in formulation of FR-4 adds to the complexity of characterizing conduction phenomena and consequently ageing and degradation. Therefore statistical means described earlier are used to predict failure. In addition, the amorphous nature of the resin makes for very difficult modeling.

However, there are some commonalities that exist through this wide variety of base materials. We will explore one such property (moisture diffusion) with specific emphasis on FR-4 base material (particularly epoxy resin).

3.3 Moisture Diffusion Theory

The study of moisture diffusion in any material can be very involved from a macroscopic view of moisture penetration to the microscopic interaction of water molecules in the material being studied. Such a study is also quite easily complicated by randomness and uncertainty of material structure as well as external conditions. However, for any diffusion related study and more specifically a study involving polymer systems there are some basic questions that need answering. These questions can then be combined with many possible issues that could complicate the diffusion process.

Shown below is a list of typical questions and issues that will be attempted at least in part in this section. Many of the answers and approaches were obtained from a diverse group of publications with varying objectives.

- Rate of Diffusion
 - How quickly does moisture penetrate?
 - What internal and external factors influence this rate?
 - How is the rate quantified and what is the typical range of values for polymer systems?
 - How long does it take to saturate the material?
 - How long does it take to form a monolayer of moisture on the surface of the material?
- Direction and Path of Diffusion
 - What is the preferred direction of diffusion? For PCBs, is this direction parallel or perpendicular to the woven fiberglass mats?
 - What is the preferred path for diffusion? Does moisture diffuse primarily through the bulk material or through the interfaces in the material (epoxy-glass interface)?

- How does moisture reside and move in the material?
- How is the direction/path influenced by internal and external factors?
- Total Absorption (Saturation) of Moisture
 - How much moisture penetrates the material?
 - How is the total absorption influenced by internal and external factors?
 - Is there a state of quasi-equilibrium achieved that might not necessarily indicate total absorption?
- Deviant or Anomalous Diffusion
 - What are the characteristics of normal diffusion?
 - What are the typical deviations observed in polymer systems?
 - What are the possible causes for such deviations?
 - How are such deviations modelled mathematically?
 - Can systems that display normal diffusion under certain conditions also display anomalous diffusion under different conditions?
- Polymer Systems including PCB Insulations
 - What are the similarities and differences in diffusion between most polymers and epoxy?
 - What are the differences in diffusion between pure epoxy and epoxy-glass systems?
 - Does moisture chemically bond with polymer chains? How does this influence metrics such as rate and saturation levels?
- Experiments and Measurements of Diffusion Metrics
 - How are the various metrics of diffusion relating to rate, direction, saturation etc. measured?
 - How are the materials initialized to similar conditions for different experiments?
- Mechanical Integrity of Materials during Diffusion
 - How does moisture absorption affect the structural strength of a material?
 - What are some of the typical dimensional changes observed for polymer systems?
- Reversibility and Repeatability
 - Can all the moisture absorbed be just as easily removed?
 - What are the dynamics of such a desorption process?
 - Is there a similar diffusion mechanism for a second absorption (after a desorption)?

- Is the material history-dependent?

With these questions in mind, we can start by deriving some basic mathematical equations that will help provide some answers.

3.4 Diffusion Mathematics

The classical limiting case of diffusion can be described using Fick's second law with a constant diffusion coefficient, D :

$$\frac{\partial C}{\partial t} = D \left\{ \frac{\partial^2 C}{\partial x^2} + \frac{\partial^2 C}{\partial y^2} + \frac{\partial^2 C}{\partial z^2} \right\} \quad (3.1)$$

where C is the moisture concentration and t is the time. For one-dimensional diffusion through an infinite plate of fixed thickness, this equation becomes:

$$\frac{\partial C}{\partial t} = D_x \frac{\partial^2 C}{\partial x^2} \quad (3.2)$$

where D_x is the diffusivity through the thickness of the material.

The general solution of the diffusion equation can be obtained for a variety of initial and boundary conditions provided the diffusion coefficient is constant. Such a solution usually has one of two standard forms. Either it is comprised of a series of error functions or related integrals (Method of Reflection), in which case it is most suitable for evaluation at small times (early stages of diffusion), or it is in the form of a trigonometric series (Method of Separation of Variables) which converges best for large values of time. Different methods to solve the diffusion equation for different initial and boundary conditions can be found in the appendix. Shown below are the final generalized solutions of sorption and desorption for different cases.

Consider the case of sorption and desorption in a one-dimensional region $-l < x < l$ which is initially at a uniform concentration C_0 , and the surfaces are kept at a constant concentration of C_1 . Then solving Equation 3.2 using the method of separation of variables:

$$\frac{C - C_0}{C_1 - C_0} = 1 - \frac{4}{\pi} \sum_{n=0}^{\infty} \frac{(-1)^n}{2n+1} e^{-D(2n+1)^2\pi^2 t/4l^2} \cos \frac{(2n+1)\pi x}{2l} \quad (3.3)$$

Similarly, using Laplace transform (useful for small times):

$$\frac{C - C_0}{C_1 - C_0} = \sum_{n=0}^{\infty} (-1)^n \operatorname{erfc} \frac{(2n+1)l - x}{2\sqrt{Dt}} + \sum_{n=0}^{\infty} (-1)^n \operatorname{erfc} \frac{(2n+1)l + x}{2\sqrt{Dt}} \quad (3.4)$$

More useful than the concentration is a function that relates the amount of moisture in a material with time. Such a function would make experimental verification easier since we would then only have to calculate the weight gain of the sample as opposed to determining the concentration at each position.

We know that the total amount of substance diffusing, M , can be given by:

$$M = \int_{-l/2}^{l/2} C \, dx \quad (3.5)$$

Applying the integral given by Equation 3.5 to 3.3 and 3.4, respectively, we can get:

$$\frac{M_t}{M_{\infty}} = 1 - \sum_{n=0}^{\infty} \frac{8}{(2n+1)^2\pi^2} e^{-D(2n+1)^2\pi^2 t/4l^2} \quad (3.6)$$

$$\frac{M_t}{M_{\infty}} = 2 \left(\frac{Dt}{l^2} \right)^{1/2} \left\{ \pi^{-1/2} + 2 \sum_{n=1}^{\infty} (-1)^n \operatorname{ierfc} \frac{nl}{\sqrt{Dt}} \right\} \quad (3.7)$$

3.4.1 Square-root Relationship

The expressions derived so far involve a single dimensionless parameter

$$\frac{x}{2\sqrt{Dt}} \quad (3.8)$$

This presents the essential square-root relationship in diffusion where:

- The distance of penetration of any given concentration is proportional to the square root of the time.
- The time required for any point to reach a given concentration is proportional to the square of the distance from the surface and varies inversely as the diffusion coefficient.
- The amount of diffusing substance entering the medium through unit area of its surface varies as the square root of time.

3.5 Numerical Values of the Diffusion Coefficient

The next step is to determine an appropriate choice of diffusion coefficient, D . We can obtain this through a series of experiments similar to those that will be discussed later in this document. However, for the purposes of a theoretical investigation, we can use values that have been determined from prior studies [58], [37], [8] and characterize the probable behavior of the printed circuit board insulation.

It is known that diffusivity of water in epoxy is strongly dependent on temperature and not as dependent on relative humidity. Vanlandingham [58], using an EPON 828 - PACM 20 system¹ obtained diffusivities at room temperature ranging between $4 \times 10^{-10} \text{cm}^2/\text{s}$ and $3 \times 10^{-9} \text{cm}^2/\text{s}$ depending on stoichiometry (ratio of epoxy to amine). For 50°C environments, the values ranged between $2 \times 10^{-9} \text{cm}^2/\text{s}$ and $8 \times 10^{-9} \text{cm}^2/\text{s}$.

Ardebili [8] tested a plastic molding compound² usually used in Plastic Encapsulated Microchips (PEMs). These hydrophilic materials had higher diffusion coefficients ranging from $7.5 \times 10^{-9} \text{cm}^2/\text{s}$ at 35°C to $5.3 \times 10^{-8} \text{cm}^2/\text{s}$ at 85°C .

Marsh [37] developed an approximated Arrhenius plot for the variation of diffusion coefficients of Epoxy and Epoxy-Glass with temperature.

$$D = D_0 e^{-\frac{A}{RT}} \quad (3.9)$$

where D_0 and A are empirical constants, $R = 1.9872 \text{ cal mol}^{-1} \text{ K}^{-1}$ is the universal gas constant and T is the temperature in Kelvin.

For Epoxy, $D_0 = 0.28 \text{ cm}^2/\text{s}$ and $A = 9940 \text{ cal/mol}$

¹EPON 828 is a variant of bisphenol A, while the PACM 20 is a type of diamine.

²The common resin used is Epoxy Cresol Novolac (ECN). The common hardener and filler used are phenolic novolac (PN) and fused silica (FS) respectively.

3.6 Gravimetric Method and Diffusion Approximations

For Epoxy-Glass, $D_0 = 0.023 \text{ cm}^2/\text{s}$ and $A = 9500 \text{ cal/mol}$

Shown in Figure 3.6 are the plots for Epoxy and Epoxy-Glass composite. Also, the data points corresponding to Ardebili's [8] and Vanlandingham's [58] test results are plotted for comparison.

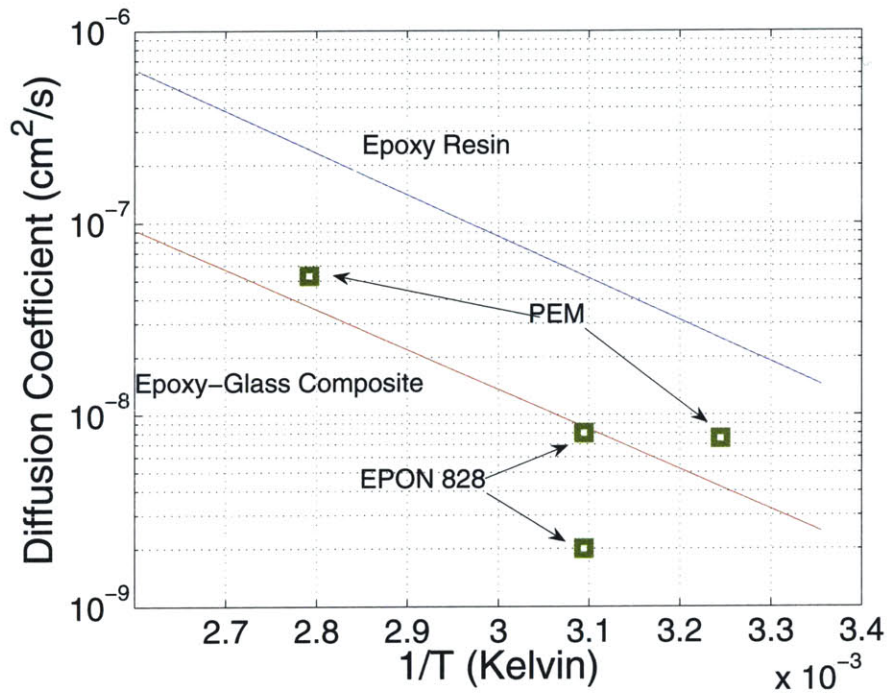


Figure 3.6: Variation of Moisture Diffusion with Temperature for Similar Materials

3.6 Gravimetric Method and Diffusion Approximations

Typically, diffusion coefficient and saturation moisture content estimates are made from weight gain/loss measurements which are also known as gravimetric measurements.

The percent weight gain is calculated as:

$$W(\%) = \frac{W_t - W_{dry}}{W_{dry}} \times 100 \quad (3.10)$$

where W_{dry} is the weight of the sample when it has little or no moisture content and W_t is

the current weight.

It is then assumed that all the weight that has been gained during absorption is entirely due to the absorbed moisture. Hence, this estimate for W determined from Equation 3.10 is the same quantity as M_t in Equations 3.6 and 3.7.

When W is plotted against $t^{1/2}$, the resulting curve for Fickian diffusion is initially a straight line and then flat for long times (Figure 3.7). An initial approximation for the diffusion coefficient can be obtained from the slope of the initial straight line.

3.7 Non-Fickian Diffusion

A large number of gravimetric (weight-gain) moisture tests conducted on epoxy resins and epoxy-glass systems have indicated that moisture diffusion in these systems are Non-Fickian [13]. Generally, this is the case with glassy polymers (or polymers below their glass transition temperature). In rubbery polymers on the other hand, the diffusion is Fickian. The essential distinction is that polymers in the rubbery state respond rapidly to changes in their condition. For example a change in temperature causes an almost immediate change in equilibrium volume [13]. The properties of glassy polymers, however, tend to be time-dependent. For example the stress may be slow to decay after such a polymer has been stretched. Deviations from Fickian behavior are considered to be associated with the finite rates at which the polymer structure may change in response to the absorption or desorption of penetrant molecules (relaxation). Polymers usually have a wide spectrum of relaxation times associated with structural changes, but all of them decrease as temperature or penetrant concentration is increased and the motion of polymer segments enhanced [13].

In his books, Crank [13] [14] distinguishes Fickian and Non-Fickian diffusion using the principle of varying relaxation and diffusion rates. In essence, for the case of Fickian diffusion, the rate of diffusion is much less than that of relaxation, whereas for Non-Fickian or anomalous diffusion, the diffusion and relaxation rates are comparable. Another case also exists where the diffusion is very rapid compared with the relaxation process. This type of diffusion is controlled by the limit of penetration of the diffusant and is usually the boundary between the swollen gel and the glassy core.

Typical characteristics of the different diffusion types are seen in the absorption-time curves. These are plots of amount of moisture absorbed or desorbed versus $t^{1/2}$. In Fickian diffusion, the plot forms a straight line at the beginning then settling to a final stable value. A common Non-Fickian plot is one that contains multiple stages where the moisture rises, reaches an

equilibrium and then rises again to reach a second equilibrium and so on. The representation in Figure 3.7 illustrates this difference.

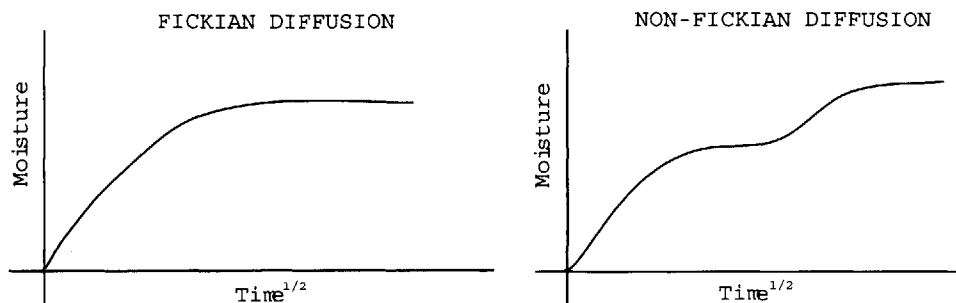


Figure 3.7: Comparison between Fickian and Non-Fickian absorption

An important observation made in many different experiments was that deviations from Fickian behavior are more pronounced in the elevated temperature environment.

To explain the multi-stage absorption plots, Marsh [37] stated that a quasi-equilibrium is reached rapidly first at the polymer surface and then by simple diffusion throughout the polymer sheet. The second stage of absorption is associated with the increase in surface concentration which occurs slowly compared with the diffusion process and is the rate determining factor for absorption.

Another early theory [13] suggested that in the quasi-equilibrium at the end of the first stage, the elastic forces in the swollen polymer network have increased the chemical potential of the absorbed penetrant to such an extent that no further absorption occurs. On standing, the elastic forces slowly relax, the chemical potential decreases and more penetrant is absorbed to establish equilibrium again.

3.7.1 Berens and Hopfenberg Absorption Model

Berens and Hopfenberg (1977) proposed a mathematical absorption model for polymeric materials that did not show Fickian behavior [51]. This model was a linear superposition of independent contributions from Fickian diffusion and polymeric relaxation. The total amount of absorption at time t , M_t , is given by:

$$M_t = M_{\infty,F} \left\{ 1 - \frac{8}{\pi^2} \sum_{n=0}^{\infty} \frac{1}{(2n+1)^2} e^{-\frac{D_x t}{h^2} \pi^2 (2n+1)^2} \right\} + M_{\infty,R} \{1 - e^{-kt}\} \quad (3.11)$$

where M_t is the weight percentage of the water absorbed at time t , $M_{\infty,F}$ is the maximum Fickian absorption at saturation (%), D_z is the mass diffusivity along normal thickness direction (cm^2/s), h is the normal thickness in the direction of diffusion (cm), $M_{\infty,R}$ is the maximum absorption due to relaxation (%) and k is the relaxation rate constant (per s). It is evident that the first term in Equation 3.11 is similar in construction to Equation B.15 presented as a solution to Fick's second law using separation of variables.

Equation 3.11 is plotted in Figure 3.8 as a linear superposition of the first term (Fickian Diffusion) and the second term (Polymer relaxation) of the equation.

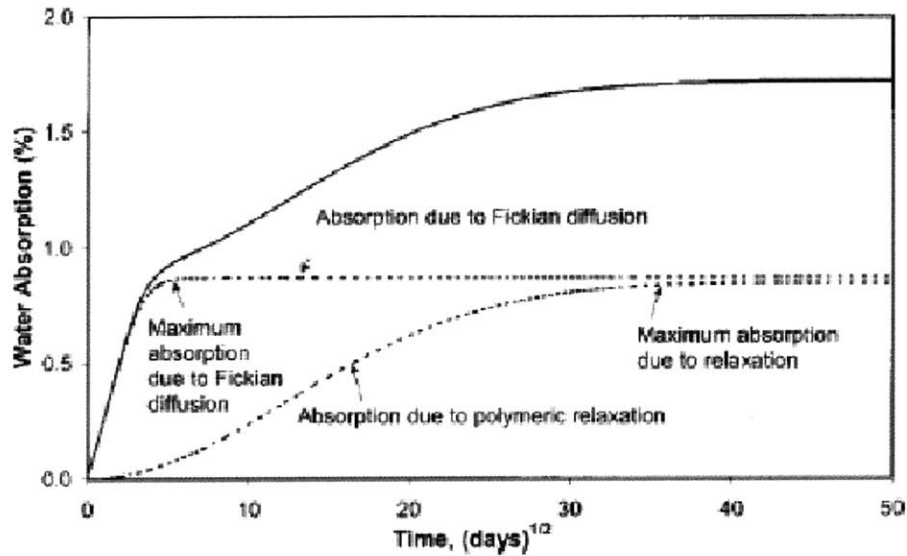


Figure 3.8: Theoretical Absorption Curves from Shao [51]

This model enables us to easily determine various parameters that can help us build a fairly complex Non-Fickian model.

More recently, explanations for the Non-Fickian diffusion processes in glassy polymers and specifically the two-stage absorption have included the effect of polymer chain topology and polarity [52]. The polymers have been examined in terms of absorption into mobile and bound phases. This theory is explained in more detail in the following section.

3.7.2 Dual Mode Sorption Theory

Many studies [13],[58], [37], [52], [8] and [51] conducted on epoxy and epoxy-glass systems have converged on the theory that water molecules diffusing into such polymer systems exist in two states: bound to the polymer chain and unbound. Therefore moisture transport in polymer systems is related to the availability of molecular-sized holes in the polymer structure and the polymer-water affinity. The polymer-water affinity is linked to the presence of hydrogen bonding sites (polar hydroxyl group discussed in Section 3.2.1) along the polymer chains, which create attractive forces between the polymer and the water molecules. The water molecules that are free to move through the holes (free volume) are often referred to as the unbound molecules. The bound water molecules attach to the polymer chain via hydrogen bonding. The unbound molecules do not cause any structural changes because they are occupying free volume. However, the bound molecules disrupt the interchain hydrogen bonding, inducing swelling and plasticize the polymer.

For epoxies, large amounts of free volume exist, particularly at temperatures below the glass transition temperature [52]. Also, the epoxy water affinity is relatively strong because of the polar hydroxyl group (-OH) created by the epoxide-ring opening reaction with primary and secondary amines. The water molecule can bond with this hydroxyl group thereby disrupting the interchain hydrogen bond that exists in the polymer.

3.8 Reversibility, Repeatability and Desorption

So far, we have discussed the basic diffusion equation and the Non-Fickian Behavior observed in polymers. There has been little or no mention about the desorption or drying process and the repetition of absorption following this drying. Also, we will discuss the results of some studies regarding swelling and strain due to diffusion.

Marsh [37] indicated that a second absorption (following a desorption process) appears largely single staged for epoxy and epoxy-glass composites. Also, this second absorption is seen to occur very rapidly compared to the first (multi-staged) absorption. These studies have also shown that the onset of residual moisture occurs roughly at the transition region (end of the first stage) where there appears to be temporary saturation. Samples experiencing absorption to values less than this quasi-equilibrium value, lost the gained moisture on desorption. However, any weight gain in excess of this temporary equilibrium resulted in retention of residual moisture. Experiments also indicated that temperatures in excess of the glass transition temperature are required to remove this residual moisture.

Also, Marsh [37] conducted experiments on both epoxy and epoxy-glass composites to check for reversibility and history dependence. For example, the materials were saturated at $65^{\circ}C$ and 30% *RH* and at $85^{\circ}C$ and 80% *RH*; then they were equilibrated at $65^{\circ}C$ and 80% *RH* and at $85^{\circ}C$ and 30% *RH*. The data revealed that the final moisture content, which includes second stage absorption, is strongly dependent on prior history. These experiments showed that a very small concentration of H_2O molecules absorbed has a large effect on those yet to be absorbed.

Vanlandingham's [58] desorption studies also indicated that epoxy-rich samples did not return to their original dry weight as was measured prior to immersion in the humid environment. These results show that elevated temperature exposure to moisture of epoxy rich samples could result in much stronger interactions between un-reacted epoxy molecules and absorbed water molecules.

Experiments [58] indicated that swelling strains, in general, increased with the moisture saturation level (final equilibrium saturation). The moisture expansion coefficient, β , is defined as:

$$\beta = \frac{\Delta l/l_0}{M_{sat}} \quad (3.12)$$

where l_0 is the initial dry dimensions, Δl is the change in that dimension due to moisture absorption at saturation. β can easily be determined from the linear fit of the plot of moisture-induced strain versus the moisture level.

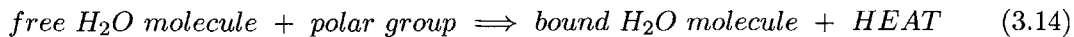
It is interesting here to note that the moisture saturation level discussed above depends on the moisture concentration of the surrounding environment. Moisture saturation has been found to depend on relative humidity according to [58]:

$$M_{sat} = a(RH)^b \quad (3.13)$$

where a and b are constant parameters and *RH* is the percentage of relative humidity.

An interesting observation of many studies is that M_{sat} has been found to be both dependent and independent of temperature of the surrounding environment.

Interactions occurring between a water molecule and a polar group are typically exothermic in nature and can be described by the equation:



This means that as absorption proceeds, the available polar groups will become saturated with water and an equilibrium will be established between bound and free sites. Increasing the temperature increases the internal heat and pushes the reaction in the opposite direction and decreasing the equilibrium uptake. Therefore, since fewer water molecules are in a bound state at higher temperatures, the saturation moisture level could potentially increase. This behavior was also proved experimentally by Soles [52] and moisture saturation level increased dramatically with temperature.

However, this is inconsistent with our previous statement that M_{sat} is both dependent and independent of temperature. This inconsistency is explained as follows - For water in epoxy, the heat of solution, ΔH_s , is negative (Equation 3.14). This is opposed thermodynamically by the heat of vaporization of water, ΔH_v . If $\Delta H_s = -\Delta H_v$ then M_{sat} will not be a function of temperature. For some systems this equality may not hold and a temperature-dependent saturation level is observed. Nevertheless, high temperature has the effect of shortening the time to reach this saturation level (M_{sat}) by increasing the diffusion rate.

These studies have indicated that moisture is bound to the epoxy such that simple drying procedures do not remove all of absorbed moisture.

3.9 Experimental Methods

This section focusses on some interesting experimental techniques and test conditions maintained in various studies done in the past. These conditions and techniques could prove as a starting point for further research and also serve as a comparison reference for validating future experiments.

3.9.1 Pre-conditioning

Most of the pre-testing conditioning was done to remove any moisture and bring the sample to its driest possible state.

Vanlandingham [58] dried the sample in a vacuum oven at $50^\circ C$ for approximately 2 weeks. the weights of the samples were monitored to ensure that equilibrium dryness had been reached.

Ardebili [8] initially dried the samples at 125°C for 24 h or more until no further weight loss was detected. This is not particularly a good choice for drying because, this would be very close to the glass transition temperature and could modify the material structure irreversibly.

ASTM D 570-98 recommended initial conditioning procedure for water absorption tests include oven baking at 50°C for 24 h. The specimens are then cooled in a desiccator prior to initial measurements.

Prior to performing the absorption experiments, Soles [52] washed the samples with soap and warm water and then dried for several days in a vacuum oven at 80°C to remove excess moisture.

Some interesting aging and quenching experiments were also done by Soles [52] where the samples are initially heated to $T_g + 20^{\circ}\text{C}$ for 24 h to establish a standard thermal history. Several samples are cooled over 2 h to $T_g - 20^{\circ}\text{C}$ and held for one week to produce the aged materials. On the other hand, the quenching of materials is obtained by taking the material directly from the oven ($T_g + 20^{\circ}\text{C}$) and immersing into an ice-water bath. Both the aging and quenching procedures are performed in a vacuum bag outfitted with device to prevent the samples from experiencing compression from the atmospheric pressure.

Essentially, most studies used weight loss measurements as a means to conclude a drying methodology. There appears to be no physical process behind the reasons for choosing a particular temperature or pretreatment time. Since test samples were very varied, it is difficult to actively criticize one method or another.

3.9.2 Absorption and Desorption Profiles

We will now discuss some tests and environments used by others in studying absorption and desorption.

In one study [58], after initially drying the samples in a vacuum oven at 50°C , these samples were placed in differing environments including 20°C and 75% *RH*, 20°C and 85% *RH* and a 50°C and 85% *RH*. Also, to check for reversibility, some of the samples were dried in a vacuum at 50°C after 2500-3500 h of conditioning.

In another study [8], after drying the samples at 125°C for 24 h, they were exposed to environments of 85°C and 85% *RH* for one week and/or 35°C and 75% *RH* for three weeks.

Another experimental study focussed on moisture absorption with the sample immersed in liquid water at different temperatures including $5^{\circ}C$, $23^{\circ}C$, $35^{\circ}C$, $50^{\circ}C$, $70^{\circ}C$ and $90^{\circ}C$.

In all the studies surveyed, there was no mention about the reason for choosing certain environmental conditions and test time. However, the numbers used give some insight into the expected behavior of polymer systems at the above-mentioned conditions. Particularly, we can begin to see what to expect if similar tests were conducted on FR4.

3.10 Interfacial Damage due to Moisture

We have so far understood the existence of water in polymers in bound or unbound form. We have also studied the mechanical impact of the bound water in terms of swelling and strains. Another important area of research especially applicable to composite structures such as FR4 are the properties of the interfaces.

Shown in Figure 3.9 is an atomic force microscope image of the impact of moisture on the interface between glass fibers and epoxy.

This sample was exposed to a moist environment and there is clear evidence of interfacial debonding (which among other things can cause a reduction in the strength of the material). The authors claim that this observed debonding was completely non-existent prior to exposure to the moist environment. This phenomena can be explained as follows. Typically, the polymeric chains in epoxy tend to bond to the glass fiber through hydrogen bonding. Through the introduction of moisture, these hydrogen bonds are gradually broken and the polymer begins to bond with the water molecules instead. The results in the slow degrading of the interfaces.

This concludes the brief survey of physical and chemical properties of polymers and in particular FR4. In the next chapter, we will focus on understanding electrical conduction and its origins in insulators.

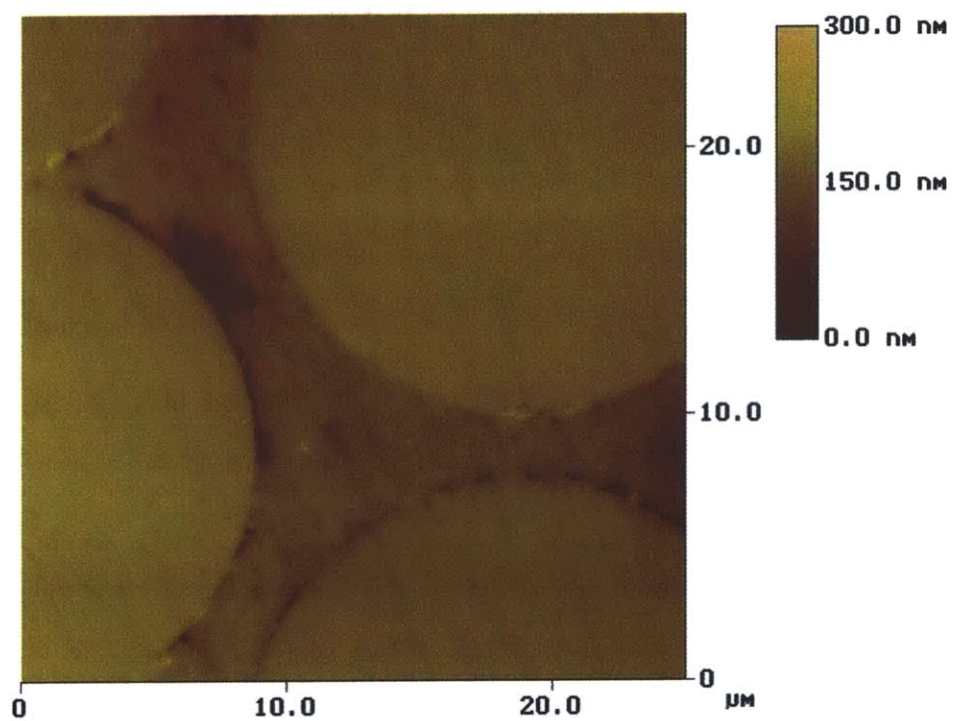


Figure 3.9: Atomic Force Microscope Image of Glass-Epoxy Debonding (Courtesy: NIST) [58]

Electrical Conduction

IN this chapter we will study different models to describe electrical conduction at various DC fields. We will attempt to classify different charge carriers, different transport mechanisms and the differences between surface and bulk conduction processes.

4.1 Introduction

Electrical conduction in polymers is a widely explored topic. In recent years, there has been an increased interest in polymer electrolytes. These are materials that are deliberately doped with ionic impurities that increase conductivity. These have applications in batteries and energy storage devices. However, our interests are different and we will focus on polymeric materials that are designed to function as insulators over a wide range of conditions.

These polymeric insulators have very low conductivity and are therefore very difficult to measure accurately. Conduction is highly sensitive to variations in micro and macro structures as well as aging history. Also, polymeric insulators contain many impurities and additives (as described earlier) as well as structural imperfections. Therefore, we do not yet have complete answers to some of the most fundamental questions that are crucial to modeling conduction such as the nature of the primary charge carrier, transport mechanisms through the material and interfacial effects (electrode-insulator, insulator-air and epoxy-fiberglass boundaries).

In the following sections, we will look at a small subset of the huge body of work in the area of conduction in polymers. We will look both electronic and ionic charge carriers and their corresponding transport mechanisms. The knowledge gained from this study will help us later interpret the results obtained from some experiments.

4.2 Electrical Conductivity

Total current density in a dielectric is made up of a drift component (charge transport due to charge motion under the influence of the applied electric field), a diffusion component (random movement of individual charge particles results in net movement from a region of high concentration to low concentration) and a displacement component (non-physical quantity due the magnetic field generated by a time varying electric field) shown in Equation 4.1.

$$J = ne\mu E - eD_n \frac{dn}{dx} + \epsilon_0 \epsilon_r \frac{dE}{dt} \quad (4.1)$$

where J is the current density, n is the concentration of charge carriers, e is the charge of an electron ($1.6 \times 10^{-19} \text{C}$), μ is the mobility, E is the applied electric field, D_n is the diffusion coefficient of charges, ϵ_0 is the permittivity of free space ($8.854 \times 10^{-12} \text{ C}^2/\text{Jm}$) and ϵ_r is the relative permittivity of the material.

For cases of static DC electric fields, $\frac{dE}{dt} = 0$. Additionally, when we apply reasonable strong electric fields, the diffusion component becomes negligible compared to the drift component. However, this is not the case at the electrode-insulator interfaces where there is a possibility of charge buildup near the electrodes resulting in electric field cancelation and consequently a pure diffusion component. However, studying that interface is a separate topic in itself that we will not be concerned with.

Therefore, simplifying Equation 4.1:

$$J = ne\mu E \quad (4.2)$$

This clearly follows Ohm's law since current is proportional to the voltage. Stated in simpler terms:

$$J = \sigma E \quad (4.3)$$

Where σ is the conductivity or $1/\sigma$ is the resistivity of the material.

Different materials display a very wide range of resistivities, from less than $10^{-25} \Omega\text{m}$ in superconductors to greater than $10^{20} \Omega\text{m}$ in some insulators. Conductors often display linear

4.3 Electronic Steady State Conduction

(ohmic) current-density dependence on electric field. This is also observed in semiconductors at low fields. However, above a certain critical field, currents in semiconductors reach a limiting value. In most insulators, small currents are found to flow on the application of a DC field and at low fields this conduction is often ohmic.

From Equations 4.2 and 4.3, the conductivity due to charge carrier species, i , is given by:

$$\sigma_i = n_i e_i \mu_i \quad (4.4)$$

where n_i (m^{-3}) is concentration of the charge carrier species i , e_i (C) is the electric charge on each carrier and μ_i ($m^2 V^{-1} s^{-1}$) is the mobility which is defined as the drift velocity (v_d) per unit field.

$$\mu = \frac{v_d}{E} \quad (4.5)$$

If there are many different types of charge carriers, then the conductivity becomes:

$$\sigma = \sum_i^N \sigma_i = \sum_i^N |n_i e_i \mu_i| \quad (4.6)$$

The important aspect of the conductivity measurement lies in the fact that there can be a big variation in concentration of charge carriers as well as the mobility across materials. Any satisfactory explanation or description of the conduction process has to account for the dependency of conductivity on the number of charge carriers and the mobility. We will look at two types of charge carriers – electrons/holes and ions/protons.

4.3 Electronic Steady State Conduction

Electronic conduction includes the movement of electrons and holes that contribute to the observed current. Before we begin looking at existing conduction models, it is useful to briefly summarize “Electron Band Theory” which is so widely used in semiconductor physics. A more detailed treatment of electronic conduction theory in insulators, can be found in each of the following sources to which the following review owes its roots including [18], [50], [55], [39] and [62]. This is by no means a comprehensive list and since the theories

presented are widely accepted, there are numerous other sources available where one might find such treatments.

4.3.1 Energy Band Theory

In isolated atoms, electrons have discrete energy levels (as per the Bohr model) given, typically, in eV (electron volts) which is an energy unit corresponding to the energy gained by an electron when the potential is increased by one volt. In a situation with two identical atoms, when they are far apart, the allowed energy levels for a given state consists of one set of doubly degenerate energy levels. This means that for each electron in one atom, there is one electron in the other atom at the same energy, However, according to Pauli's Exclusion Principle, no two electrons occupying the same space can have the same energy level. Electrons can occupy the same energy levels only if they are of opposite spins. Therefore, when these two identical atoms are brought closer, the doubly degenerate set of energy levels will split into two levels by the interaction between the atoms. Similarly, if N isolated atoms are brought together to form a solid, the orbits of the outer electrons of different atoms overlap and interact with each other. This interaction, including the forces of attraction and repulsion between atoms, causes a shift in the energy level, as in the case of two interacting atoms. However, instead of two levels, N separate but closely spaced levels are formed. When N is large, it results in an essentially continuous band of allowed energies. The energy band theory was developed for ionic or covalently bonded crystals to explain the large variations in charge carrier concentrations. In covalently-bonded crystals at a temperature of absolute zero all the electrons occupy the lowest possible energy levels with two electrons of opposite spins in each level. If the atom has an even number of valence electrons then the highest occupied band will be exactly full and if it has an odd number of valence electrons it will be exactly half-full. In the latter, if the temperature is increased, the electrons can easily acquire kinetic energy from electrostatic interaction and move into higher energy levels within the same half-filled band. However, in the former case, since the band is already completely full and to jump to higher energy levels, the electron will have to jump to a higher band. Depending on the energy gap between the bands this might be possible.

The Fermi-Dirac distribution function gives the probability that an electron occupies an energy level with an energy, E , at a temperature T .

$$P(E, T) = \left[1 + e^{\left\{ \frac{E - E_f}{k_B T} \right\}} \right]^{-1} \quad (4.7)$$

4.3 *Electronic Steady State Conduction*

where E_f is the Fermi energy level, k_B is the Boltzmann's constant (8.617385×10^{-5} eV/K)

The Fermi energy level, E_f , corresponds to the energy level at which Equation 4.7 predicts there is a 50% chance of finding an electron.

The highest filled band at absolute zero is termed as the “valence band” and the first unoccupied band is known as the “conduction band”. The “band gap” (forbidden band) is region between the bottom of the conduction band and the top of the valence band. The electrons in the conduction band have sufficient energy to break away from the atom or bonds and contribute to conduction. The electrons in the valence bands are, however, not available for conduction. The density of states gives the number of available states in a given range of energies per unit volume.

4.3.2 **Charge Carrier Generation, Transport and Traps**

In conductors, the conduction band is either partially filled or overlaps with the valence band, so there is no band gap and the uppermost valence band electrons can move to higher energy states within the same band when they gain kinetic energy (from applied electric field). Thus, conduction occurs easily. In insulators, there is a large band gap and the electrons occupy almost all the energy levels in the valence bands and nearly none in the conduction bands. Therefore, typically, thermal energy or energy from an applied field is insufficient to raise these electrons to the conduction band. Consequently, they do not conduct current. In semiconductors, the band gap is much smaller. At absolute zero all the electrons are in the valence band and none in the conduction band. However, under normal room temperature, the thermal energy is sufficient to excite the electrons into the conduction band. Since there are many states in the conduction band, a small potential is enough to move these electrons resulting in a good current at room temperature and no currents at very low temperatures. This is fundamentally, the concept of intrinsic semiconduction where the impurity concentration is very low compared with the thermally generated electrons and holes.

When a semiconductor is doped with impurities, the semiconductor becomes extrinsic and the impurity energy levels are introduced. The impurity atom either introduces an electron or a hole that has relatively low binding energy to its host and can be “ionized” to become a conduction electron/hole. These impurities, therefore create donor/acceptor energy levels in the band gap. The donor levels (electrons) are typically close to the valence band and the acceptor levels (holes) are typically close to the conduction band.

At absolute zero, the crystal is ideal and consequently the lattice spacing is periodic giving

us the band structure described. However, at higher temperatures, due to lattice vibrations there is a distribution of interatomic spacings causing temporal changes in the band gap. Also, crystal defects resulting in incompletely-bound atoms are compensated by the removal or addition of electrons and consequently behave as “localized states”¹ within the band gap. These states are also known as “traps” because electrons entering these states might need considerable energy to leave them.

We will now look the various electronic conduction mechanisms at low and high electric fields.

4.3.3 Ohmic Conduction (Low Field)

This is the typical conduction mechanism found in metals and semiconductors and it describes the movement of an electron in crystal lattices. This model usually predicts high mobilities and usually has a negative temperature coefficient. There is a linear voltage current relationship tending to follow Ohm’s Law.

In the absence of an electric field, the electrons move randomly and the mean kinetic energy is dependent on the the lattice temperature. On applying an electric field, these electrons move in a direction opposite to the field with mean velocity termed as “drift”. Even in the influence of high fields, the distribution of electron velocities only vary slightly. Additionally, the mean free path and and the mean free time are mostly constant meaning that the mobility is also constant. This in turn implies that current density is linearly related to the electric field (following Ohm’s Law).

In situations where there are crystal defects or disorder, there is the possibility of localized states that can trap electrons which in turn causes the charge carrier concentration to decrease to a new value. Also, in the presence of traps, the charge carriers take longer to drift the same distance at constant concentration. Therefore, we observe lower conductivities

4.3.4 High Field Conduction Mechanisms

There are usually considerable deviations observed from Ohm’s Law for most insulators occurring at high fields. This deviation arises in these insulators because the solid is usually unable to transport all the charge injected from the metal electrodes.

¹Localized states do not extend throughout the material and only exist in the vicinity of the defect.

4.3.4.1 Electron Injection

The energy band diagram of electrode-insulator interface is highly complex because of physical and chemical defects (crystal imperfections and incomplete bonds), chemical impurities (oxidation, moisture) and trap states. There exists a potential energy barrier between the electrode and the interface and the application of high fields helps in either the reduction of the height or width of the barrier.

Schottky Injection is an injection process where the barrier height is modified. The barrier is formed due to the electrostatic attraction between the injected electron and the metal (the metal is partially positively charged since the electron has left it). The attraction results in a gradually changing barrier due to the potential energy of the electron and consequently the height and the distance to the maxima can be found. The current density is determined from the rate of arrival of energetic electrons at the interface.

The *Fowler-Nordheim Injection* mechanism works on the modification of the barrier width. At very high fields (10^9V/m) in the insulator, the potential barrier next to the contact becomes very thin. It is well known from classical mechanics that a particle cannot enter a region in which the total energy is less than the potential energy required. However, particles with particle-wave duality (electrons) do have a certain small probability of existence on either side of thin barriers. Electrons are made to pass through these thin potential barriers despite having insufficient energy to surmount them (Tunneling). Additionally, the tunneling current is almost completely independent of temperature.

4.3.4.2 Steady State Conduction

Space Charge Limited Conduction (SCLC) explains the situations where injected charge has difficulty in moving through the bulk. The space charge formed at the electrodes and in the bulk limits further movement of charge. Therefore, this mechanism is highly dependent on thickness. The theory is developed in terms of an energy band structure with traps and assumes uniform charge distribution in the bulk.

Initially, it is assumed that there are no traps or thermally generated carriers, and only negatively charged species injected from the electrodes. The famous Mott-Gurney Square Law [39] (Child's Law for solids) is derived where the current density is proportional to the square of the voltage:

$$J = \frac{9\epsilon_0\epsilon_r\mu V^2}{8d^3} \quad (4.8)$$

where V is the applied voltage and d is the crystal thickness.

In the presence of traps, however, there is a reduction in the number of charge carriers. At high voltages, the charge carrier number density being injected equals the number density of traps. Therefore, there is an initial ohmic conduction due to thermal charge carrier generation, then trap limited SCLC, then all the traps at a certain energy level fill up, then there is trap free SCLC.

The *Electron Hopping* mechanism describes conduction due to the movement of electrons from one localized state to another of similar energy. It can be inferred from the idealized band structure described previously that density of states in the band gap is zero and increases very quickly at the band edges. However, in reality, these edges are not so abrupt, instead the density of states gradually decreases in the gap. In insulators, the Fermi energy is less than the conduction edge. The density of states is usually very low near the Fermi energy level but much higher near the edges of the band gap. There are very few carriers in these high energy edges, which being sufficiently close enable carriers to easily move from one to another. At the low energy states there is a high carrier concentration, but the states are too far apart for movement. We have also noted earlier, that direct excitation to the conduction band was highly unlikely, due to the high energy required. It has been suggested that electrons, instead could hop from one state (of low energy) to another one of similar energy far apart. This might be a state that has a higher density of surrounding states and consequently, the electron can slowly make its way up through the gap either by tunneling or hopping over these small barriers. The conductivity relation can be derived from the probability of being at a desired energy level (Equation 4.7) and the probability of tunneling to a neighboring site separated by a certain distance.

The *Poole-Frenkel* mechanism is the steady state bulk conduction analog of the Schottky effect. The barriers heights localizing carriers within the bulk are lowered versus the barriers at the electrode-insulator interface. This mechanism requires a fairly wide band gap and the existence of energy states in the center of the band gap from donor and acceptor species. Defect states (without donors/acceptors) are usually much closer to the band edges and therefore are not sufficient.

4.3.5 Shortfall of Band Theory in Polymers

The biggest argument against the use of band theory and electronic conduction in polymeric insulators is the fact that the band gaps are extremely large. The large band gap in polymers is due to primarily the high energies required to dissociate electrons from the nuclei. Also, for inter-chain delocalization (needed for electron transport) higher energies are required since the electronic conduction process must overcome the polymer molecule's ionization energy before it can transfer to another chain.

The energy band theory is formulated based on the periodicity of ionic or covalently bonded solids. However large scale disorder in polymers prevents the formation of a classical band structure. In fact, it is believed [18] that electronic conduction primarily occurs (if so) along the length of the polymer chains where regular lattice conformation is maintained. Chain ends, pendant groups and external impurities cause further disruption.

According to Seanor [50], polymers can be thought of as semi-crystalline consisting of both amorphous and crystalline regions. Charge trapping primarily occurs at the boundaries between these two regions. Trapping also occurs at conformational defects and between molecules. The presence of trapped charge results in local polarization and distortion leading to modification of the energy band structure. This in turn would make it difficult for the trapped charges to escape. Also high energy bombardment of electrons causes bond scission, polymerization, possible crosslinking and increased trap concentration. Furthermore, dipoles could lead to local variations in energy levels resulting in periodic trapping

Conductance in many polymeric insulators show a strong Arrhenius type temperature dependence. This cannot be attributed to thermal activation of electrons across the semiconductor gap because the polymeric band gaps are too large and the probability of an electron occupying the lowest level of the conduction band is very low. In fact, electronic conductivity is believed to decrease with increasing temperature as we approach and cross the glass transition temperature (T_g).

The Ohmic conduction mechanism fails to describe conduction at low fields in polymers for many reasons. Firstly, polymers display very low mobilities and Ohmic conduction predicts much higher mobilities. Increase in temperature actually causes Ohmic conduction to decrease due to increased lattice vibrations and consequently decreased mean free time between collisions. Additionally, in polymers, electrons are unlikely to be free to move at all and those that do have sufficient energy to reach the conduction band are likely to be scattered very quickly and fall back into a trapped state. As a general rule, crystallinity lowers conduction irrespective of the mechanism.

Even so, many polymers display electronic conductivity through other non-ohmic mechanisms at certain conditions while others display ionic conduction which will be the topic of the following sections.

4.4 Ionic Steady State Conduction

The inadequacies of the electronic steady state conduction theory suggests the need for another theory that explains the various phenomena common to many polymers such as Arrhenius temperature activated conduction. In this section we will review ionic conduction and the various models that have been proposed to explain different observations. The concepts and theories in this section have been obtained primarily from [18], [50], [55], [39] and [62]. Additionally, some seminal research work as well as recent publications have been incorporated into the review which will be cited at the appropriate location.

The most effective way to confirm and prove ionic conduction is through mass transport observations. However, such mass transfer experiments are very difficult to perform and observe. We briefly touched upon an extreme example of mass transfer in Section 2.4 when we discussed electrochemical breakdown processes and electromigration phenomena. Here the mass transfer processes are clearly visible in the form of dendritic growth and electrode barrier discoloration. However, for low field degradation processes this is not completely clear and in fact it is one of our goals to convince the reader that in fact the observed leakage conduction in PCB insulation (FR-4) is ionic and therefore existing accelerated testing schemes are incapable of accurately measuring life.

The topic of ionic conduction is usually associated with a study of electrical conduction in electrolytes. However, Seanor [50] pointed out that ionic conduction does not follow simple theoretical analysis or electrolyte conduction concepts. Waldren's rule (relating mobility and viscosity) and also simple concepts of electrolyte conduction (relating conductivity to ionic concentration) are not obeyed in polymers. Waldren's rule relates the viscous drag on an ion to the accelerating force of the electric field. Waldren's rule fails due to the macroscopic nature of viscosity measurement techniques which might be valid in bulk electrolytic liquids where the dimensions of the ion and the molecular matrix are of the same order and therefore it is safe to assume hydrodynamic continuum. Solid state polymers, however, have many holes and voids that are of similar dimensions to that of the ions and therefore local density fluctuations dominate ionic motion.

Ions act on the local structure to alter the mechanical properties of the insulator which in turn are reflected in the electrical properties. Therefore, the electrolyte theory also fails

because this theory assumes continuum concepts that do not apply for polymers due to the molecular disorder.

Another aspect of bulk electrolytes that makes it so very different from polymeric insulators is the concentration of charge carriers. It is clear that the low conductivities of polymers could be due to the low mobilities, low charge concentration or both. Therefore, it is highly likely that the carrier concentration of polymers is far lower than even weak electrolytes that are commonly modeled as ionic conductors and consequently a different mechanism has to be developed to explain situations with low mobilities and charge concentrations.

There can be fundamentally two types of ionic conduction mechanisms [18] - intrinsic and extrinsic.

4.4.1 Intrinsic Ionic Conduction

Intrinsic ionic conduction mechanisms proceeds by the dissociation of the chain and transport of protons through alternatively breaking and forming hydrogen bonds with neighboring chains.

The mechanism of intrinsic ionic conduction has its basis in a paper by Agmon [6] describing a reason for high mobility of protons in water. The Grotthuss Mechanism (after Christian J.D.T. von Grotthuss) is a process whereby protons tunnel from one water molecule to the next via hydrogen bonding. Additionally, proton transfer in water was shown to be strongly coupled with the dynamics of the local environment and the density of ionic defects was found to increase exponentially with temperature [44].

Such a form of protonic transport results in a build up of space charge and also causes electrode blocking. The mechanism requires the favorable orientations and positions of chains. Consequently, intrinsic conduction should increase with temperature and only exist at temperatures over glass transition temperature (T_g). Since we are concerned with temperatures much less than T_g during the typical lifetime of an automotive PCB, this mechanism is an unlikely candidate.

4.4.2 Extrinsic Ionic Conduction

Extrinsic conduction proceeds through the percolation of ions (generated from electrolytic reactions) through the free volume. This has been observed in a number of experiments and is the most likely candidate, especially for technical insulators such as PCBs where there

are many free radicals from chemical additives and environmental contaminants.

Extrinsic conduction mechanisms can be distinguished from intrinsic mechanisms by performing experiments at different pressures. If we were to increase pressure then extrinsic ionic conductivity should decrease because there would be a reduction in free volume. On the other hand, intrinsic ionic conduction would increase with pressure because this would enhance charge transfer between chains. However, in our present work we will not perform any such (pressure) tests and, therefore, the information presented above is intended to guide future experiments.

4.4.3 Ionic Hopping Model

At low DC fields (< 1 MV/m) and at low temperatures (below T_g) it is believed that ionic conduction in polymeric insulators proceeds partially (ionic percolation does not follow a smooth, straight path) through pure extrinsic conduction. Conduction is observed to be an activated process with ions hopping over barriers. The barriers could be in the form of spatially separated vacancies or in the form of the energy needed to overcome hydrogen bonding. The question arises as to where the hydrogen bonding would occur. It was shown in Section 3.2.1 that FR-4 is made up of an epoxy polymer that is highly polar and has a number of side hydroxyl (OH) groups. These form potential sites for hydrogen bonds to form.

The ionic hopping mechanism was first developed by Mott [39] to explain ionic conduction mechanisms in crystalline solids² and described in fair detail by Dissado [18] and Seanor [50].

The theory can be described in terms of movement of ions or vacancies through a lattice structure. The lattice model considers both the charge concentration and their mobility as a function of temperature. In fact, low-field ionic conduction in polymers is found to obey the Arrhenius type relationship.

$$\sigma(T) = \sigma_0 e^{\frac{-\phi}{k_B T}} \quad (4.9)$$

where σ is the conductivity and ϕ is the activation barrier.

²Sir Nevill F. Mott did a lot of work in studying electrical conduction in amorphous materials and consequently won the Nobel Prize for “his fundamental theoretical investigations of the electronic structure of magnetic and disordered systems”.

In the lattice model, the ions (or charge carriers) are considered to be thermally activated and to be located in potential wells and so their mobility is limited by the ease with which they can escape these wells.

If we consider a typical cubic crystal as shown in Figure 4.1:

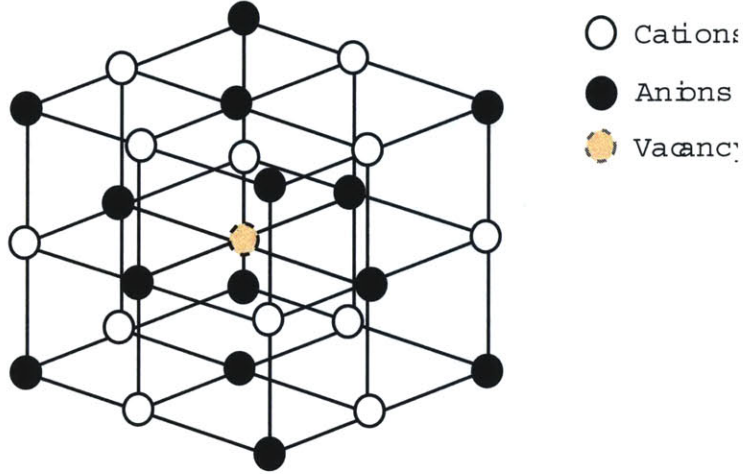


Figure 4.1: Cubic Crystal Structure with a vacancy in the center instead of a Cation (Adapted from [18])

Any of the 12 cations could fill the vacancy. However, they have to overcome the coulombic forces which hold them in place. From classical statistical mechanics, the probability that this nearest neighbor transition takes place during any interval “ dt ” is:

$$P(\text{transition}) = \nu_0 e^{\frac{-\Delta G}{k_B T}} dt \quad (4.10)$$

where ΔG is the activation energy and ν_o is the “attempt to escape frequency”.

This model makes two fundamental assumptions which we will relax a little later in this section [19],[20], [21], [22],[23], [12] and [47]. The model assumes that we have a constant barrier of activation. It also assumes that the density of the localized states is constant. In other words, the potential felt by the charge carriers all have an equal minima.

Now, if we applied an electric field of magnitude, E along one of the axes of this crystal such that the vacancy is neighbored by only 2 cations along this axis. This is analogous to a one dimensional model in the sense that only one of the two nearest cations can fill the vacancy and hence we are concerned with overcoming the coulombic forces that hold them.

Electrical Conduction

The potential barrier inhibiting the movement of the cations or the vacancy is affected. In fact, the potential barrier to move the vacancy in the direction of the field is reduced by $\frac{1}{2}Eea$ where a is the spacing between the cations. Similarly, the potential barrier inhibiting the movement in the reverse direction will be increased by the same amount.

The probability of transition in the forward direction is:

$$P(+a) = \nu_0 e^{-\frac{\Delta G - \frac{1}{2}Eea}{k_B T}} dt \quad (4.11)$$

The probability in the reverse direction is:

$$P(-a) = \nu_0 e^{-\frac{\Delta G + \frac{1}{2}Eea}{k_B T}} dt \quad (4.12)$$

Total probability of transition is:

$$P_T = P(+a) - P(-a) \quad (4.13)$$

$$P_T = \nu_0 e^{-\frac{\Delta G}{k_B T}} dt \times 2 \sinh \left[\frac{Eea}{2k_B T} \right] \quad (4.14)$$

This expression, defines the proportion of a large number of carriers that move a distance “ a ” in time “ dt ”. The drift velocity then becomes $v_d = aP_T/dt$ and

$$v_d = a\nu_0 e^{-\frac{\Delta G}{k_B T}} \times 2 \sinh \left[\frac{Eea}{2k_B T} \right] \quad (4.15)$$

For small values of x , $\sinh(x) \approx x$. If the electric fields are low ($E < 10^8$ V/m), this approximation holds and we get:

$$v_d = \frac{Eea^2\nu_0}{k_B T} e^{-\frac{\Delta G}{k_B T}} \quad (4.16)$$

Then the field dependent mobility, $\mu = v_d/E$ becomes:

$$\mu = \frac{ea^2\nu_0}{k_B T} e^{-\frac{\Delta G}{k_B T}} \quad (4.17)$$

In addition to mobility the concentration of the charge carriers can also influence the conductivity. If we assume that the charge generation process is thermally activated then:

$$n(T) = N e^{-\frac{E_A}{k_B T}} \quad (4.18)$$

From equation 4.2, we can find the current density:

$$J(T) = \frac{Ee^2a^2\nu_0N}{k_B T} e^{-\frac{E_A+\Delta G}{k_B T}} \quad (4.19)$$

Ionic conduction in polymers according to Dissado [18] has a couple of characteristic features. Firstly, it is clear from experimentation that the mobilities in polymers are very low and this is easily predicted in the ionic hopping model. Also, after the application of a step voltage, there is an initial decay observed. Dissado says that this is due to the build up of cations and anions at the electrodes thereby blocking (restricting) conduction. Even though the current decay phenomena is universally accepted, the reasoning is still under question. The topic of transient step responses is still a subject of active research and we will explore it in more detail in Section 4.5.

4.4.4 Activation Energy, Random Barriers and Percolation

Since the ionic hopping model described was developed for crystalline solids, the question now arises regarding the applicability of such a model to polymeric materials which are usually amorphous and highly disordered. Such a model can still hold if one were to think of the mechanism as “hopping over a potential barrier”. In the case of lattice or periodic crystalline structures, this potential barrier was the coulombic force holding the cations and anions in place. However, in polymers this potential barrier could be the energy required to escape the confines of a specific microscopic void or the energy required to escape hydrogen bonds that might exist between the ion and the polar side groups on the polymer chain.

We stated after Equation 4.10 that the model assumes a constant barrier height and constant potential minima.

We will relax the assumption of the constant potential barrier height with the presentation of the Random Barrier Model [23]. Jeppe Dyre presented this outstanding new theory in the hope to develop an analog for the ideal gas model for ionic conduction in non-crystalline material [19], [20], [21], [22] and [23]. The model was primarily focussed on the issue of universality in AC conduction in many different materials. Jonscher [28], [29] and [30] later presented a series of papers along this line of AC behavior and there were many universal features in AC conduction that were well explained through this theory. However, our interest here lies in DC ionic conduction in polymers. The universal feature existing in DC conductivity is the Arrhenius temperature dependancy.

Shown in Figure 4.2 is the simple ionic conduction model with constant potential barriers to ionic motion and constant site energies (well depth). The Random Activation Barrier Model varies the conduction landscape through a random distribution of potential heights. A more complex version of the model involves varying the site energies.

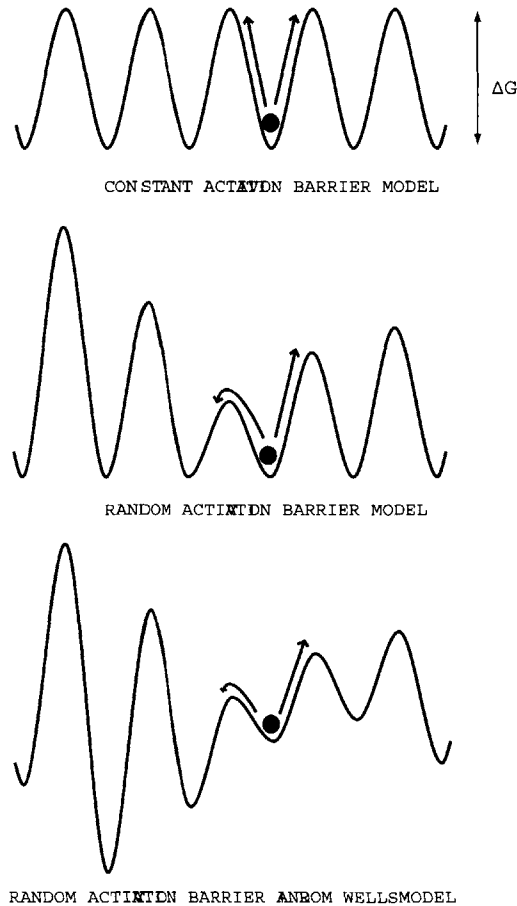


Figure 4.2: Mechanism of Ionic Hopping over a Potential Barrier

As a reminder, the conductivity (from experimental evidence and the simple ionic model) can be given by:

$$\sigma(T) \propto \sigma_0 e^{-\frac{\Delta G}{k_B T}} \quad (4.20)$$

It might be argued that the Random Barrier Model assumes the existence of multiple randomly distributed activation barriers (ΔG). Therefore, it might predict a non-Arrhenius DC conductivity with multiple activation energies. Particularly, at low temperatures, the smaller (but fewer) activation energies dominate while at higher temperature, the activation energy increases. However, experiments have indicated that polymeric insulators display a simple Arrhenius relationship with one activation energy.

4.4.4.1 Percolation Theory

As Dyre [23] clarifies, this conflict can be resolved through an understanding of percolation theory. Consider a 2 dimensional square lattice with a specific probability associated with links linking each site. These links can be thought of as the activation energies (ΔG) and are randomly distributed and uncorrelated with each other according to the probability distribution $p(\Delta G)$. Suppose that the links linking neighboring lattice sites are marked according to increasing barrier height, or in other words, each time we choose a barrier height, we include a distribution of heights below the chosen height represented by the links. If we keep increasing the maximum barrier height, at some point we will reach the percolation threshold. The “percolation threshold” (p_c) is the probability that represents the onset of an infinite cluster of marked links. Basically, when an infinite cluster is reached no larger barriers greater than the chosen barrier is required for ionic conduction. The largest barrier on the cluster represents the bottleneck to ionic motion and this barrier completely dominates the overall rate - the DC activation energy (ΔG_c).

The relation between the percolation threshold and DC activation energy is given by:

$$\int_0^{\Delta G_c} p(\Delta G) d\Delta G = p_c \quad (4.21)$$

Physically, moving charge carriers must every so often overcome the largest barrier on the percolation cluster. The overall activation energy (ΔG_c) determines the rate of mean square displacement. DC conductivity is proportional to this mean-square displacement per unit

time in zero external field ³.

Cordes [12] presents a small variant of the random barrier model where the site energies of the disordered lattice are in fact different (shown in the last picture in Figure 4.2). Even though this is usually applicable in electron hopping transport and these site energies represent varying energies with respect to the Fermi level, it can be formulated in terms of an ion hopping model as well.

The different site energies are representative of differing types of sites in a disordered polymer. Ions can reside in hydrogen bond traps or just in available free volume. In either case, it is possible to hypothesize that due to differing local fields and local electrostatic interactions (with other ions), one site can be more favorable than another and consequently, one site might be of lower energy than another.

This area involving the study of the random barrier landscape and ion hopping is one of active research. Earlier, we alluded to the fact that this model was developed with need to understand a universality in AC conduction. To extend this idea, it would be nice to unify AC and DC conduction and thereby have one mechanism that explains both. AC conduction can be due to ion motion over limited distances while DC conduction involves motion over extended distances. In the next section, we will discuss the transient behavior of current after the step application of a DC field.

³Fluctuation-Dissipation Theorem

4.5 Transient Conduction Mechanisms

In addition to steady state conduction mechanisms, we are also interested in understanding what happens at the instant a DC voltage is applied. Most insulators typically undergo various forms of relaxation. Relaxation [30] is the recovery of strain on the removal of a stress. Therefore, it is time-dependent after the sudden removal or sudden application of a steady stress. The time-domain measurement of interest here is the variation of current with time. Frequency-domain measurements are made by subjecting the material to harmonically varying stresses of a certain angular frequency. In systems (materials) that have a linear response with an applied signal, the time-domain and frequency-domain measurements are Fourier transforms of one another.

We briefly touched upon physical relaxation involving the repositioning of polymer chains in the previous chapter due to temperature (α and β chain relaxations) and moisture ingress (Non-Fickian responses). However, here we will focus on dielectric aspects and more specifically we will try to link the steady state conduction mechanism of ionic hopping with the transient currents.

Jonscher [30] distinguishes two major types of dielectric responses which are dipolar responses and charge-carrier responses. While dipolar polarization leaves a zero residual on discharging, the charge-carrier responses give only a partial recovery and leave a finite polarization in the system. In the time-domain the charge-carrier systems display a divergent behavior for the integral of the current.

The most ideal response is what is known as the “*Debye Response*”. This response is obtained for a group of independent noninteracting polarizing entities which have the same waiting time before making a transition. The Debye response is typically obtained with a series combination of a frequency-independent capacitance and resistance. In the time-domain this can be expressed as a purely exponential time dependence:

$$i(t) \propto e^{-t/\tau} \tag{4.22}$$

However, it is widely acknowledged that a pure Debye responses are never observed and there is fair amount of variation between responses. The more general and accepted (universal) rule that applies to most materials is a *Curie-von Schweidler* fractional power law in both the time and the frequency domain.

$$i(t) \propto t^{-n} \tag{4.23}$$

where the fractional power n usually varies from 0 to 1.

A popular interpretation of this power law behavior and the deviations from the Debye form is the “Distribution of Relaxation Times” theory. This theory assumes that the system contains a large number of parts with many relaxation times. While this works out mathematically, the theory can be discarded since it does not explain why many different materials with the universal type of response all have the same distribution of relaxation times [30]. We still mentioned the theory because of its popularity in literature.

Both types of dielectric responses - dipolar and charge-carrier systems display this power law with similar fractional powers at very small times prior to the onset of the Debye time constant. However, at later times the two responses diverge quite a bit. In fact the fraction power n becomes much higher for dipole responses and lower for charge-carrier systems. The initial common response is what Jonscher [28], [29] and [30] calls the “universal response”. This universal response is followed until such time that the total polarization due to the dipoles is neared. At this stage higher fractional powers for dipolar responses limit the total polarization. The lower fractional powers for charge carrier systems, on the other hand, indicate the limitless total polarization since the displacement of individual charge carriers is open ended and constitutes the DC conduction at infinite time.

This is illustrated in Figure 4.3 where both the convergent dipolar and the divergent charge transport responses are compared with the typical straight line plot (on a log-log scale) of the standard power law.

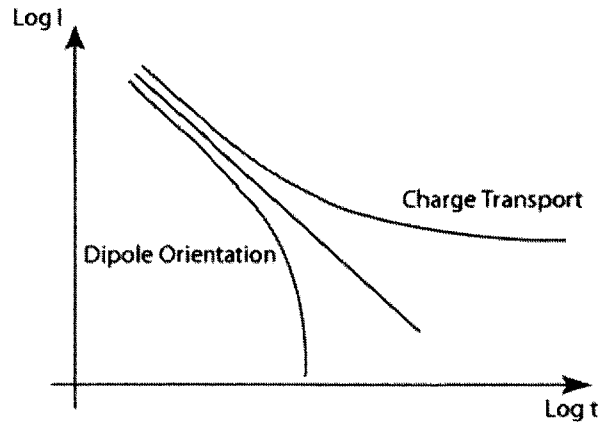


Figure 4.3: Comparison between Dipolar and Charge Transport Power Law Relations

The decrease in the fractional power, n , of the time-domain response current to a step DC voltage for charge-carrier systems at long times presents the onset of “Low Frequency Dispersion” (LFD) [29]. The LFD phenomena signifies a finite and reversible storage of charge in the material or at the interface.

The similarity between hopping charge carrier mechanisms and the dipolar responses in small times underlines the fact that they both appear to be good approximation as dipoles, in that hopping carriers jump back and forth (reverse directions) between relatively infrequent forward movements (Random walk Theory/ Percolation Theory) linking both AC and DC conduction mechanisms and eventually leading to DC conduction in steady state.

Adamec and Calderwood [5] have explained the electrical polarization phenomena in polymeric dielectrics in terms of a number of different factors ranging from dipole relaxation phenomena to electrode blocking and trapping of charge carriers in the bulk. They have used the distributed relaxation times approach stating that polymeric chains have a broad range of relaxation times associated with them. They also discuss transient conduction in terms of physical relaxation phenomena at especially high temperatures. They verified that in most polymers dipole polarization cannot account for all the observed transient (absorption) currents and there is a significant contribution from the transport of free charge carriers that are not injected from either electrode but are instead in the bulk prior to the application of an external electric field.

Transient currents in many polymeric systems are known to display fractional power laws. Additionally, many polymeric systems are shown to have hints of LFD meaning that for large times, the current falls less quickly with time. In fact, some studies indicate that the DC current observed in steady state is only pseudo-constant and instead actually decreases gradually. Lowell [36] takes the theory formulated by Jonscher a bit further and applies it to polymeric systems. He supposes that there are mobile charges in the bulk that contribute to not only conduction currents (ionic hopping) but also to transient (absorption) currents. The model shows that the transient motion of charges in a loose network of polymer molecules can give rise to decaying currents that follow fractional power laws. This model is very similar to hopping models except that the elasticity of the polymer matrix is incorporated.

According to the Lowell model, the flexibility of the polymer chains allows limited motion of trapped charges and also enhances the probability of transfer from one chain to another.

The expression to describe current density due to the limited motion of charges attached to the polymer chain is derived to be [36]:

$$J(t) = ne\mu E [e^{-\chi_1 t} - e^{-\chi_2 t}] / t \quad (4.24)$$

Here χ_1 and χ_2 represent the range of resistances offered by the viscous and elastic forces from polymer chain entanglement. This equation displays the inverse proportionality to time that is consistent with the Curie-von-Schweidler power law.

Equation 4.24 is only representative of the “universal” part of the dielectric response and we, therefore, cannot distinguish whether it is due purely to dipole re-orientation or the limited movement of trapped charge carriers. However, as mentioned earlier [30] there is a significant deviation from the power law in many materials and this deviation can help in determining the mechanism of the dielectric response.

Lowell describes this deviation as the transfer of the charge carrier from one chain to another. He claims that motion of the chains due to the applied field greatly increases the probability of such a transfer. He determined that the current due to such transfer processes results in an excess current (ΔJ) over Equation 4.24 given by:

$$\frac{\Delta J}{ne\mu E} = p\alpha' e^{-\alpha p t} [\alpha E_i(\alpha p t) - \alpha' E_1(\alpha' p t) + \alpha \ln(\chi_2/\alpha p) + \alpha' \ln(\chi_2/\alpha' p)] - \frac{(1-\alpha)}{t} (1 - e^{-p t}) \quad (4.25)$$

where α represents the fraction of the charges permanently trapped, p is a parameter which is a function of the applied field, mobility and the mean free path and $\alpha' = 1 - \alpha$. Das-Gupta [15] has presented a good range of experimental results that match very well with Lowell’s model.

In summary, we have presented a look at various models that attempt to explain the universal behavior of many insulators as well as link the underlying mechanisms for transient and steady state currents.

4.6 Surface Conduction and Interfacial Effects

Surface conductivity experiments have indicated that some behavior is common to both the surface as well as the bulk. For example, the power law still holds for most surfaces. However, surface conduction is highly complicated mainly because of the direct influence of external impurities. Additionally, on a microscopic level, there are numerous dangling

bonds and many other chemical reactions that result from interactions with the atmosphere. Therefore, it can be very difficult to experimentally keep the surface of the test material in controlled conditions. Also, of considerable importance is the role of adsorbed moisture on polymeric surfaces that can create almost bulk electrolytic environments for charge transport.

Surfaces can be either hydrophobic or hydrophilic and can switch from being in one type to another depending on the exposed environment. Typically, the single most influential surface impurity in the service life of any insulator is humidity and moisture adsorbed on the surface as a result. In the next section, we will discuss the role of water in surface and in the bulk.

Additionally, degradation along the interfaces between the epoxy and the fiberglass (seen in Section 3.10) can help increase conduction. When the hydrogen bonds between the fiberglass and the bulk epoxy are broken by water molecules, there is an observed increase in free volume. This in turn can cause an increase in extrinsic ionic conduction.

4.7 Role of Water

In Chapters 2, 3 and 4, we have constantly referred to the role played by moisture in electrical conduction. It is very clear in literature that there is constant disagreement whether moisture plays a direct or an indirect role in conduction. We mentioned in Chapter 3 that water typically exists in polymers either bound to the polymer chains through hydrogen bonds or unbound in the free volume. This can be linked to the intrinsic and extrinsic conduction mechanisms discussed that might hint at the direct involvement of water in conductivity. However, we also stated that water tends to modify local polymeric structure and cause swelling. This makes one believe that maybe water is opening up free volume for other ionic species to drift through. Water can additionally contribute ions through hydrolysis or through hydration of external impurities.

The role of water is a very complicated one and can only be properly understood through experimentation. In the next Part consisting of Chapters 5, 6 and 7, we will describe the various components of our experimental test setup and procedure.

Part II

Experiment

Design of the Test Sample

THIS chapter presents the design of two generations of test samples. Each sample has a specifically chosen set of conductive traces patterned on it. Dimensions and purposes for each pattern on the test boards are described in detail.

5.1 Introduction

We have, thus far, described the need to study and understand DC leakage conduction in PCB insulation. In the next few chapters we will describe the various components of our experimental work. We will first look at the design of the test sample. In this regard, we have selected the base material of the PCB to be FR4 with copper traces.

To measure DC conduction through FR4, we will have to set up a constant electric field through it using metal electrodes. Metallic Copper, used as PCB cladding makes for good test electrodes. In Chapter 1, the patterns on a typical IPC test board was presented. That board shown in Figure 1.4 consisted of many characteristic interdigitated copper traces patterned as a comb. These patterns present a good starting point for any study in electrical leakage in insulators.

The design of a suitable test sample is essential to help isolate desired parameters and eliminate interference and noise in the measurements. Additionally, we are interested in understanding the dynamics of the conduction mechanisms in the PCB. This means that we are interested in studying the different possible conduction paths that might exist. A simple way to isolate the different conduction paths is to vary the spacing between conductors on the PCB. Shown in Figure 5.1 are the dominant conduction paths for different spacings. Both the small and large combs are interdigitated finger patterns similar to the ones seen in Figure 1.4, while the circular disc pattern, shown below, is made up of disc shaped copper electrodes on each side of the insulation material. While the dominant conduction mechanism in the small comb pattern is believed to be on the surface and for the circular disc is through the bulk, the large comb pattern might have both surface and bulk mechanisms playing an important role.

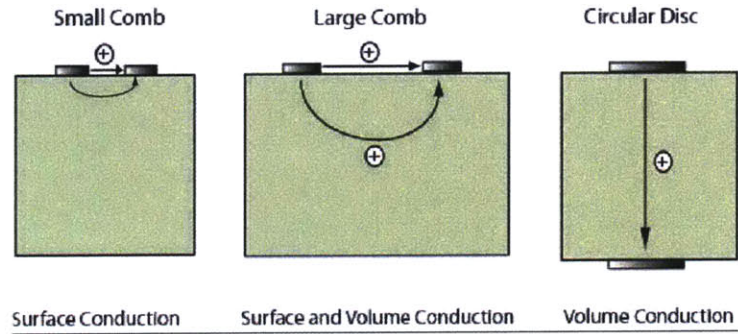


Figure 5.1: Dominant Conduction Paths

In this chapter, we present the motivation and design for two generations of test samples. The lessons learned from the first generation test samples are used in the design of the improved second generation.

5.2 First Generation Test Sample

A suitable board was designed combining patterns from IPC standards and industry documentation as well as some of our own ideas. Figure 5.2 shows the PCB layout view of our first generation board.

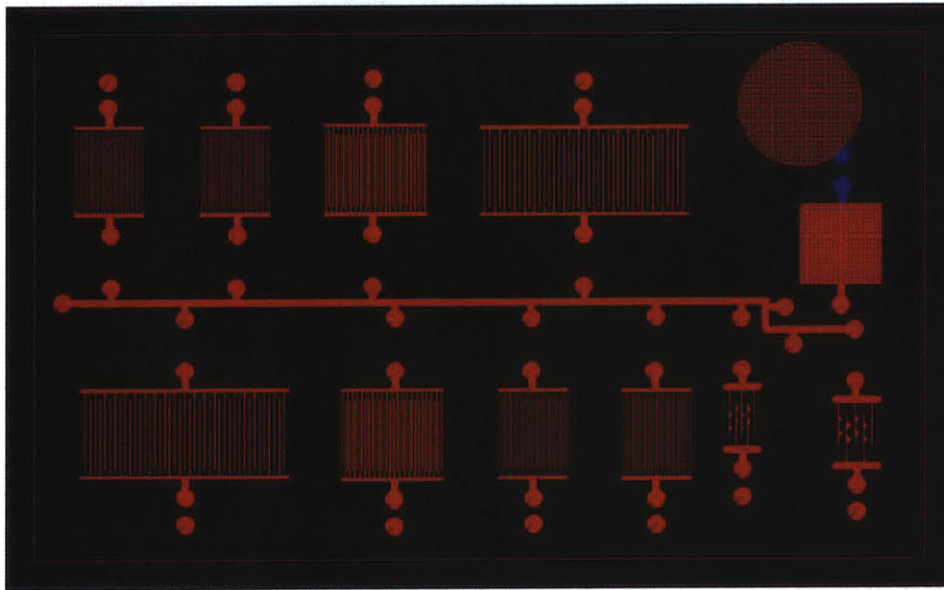


Figure 5.2: The Test Coupon Design

It can be seen from Figure 5.2 that there are twelve patterns on the sample board. These twelve patterns can be further subdivided into different pattern groups. There is a basic comb pattern (with interdigitated conductive fingers), a square pattern (similar to the disc pattern in Figure 5.1)¹, a circular acoustic pad (on the upper right) and a comb pattern with triangular dimples. Among the comb patterns, there are three sizes. These sizes are determined by the gaps between each individual conductor. The length and number of conductors in each of the comb patterns are almost the same. It is evident from the figure that there are 8 comb patterns or 4 patterns repeated twice. The two smallest patterns are actually the same and therefore there are 4 occurrences of the smallest pattern. There are two medium patterns and two large patterns. Shown in Figure 5.3 is a photograph of the sample board placed on a stand. The apparent color and variation of color in the conductor in Figure 5.3 is a consequence of variations in lighting. To the eye, the conductor had a silver sheen, normal for clean, unoxidized tinned copper. Additionally, the base insulating material was darker shade of yellow. Depending on the nature of the FR-4, there could be

¹In Figure 5.2, only the top layer is visible

variations in color.

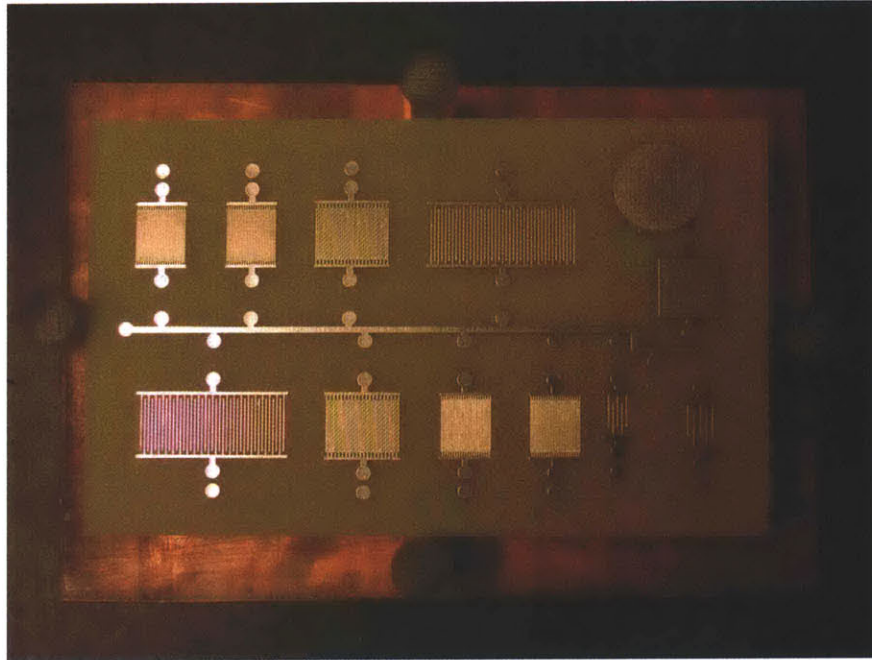


Figure 5.3: The Test Coupon Design

The square capacitance pattern was used to measure conduction through the volume (bulk). The small, medium and large interdigitated finger patterns were used to measure the range between exclusive surface conduction and exclusive volume conduction. In a small pattern, the distance between adjacent fingers are very small and therefore it is theorized that the most dominant conduction mechanism is through the surface. On the other hand, the distances between fingers on the large pattern are much larger and almost on the order of the thickness of the board. Therefore, it is visualized here that both the surface as well as the volume have strong influences on the conduction mechanism. The circular disc shaped pattern was used for acoustic imaging. The two finger patterns with dimples on the lower right hand corner of the board were intended to measure electrical stress concentration and study the growth of dendrites through high-speed and high magnification cameras.

Additionally, it was decided that these patterns be placed a good distance apart unlike the IPC test boards shown in Figure 1.4. This was an attempt to ensure that we have no leakage between the patterns that might have otherwise interfered with our measurements.

5.2.1 The Pattern Dimensions

Figures 5.4, 5.5 and 5.6 show the dimensioning of the different patterns. Table 5.1 indicates the sizing scheme used in our sample board based on the dimension of these figures.

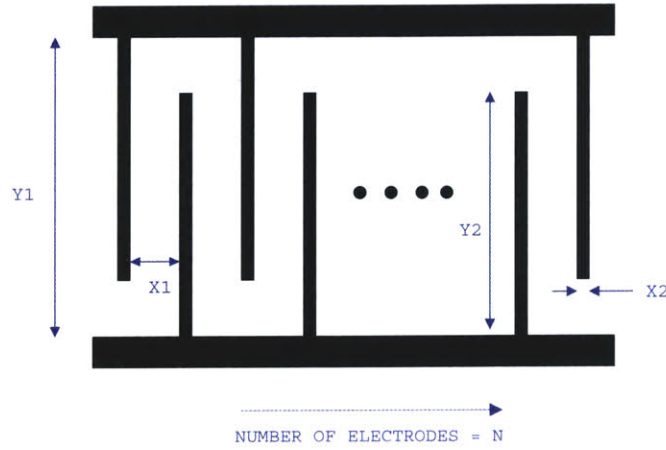


Figure 5.4: Dimensions of the Comb Pattern

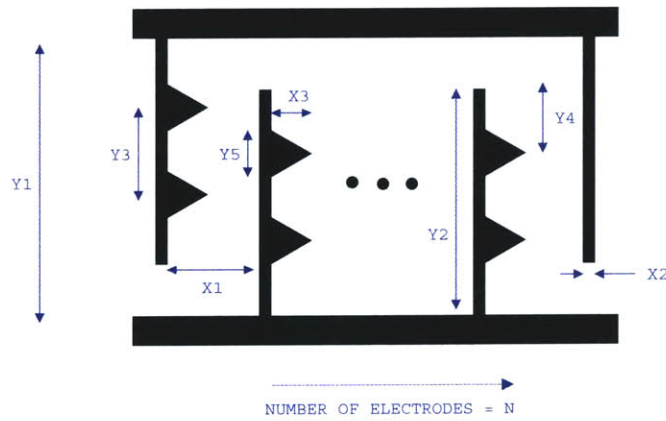


Figure 5.5: Dimensions of the Comb Pattern with Triangular Dimples

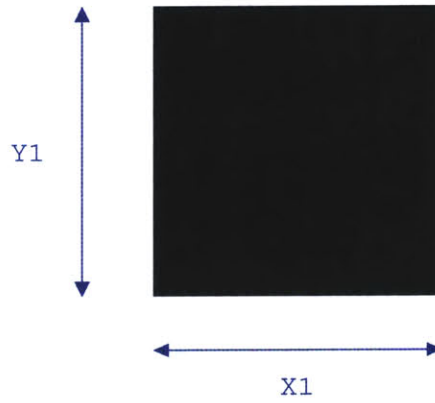


Figure 5.6: Dimensions of the Filled Square Pattern

	Comb			Comb with Dimples		Square
	Small	Medium	Large	Small	Large	
N	41	41	41	5	5	-
X1	8	11.8	35.4	48.6	68.3	776
X2	8	11.8	11.8	11.8	11.8	-
X3	-	-	-	27.5	32.1	-
Y1	792	809	785	516.4	559	776
Y2	746	749	737	418	413	-
Y3	-	-	-	117.4	136.7	-
Y4	-	-	-	68.85	123.65	-
Y5	-	-	-	59.1	67.3	-

Table 5.1: Dimensions (in mils) of the Patterns on the First Generation Sample

5.2.2 Motivation to Redesign The Test Sample

As we were doing the tests on the first generation boards, we were thinking how we could improve this sample board to make the results more accurate and representative of what we wanted to measure. These improvements could be implemented in the next generation of boards we would design.

Specifically, the need for a new board and possibly new patterns and arrangements once again stems from the need to isolate one process from another with conductive ground barriers. The first generation boards did not electrically isolate one pattern from another. Even though the patterns seem to be electrically isolated from one another by distance, there remains a possibility for stray leakage paths that are created and re-enforced during testing. This would result in inaccurate current readings and since we are observing very low currents in the pico and nano ampere range, these stray leakages might prove to be significant.

Also, it is desired to keep the number of testing variables to an absolute minimum. This means that we would like to keep our test board to a basic bare copper trace on FR4 material only. Most of the IPC insulation testing standards indicate the use of bare copper traces on FR4. The copper traces on the first generation boards were covered with tin/lead solder. PCBs used in commercial electronics do have a tin/lead solder layer that might actually be an important contributing factor to the overall degradation process. However, for the purposes of research and understanding, we want to remove all the complexities at first and then add them back in a controlled manner to gain a complete understanding of the system.

The connecting pads on each pattern on the first generation boards were above and below each sample when the sample board is made to stand vertically along the long edge. In high temperature and high humidity conditions as in the environment chamber, residual solder flux from soldering leads to the connecting pads on our vertically mounted test boards will tend to leak from the solder joints and might disrupt good measurements. In reality, leaked solder flux could also be catalysts in the degradation process. However, as discussed earlier, we want to simplify the problem as much as possible and then add complexities step-by-step.

It was also observed that the square pattern was placed on the right hand side of the board near the edge. As mentioned earlier, the square pattern is used to measure the conduction through the volume. A majority of our tests will be in conditions of high temperature and high humidity. Moisture diffusion into the board is important in this regard and has to be understood well. The question arises whether moisture diffusion occurs through the surface

Design of the Test Sample

and then into the volume or through edges and into the volume or both and if so which is more dominant. As mentioned, the square pattern on the first generation board is on the edge and therefore there might be moisture diffusing from the edge as well as from the surface surrounding the pattern. It would be nice to see the changes in bulk conduction with more moisture diffusing directly from the surface above. This can be accomplished with a porous bulk pattern which permits surface diffusion.

The corners of fingers on the interdigitated patterns on the first generation sample boards were sharp and these sharp points create very high fields in their vicinity. Such high fields could result in other conduction mechanisms and degradation phenomena such as electronic charge injection from the electrodes and disrupt the direction of this thesis. Therefore, care has to be taken to ensure smooth and rounded edges.

5.3 Second Generation Test Sample

To make our way towards better, repeatable and more reliable measurements, a new board was designed.

As shown in Figures 5.7 and 5.8, this sample board is overall of the same dimensions as the old one but has fewer and different patterns.

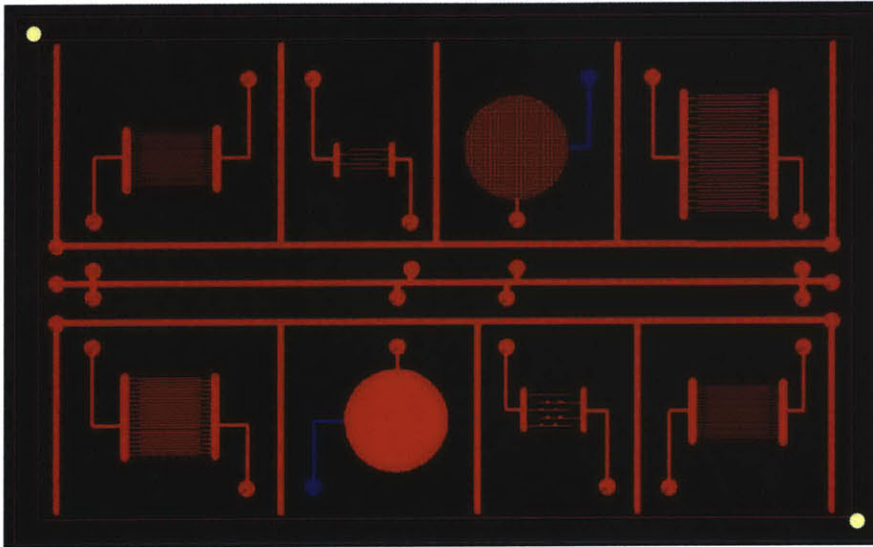


Figure 5.7: 2nd Generation Board

It is clear that all the patterns are electrically isolated from one another by the guard rings that can be grounded. There might be some leakage from the pattern on to the guard rings, but these will not be picked up by the measuring (sensing) lead and would therefore not affect measurements. At some future juncture, it will be interesting to observe the leakages into the guard rings.

Care has been taken to ensure that the connecting pads on each pattern are not directly above and below the pattern and therefore, if solder flux leaks, it will not disturb the pattern.

Additionally, the second generation board now consists of bare copper traces on FR4 material, unlike the first generation that had the layer of reflowed tin/lead solder on top of the copper traces.

In the second generation board, we have replaced the square patterns (measuring volume conduction) with circular disc patterns. As described earlier, we want to restrict the stress

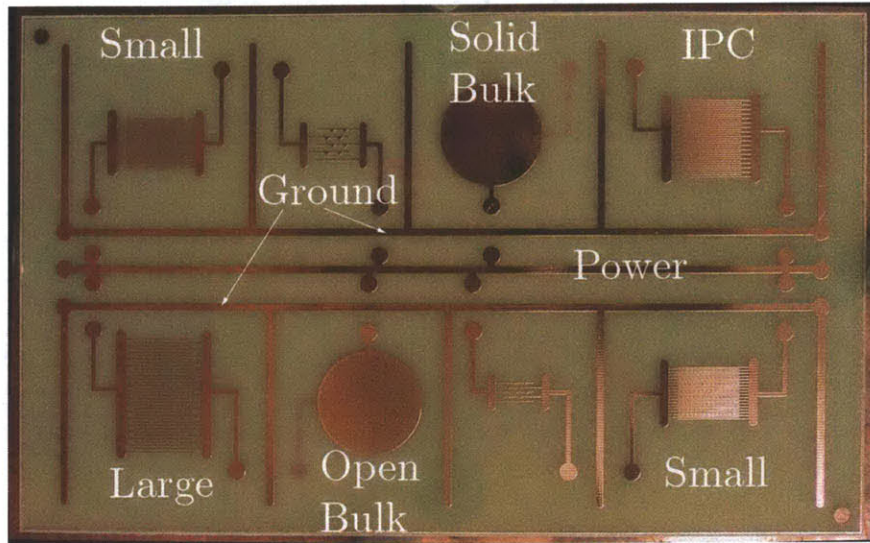


Figure 5.8: 2nd Generation Board

concentration based measurements to the dimple patterns. In the square pattern, we had sharp edges and the electric field around these edges are very high and therefore might influence measurements. It was determined that circular patterns are more suitable since it would not contain any sharp points. Additionally, we also added a porous circular pattern. This will enable us to compare the diffusion of moisture through the edges and through the surface.

We have also removed some patterns from the old board such as the acoustic pad and some other redundant patterns. Most of our tests were measuring conduction and surface and volume currents. We felt that acoustic measurements were not required now and would therefore only be occupying test space on the board. Similarly, the first generation board had too many small patterns and it was felt that two of those were sufficient. Additionally, we only decided to keep one large pattern and a modified medium pattern. This dimensions of this modified medium pattern would be as per the IPC standard. Shown in the Table 5.2 are the dimensions of all the patterns on the second generation board with respect to Figures 5.4 and 5.5.

We have described the design of a test sample board and the reasoning behind the choice of patterns on it. We improved on one generation of test samples with a newer more optimal design. Appendix A has more detailed derivations of various geometric quantities and calculated values for each generation of samples. In the next chapter we will see the entire measurement system which will be used to conduct experiments on our test sample boards.

5.3 Second Generation Test Sample

	Comb			Comb with Dimples		Circular Disc
	Small	Medium	Large	Small	Large	
N	35	35	35	5	5	-
X1	8	8	24	36	72	Diameter: 1091
X2	8	12	12	12	12	-
X3	-	-	-	12	36	-
Y1	844	844	844	500	556	-
Y2	748	748	748	406	460	-
Y3	-	-	-	118	136	-
Y4	-	-	-	54	170	-
Y5	-	-	-	27	67	-

Table 5.2: Dimensions (in mils) of the Patterns on the Second Generation Sample

The Measurement System

THIS chapter presents the components of the entire automated data acquisition system. An initial introduction to the measurement methodology is followed by a detailed look at each component. Finally, the components are brought together to evaluate the overall system. In addition we will look at the other measurement metrics such as weight and thickness.

6.1 Introduction

In the previous chapter, we looked at the design and reasoning behind the patterns on our test sample. Here, we will look at the entire system that is used to measure currents through the test sample as well as components associated with weight and thickness measurements.

Shown below in Figure 6.1 is a schematic of the basic test circuit to measure leakage currents. The test sample is placed inside an environmental chamber and a specific pattern on this sample is biased to a 100V supply through a suitable current limiting resistor. An electrometer or a similar low current measuring instrument is used to determine the conduction through the material. Each pattern is connected to a dedicated measuring instrument. An automated data acquisition system is used to connect the instruments to a computerized interface where signal processing and analysis can be performed.

The following sections provide detailed descriptions for each component beginning with the current measurement instrumentation.

6.2 Low-Current Measurement Instrumentation

For measuring very low currents in the pico and sub-pico ampere range, we will use a combination of electrometers and lab-built logarithmic amplifiers.

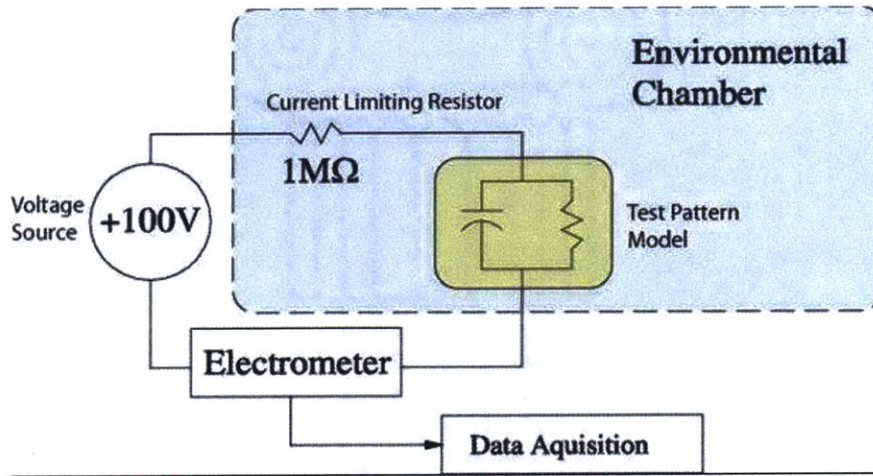


Figure 6.1: Basic Test Circuit

6.2.1 The Electrometer

We will use the Keithley 617 Electrometer as our primary instrument. The other home-built instruments will be calibrated to match the Keithley 617.

6.2.2 The Logarithmic Amplifier

In addition to the Keithley 617, we built a couple of logarithmic amplifiers. This device provides a logarithmic output for a linear input current or voltage. The circuit is based, as are most logarithmic circuits, on the inherent logarithmic relationship between collector current and base-emitter voltage in appropriately biased bipolar transistors.

$$V_{BE} = V_T \ln\left(\frac{I_C}{I_S}\right) \text{ where } V_T = \frac{k_B T}{e} \quad (6.1)$$

- k_B = Boltzman's constant = $1.381 * 10^{-23}$ J/K
- T = Absolute Temperature (Kelvin)
- e = Electron Charge = $1.602 * 10^{-19}$ C
- I_C = Collector Current
- I_S = Reverse Saturation Current

For our tests, we will be using a Burr-Brown LOG112 Logarithmic Amplifier integrated circuit. Shown in Figure 6.2 is an electrical schematic of a simplified logarithmic amplifier circuit:

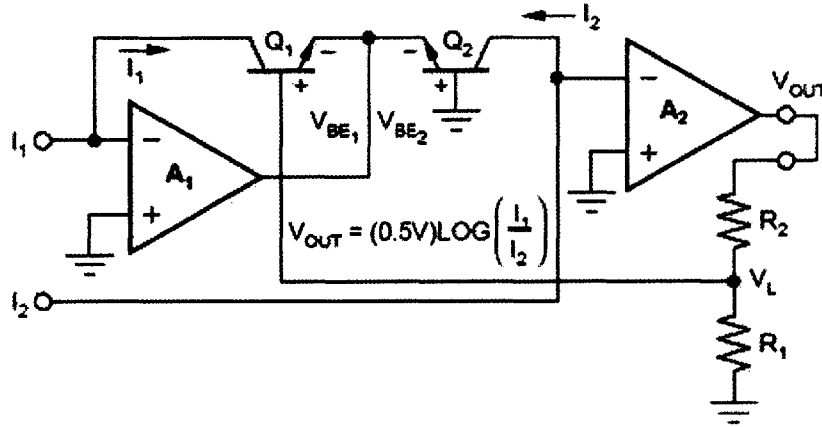


Figure 6.2: Simplified circuit of the LogAmp IC

From the circuit:

$$V_L = V_{BE1} - V_{BE2} \quad (6.2)$$

Therefore,

$$V_L = V_{T1} \ln\left(\frac{I_{C1}}{I_{S1}}\right) - V_{T2} \ln\left(\frac{I_{C2}}{I_{S2}}\right) \quad (6.3)$$

However, if the transistors are matched and isothermal, then $V_{T1} = V_{T2}$, $I_{S1} = I_{S2}$ and simplifying:

$$V_L = V_T \ln\left(\frac{I_1}{I_2}\right) \quad (6.4)$$

$$V_L = (2.303)V_T \log\left(\frac{I_1}{I_2}\right) \quad (6.5)$$

The Measurement System

$$V_{OUT} = V_L \frac{R_1 + R_2}{R_1} \quad (6.6)$$

Now, if we assume that $R_1 = R_2$, V_T is calculated as per Equation 6.3, V_L is calculated as per Equation 6.5 and substituting into Equation 6.1:

$$V_{OUT} = (0.5V) \log\left(\frac{I_1}{I_2}\right) \quad (6.7)$$

To incorporate this chip into the system, we will have to include circuitry to control the input current as well as a circuit to generate a reference current (I_2). Also, we will have to supply power to the entire circuit and shield it from electromagnetic interference. It will also have to be calibrated to be able to read our desired range of currents.

Shown in Figure 6.3 is a circuit providing for many of these needs:

6.2 Low-Current Measurement Instrumentation

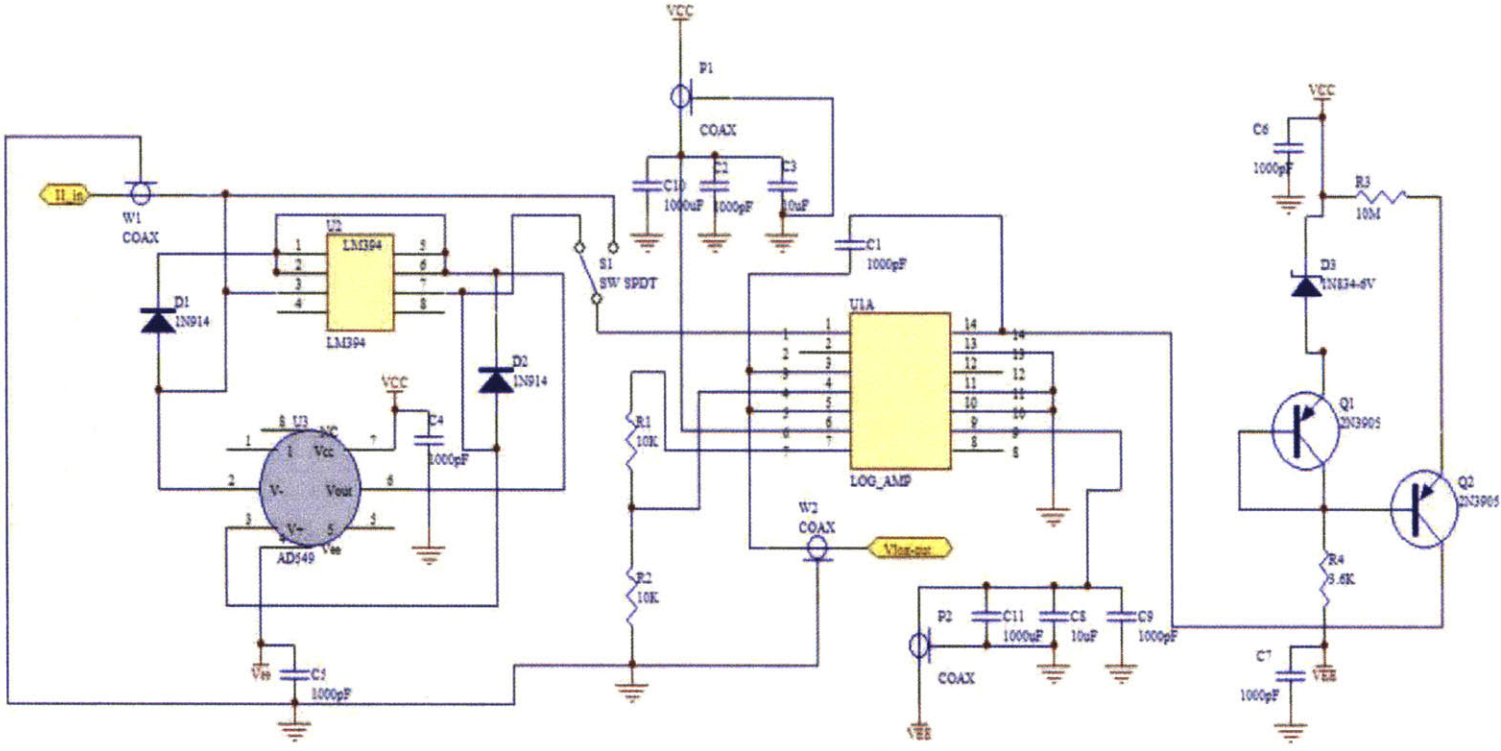


Figure 6.3: Overall Circuit

The Measurement System

The circuit can be divided into 3 portions. The central part consists of the logarithmic amplifier chip with the output resistors and the power supply along with a few capacitors. This includes the important compensating capacitor (C_1) in the feedback path. Frequency compensation for the circuit is obtained by this capacitor. For any application, the smallest value of this capacitor which may be used, is determined by the maximum value of I_2 and the minimum value of I_1 . Larger values of the capacitor (C_1), make the chip more stable, but reduce the frequency response. The right hand section of the circuit is the reference current generation part consisting of two transistors, a voltage regulating zener diode and a reference resistor (R_3) which decides the value of the reference current using the simple relation $I_{REF} = V_{zener}/R_3$. This is a temperature compensated reference current source. The left hand section of the circuit consists of the current inverter. Since the logarithmic amplifier cannot accept negative inputs, we have to invert the current to measure negative values. This part of the circuit is an optional portion that needs to be connected only if we will be measuring negative currents.

Shown in Figure 6.4 is the performance of the circuit, with the above stated modifications, to positive input currents on a log scale:

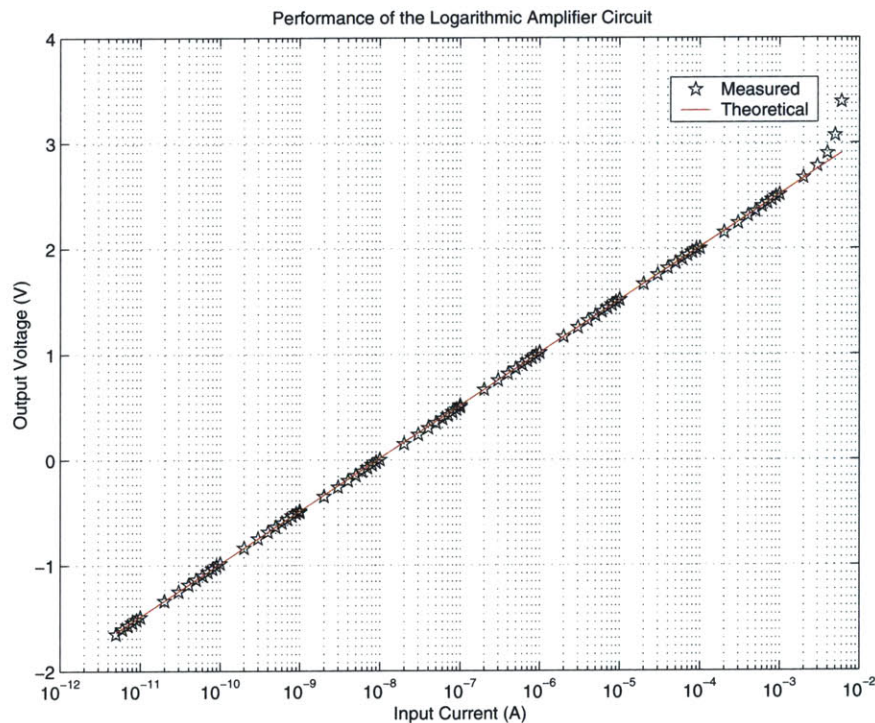


Figure 6.4: Performance of the Logarithmic Amplifier with Positive Input Current

Also, shown in Figure 6.5 is the performance of the circuit with negative input currents

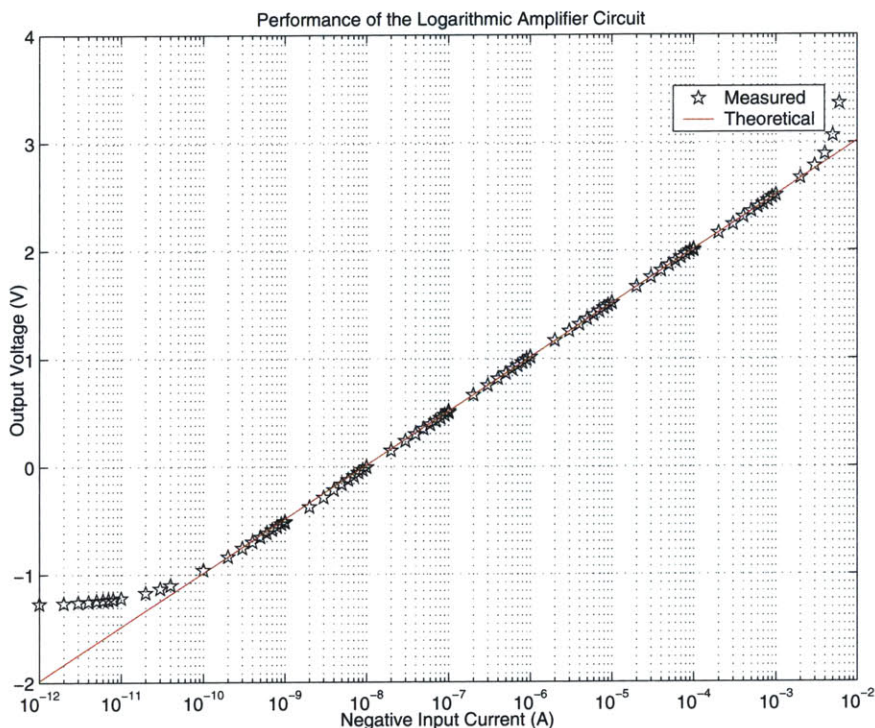


Figure 6.5: Performance of the Logarithmic Amplifier with Negative Input Current

It is evident from Figure 6.5 that we are not able to reach very small currents when we were trying to measure negative inputs. This is due to the limits set by the inverting circuit (amplifier and transistor pair).

Also, at positive currents of below 5pA (which is quite commonly encountered by insulators in dry conditions), the logarithmic amplifier does not have a stable response. To resolve this difficulty and increase the performance range of the amplifier, we add a constant current of 5pA to the input of the logarithmic amplifier. Figure 6.6 shows the schematic of this method.

We generate a constant 0.5V source using the existing power supply of the logarithmic amplifier, a voltage regulator and a voltage divider. This source is then placed in series with a 100G Ohm “Ohmite” resistor creating a constant 5pA current. This additional circuit is installed inside the same casing as the logarithmic amplifier.

Using this technique, the low current limit of the logarithmic amplifier has been extended to 0.5pA. We still obtain stable readings below this number, however, the noise levels are significant and compromise accuracy.

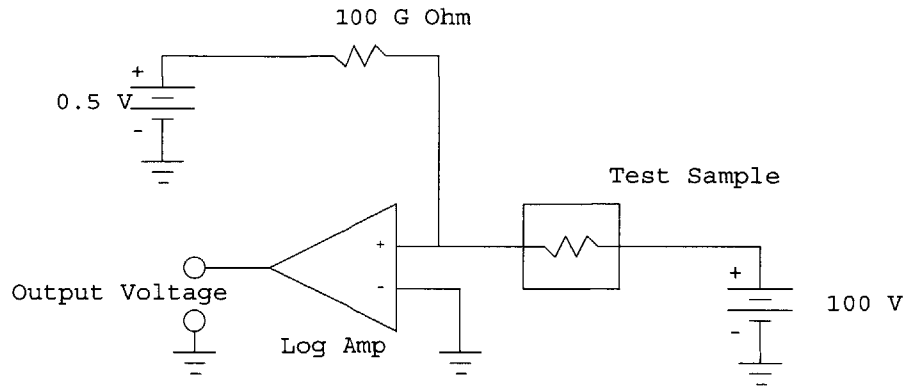


Figure 6.6: Constant Current Addition of 5pA

6.3 Chambers and Measurement of Environmental Conditions

Since we are interested in understanding the performance of PCB insulation in adverse environments and most reliability assessments are performed in extreme conditions, we will need an environmental chamber where we can control the temperature and humidity.

The Dupont Chemical Company loaned this project a used “Vista Scientific” environmental chamber. The chamber comes with a Watlow Series 920 PID controller to control the temperature and relative humidity. Some parts of the chamber initially needed to be replaced. The chamber was tested and an acceptable level of performance was achieved. An additional feature of the chamber is its programmability. We programmed the chamber to run through a temperature down ramp from 85°C to 35°C over 5 hours. The chamber, however, needs a constant supply of water that can be provided through a water reservoir on the back. In high moisture conditions (85°C/85% RH) the water can be consumed at a very high rate (about 2 gallons per day). To avoid the evaporator from being burned out, there has to be water always available. In all our experiments, we used distilled water.

In addition to the temperature measurements made by the thermocouple that is part of the chamber, we will measure the temperature on our samples using two digital temperature sensors. These two digital sensors are epoxied directly onto the test sample board at diametrically opposite corners. The two temperature sensors are MAXIM DSB20 one-wire devices.

The chamber is equipped with a wet-dry bulb thermometer, which means that it can make a fairly accurate measurement of the relative humidity inside the chamber. However, we have

also attached a relative humidity sensor inside the chamber. The RH sensor is a Honeywell HIH3610 device.

We also purchased a VWR Vacuum Oven which was used to remove all the moisture content from the test samples. The conditions we used were a vacuum of about 60 mTorr and 50°C. To maintain a clean vacuum we set up a nitrogen cold trap¹. We were required to refill the liquid nitrogen container every 7-9 hours. We also connected the inflow vent opening on the vacuum oven to a source of gaseous nitrogen. When pressurizing, we used this nitrogen gas to purge the oven and the drying test sample.

6.4 Automated Data Acquisition System

Having discussed the test sample, measurement instrumentation and the chamber separately, we will now focus on how we plan to record, store and display the measurements automatically. The data is acquired primarily through three different means. Depending on the measurement and the measuring instrument, it can either be interfaced through an Analog-to-Digital converter to a serial port, directly through a GPIB port or via direct serial connection.

Figure 6.7 shows the complete block diagram for our system interface.

6.4.1 A/D Converter and Serial Interfacing

The Analog-to-Digital converter is an 'Ontrak 'ADR2000'. It has 8 analog inputs and has an RS232 interface. The A/D converter has been installed in a metal case and equipped with RG58 coaxial connectors.

Two logarithmic amplifiers are connected to Channel 0 and Channel 1 of the A/D converter. The relative humidity sensor is connected to channel 7. The outputs for the logarithmic amplifiers vary from -2 to +2 volts while the RH sensor has an output voltage range of 0 to 5 volts.

The A/D converter interfaces through RS232 to the PC. We then set up and read the output from the A/D from within LABVIEW®.

¹A cold trap consists of a glass apparatus immersed in liquid nitrogen. The gases being removed from the vacuum oven are made to pass through this glass apparatus on their way to the external environment. The removed gases condense and are therefore unable to return to the vacuum oven.

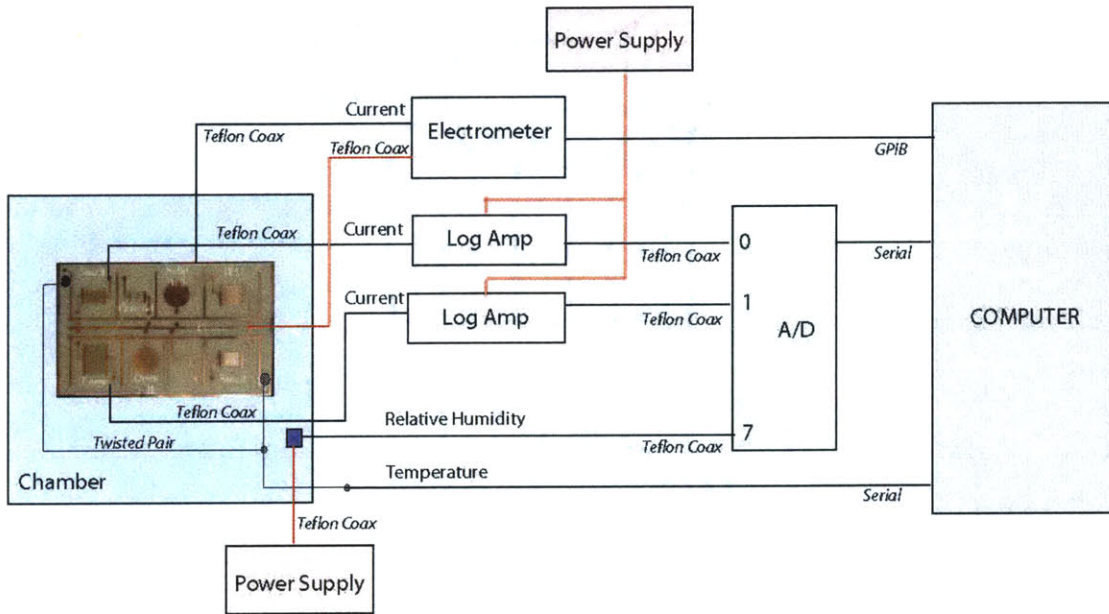


Figure 6.7: Full Block Diagram of the Automated Data Acquisition System

6.4.2 GPIB

The Keithley 617 electrometer is equipped with an IEEE 488 type interface or more commonly known as General Purpose Interface Bus (GPIB). A special IEEE 488 cable and a PC equipped with a GPIB card are sufficient to read data from and control parameters on the Keithley electrometer. The GPIB commands to read and control parameters are entered inside the LABVIEW® space.

Since the Keithley is also our power supply for the test sample, we will have the ability to control the supply voltage through the LABVIEW® graphical user interface.

6.4.3 Direct Serial Interface

The temperature sensors installed on the board interface directly through a serial connection to a secondary serial port on the PC. The software to read the measurements from the temperature sensors was graciously given to the project by Dr. Chathan Cooke.

The system will be able to read many temperature sensors connected in parallel.

6.4.4 LABVIEW® Graphical User Interface

We have looked at the various connection protocols used depending on the device. Combining all these instruments, sensors and devices into one program is essential. Most importantly, we will need a time stamp based on a common reference on each measurement.

Shown in Figure 6.8 is the front end graphical user interface for the “MIT Automated Data Acquisition System”, implemented with National Instruments LABVIEW® software.

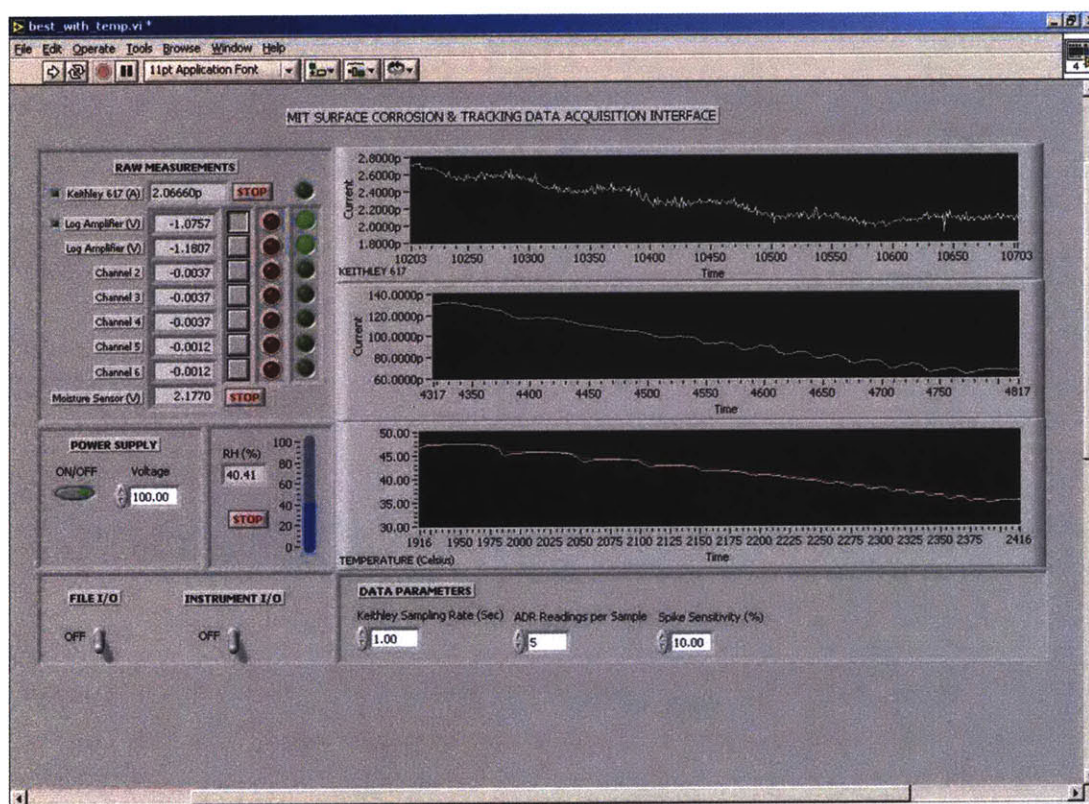


Figure 6.8: Automated Data Acquisition System GUI Screenshot

The software is fairly robust with respect to both data acquisition as well as data storage. There are features to verify the integrity of the data being obtained and display error signals in the event of spurious measurements. Additionally, it features real-time data storage meaning that in the unfortunate event of a power failure, most of the acquired data is not lost. More specifically, the acquired data is stored and saved onto data files in the computer approximately every minute so that in case there is power failure, only the last minute of data is lost and rest is secure. The data files are stored as a matrix in a text file and can easily be imported into any other post processing software. All the post processing

work for this project was performed using MATLAB (Appendix D).

6.5 Miscellaneous Cables and Connectors

Choice of cables as well as their arrangement are very important when trying to make accurate measurements in the pico-ampere range. There is plenty of scope for external disturbances to infiltrate measurements and the next chapter presents an in-depth look at the different sources of these extraneous effects and how they can be countered.

All the cables entering the environment chamber are Teflon[®] insulated coaxial cables. We have used coaxial cables for its shielding properties and Teflon[®] in itself has many advantages. Teflon[®] is highly impermeable to moisture and also has a very low thermal coefficient of expansion. Therefore, it makes a perfect insulator to measure leakage currents through other less insulating materials such as FR-4. Figure 6.7 shows all the cables used in the experimental setup.

The termination connections on the test samples are metal leads that have been soldered on to the pattern. The teflon coaxial cables are connected to these leads through copper alligator clips. These, while having a good tight connection, also enable us to connect and disconnect the patterns quickly. The connections outside the environment chamber to and between instruments are made through RG58 crimp type terminal coaxial connectors. Once again, these connectors have the center conductor insulated with Teflon[®].

6.6 System Calibration and Performance

Before we begin any experiment on the test sample, we will have to verify the performance of the entire system. This is extremely important for many reasons. Firstly, we would like to verify that our system works well as a whole. We have thus far only confirmed the performance of each individual part separately. Secondly, we would like to have faith in our measurements. Therefore, we will need some kind of test result that indicates accuracy in measurement. Additionally, we would like to have a calibration procedure which we can go back to at a future time to re-confirm our data acquisition system performance. Errors generated due to noise and disturbances have been mostly eliminated. The details of disturbance cancelation are discussed in lengthy detail in the next chapter.

For the purposes of the calibration test, we will use a 1 TeraOhm (1T) resistor. The

6.6 System Calibration and Performance

availability of these devices is very limited and we were fortunate to get one from Dr. Cooke. Typical order and delivery times for TeraOhm resistors are around 10-12 weeks. This was too long to wait to order and receive multiple resistors. Therefore, we measured each channel separately. While one channel was connected to the 1T resistor, the other two were connected with 100 GOhm (100G) resistors.

The three resistors were placed inside the environment chamber at a constant temperature of around 30 Celsius. However, the temperature in the chamber was oscillating about the desired temperature setting.

The Keithley 617 electrometer was calibrated separately early in the project and was our basis for accurate measurements. Therefore, it was assumed that the measurements made by this electrometer were precise and our logarithmic amplifiers could be compared and calibrated to it. The electrometer has the capability to measure currents in the femto ampere range. Therefore, it is ok to trust its measurements in the pico- and upper sub-pico-ampere range.

As mentioned earlier, we also used the Keithley 617 as the bias power supply. We varied the input voltage through 4 steps from 0V to 1V to 50V and finally 100V. We waited at each step for about 0.5 hr. before moving on. This procedure was repeated for each of the cases when the 1T resistor was connected to the Keithley and the two logarithmic amplifiers.

Figure 6.9 shows the plot of the results obtained when the 1T was connected to each of the measurement instruments.

In Figure 6.10 we can see a zoomed in view of the first two steps of the calibration test.

It is evident from Figures 6.9 and 6.10 that there seems to be a constant oscillation through the test. As mentioned earlier this is due to the temperature oscillation in the chamber. This was a concern and we consequently corrected it before we made any measurements on the test sample. Figure 6.11 shows the variation of temperature over the span of the first 1 hour.

Comparing the oscillations seen in Figure 6.11 with those in Figure 6.10, we can confirm that the oscillation was solely due to temperature. A simple thermal test on the 1T resistor verified its temperature response.

Figure 6.12 shows the oscillation of relative humidity in the chamber during the calibration. Even though the frequency of oscillations in the relative humidity are similar to the current, the dominant controlling factor for these oscillations are still believed to be temperature. There are a couple of reasons for attributing the oscillations in the current to temperature.

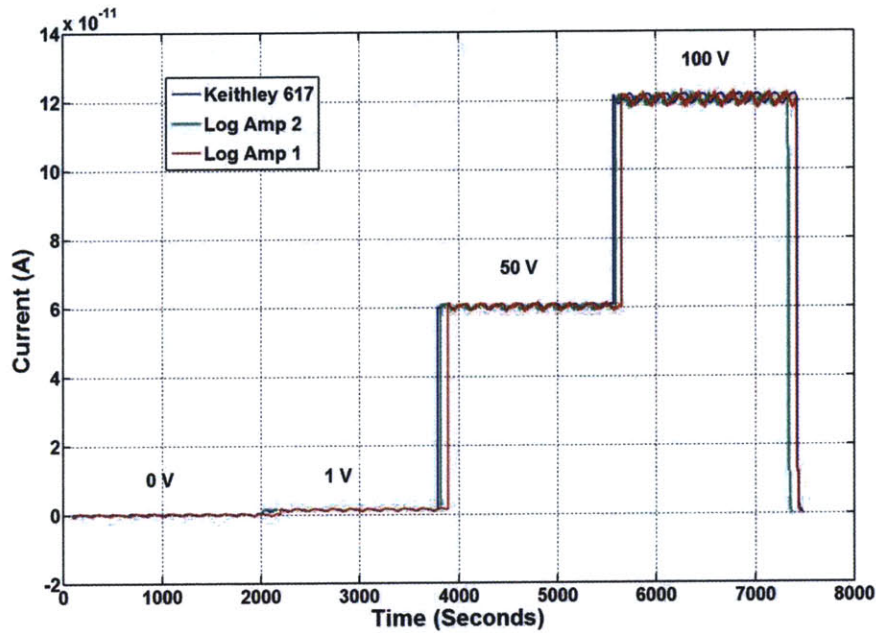


Figure 6.9: System Calibration

Firstly, the chamber is quite dry since the relative humidity readings are very small. Also, the resistor is coated with hydrophobic material. Therefore, the small changes in an already dry state cannot explain the extent of the oscillations. Secondly, Temperature plays a more dominant role in conduction in most materials.

Figures 6.9 and 6.10 show that the logarithmic amplifiers match the Keithley 617 electrometer very well. Also, the previously described constant current injection circuit included in the logarithmic amplifiers help us in measuring currents below the logarithmic amplifier capability of 5pA. Figure 6.10 shows that using the logarithmic amplifiers, we can measure currents accurately as low as 0.5pA. This is evident from the separation between the 1pA and 0pA measurement. At a given constant temperature (without oscillations) this lower limit of measurement can be stretched.

These system performance tests have helped us identify shortcomings in the system and improved our confidence of measurements.

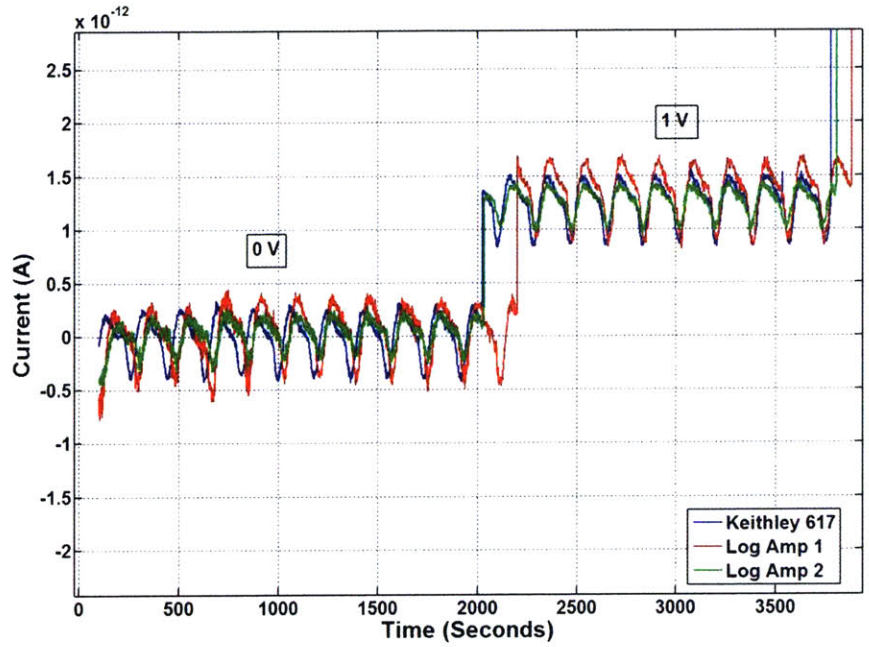


Figure 6.10: System Calibration

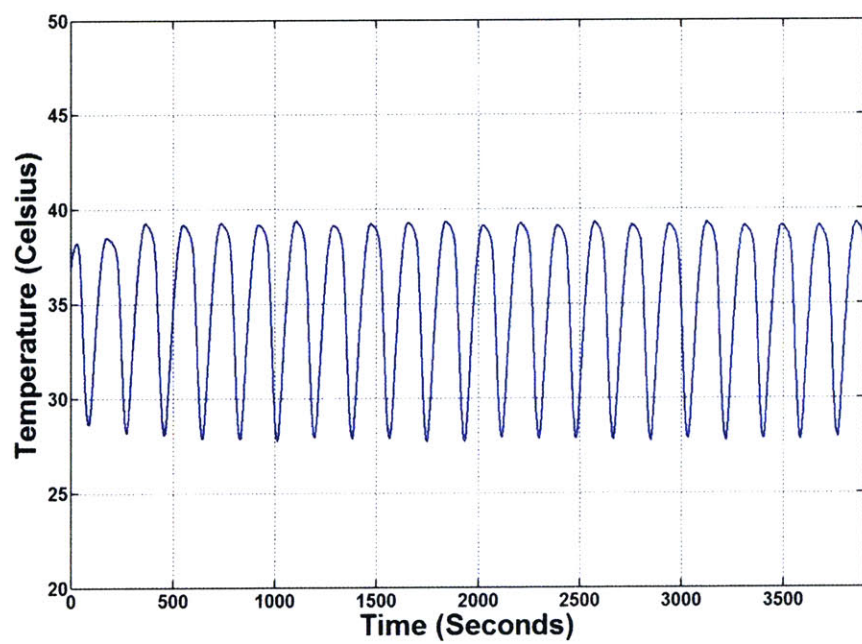


Figure 6.11: Temperature Oscillation in the Chamber during System Calibration Tests

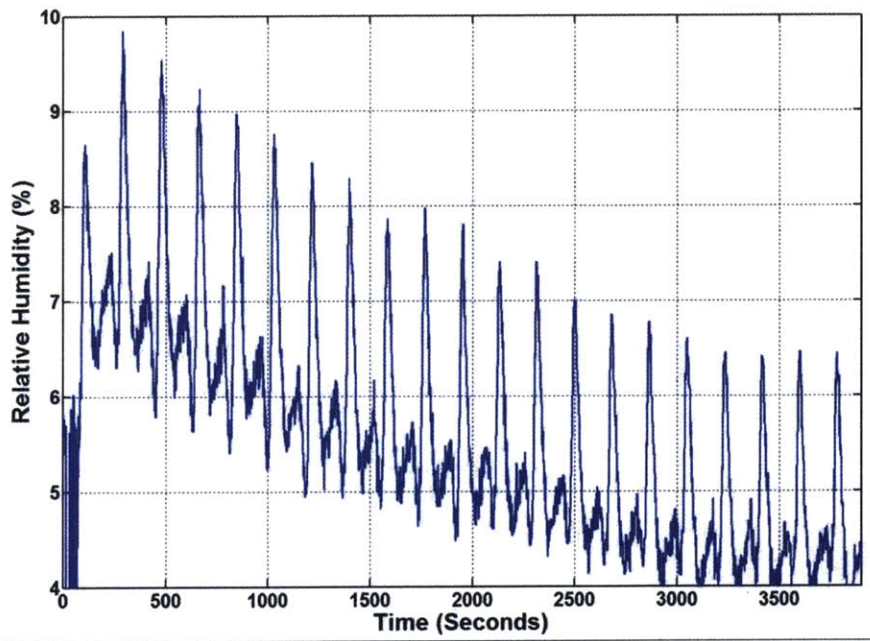


Figure 6.12: Relative Humidity Oscillation in the Chamber during System Calibration Tests

6.7 Weight Measurement Methodology and Instrumentation

So far all the discussion has been toward experimental methods and test setup used to measure electrical conduction through the insulator. However, we have seen in Chapters 3 and 4 that moisture might play an important role both in facilitating electrical conduction as well as in accelerating other degradation processes. We will now look at an experimental methodology to study moisture ingress.

To experimentally study moisture diffusion into (out of) the insulator a commonly used metric is the weight gain (loss) percentage which is obtained through gravimetric measurements (Section 3.6). However, since these insulating materials like FR4 are designed to absorb very little moisture, we can expect only small changes in weight. Therefore, accuracy and consistency are essential in determining the amount of water in the material.

We will use an ACCULAB VI-3 scale with the accuracy of 0.003g to take our measurements. The scale has to be regularly calibrated to ensure the effects of temperature do not modify these readings. The calibration weight used is 200.000 grams.

Also prior to each measurement the test sample has to be appropriately acclimatized. For example, if we take a sample out of a chamber which was at 85°C/85% RH and place it directly onto the scale, we will not obtain an accurate reading and the scale will have to be re-calibrated before the next measurement. This is because there is a fair amount of heat exchanged between the hot sample and the metallic plate on the measurement scale. This heat exchange causes some error in measurement. On the other hand, we cannot leave the sample exposed to ambient air to come to equilibrium with temperature because in doing so, it will lose some of the moisture it had absorbed at the higher temperature condition in the chamber. Instead, we placed the samples (fresh out of the oven) in Ziploc® bags that present a barrier to moisture change. We leave these bagged samples in ambient conditions for 15 minutes prior to each measurement. 15 minutes was chosen because the samples seemed to cool down sufficiently in that time.

The measurements are taken with the sample in the center of the weighing scale to ensure the weight is evenly balanced about the center. Multiple measurements are made for each test sample until three consecutive equal measurements within an error of 0.003 grams are obtained. The scale is recalibrated before measuring each test sample.

Since we are interested in percentage weight gain and changes from an initial or final condition, consistency between measurements is very important. The procedure described above consistently enables us to obtain defensible results.

6.8 Thickness Measurement Methodology and Instrumentation

We know from Chapter 3 that moisture and other impurities have many different effects on the insulating material in addition to providing ions for electrical conduction. We have seen that the absorbed moisture can also bond with the material and cause swelling. Since all the moisture does not contribute toward swelling, there should be a difference between the volume of the absorbed water and the volume increase from swelling. Thickness measurements may indicate the extent of hydrogen bonding and state of water molecules in the material.

Moisture uptake in these materials is very small, correspondingly the increase in volume is also very small. The thickness measurement will have to be very accurate, up to the single digit micrometer values. In our measurements, we use a Mitutoyo Micrometer with an accuracy of 0.001 mm.

To be able to take these thickness measurements anywhere near the accuracy of the instrument, we will need a stand to hold the test sample and a good test procedure. Shown in Figure 6.13 is the drawing of a stand we built to hold the test sample.

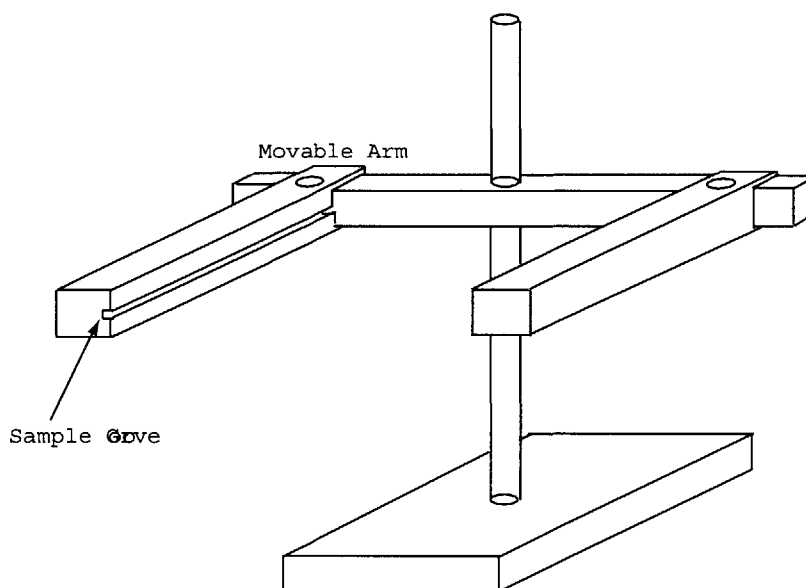


Figure 6.13: Thickness Measurement Stand Drawing

The next step is determine and mark a good location on the sample so that consistent measurements can be made. The specific location of the mark is not as important as being

6.8 Thickness Measurement Methodology and Instrumentation

able to measure at the same mark each time. Show in Figure 6.14 is a photograph of the test sample with marks at each of the 2 locations of measurement. There are 4 markers around each location and the spindle of the micrometer is placed within these marks accurately. The two locations were chosen for ease of measurement.

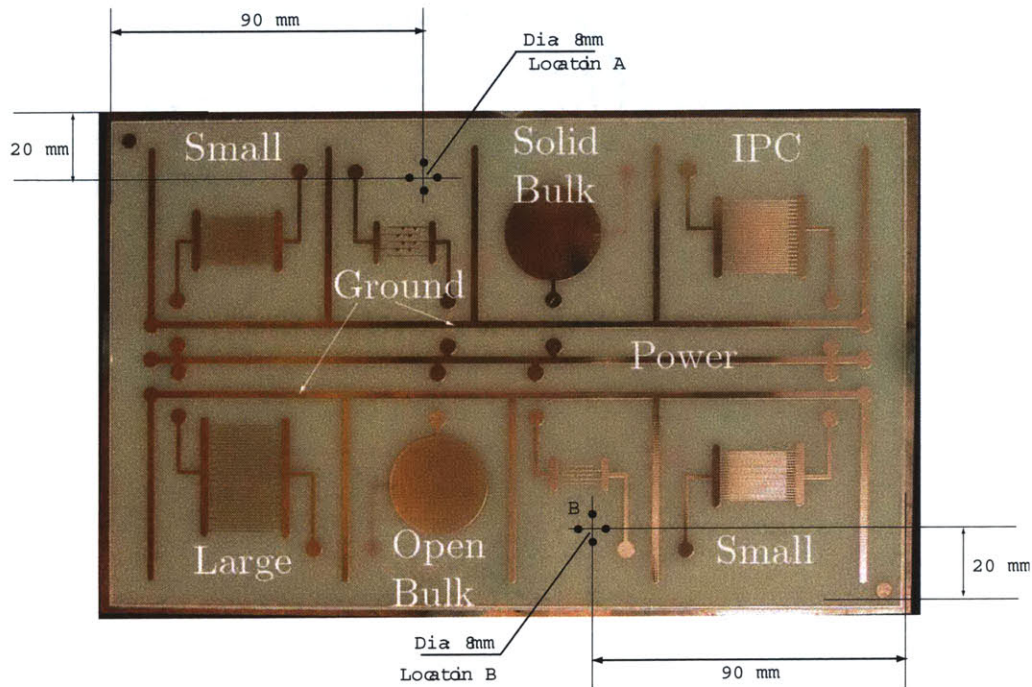


Figure 6.14: Locations for Thickness Measurements

The measurements are repeated three times, alternating between the two locations each time. It was ensured that there would not be a variation of more than 0.002 mm between any of the three measurements.

In this chapter we have looked at all the different parts of the measurement system. We have evaluated system performance and developed a procedure for consistent measurements. We have brought up the issue of noise and disturbance at various places. In the next chapter, we will deal with the various sources of noise and how we eliminated most of the errors due to such noise sources.

Extraneous Effects and Disturbances at Very Low Currents

THIS chapter presents one of the most important aspects of practical measurement - noise. The acknowledgement of and protection against the various sources of noise and disturbances in the system is essential in ensuring reliable data. We will also present some of the techniques used to eliminate these effects.

7.1 Introduction

Noise can be added to a system at various stages - the device under test could have some inherent noise parameter, noise can be added internally by the measuring instruments, noise can be "picked up" in the cabling, there can be noise in the input stages of analog-to-digital converters, if the signal is being digitized there can be various sampling noises added. Once in the digital domain, a signal is more secure, but still such things as rounding errors in calculations and drop outs in communications can introduce more noise. We will, therefore, use the term "noise" loosely to include all extraneous effects, unwanted measurement artifacts and disturbances.

In this chapter, we have chosen to divide noise into two groups - Internal and External Noise. This distinction may be a little arbitrary, but it helps in understanding the impact and preventative measures that may be effective. Internal noise is that which is created within the system. This includes noise generated within the measuring instrumentation as well as interaction between different parts of the overall data acquisition system. External noise is due to interaction with the surrounding environment. It also includes general randomness in measurements and physical disturbances caused by the experimenter.

Tackling the noise problem can be a very difficult and time-consuming one. This is because the nature of the problem is such that there will always be noise no matter how much care is taken. Also, determining the exact cause of noise observed in data can be challenging due to the complex interaction between these different interfering phenomena. Therefore,

it is only possible to understand the different phenomena and reduce error due to noise to a level that is acceptable.

7.2 Internal Sources of Disturbance

7.2.1 Alternative Leakage Paths

This can be renamed as “Parameter Noise” since this is the noise inherent to the device being measured. The device under test in our case is the test sample board. Since we are measuring leakage currents of the order of a few pico-amperes (in a dry state), there is the good possibility of undesirable leakage paths that could contribute to the measured current. For instance, lets consider the solid circular disc pattern in Figure 5.8 (First row from the top and third from the right). The desired conduction path for this pattern is through the bulk material perpendicular to the surface. However, since this pattern is in the top row, there is a possibility of a stray leakage path over the top of the board, across the edge, and onto the other side. It is very easy to ignore this detail, observing that the distance over the top is much larger than through the bulk. This assumption might be fair in a material that is completely homogeneous and does not age with time. However, FR-4 is extremely heterogeneous in nature, therefore simple scaling may not be applicable. Additionally, any undesirable conduction paths could be reinforced through time and eventually become a dominant pathway.

To partially resolve this difficulty, we painted silver guard rings connecting the printed ground barrier around the bulk pattern on the front side of the board and all around the pattern on the back. These guard rings were connected to the common ground. We observed a good reduction in unwanted spikes in measurement and the response was much cleaner. This difficulty is only partially resolved because there still could be conduction paths to ground that we are now not measuring. A complete understanding will involve measuring these ground currents separately and eliminating the alternative leakage paths.

Figure 7.1 shows a complicated plot of the response of leakage current to step changes in temperature and humidity. This plot contains plenty of additional information that we will explain later and we urge the reader to only focus on the curve corresponding to the current at this time. This response should be fairly smooth in the flat sections. However, due to the absence of any silver guard rings we can see considerable spiking activity.

When we include the silver guard rings and repeat such a test, we can see from Figure 7.2 that the plot is much smoother

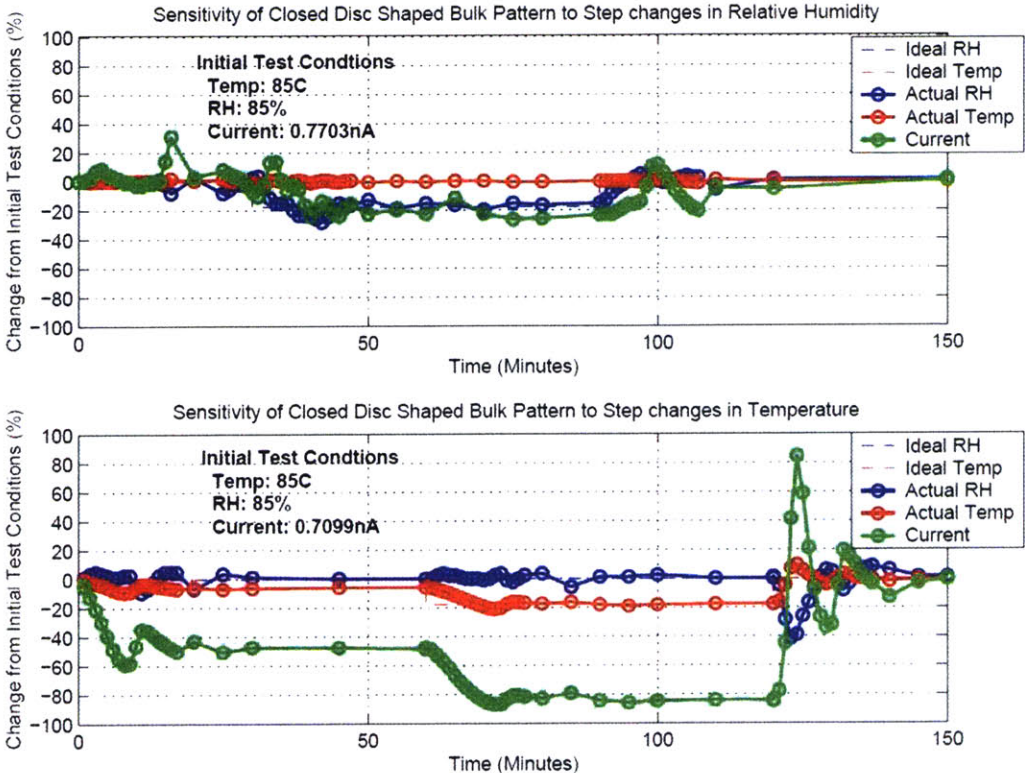


Figure 7.1: Sensitivity of Current without Silver Guard Rings

Also, as described in Chapter 5 we designed a second generation of test samples with copper guard rings around the patterns to electrically isolate them from each other.

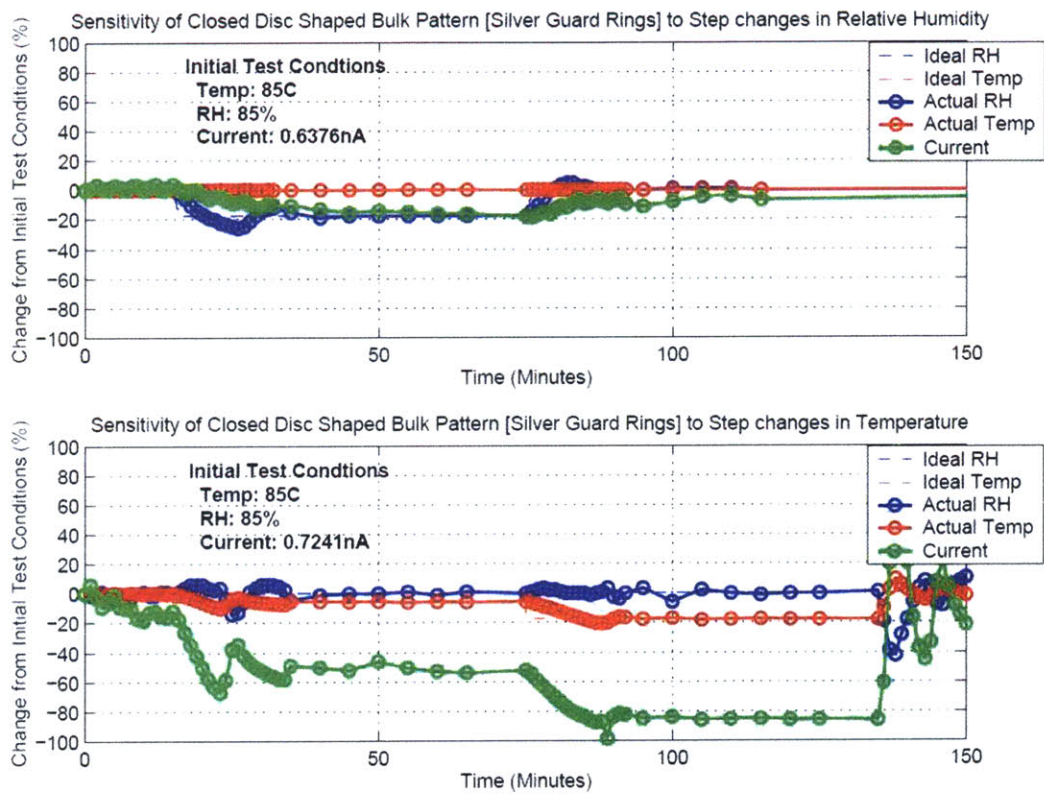


Figure 7.2: Sensitivity of Current with Silver Guard Rings

7.2.2 Ground Loops

Ground loops commonly occur in multiple-instrument or cascaded device-instrument setups where each functional block of the entire system is connected to its own ground. It is implicitly assumed that a ground in a wall socket is at the same potential as the ground on another wall socket nearby. This is not quite true and in fact, different parts of the electrical grounding system can vary by several volts. This arises not only from the resistance of wiring but its inductance. If the currents change very rapidly, the voltage drops in the ground system can approach several hundred volts for short periods of time. The voltages themselves can obviously provide a great source of interference for a measurement loop, but the currents which cause them can also induce significant currents and voltages in the signal wires located nearby. Circulating currents in ground loops may also be periodic in addition to being transient events.

This problem can be eliminated by connecting all the instruments and devices to ground only at a single point. It can also be eliminated by running a thick braided shield cable between all the instruments to physically eliminate the potential difference between different grounds. The best way to identify and remove ground loops is by experimentation. We did not face too much difficulty with this because most of the instruments were connected to closely spaced wall outlets. Nevertheless, we did observe a constant deviation from the desired voltage at the input of our analog-to-digital converter. This constant error was not proved to be necessarily due to ground loops. However, since the error was not seen during performance tests of each component individually, it was suggested that the error might have been due to system ground loops. This constant error was eliminated through software correction.

We ran a test case where we varied the input current from 100pA to 700pA through a step profile and observed the responses. Figure 7.3 shows the constant DC voltage errors from desired values which does not appear constant because of taking the anti-log in software. This figure also shows us some AC noise. We will discuss that later in this chapter when this plot will be repeated.

However, we can see the readings match desired levels in Figure 7.4 when the software correction of about 11mV is incorporated. This value varies slightly between devices and has been tested many times before arriving at the chosen number.

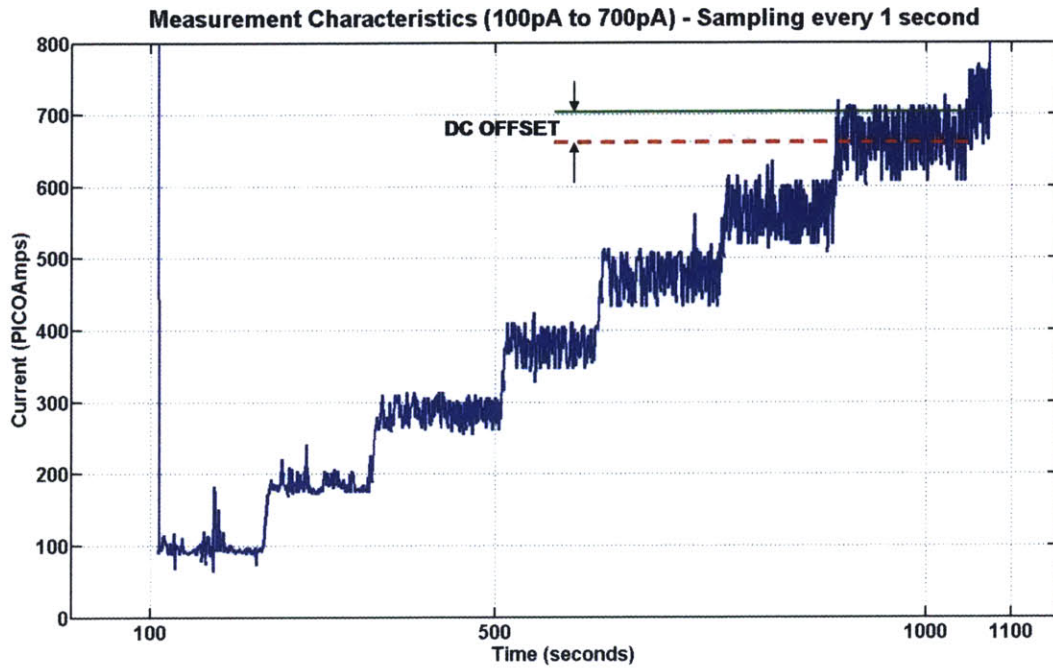


Figure 7.3: DC error in data

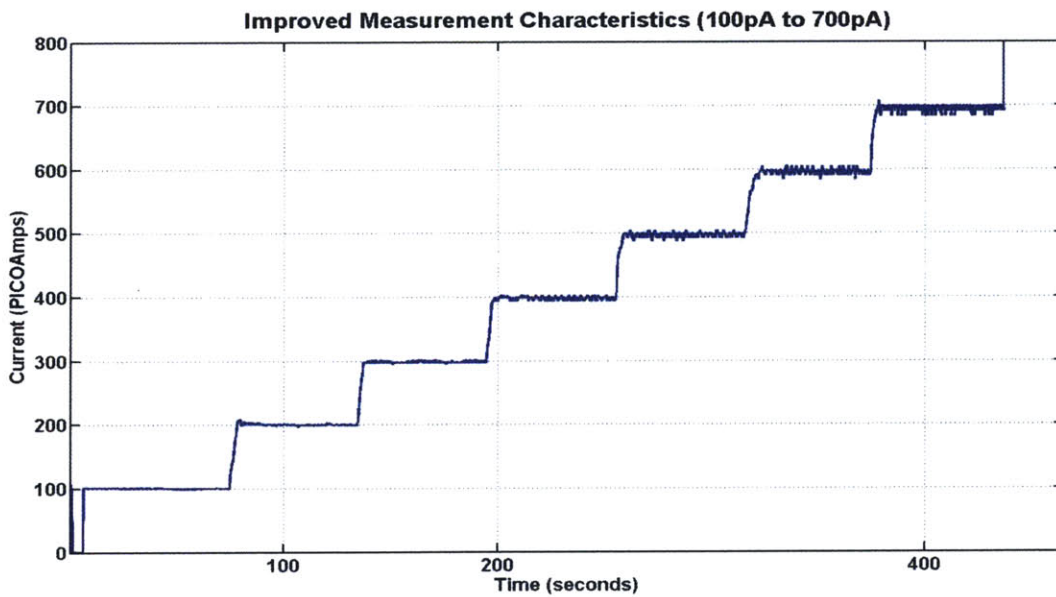


Figure 7.4: DC error has been corrected in data

7.2.3 Capacitive Coupling

When we have a changing electric field that can capacitively couple into the sensor, its signal conditioning equipment or its wiring, we have a source of error. Cable shielding is used to minimize or eliminate capacitively coupled interference. Shielding consists of a metallic sheath surrounding the instrument wires. This is intended to be a Gaussian or equi-potential surface on which electric fields may terminate and return to ground while leaving the internal wires uncoupled to these fields.

In our setup, coaxial cables and connectors were used to completely eliminate any capacitive coupling in these components.

7.2.4 Channel Crosstalk

The A/D converter has 8 analog input channels and we observed crosstalk between the the desired channel and the unconnected channels. Figure 7.5 shows the output of the A/D converter with “Channel 0” connected to a step-changing source (as described in the earlier part under ground loop dc error). Once again it is suggested to focus only on the problem of crosstalk in these plots. The other noise factors are dealt with separately.

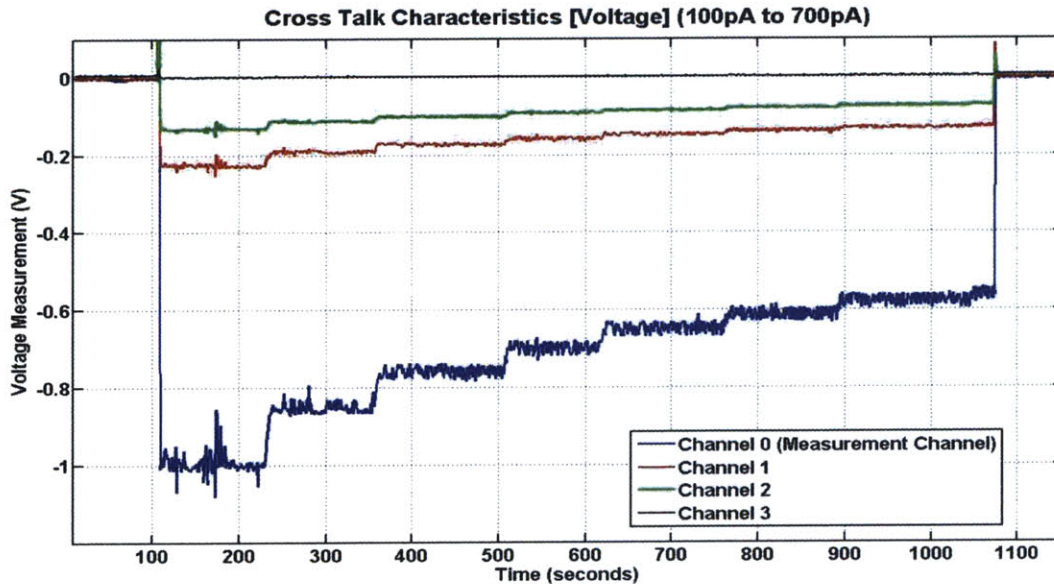


Figure 7.5: Crosstalk between Nearby Channels

It is clear from Figure 7.5 that the nearby channels are showing a similar response to Channel 0 even though they are not connected to anything. We eliminated this by connecting a 100K Ohm resistor from each input of the A/D converter to ground. This provided an alternative path of least resistance to ground for the unwanted currents since 100K Ohm is much less than the input impedance of the A/D converter.

Figure 7.6 shows the cross-talk free output.

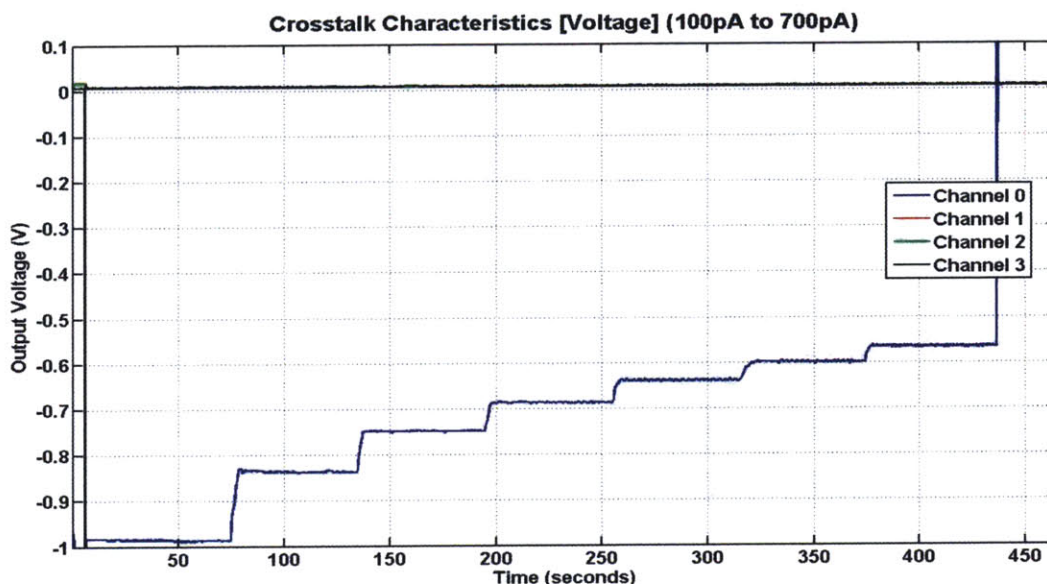


Figure 7.6: Crosstalk between channels has been eliminated

7.3 External Sources of Disturbance

7.3.1 Random Noise Elimination through Averaged Down Sampling

The various external sources of noise can be grouped together as overall random noise and can be eliminated at once through simple signal processing techniques. The sources of external noise (except impulsive noise) is usually random variations from a desired measurement. We employed an averaged downsampling (ADS) algorithm where each ADS measurement is an average of all the measurements in a desired window. The window is then moved to the next set of readings and the averaging is performed again. This technique was able to retain the average value and step changes in measurement for small window sizes while eliminating random noise.

Mathematically, this operation can be performed as follows:

Let the frequency of the current measurement be ω_1 and let the desired downsampled frequency be ω_2 . Since we are performing a downsampling operation, we know that $\omega_1 > \omega_2$.

The averaging window size becomes:

$$W = \frac{\omega_1}{\omega_2} \quad (7.1)$$

where W is a positive integer.

Let the data sequence be represented as $x(n)$ and the averaged down sampled data sequence be $x_d(n)$

Then,

$$x_d(n) = \frac{1}{W} \sum_{k=(n-1)W+1}^{nW} x(k) \quad (7.2)$$

In our data acquisition system, we established that the maximum sampling frequencies for the Keithley 617 electrometer was 1Hz and the data from the A/D converter was 5Hz. We implemented the averaged downsampling technique only on the A/D data since Keithley frequency was within an acceptable limit. To match the frequency of the A/D data with the Keithley at 1Hz we used a window size of 5.

Figure 7.7 shows the noisy raw data without any post-processing.

Figure 7.8 shows the implementation of the averaged down sampling technique.

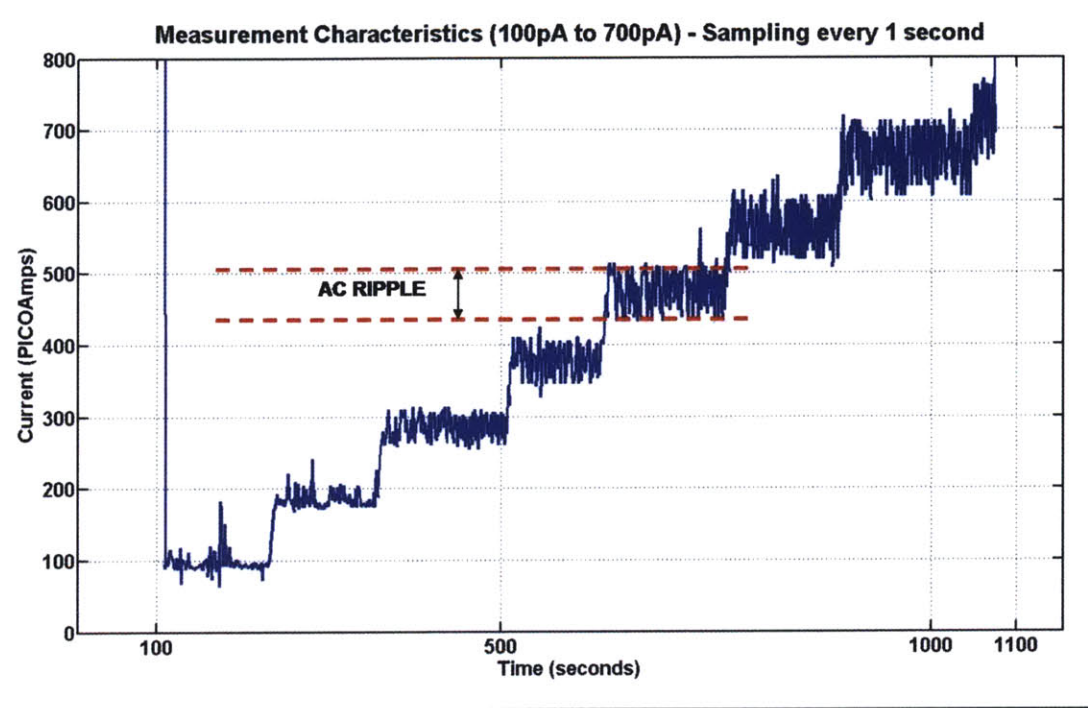


Figure 7.7: Random Noise

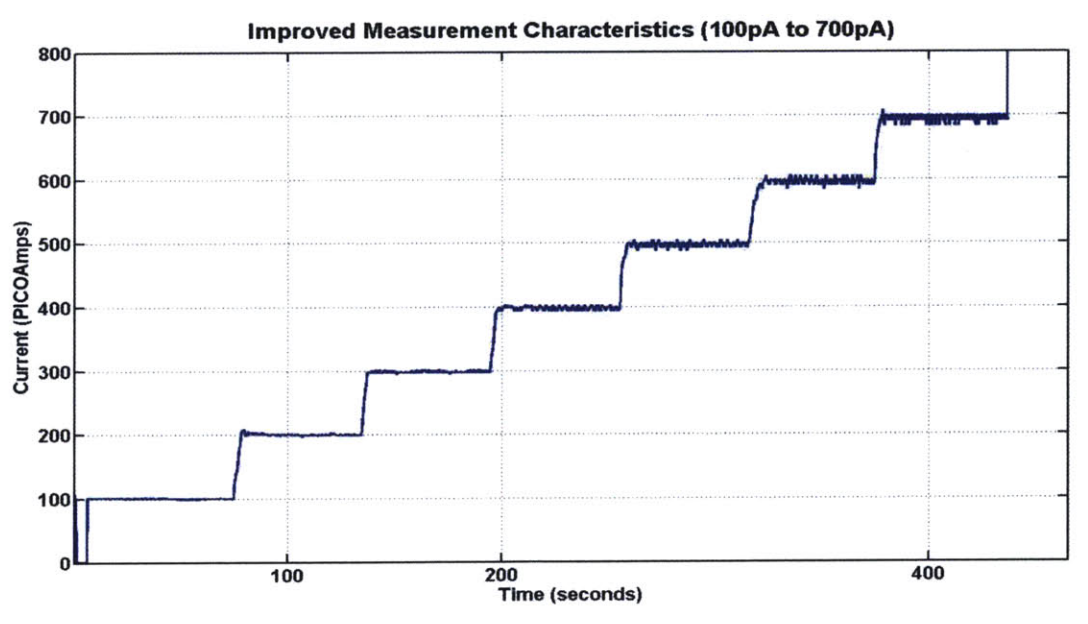


Figure 7.8: Averaged Down Sampled and Scaled Output

7.3.2 ESI

Electrostatic Interference (ESI) occurs when an electrically charged object is brought near a previously uncharged object. Usually, the effects of an electrostatic action are not noticeable because the charge dissipates quickly in low impedance levels. However, high impedance levels of the measurement instrumentation and the test samples do not allow these charges to decay rapidly and can therefore cause erroneous readings. DC electrostatic field can cause undetected errors or noise in measurements. AC electrostatic fields can cause errors by driving amplifiers into saturation, or through rectification that produces DC errors. Electrostatic interference is easily recognizable when hand or body movements near the experiment cause fluctuations in readings. Shielding is a quick and easy solution to this problem and has been extensively used in our experiments. In addition to the wires and connectors, the logarithmic amplifiers and A/D converters have been placed inside metal casings. We also used “caution tape” to ensure minimal human disturbance during the experiment.

7.3.3 EMI and RFI

Electromagnetic Interference and Radio Frequency Interference (over a broader frequency range) can be caused by steady sources such as TV or radio broadcast signals, or it can result from impulse sources as in the case of arcing in high voltage environment. The effect of RFI can be seen as an unusually large offset, or, in the case of impulse sources, sudden erratic variations in the measurements. A simple precaution that can be taken is to keep the measurement instruments and test samples as far away from a RFI source (Computer Monitor, TV etc.) as possible. Also, shielding all devices can help prevent noise due to RFI.

7.3.4 Cable Interference

An unexpected source of noise can be the cable between the device under test and the measuring instruments. The cable can exhibit piezoelectric charge generation when mechanically moved or stressed. The result is a most noticeable with high impedance measurement devices such as the electrometer.

A similar but less well known cable induced noise is the triboelectric effect. This occurs when friction between the cable’s insulator and conductor generate a surface charge. Again, the result is a most noticeable with high impedance devices.

Extraneous Effects and Disturbances at Very Low Currents

Both these sources of disturbance can arise where devices are placed on a moving structure or when cables are able to move for other reasons such as machine vibration or human disturbance.

Simple solutions that we implemented to reduce the effect of cable noise are to minimize the length of cable between test sample and measuring instrumentation and minimize cable movement.

This concludes the description and performance of the entire experimental setup. We have looked at the test sample board in detail and understood the significance of each pattern printed on it. We then described each part of the leakage current, weight and thickness measurement systems. We also studied the various sources of noise and the nature of error observed. Finally, we implemented some simple hardware and software techniques to combat internal and external noise and disturbances.

Part III

Analysis

Preliminary Experimental Results

THE details of many different experiments performed are listed in this chapter in chronological order. The results and measurements from these experiments are also discussed here. The results include those from tests performed on all the first generation samples and all of the second generation samples that were tested.

8.1 Introduction

We will now look at the procedure and results of all the experiments along with a brief interpretation following each experiment. Preliminary tests were performed on both the first and second generation samples that provided a good launching pad for a more organized testing method seen in the Hygrothermal Experimental Scheme (the results of which will be discussed in the next chapter). The results of all these experiments provide both quantitative and qualitative insight into the nature of the charge carrier, role of moisture in conduction and generation physical properties of the insulation.

8.2 Naming Conventions

Prior to the development of the automated data acquisition system described earlier, some preliminary tests were conducted on both generation of samples. Before we begin analyzing the results, some basic naming conventions have to be established. The primary naming convention for the boards is as follows:

“FR4-Generation Number-Sample Number”

For example, FR4-1-3 refers to sample number 3 of the first generation boards. We have 3 first generation boards and 6 second generation boards. These primary names were etched

Preliminary Experimental Results

onto the back of the test samples on arrival. The second generation samples also have an additional alternative naming convention which is based on their purpose.

“Purpose-Sample Number ”

The “purpose” is either to monitor currents designated as “CB” (Conduction Board) or purely for weight measurement designated as “WB” (Witness Board). For example “CB2” refers to conduction board number 2. The alternative sample number need not be the same as the primary sample number. The conversion from the alternative to the primary naming scheme for the second generation board is shown in the table below:

Alternative Name	Primary Name
WB1	FR4-2-2
WB2	FR4-2-5
CB0	FR4-2-1
CB1	FR4-2-6
CB2	FR4-2-4
CB3	FR4-2-3

Table 8.1: Naming Convention for the Second Generation Test Samples

The description of the testing scheme is detailed in the following sections.

8.3 Preliminary Experiments on First Generation Samples

These tests were aimed at a general understanding of currents in PCB insulation. The results that will be discussed in this section only indicate trends and general comparison basis and not any specific quantitative characteristics.

8.3.1 Faraday Cage Tests

The first group of experiments were those in the Faraday cage placed in the laboratory conditions. The laboratory conditions are not controlled and temperature and humidity fluctuate constantly depending on the weather outside. These initial experiments were done to get the project running and to help us develop an understanding of the kind of currents and experimental difficulties we might encounter.

8.3 Preliminary Experiments on First Generation Samples

Initially, the weight, dimensions and dielectric constants of the three samples were measured and this is shown in Table 8.2:

	FR4-1-1	FR4-1-2	FR4-1-3
Weight (g)	93.075	94.309 - 94.370	92.604 - 92.650
Length (in.)	9	9	9
Width (in.)	5	5	5
Thickness at the Center (mils)	58.85	59.5	61
Thickness at the edge (mils)	56.0 - 58.4	57.5 - 59.6	55.7 - 60
Dielectric Constant (@ 1KHz)	5.29	5.44	5.29

Table 8.2: Board Characteristics

After initial weight and dielectric constant measurements, we decided to measure the currents in these boards when subject to three different environmental conditions. These were (1): “as arrived” condition where tests were directly carried out on the board without any pre-conditioning; (2): the “oven baked” condition where the boards were baked in an oven to remove moisture content as a part of pre-conditioning and then tested; and (3): “water soaked” condition where the boards were immersed in water prior to testing.

These tests were also a means to develop a suitable measuring setup that would help eliminate background disturbances and noise in our measurements. As mentioned in Chapter 7, this is critical since our current measurements are extremely small values running into the pico- and nano-amperes.

Also, the only patterns used for measuring surface effects in these tests were the small and large patterns on each board. The bulk measurements were done using the square pattern. In all the three boards, the small pattern that was used for measuring the currents was the second pattern from the left on the top row in Figure 5.2. A different large pattern was used for each board.

After being placed in the Faraday cage and connected as shown in Figure 8.1, the bias voltage¹ was adjusted depending what we were measuring. In other words, depending on whether we were charging or discharging, we could set the bias voltage.

All the tests were done for approximate period of 24 hours and the intention was to understand the rapid response of these boards. Also, it is important to note that the patterns for each test were measured one at a time.

The current data was collected on a logarithmic schedule of times since moisture is one of

¹The bias voltage in this case is defined as the voltage applied across the desired pattern to measure the current.

Preliminary Experimental Results

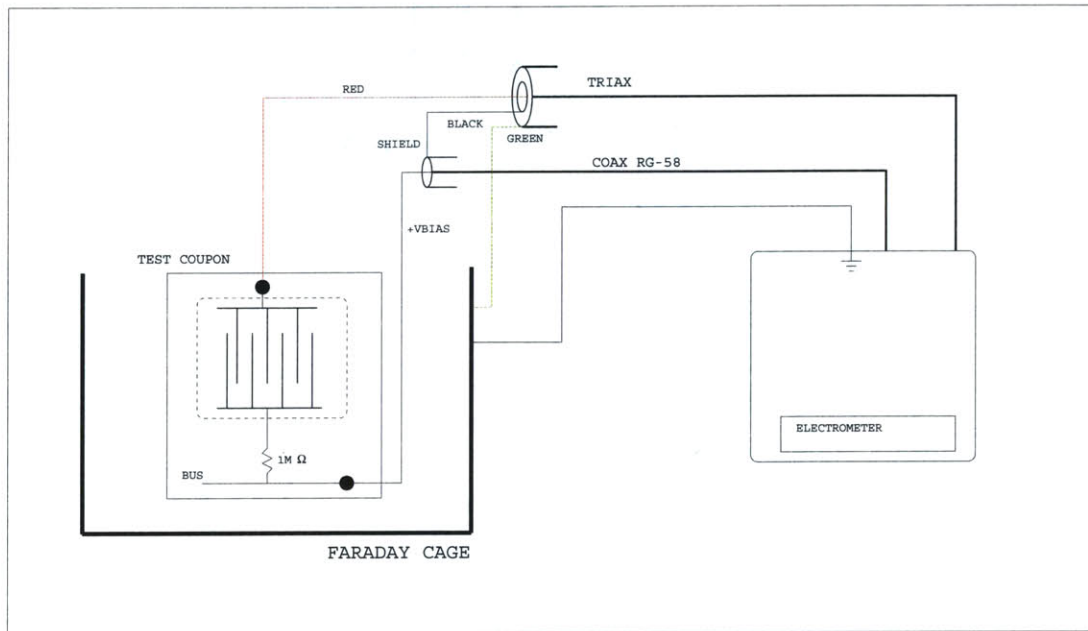


Figure 8.1: Schematic of the Test Setup

the main contributors to conduction and moisture diffusion is approximately exponential with time.

8.3 Preliminary Experiments on First Generation Samples

8.3.1.1 As Arrived Condition

The first test in the series of tests was the so called “As arrived” test. The FR4-1-3 sample was selected for this test and removed from the Ziploc[®] storage bags and connections were soldered on the pattern being measured. The test setup was exactly that as shown in Figure 8.1.

To understand how different geometries, different spacings and different locations on a board can affect current under fairly similar environmental conditions, Figures 8.2 and 8.3 were plotted to show separately the results of the charging and discharging experiments.

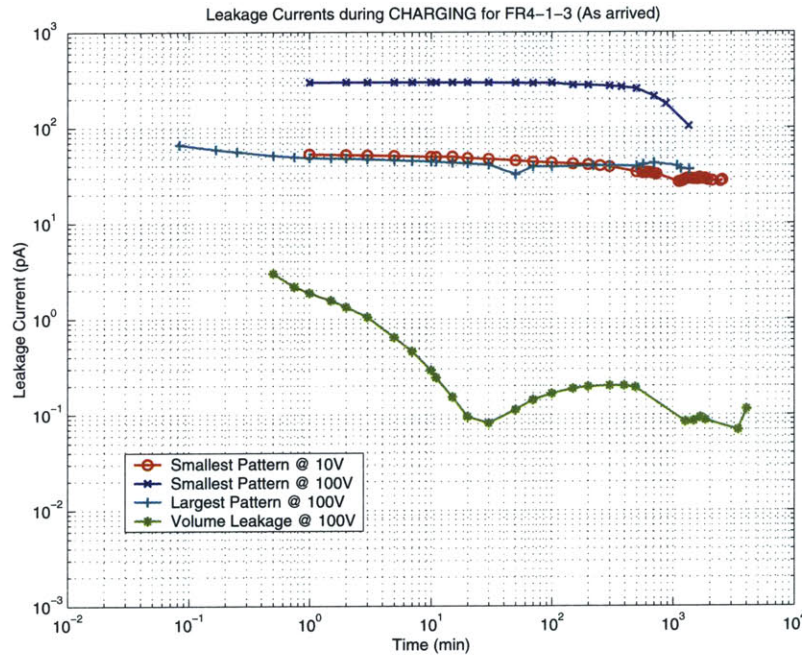


Figure 8.2: “As Arrived” Current Measurements during Charging

During charging, the small pattern charged at $10V^2$ and the large pattern charged at 100V displayed almost the same currents through the duration of the test. Also, the small pattern charged at 100V had currents about 6 times higher than that of the large pattern. As a reminder, the large pattern had a spacing of about 4.5 times that of the small pattern. The currents for both the large and small pattern were quite constant until about 500 minutes at which point they began to decrease. The plot of square pattern (used to measure the volume current) has a few bumps. These could be due to various environmental factors during the test and is an indication of the sensitivity to moisture and other atmospheric

²This was the only test in the entire thesis where the patterns were charged at 10V.

Preliminary Experimental Results

reactants. There were periods when the outside weather changed from clear skies to rain to snow. These changes may have caused some fluctuations in the temperature and humidity conditions indoors as well. Also, the volume leakage was much lower than the leakage due to the large or the small pattern.

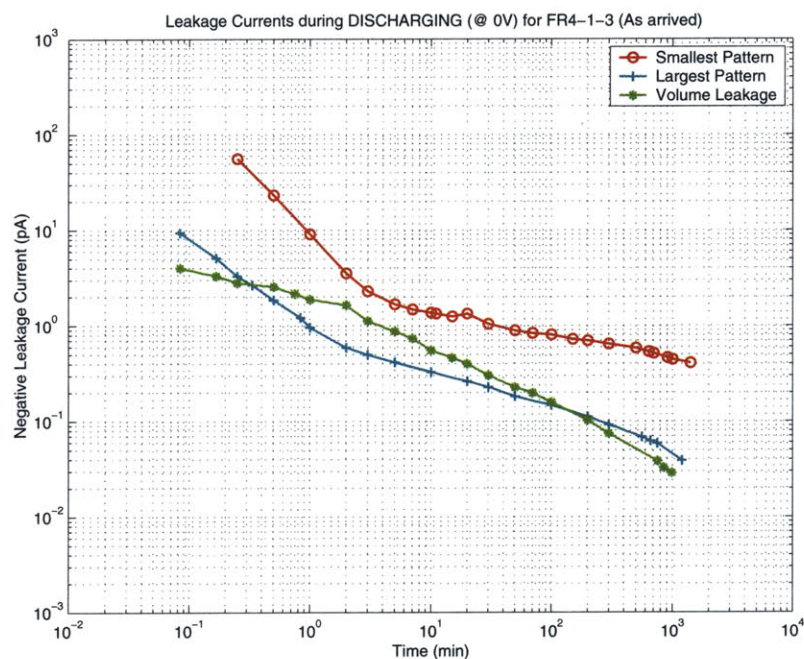


Figure 8.3: "As Arrived" Current Measurements during Discharging

Immediately after the charging portion of the test on each pattern, the electrometer voltage was set to zero. The current which flowed in the discharge test was recorded.

As shown in Figure 8.3, during discharging, the small pattern had higher currents than the large pattern. However, the large and the small patterns are almost exactly parallel to each other. Approximately, the small pattern has currents that are about 6-7 times greater than the large pattern. The volume current also has a decreasing trend but fluctuates between being greater and less than the large pattern.

8.3 Preliminary Experiments on First Generation Samples

8.3.1.2 Oven Baked Tests

For the next group of current tests, the FR4-1-1 was selected and this was placed in a environment chamber for around 2 weeks at 100°C and very low relative humidity (approx 20%). This was done to remove as much moisture as practical.

Shown in Figures 8.4 and 8.5 are the different test patterns charging and discharging after being baked in the chamber for about 2 weeks at 100°C.

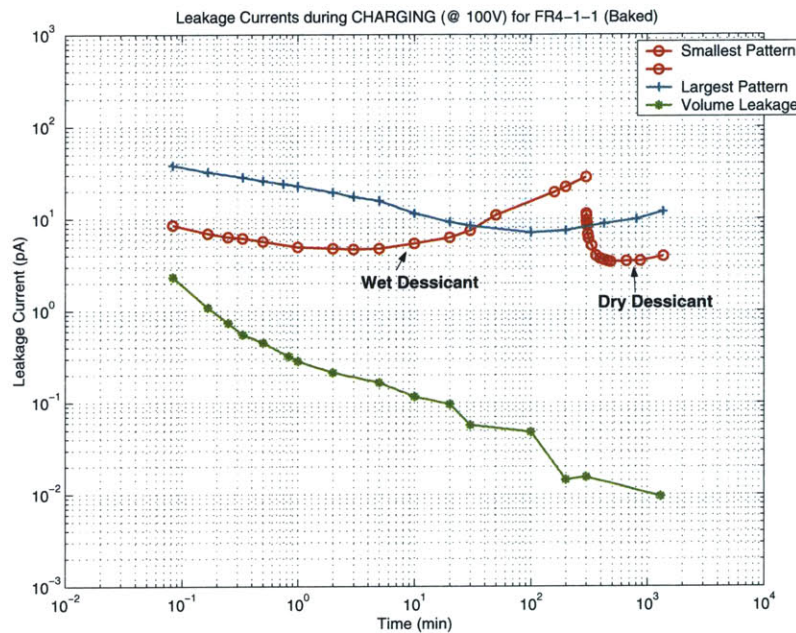


Figure 8.4: “Oven Baked” Current Measurements during Charging

A desiccant was added in a tray and kept alongside the board to absorb any ambient moisture. However, initially this desiccant was completely saturated and was not effective in removing moisture from the ambient air around the board. Therefore, we see an increase in currents. However, once the error was realized and the wet desiccant was replaced with a dry one, the currents dropped down indicating that the desiccant was absorbing the moisture from the air and the board. Ignoring this discontinuity, the large pattern and the small pattern have parallel graphs for current. However, in this case, the large pattern has higher currents than the small pattern. As a reminder it is important to note that the large pattern being measured in this test is very close to the edge. Therefore, there could be some edge effects that might contribute to the higher current values. The volume pattern once again had a steady line of decreasing currents that were much lower in value compared to the small or the large pattern.

Preliminary Experimental Results

The observed deviations due to the accidental introduction of the moist desiccant helped emphasize the influential role played by moisture in electrical conduction.

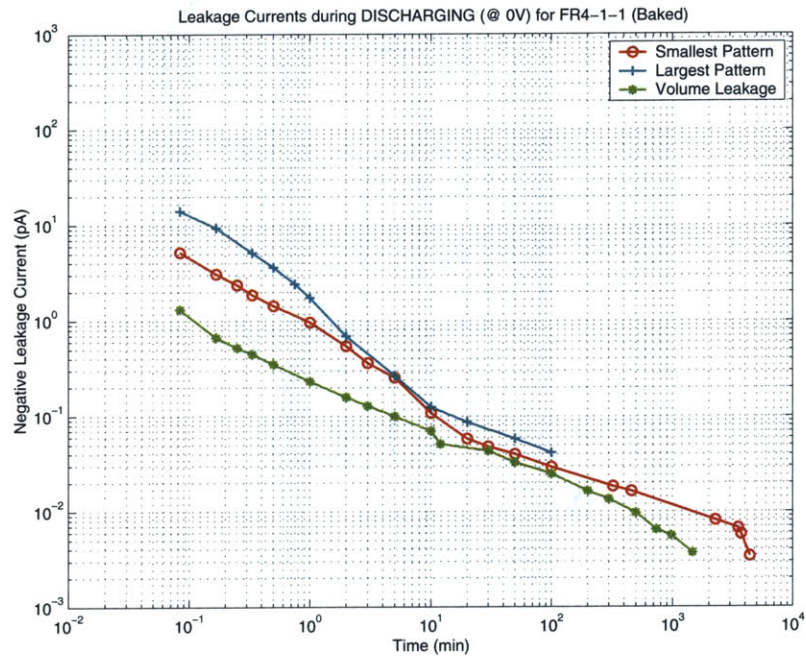


Figure 8.5: “Oven Baked” Current Measurements during Discharging

Similarly, the discharging curves show a good continuity to the charging process. Once again the large pattern had higher currents than the small pattern.

The key observation in the charging and discharging processes are the fact that when the board was baked, the large pattern actually had higher currents than the smaller pattern.

8.3.1.3 Water Soaked Tests

For the final group of current tests, the last remaining board (FR4-1-2) was selected and this was first baked in the chamber for about 1 hour at 100°C and low humidity (approx 20%) and then immersed in a bowl of distilled water at 23°C for 24 hours. This test follows the procedure indicated in the IPC-TM-650 Method 2.6.2.1 on “Water absorption, Metal Clad Plastic Laminates”.

Shown in Figures 8.6 and 8.7 are the different test patterns charging and discharging after being soaked in distilled water for 24 hours at 23°C.

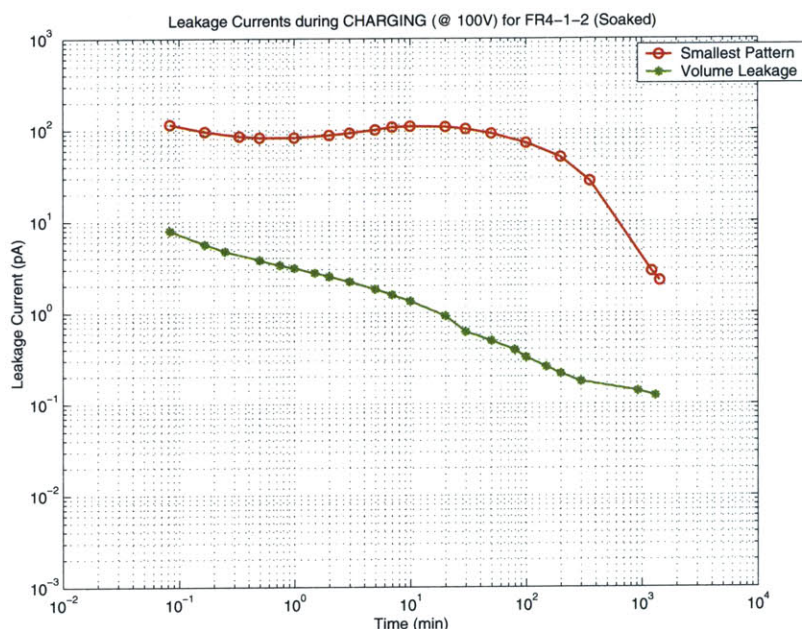


Figure 8.6: “Water Soaked” Current Measurements during Charging

For the charging process in the water soaked tests, the large pattern was not measured. There was a sharp fall of current in the small pattern after about a 100 minutes of testing. This could also be observed as an unusually gradual decline (and even an increase) in currents in the first 10 minutes of testing followed by a drop in current to compensate for the initial slow drop. The volume displayed the almost linear decline in currents and had a much lower value than the small pattern.

During discharge, currents in the small pattern were very linear (on the log scale). The currents in the volume were similarly linear as well.

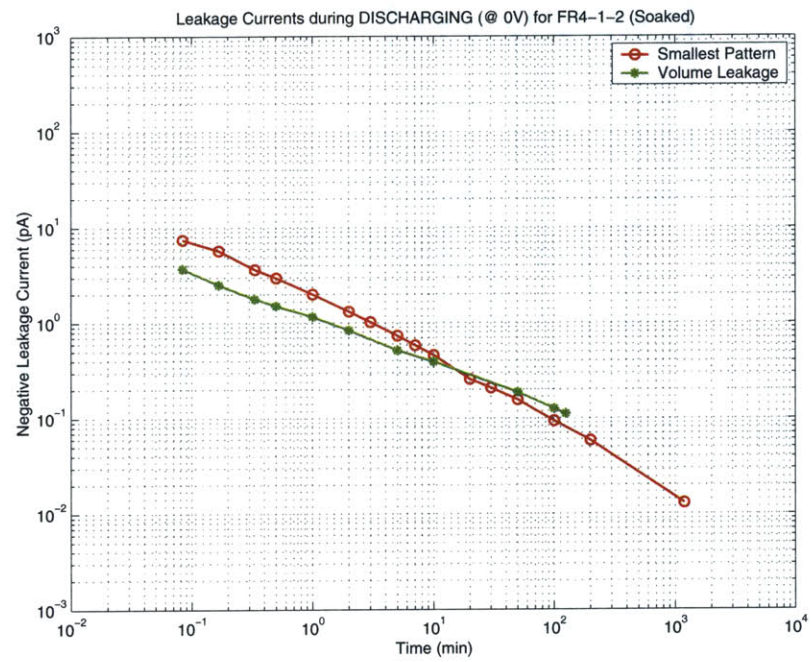


Figure 8.7: “Water Soaked” Current Measurements during Discharging

8.3.1.4 Comparison between Boards

Now, since we have an initial understanding of some of the patterns and how they compare against each other for a given test condition, we will look at each pattern individually and see how it reacts to differing test conditions. Clearly, since the board was exposed to the laboratory environment during the whole test, we should see some variations in results depending on the weather conditions, but this should not deter us from observing trends in the three environmental conditions.

A comparison of the varying test conditions on the small pattern during charge and discharge is shown in Figures 8.8 and 8.9. The discharging process shown in Figure 8.9 was preceded by the 100V charging process.

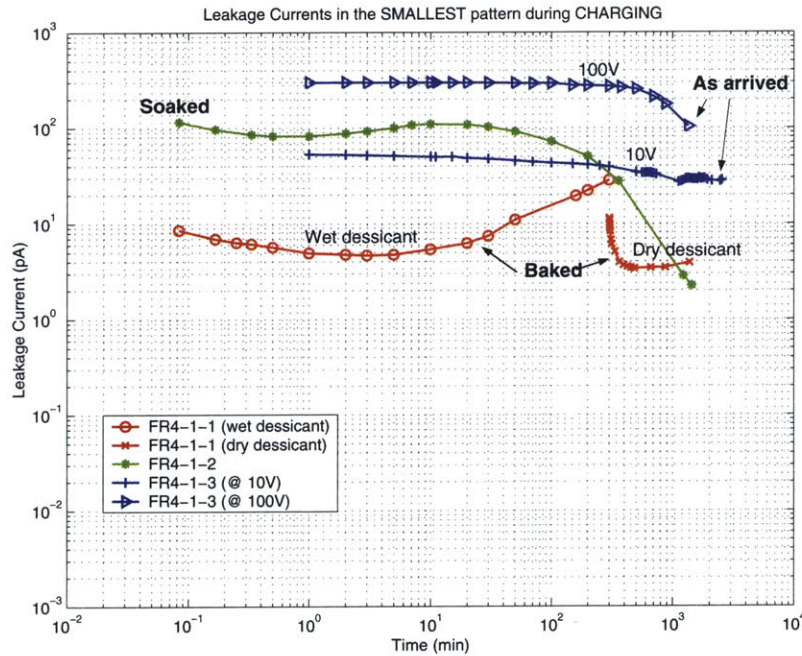


Figure 8.8: “Small Pattern” Current Measurements during Charging

During charging it is evident that the soaked boards have higher currents than the baked boards. This is clearly consistent with the fact the increased moisture absorption aids in the increase of currents. However, the “as arrived” boards have higher currents at 100V. We cannot say much about why this is so mainly because we don’t about the initial conditions (including moisture content) of the “as arrived” boards.

The discharging of the small pattern for all different test conditions displayed almost linear log-log plots with the “as arrived” boards with the maximum currents. Also, as expected

Preliminary Experimental Results

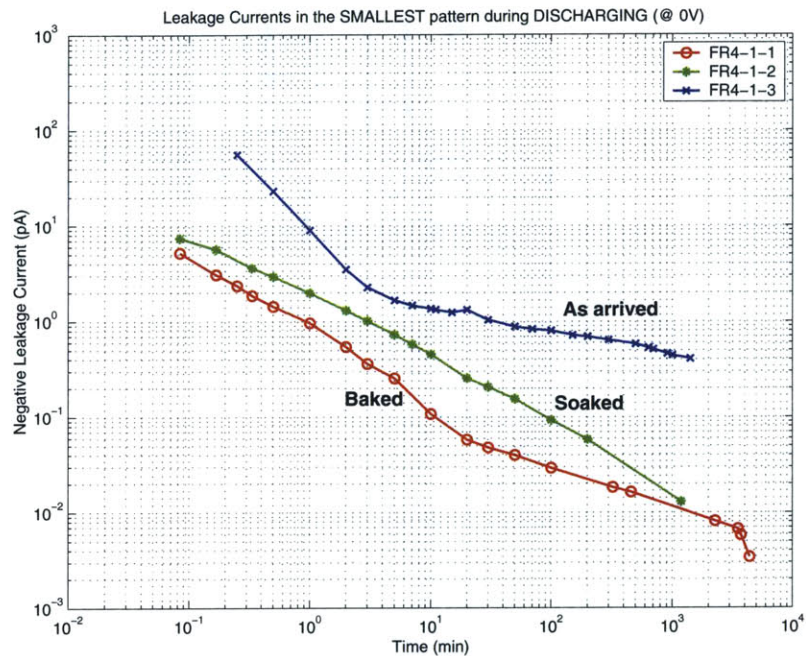


Figure 8.9: “Small Pattern” Current Measurements during Discharging

the soaked plots are higher than the baked plots.

A comparison of the varying test conditions on the large pattern during charge and discharge is shown in Figures 8.10 and 8.11

It is clear from Figure 8.10 that the baked boards had lower discharge currents than the “as arrived” boards. But it is also interesting to see a late increase in currents in the baked boards. One reason for this could be a gradual increase in moisture absorption as the desiccant gets saturated.

In the discharge case, interestingly enough, the baked boards had a higher initial current value than the “as arrived” boards.

A comparison of the varying test conditions on the square pattern through the volume during charge and discharge is shown in Figures 8.12 and 8.13

Volume currents shown in Figure 8.12 have a very predictable trend. The soaked boards have the highest currents and the baked boards have the lowest currents. The “as arrived” boards ripple back and forth between the two boundaries (soaked and baked). As mentioned earlier, the rippling could have been because of the change in external weather conditions.

8.3 Preliminary Experiments on First Generation Samples

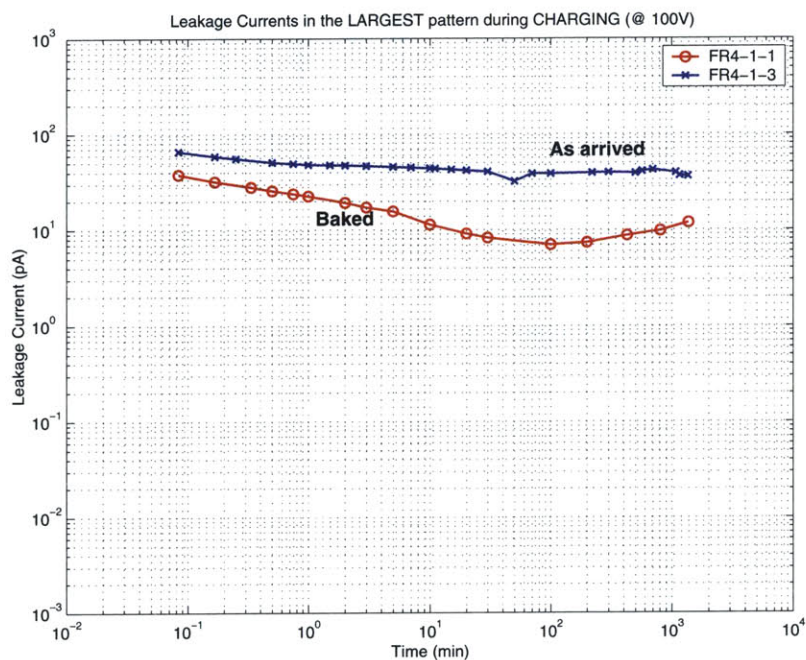


Figure 8.10: “Large Pattern” Current Measurements during Charging

Figure 8.13 also has a very linear trend on the log-log plot. However, the “as arrived” plot is higher than that of the soaked and baked plots. Once again, since the initial conditions of the “as arrived” plots are not known, there isn’t a strong explanation of this trend.

Preliminary Experimental Results

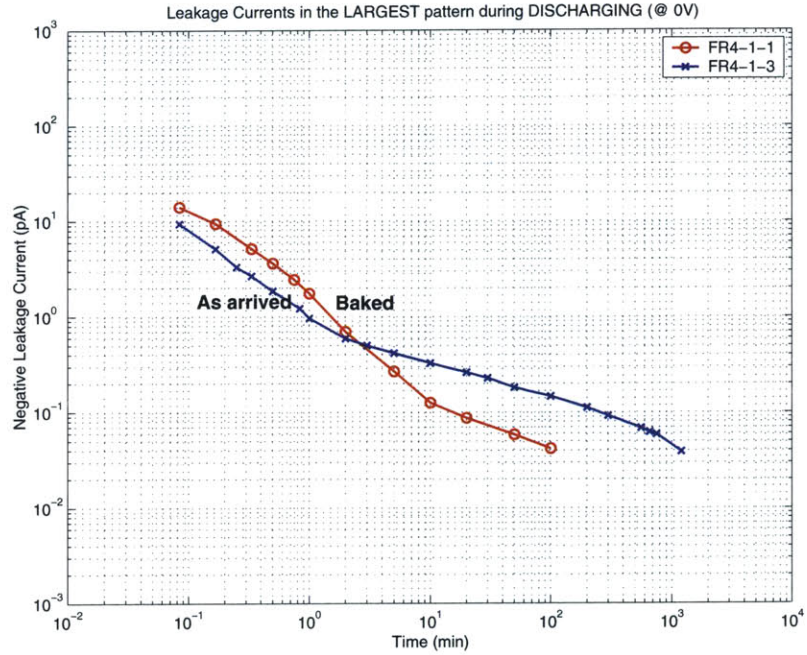


Figure 8.11: “Large Pattern” Current Measurements during Discharging

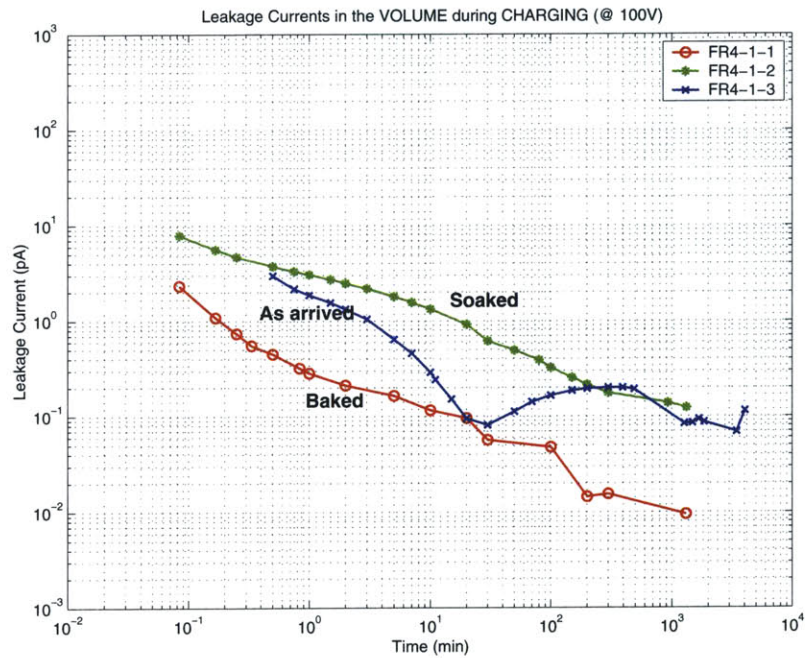


Figure 8.12: “Square Pattern (Volume)” Current Measurements during Charging

8.3 Preliminary Experiments on First Generation Samples

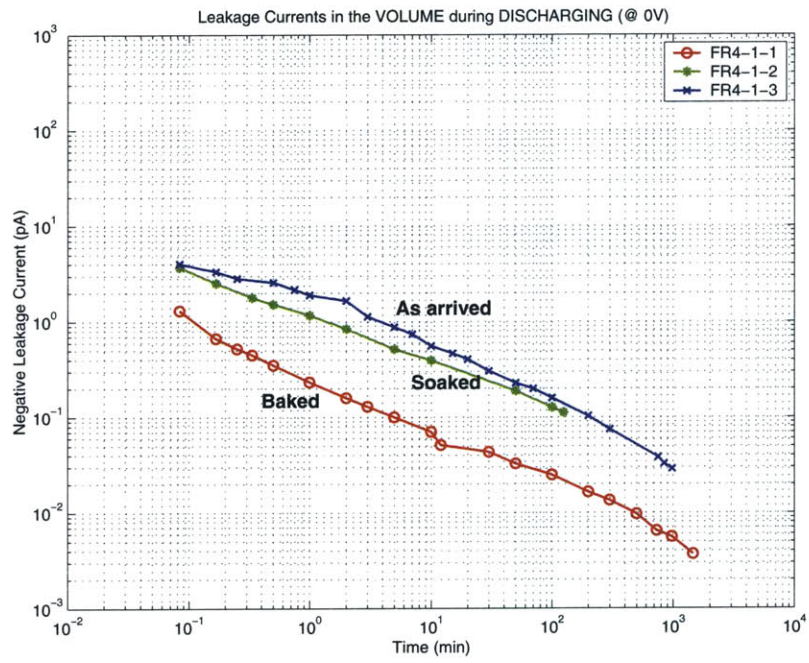


Figure 8.13: “Square Pattern (Volume)” Current Measurements during Discharging

8.3.2 Environment Chamber Tests

Now that we had a good feel of the experimental process in the Faraday cage, it was time to move on to the next phase which is experiments in the environment chamber.

Some questions now arise as to what should the chamber temperature and humidity be when the board is placed inside, how should the board be brought up to desired operating temperature and humidity without the risk of condensation, what is a good operating temperature and humidity and when should the voltage be turned on? As described earlier, some standards specify answers to some of these questions but without much explanation.

After some thought it was decided to follow the protocol illustrated in Figure 8.14. The chamber is required to be stable at 25°C and 50% RH before the board can be placed in. Once the the board is placed inside, it should remain at the same conditions for 1 hour. Next, the temperature set point has to be raised to 85°C and the humidity should remain 50% for the next 1 hour. Even though a substantial quantity of water vapor is added to the chamber, the temperature of the board increases fast enough to ensure that no condensation takes place on it. The humidity can then be raised to 85% to reach our desired condition of 85°C and 85% RH. These desired conditions seemed to be what many standards converged upon. A similar profile can be adopted for different test conditions making sure that the desired temperature is first reached prior to the desired relative humidity.

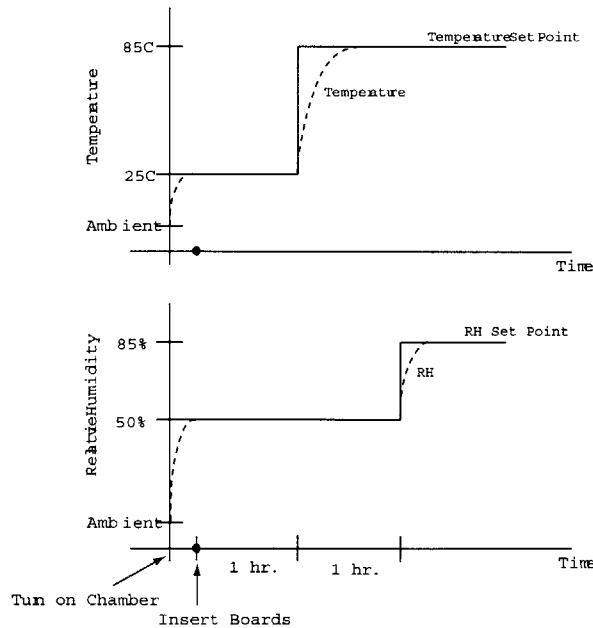


Figure 8.14: Acclimatization Profile for the Environment Chamber Tests

8.3 Preliminary Experiments on First Generation Samples

The next task was to decide the placement of the board in the chamber. A stand for the board was built and the board was placed vertical (face forward) on the stands. The board was also placed centrally such that it was in the direct path of the circulation fan in the chamber. Leads were connected through an opening in the chamber that is thermally insulated from the outside by rubber stoppers.

The board chosen for the first run of experiments was the same board that was used for the “as arrived” Faraday cage experiments (FR4-1-3). This board was placed in the chamber at 85°C and very low RH.

Once again all the experiments were carried out for approximate period of 24 hours. The time and the current were recorded.

One of the small patterns was biased at +100V for about 24 hours. Then it was discharged at 0V for the same time period. The current was recorded on a logarithmic time scale.

The same charging and discharging cycle was repeated for the bulk and then the large pattern.

Next, the chamber humidity was slowly increased to 85% and the board was let to sit there for at about 24 hours. Then, the small, large and bulk patterns were put through the charge and discharge cycles.

Shown in Figures 8.15, 8.16 and 8.17 are graphs of consolidated results comparing the currents in FR4-1-3 inside the Faraday Cage (indicated in the legend as “Ambient”) as well as in the chamber at the wet and dry conditions. Additionally, for comparison, the small pattern on FR4-1-1 (“oven baked”) is also plotted in Figure 8.15.

Each figure indicates a different pattern that was tested. The x-axis indicates time in minutes and the y-axis shows the current in nano-amperes. The top plot in each figure indicates charging at 100V and the bottom plot indicates discharging at 0V. The data on each plot are from some of the results from the Faraday cage experiment (indicated in the legend as “Ambient”), the chamber experiments when the board was placed in the chamber at 85°C and low RH and when the chamber was at 85°C/85%. Also, the legend shown in the bottom plot applies to the top plot as well. The plots in Figures 8.15 – 8.17 do not show much consistency. In some plots it appears as if the high humidity conditions displayed higher currents than the low humidity conditions. However, the vice-versa was observed in other plots. This could have been due to number of factors that weren’t completely controlled during the experimentation in addition to the drawbacks of the first generation boards presented in Section 5.2.2.

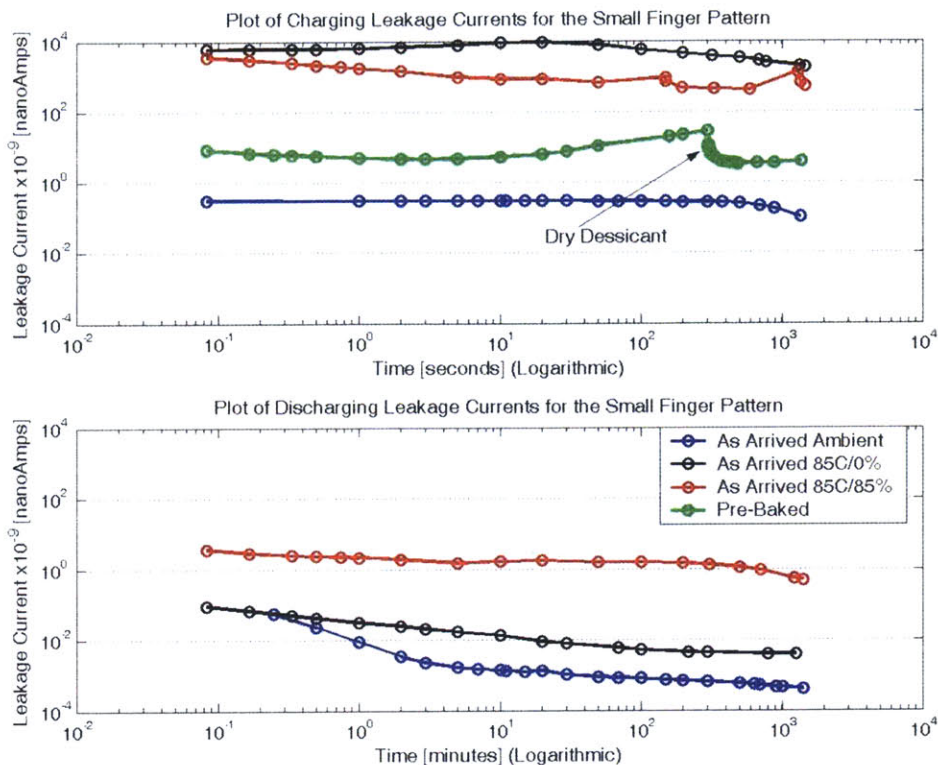


Figure 8.15: Leakage Currents: Small Pattern [1st generation board]

When the large pattern was being measured, an interesting observation was made. As the controller in the chamber tried to maintain 85°C and 85% RH, it cycled both the temperature and humidity. These small changes in condition also influenced the current. It seemed as if the current was following both the temperature and humidity changes with a very small time lag. Obviously, these subtleties were not recorded in the regular logarithmic time scales. To understand this behavior better, we decided to repeat the charge and discharge cycles and to follow it up with a short humidity sensitivity analysis. To analyze the sensitivity to moisture we varied the humidity by a few percent and recorded the changes in current.

Then, the charge and discharge cycles were repeated for the large pattern followed by the sensitivity analysis. Additionally, we also charged the pattern at -100V followed by a 0V discharge to see the behavior of the board in a reverse field. The bulk and then the small pattern were also subject to the same charging, discharging and sensitivity cycles

This concluded all tests on the first generation boards. As described earlier (Section 5.2.2)

8.3 Preliminary Experiments on First Generation Samples

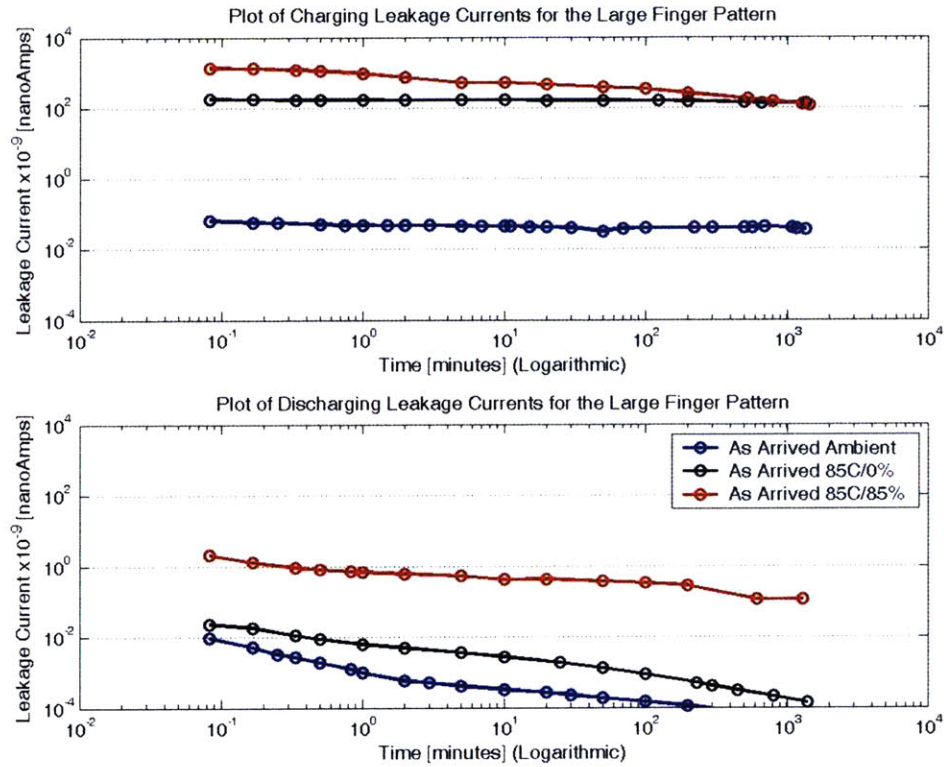


Figure 8.16: Leakage Currents: Large Pattern [1st generation board]

there were some improvements that needed to be made and therefore a new board was designed.

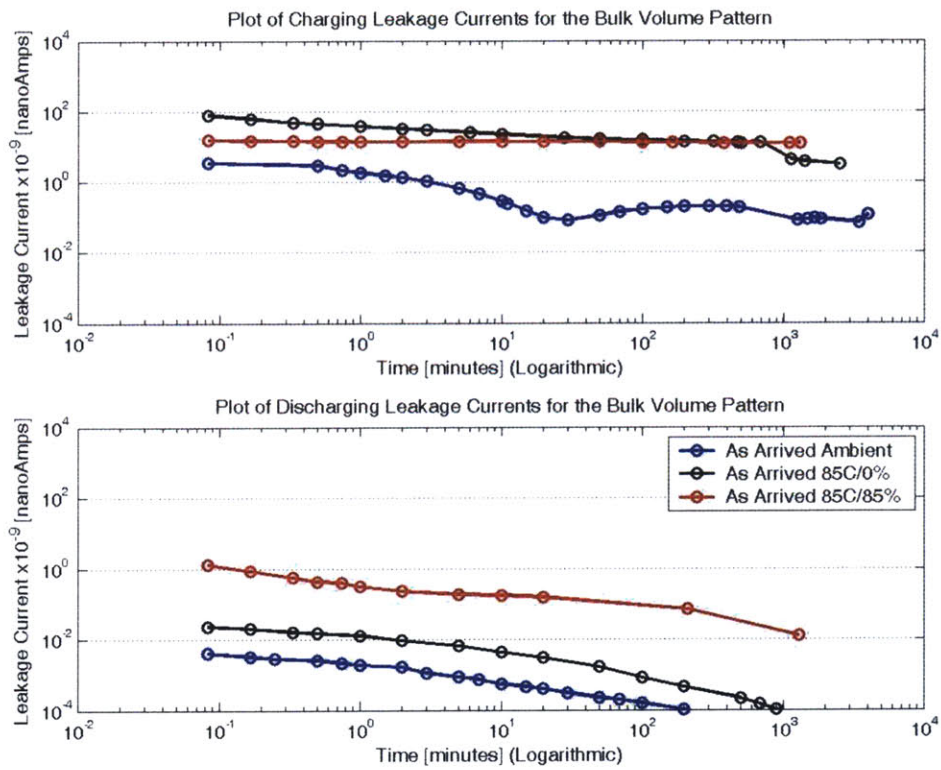


Figure 8.17: Leakage Currents: Bulk (Volume) Pattern [1st generation board]

8.3.3 Generation Conclusions from First Generation Samples

Some important observations can be made from these plots. The general trend of all the plots is that they are all approaching some steady state value. Additionally, there is some degree of sensitivity to moisture. As expected, the currents are greater for the small pattern than the large and the volume. To further study the role of moisture in electrical conduction, we will perform some preliminary experiments on the second generation of test samples.

8.4 Preliminary Experiments on Second Generation Samples

To start the experiments on the newer second generation samples, it was decided that we place two boards (CB0 and CB1) in the chamber this time. We would test CB0 immediately (after 1 hour of equilibration in the specified condition) while CB1 would be tested after it has been conditioned for a longer time. This way, we could judge the impact of moisture diffusion which is usually a time consuming process.

8.4.1 Initial Polarization Tests (CB0 and CB1)

Similar to the experiments on the first generation samples, we put CB0 through the same charging and discharging on the small, closed bulk, porous (open) bulk, large and dimpled patterns at 85°C and 85% RH.

Shown in Figure 8.18 is the charging and discharging of all the patterns on CB0 at 85°C/85% RH.

As expected, we observed the highest currents in the small and the large patterns. Interestingly, the porous bulk pattern had higher leakages indicating, once again, that the overall impact of moisture.

CB0 was now removed from the chamber and CB1(conditioned) was connected. The small pattern on this board was subject to the same charging, discharging and sensitivity cycles. We also tested the closed bulk pattern.

Figure 8.19 indicates the charging of the small and bulk (volume) patterns on CB1. The expected impact of conditioning is not easily detected.

Preliminary Experimental Results

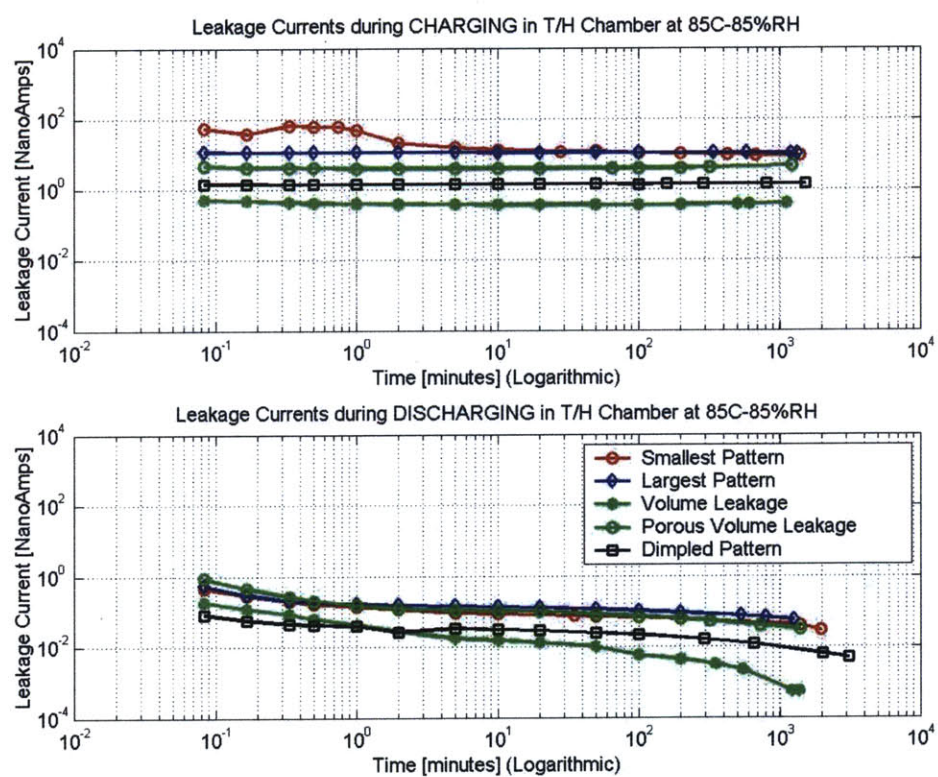


Figure 8.18: Leakage Currents: All Patterns at 85°C and 85% RH [CB0]

8.4 Preliminary Experiments on Second Generation Samples

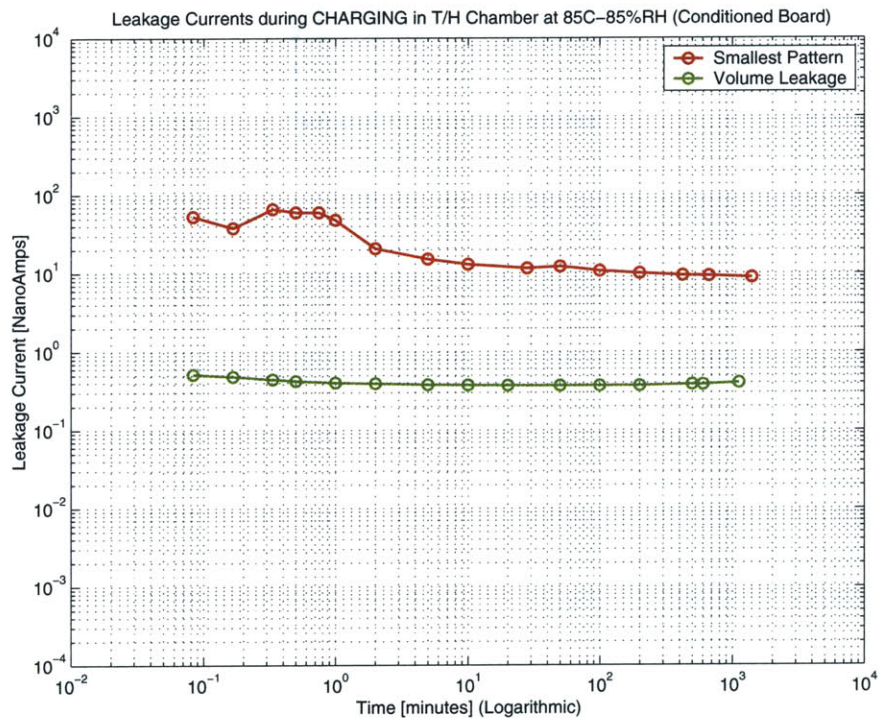


Figure 8.19: Leakage Currents: All Patterns at 85°C and 85% RH and conditioned [CB1]

8.4.2 Initial Thermal and Moisture Sensitivity Tests

It was decided, at this time, that we would do a full temperature and relative humidity sensitivity analysis – one that would resemble step inputs.

- RH Cycle: 85°C/85%, 85°C/70% (1 hr.), 85°C/85%
- Temperature Cycle: 85°C/85%, 80°C/85% (1 hr.), 70°C/85% (1 hr.), 85°C/85%

We recorded time, current, temperature and humidity for each test run. The results of the test indicated a strong effect of temperature and humidity (as will be discussed in detail in the next chapter) on current. However, this generated some concern since we couldn't provide a good reason for such an instantaneous effect on current.

Therefore, we began thinking whether there might have been some other stray leakage path or some external effects that could cause such a strong dependence of temperature and humidity on current.

As a simple test, we disconnected the leads from the board and observed the electrometer readings with the voltage still on 100V. The meter was still reading significant currents.

We then repositioned the wires, making sure that the insulation of the supply and sensing wires did not touch any part of the board and then repeated the testing at 100V. This fixed the problem and we were now only reading small noise. After this experience, control of the lead dress has been adopted as a universal part of our test methodology.

We then reconnected the board and ensured that the wire insulation was not touching the board. The RH and temperature sensitivity cycles were repeated. There was still a strong dependence on temperature and humidity. So both the lead dress and the properties of the board contributed to our original observations. Now, we cannot say with certainty that all the results obtained from prior experiments were not affected by this source of disturbance. We can, however, guarantee that the position of lead dress was carefully monitored and controlled during all the remaining experiments discussed in this thesis. Furthermore, the aim of most of our preliminary tests was to gain a qualitative understanding of the leakage process and not delve to deeply into the quantitative aspects.

The closed bulk being tested is located on the top part of the board. It is a possibility that there might have been some leakage over the top surface of the board onto the other side (discussed in Section 7.2.1). To isolate both sides, we painted a coat of silver paint on both sides around the pattern and connected it to ground. The pattern was then recharged at

8.4 Preliminary Experiments on Second Generation Samples

100V and then both the temperature and humidity sensitivity cycles were performed. The results were mostly the same, albeit much less noisy, indicating that we might have been measuring the right currents from the start. Also, the leakage currents displayed a much higher sensitivity to temperature than to humidity.

In Figure 8.20 the behavior of the boards can be seen to a typical sensitivity test. The vertical axis shows the percent change in the temperature, relative humidity and current from a certain initial value.

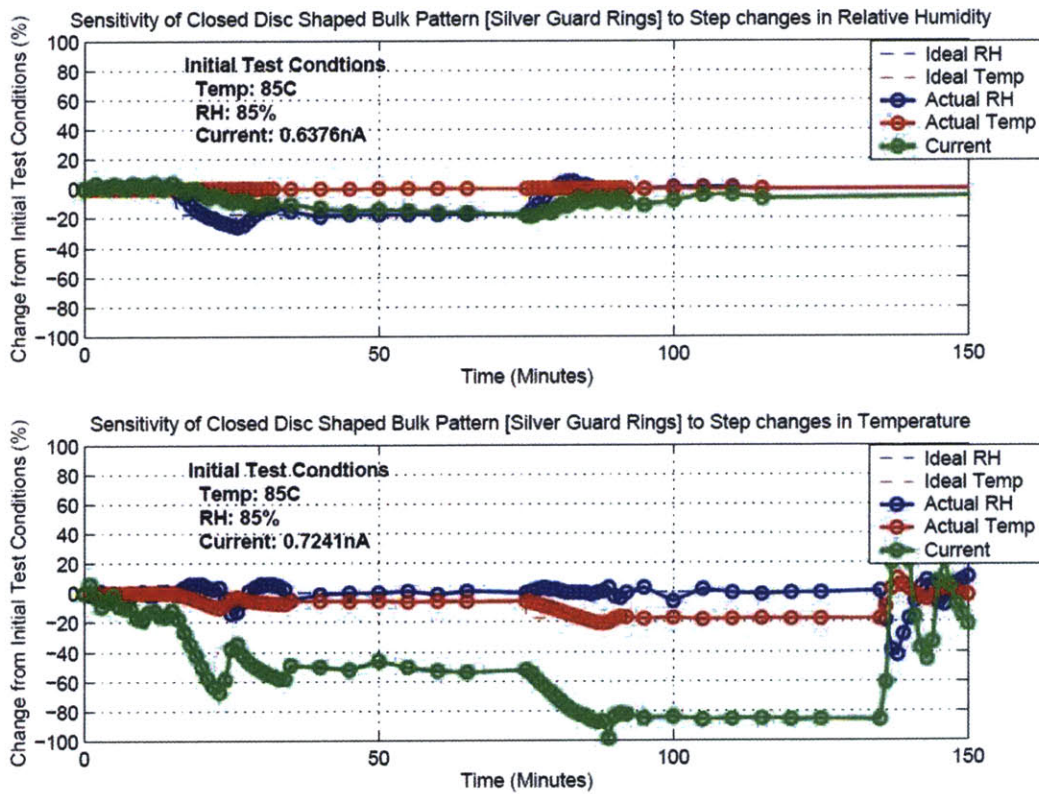


Figure 8.20: Sensitivity of Leakage Current in CB1

8.4.3 Wide-Range Thermal and Moisture Sensitivity Tests

To confirm these results and improve our range of data, we decided to extend these tests over a wider range of temperatures and test at different fixed humidity levels.

Therefore new temperature step profiles for different constant humidity conditions were used. This profile stepped down from 85°C to 35°C as shown in the example below:

- Temperature Cycle: 85°C/85%, 75°C/85% (1 hr.), 65°C/85% (1 hr.), 55°C/85%, 45°C/85%, 35°C/85%

The constant humidity levels we used were 85%, 40%, 20% and 0% (some level less than 20%).

The results are presented in Figures 8.21, 8.22, 8.23, 8.24 and 8.25. The most important trend common in these figures is the Arrhenius temperature dependence across all patterns. As described in Section 4.3.5, this Arrhenius temperature dependency is a sign of possible ionic conduction mechanisms.

8.4 Preliminary Experiments on Second Generation Samples

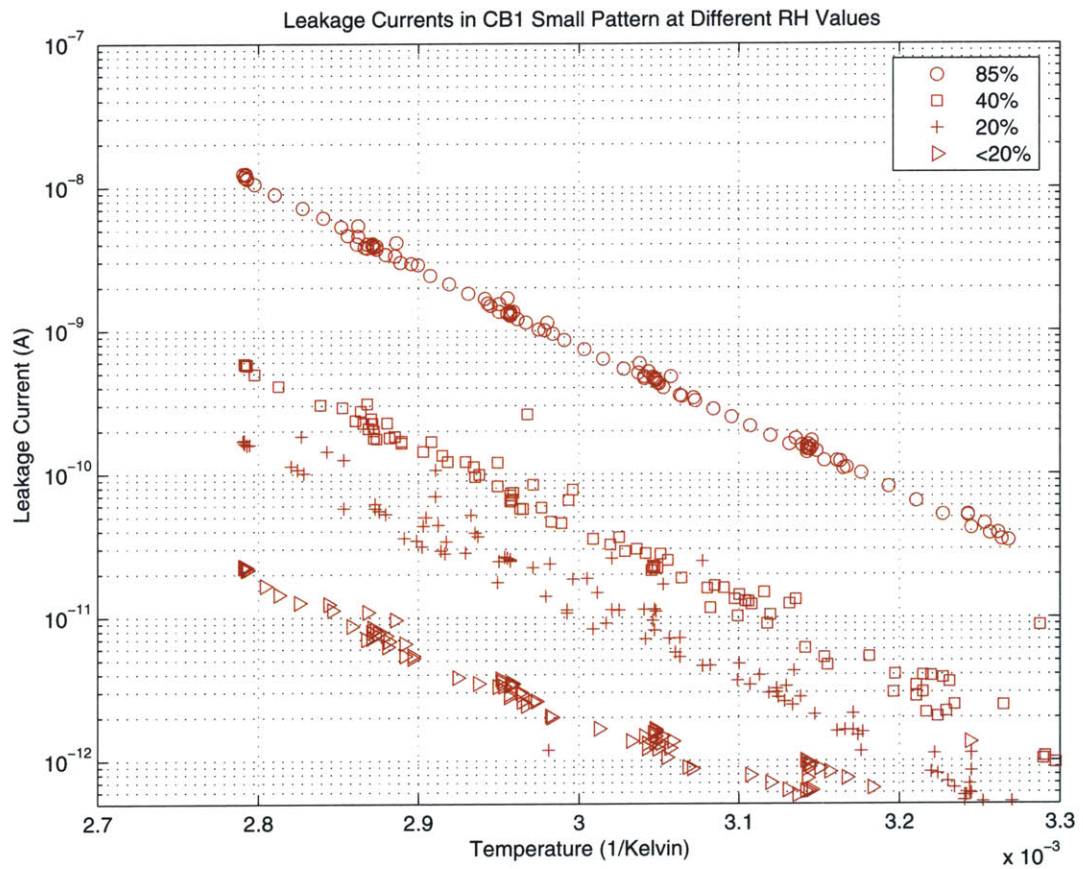


Figure 8.21: Leakage Currents in the Small Pattern in CB1

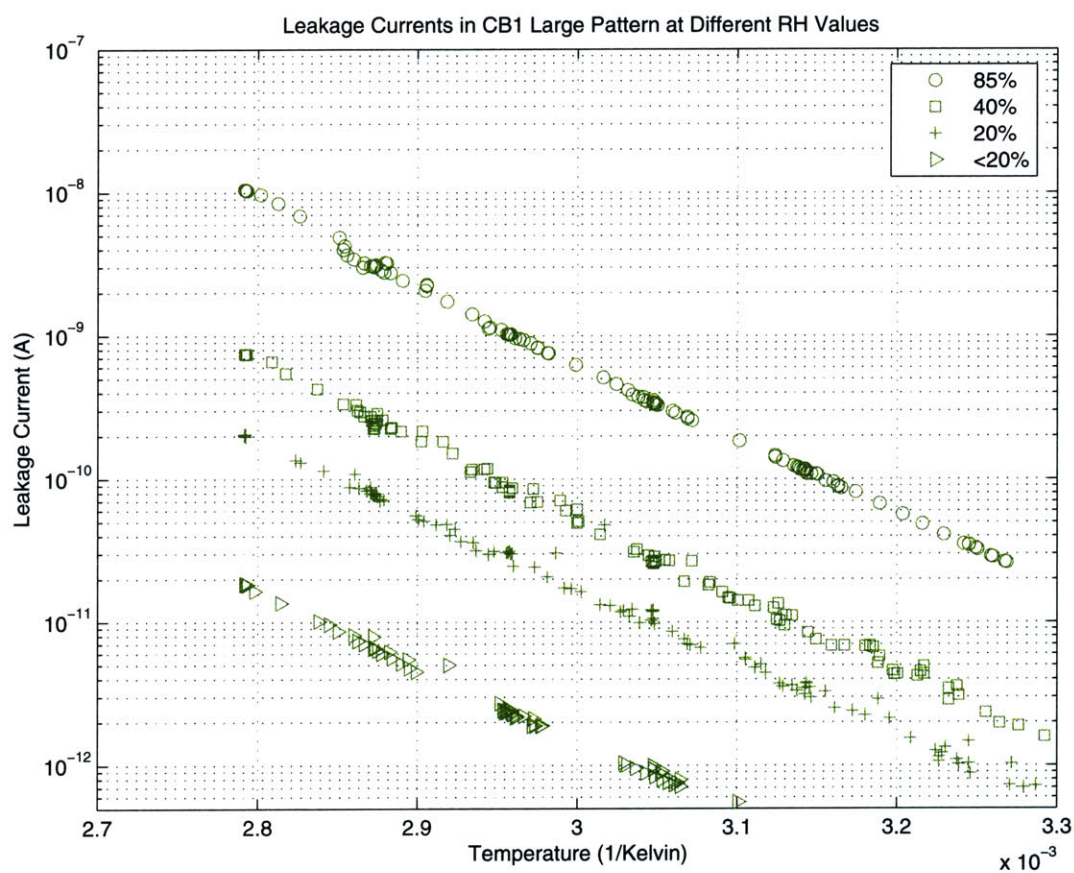


Figure 8.22: Leakage Currents in the Large Pattern in CB1

8.4 Preliminary Experiments on Second Generation Samples

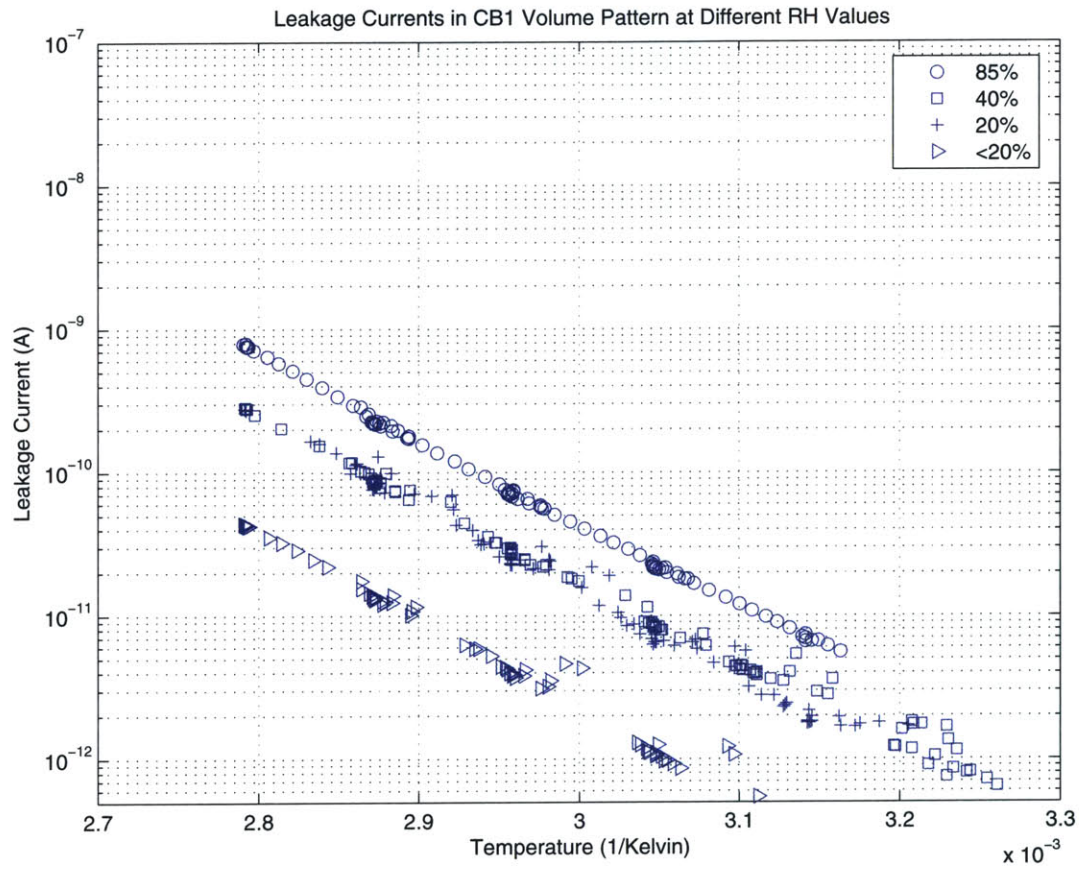


Figure 8.23: Leakage Currents in the Volume Pattern in CB1

8.4.4 Size-Scaling Effects Tests

To study the effect of scaling on the currents, we connected two small patterns in parallel and measured currents through the combined pattern using the previously described temperature step profile. The relative humidity was kept very low throughout the test. Figure 8.24 shows the results of this test.

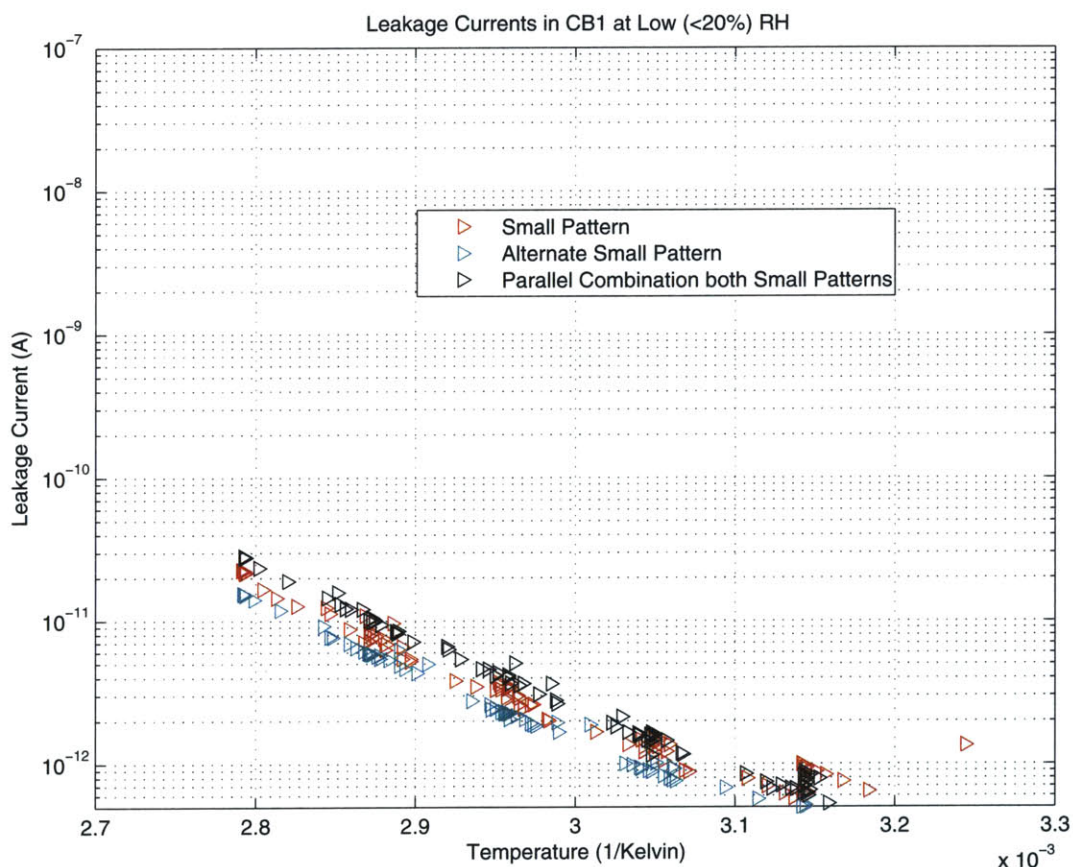


Figure 8.24: Leakage Currents in the Small Patterns and their Parallel Combination at low RH in CB1

There seems to be a fair degree of linearity in the total length of fingers. Figure 8.24 indicates that if we double the number of fingers by connecting two small patterns in parallel then the currents approximately double in value. Such behavior puts us confidently in the low field regime since there are no particular non-linearities that might otherwise happen at higher fields where injection mechanisms are dependent on the length of available conductors.

8.4.5 Voltage Sensitivity Tests

To observe the variation with voltage, we looked at the response of all the patterns to a similar profile at 20V. Once again, the test was conducted using the same temperature profile discussed above and at very low relative humidity.

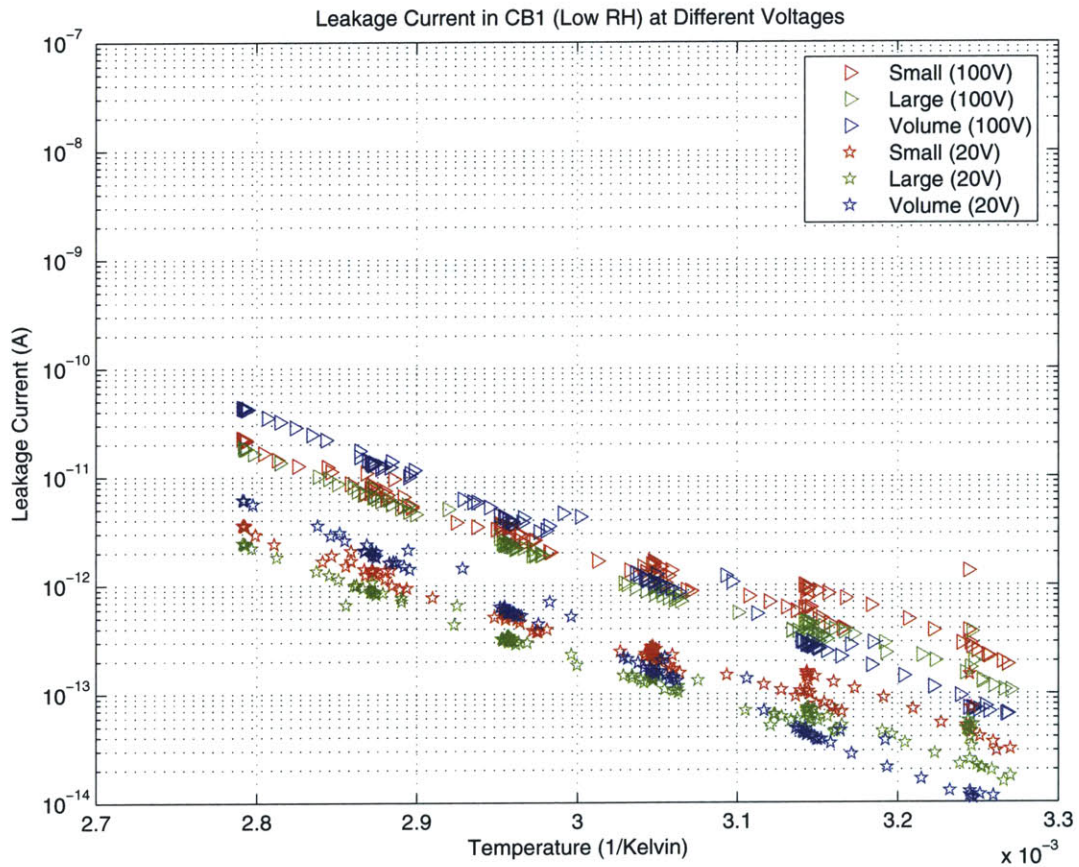


Figure 8.25: Leakage Currents in CB1 (Low RH) at 20V

Figure 8.25 shows that there seems to be an ohmic relationship between voltage and current in the insulation. Here the leakage currents in each pattern at 20V is about 5 times lower than those previously described at 100V. At low fields, ionic conduction displays a simple ohmic relationship.

8.4.6 General Conclusions from Second Generation Samples

If we do believe that ionic conduction is the primary transport mechanism then the question arises as to what we are actually transporting. Since these experiments were not performed in clean room environment where external impurities could be controlled, the charge carriers could be products of reactions between the insulator and the surrounding environment or water molecules and hydrated ionic species or a combination of all of the above. This presents a very complicated problem where isolating the most dominant charge carrier is very difficult. Figures 8.21, 8.22 and 8.23 indicate that the amount of atmospheric moisture plays a fairly important role in conduction and might in fact facilitate charge generation and transport. To better characterize the amount of moisture in the insulation, a more controlled series of experiments is in order where the weight of the board can be monitored more closely. The results of such a series of controlled experiments is presented in the next chapter.

The Hygrothermal Test Plan

IN this chapter we present the procedure and results obtained from the series of hygrothermal tests that were conducted on five second generation samples. An interpretation of the effect of moisture along with a possible conduction mechanism and model are presented here.

9.1 Introduction and General Overview

In Chapter 8 we observed the general trends in conduction in PCB insulation. The initial Faraday cage results roughly indicated that there might be some kind of moisture effect. This was evident in differing values of leakage currents in three pre-conditioned samples. Later tests in the environment chamber also helped strengthen this hypothesized moisture dependency. The testing focus was then shifted to a new and improved second generation of test samples that featured better pattern and base material design. Two test samples (CB0 and CB1) were used to measure the impact of moisture conditioning. As presented earlier, the results indicated a clear Arrhenius temperature dependency and an obvious dependence on environmental moisture conditions. The patterns, however, were measured one at a time and the readings were taken by hand.

With the development of the data acquisition system described in Chapters 5 and 6, the patterns could now be measured simultaneously and more frequently. There was a need to carefully control as many aspects of the experiment as possible. Previous experiments on CB1 lacked the careful approach and measurement metrics needed to understand the role of moisture in the conduction process. One of the goals of the hygrothermal experimental scheme was to determine not only the role played by environmental conditions on conduction, but also the impact of absorbed moisture on leakage currents. This was made possible through the weight gain/loss measurements.

9.2 Hygrothermal Experimental Scheme

The Hygrothermal Experimental Scheme was a fully planned out testing scheme which involved the use of multiple test samples (CB and WB) being simultaneously treated at different conditions. In principle, we equilibrated the test sample to a certain environmental condition and observed its effect on the leakage currents through the bulk of the PCB as well as through the surface. This scheme was performed in a very controlled manner to ensure consistency across patterns and samples.

Shown in Figure 9.1 is the approximate time-line of tests for all the 5 test samples.

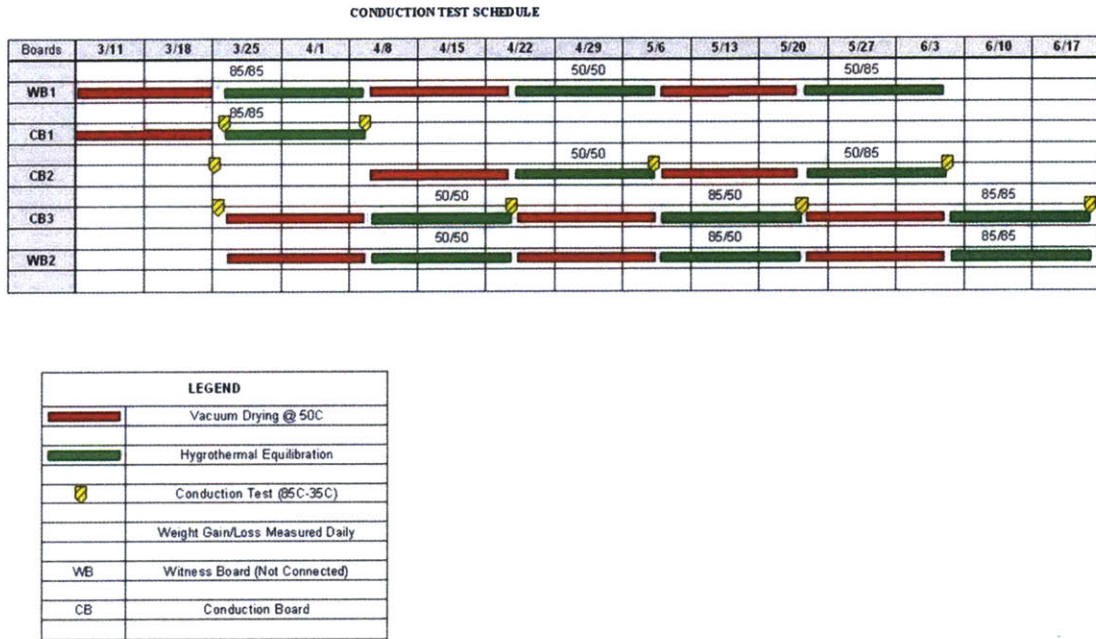


Figure 9.1: Hygrothermal-Conduction Experimental Scheme

It can be seen from the schedule that we alternatively soaked and dried the boards every two weeks. At the end of each conditioning cycle the conduction board that was in the environment chamber was put through a modified conduction test described next.

9.2.1 Modified Conduction Tests

After installing the new data acquisition system we were able to take measurements on a more controlled and regular basis. We were also able to set the environment chamber

9.2 Hygrothermal Experimental Scheme

to automatically change the temperature based on a preselected profile. The modified conduction test involved measuring currents when a voltage of 100V was applied across the patterns while we gradually decreased the temperature from 85°C to 35°C over a period of 5 hours. The samples are subjected to a voltage bias after reaching a hygrothermal equilibrium.

Shown in Figure 9.2 is the modified conduction scheme. Here T_1 represents the temperature of the hygrothermal equilibrium.

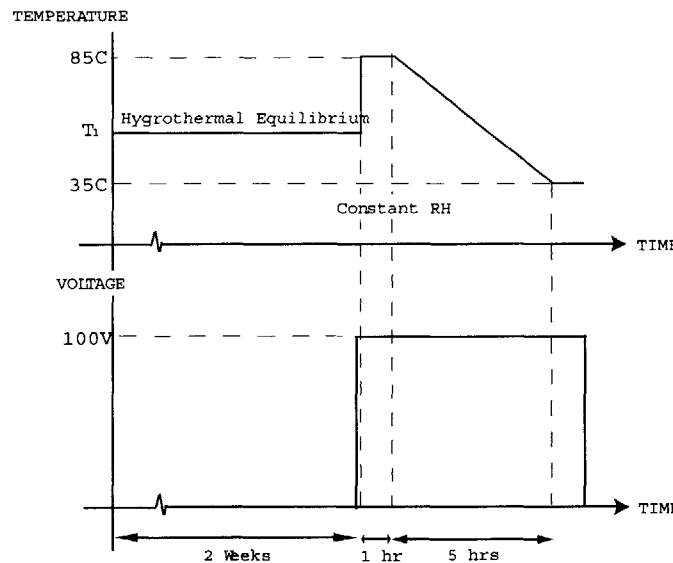


Figure 9.2: Modified Conduction Test

CB1, however, was retired after one round of testing because, it was comparatively older than the others. Also, since it had already undergone multiple rounds of aging, the physical structure of the material may have undergone substantial change. These factors made the board unsuitable for an accurate comparison. Also, CB0 was never used because we realized that adequate care may not have been taken earlier to prevent it from being contaminated with impurities. All the other samples were always handled with utmost care and kept clean through the use of gloves and Ziploc[®] bags.

Also, the first 50/50 condition was repeated for both sets of boards so that we could understand the differences in conduction between samples from the same group.

The scheme starts off by drying CB1 and WB1 in a vacuum oven. However, prior to beginning the experimental scheme, we cleaned CB1 and WB1 in running distilled water and then dried them by purging N_2 gas through the vacuum oven for 10 days at atmospheric pressure. The aim was to get CB1 to the driest possible state before measuring leakage

The Hygrothermal Test Plan

currents. We did a modified conduction test as per Figure 9.2 after this purging procedure (before the beginning of the hygrothermal experimental scheme). The conduction test on a dry sample indicated the existence of inherent leakage currents in the insulation in a state which represents our best effort to create the absence of moisture.

During the entirety of the experimental scheme, we measured the weight of all the samples using the methodology described in Section 6.7 on a daily basis. Also, we monitored thickness changes as per the methodology described in Section 6.8 for all the samples at the end of a two week cycle.

9.3 Weight Change Results

Shown below in Figure 9.3 and 9.4 is an overview of the weight responses of all the boards as they underwent different conditioning cycles.

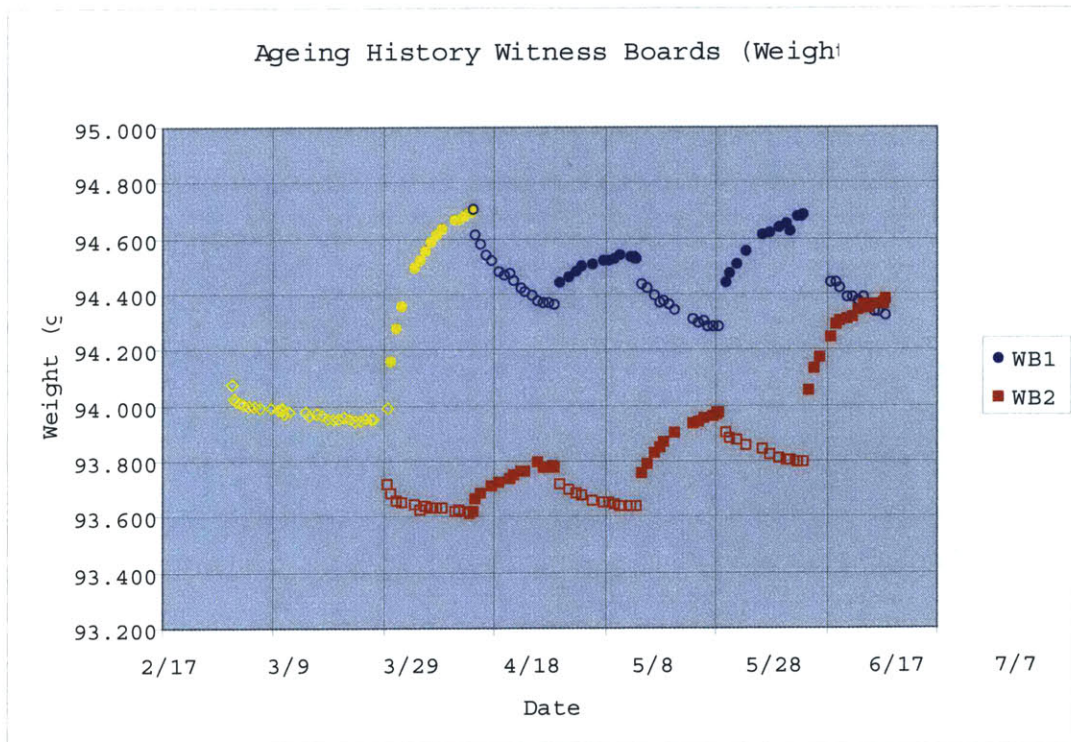


Figure 9.3: Ageing History of the Witness Boards

Similar colors are used to represent the pairs of samples that underwent the conditioning

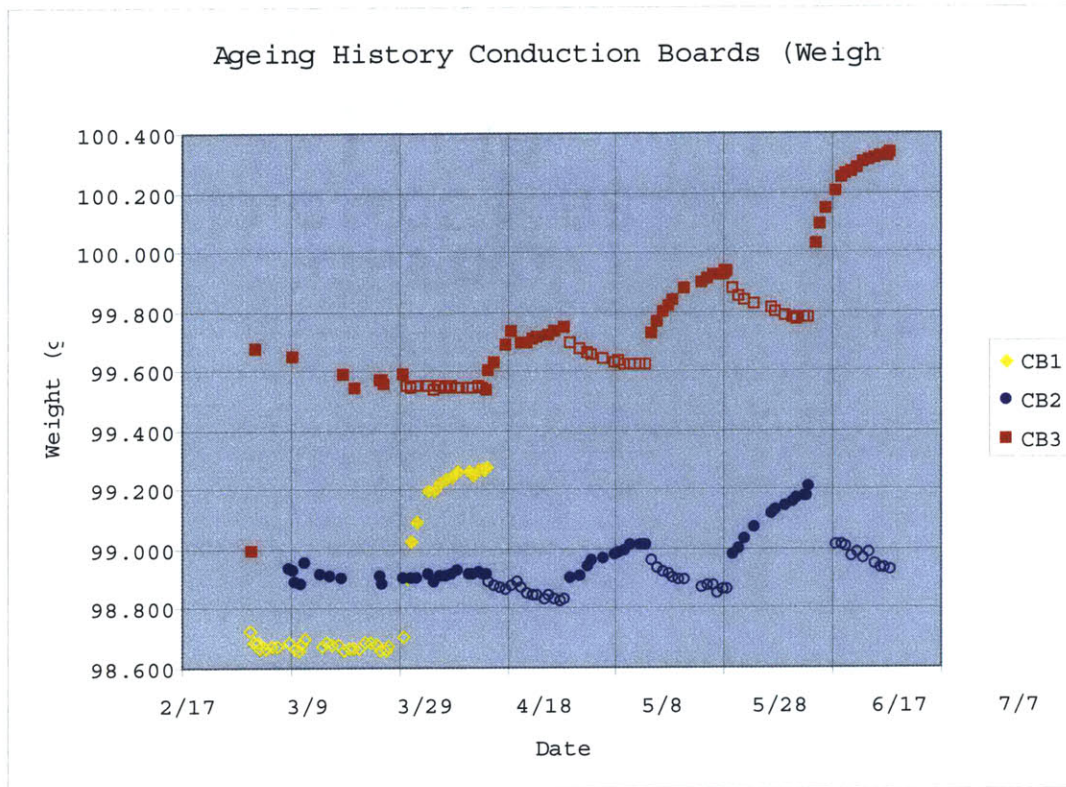


Figure 9.4: Aging History of the Conduction Boards

cycle. Initially, WB1 and CB1 were placed in the environment chamber at 85°C and 85% RH and are shown in yellow in Figures 9.3 and 9.4. Afterwards, WB1 and CB2 (shown in blue) and WB2 and CB3 (shown in red) were each subjected to the marked test conditions. The empty circles and squares correspond to vacuum drying while the filled circles and squares correspond to either ambient conditions or a temperature and relative humidity stress.

Some simple inferences can be made from these two figures such as, during soaking (temperature and humidity stress) there was almost always weight gain while during drying (vacuum at 50°C) there was almost always weight loss. Also, the first drying cycle always produced the lowest weights for all the boards. Furthermore, the minimum weight of all the boards after a drying treatment was almost always greater than the minimum weight for the same board obtained from any previous treatment. This indicates that some of the water becomes increasingly hard to remove and might provide evidence for the bound state of water. The exception to this hypothesis is WB1 where the third drying treatment resulted in a lower weight than the second drying treatment. This could be because the

The Hygrothermal Test Plan

characteristics of the 85°C/85% RH diffusion process has resulted in much more water being absorbed than what can be removed from an equal length drying cycle in a vacuum at 50°C. Therefore, the third vacuum may have been still removing some of the moisture from the 85°C/85% RH treatment. Next, the observed weight gain for the boards at 50°C/50% RH followed similar characteristic paths and final values. Additionally, WB1 at 85°C/85% RH gained more moisture than CB1 at 85°C/85% RH. This could be because of the fact that since CB1 was aged prior to the hygrothermal test series, it might have been close to saturation and hence unable to absorb as much water. Therefore, this difference in weight gain between the WB1 and CB1 might in fact indicate the amount of bound water. The initial 85°C/85% RH stress on WB1 appears to have dramatically changed its diffusion characteristics for consequent tests.

9.3.1 Net Weight Gain

Next, we look at the total weight gain for each of the boards for each hygrothermal condition. For this we first determine the dry weight of the board, which is the lightest the board has ever been through the entire course of the test sequence. This always occurs sometime towards the end of the first vacuum drying cycle. Table 9.1 shows the dry weight for each board and the net incremental weight gain for each of the test conditions when compared with this dry weight.

Boards	Dry Weight (g)	50/50 Gain (g)	85/50 Gain (g)	50/85 Gain (g)	85/85 Gain (g)
WB1	93.948	0.582	-	0.727	0.744
WB2	93.612	0.166	0.359	-	0.756
CB1	98.657	-	-	-	0.609
CB2	98.823	0.188	-	0.355	-
CB3	99.537	0.208	0.4	-	0.791

Table 9.1: Dry Weight (g) and the Net Weight Gain (g) after each Conditioning Cycle

The boards seem to have gained similar weights for a given test condition except for WB1. The net gain of WB1 for all the test conditions are significantly higher than the other boards. This may be because WB1 was subjected to a high temperature and high humidity condition of 85°C/85% RH first. This table and all the data prior clearly indicate that history of the board plays a vital role in its diffusion characteristics. It might also indicate that the 85°C/85% RH condition might almost be an extreme that might change the basic performance of the boards.

9.3.2 Weight Change during Modified Conduction Test

Before we begin to describe the results of the modified conduction tests (Section 9.2.1), we have to quantitatively verify that the duration of the test (approximately 5 hours) does not have an impact on moisture absorption. Weight measurements were taken before and after the conduction test and these are shown below in Table 9.2.

It is clear from Table 9.2 that the weight change is a very small percentage of the total weight change of the board in going from one test condition to another indicating that the duration of the test and specific test conditions do not impact the condition of the board too much.

Board	Condition	Weight Before Conduction Test (g)	Weight After Conduction Test (g)	Net Weight Change (%)
CB1	N_2 Dry	98.657	98.677	+0.020
	Vacuum Dry	98.661	98.674	+0.009
	85/85	99.266	99.273	+0.007
CB2	Ambient	98.925	98.889	-0.030
	Ambient	98.909	98.884	-0.025
	50/50	99.011	99.010	-0.001
CB3	Ambient	99.568	99.557	-0.011
	50/50	99.745	99.748	+0.003
	85/50	99.937	99.935	-0.002
	85/85	100.328	100.333	+0.004

Table 9.2: Net Weight Change During the Modified Conduction Test

9.4 Thickness Change Results

It was also noted in Section 3.7 that water molecules hydrogen bonded to the polymer chain cause re-alignment of the chains and consequently expansion of the solid. The unbound water occupying the free volume on the other hand does not immediately cause such expansion. To study this behavior, we measured the board thicknesses in two locations as was indicated in Section 6.8 after each hygrothermal conditioning cycle. Shown below in Figures 9.5 and 9.6 are the corresponding plots of the measured thickness. The plots are organized so that one can compare two boards that underwent the same hygrothermal condition. The colors help distinguish between the two boards, the markers differentiate the two measured locations on the boards and the marker sizes are representative of the inherent error in measurement.

In Figure 9.5 we can see the thickness variations of WB1 and CB2. Overall, the general trend of the curves follow those of the WB1 and CB2 in Figure 9.3 and 9.4. However, WB1 is much thicker at the beginning and this can also possibly be attributed to the 85°C/85% RH test administered at the start.

Figure 9.6 shows us the expansions and contractions of WB2 and CB2. Once again, comparing similar weight gain plots in Figures 9.3 and 9.4, we can see the trend similarity.

In general, however, there is very little expansion and this might indicate that the fiberglass might actually be restricting the expansion and therefore might be forcing the water to occupy the free volume instead. The restricted expansion could also imply that the polymer chains might be shifting and adjusting to accommodate the bound water molecules.

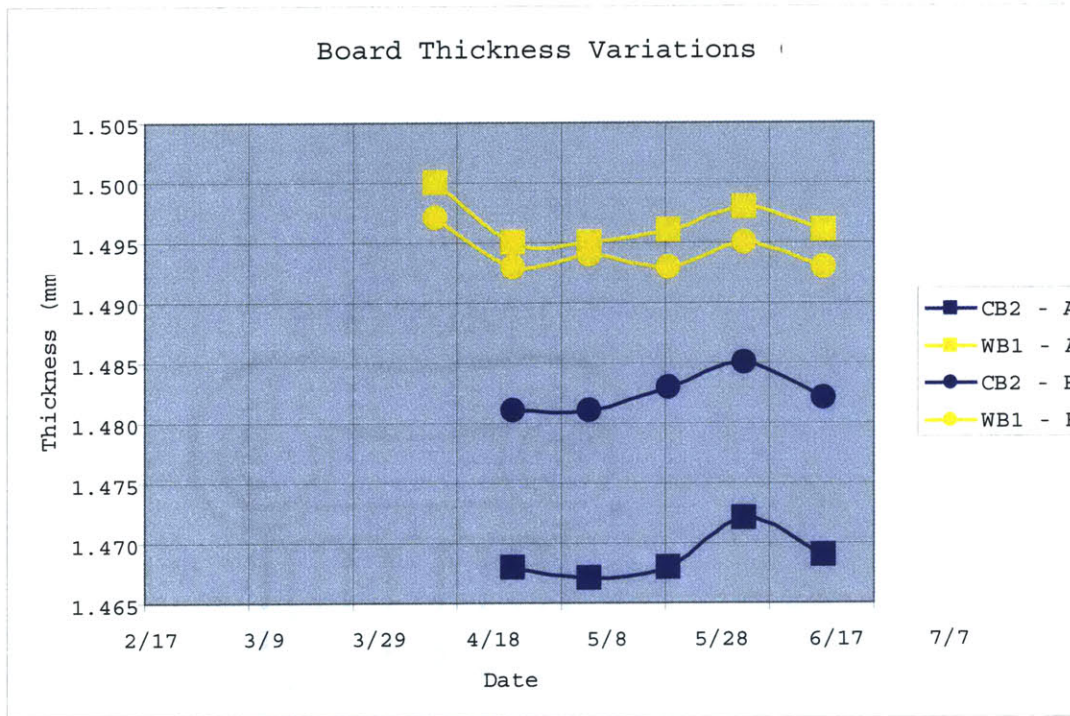


Figure 9.5: Thickness History of WB1 and CB2

In the next few sections we will look deeper into the weight gain measurements and then see how the moisture uptake influences conduction.

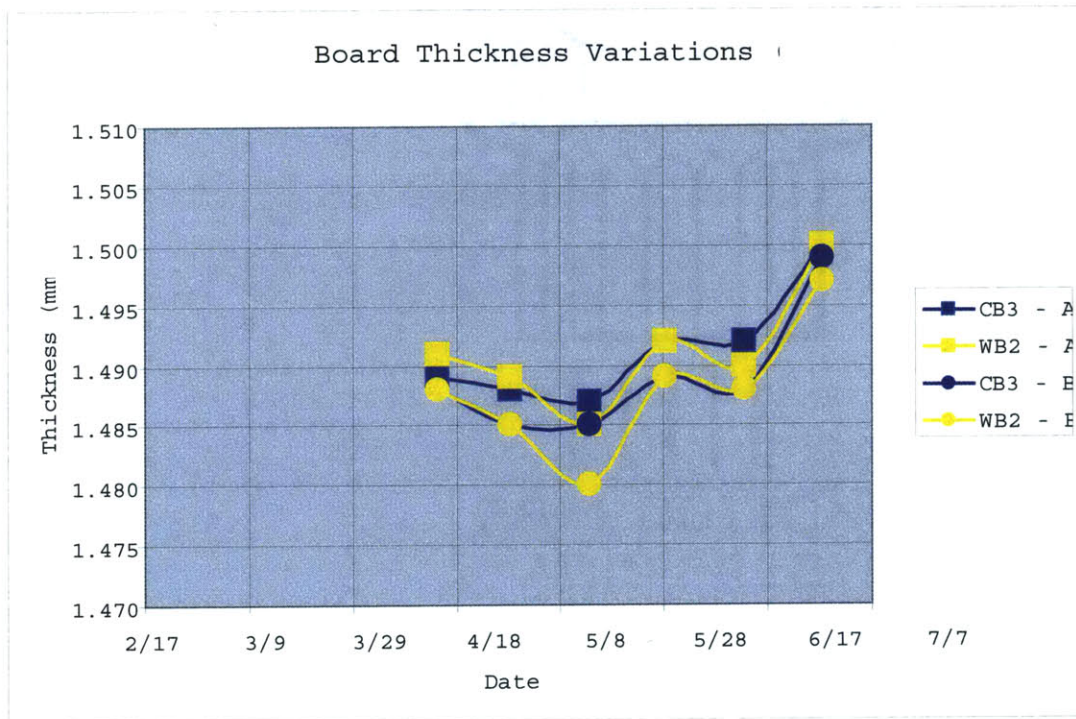


Figure 9.6: Thickness History of WB2 and CB3

9.5 Moisture Diffusion Characteristics

In earlier discussions about moisture diffusion in Chapter 3, it was shown that if we assume Fick's law to be applicable, then we can derive the relationship for concentration of water in the material as well as its integral resulting in the total moisture content. These were given, respectively, by Equations 3.3 and 3.6. However, it was also mentioned that in many polymers due to the dual state of water (bound and unbound), Fick's law may not apply. The difference in the characteristic curves (Moisture content versus square root of time) was illustrated in Figure 3.7.

9.5.1 Fickian Approximations

We will now attempt to see the nature of moisture diffusion for all the test samples at various different conditions by fitting the weight change data to Fick's law through Equation 3.6 for the two parameters of Diffusion Coefficient and Saturation Moisture Content. A non-linear least squares algorithm implemented in MATLAB was used. Shown below in Figures 9.7, 9.8, 9.9, 9.10 and 9.11 are the plots of the data along with the corresponding fits.

The ordinate shows the percentage moisture content which represents the amount of moisture gained from the beginning of that particular test condition on a percent basis. Therefore, the zero on the ordinate does not necessarily indicate the driest weight. Remember, it was evident from Figures 9.3 and 9.4 that each vacuum drying treatment was not able to remove all the moisture gained from the previous step.

Figures 9.7, 9.8, 9.9, 9.10 and 9.11 clearly indicate that the data fit very well and therefore it can be said with confidence that for the time frame of consideration (approximately two weeks), Fick's law is adequate in completely describing moisture diffusion dynamics.

A similar fitting procedure was followed for the desorption process in all the boards and the fits are given in Appendix C.

Additionally, the calculated values of the diffusion coefficient and the saturation moisture content are presented in Tables 9.3 and 9.4.

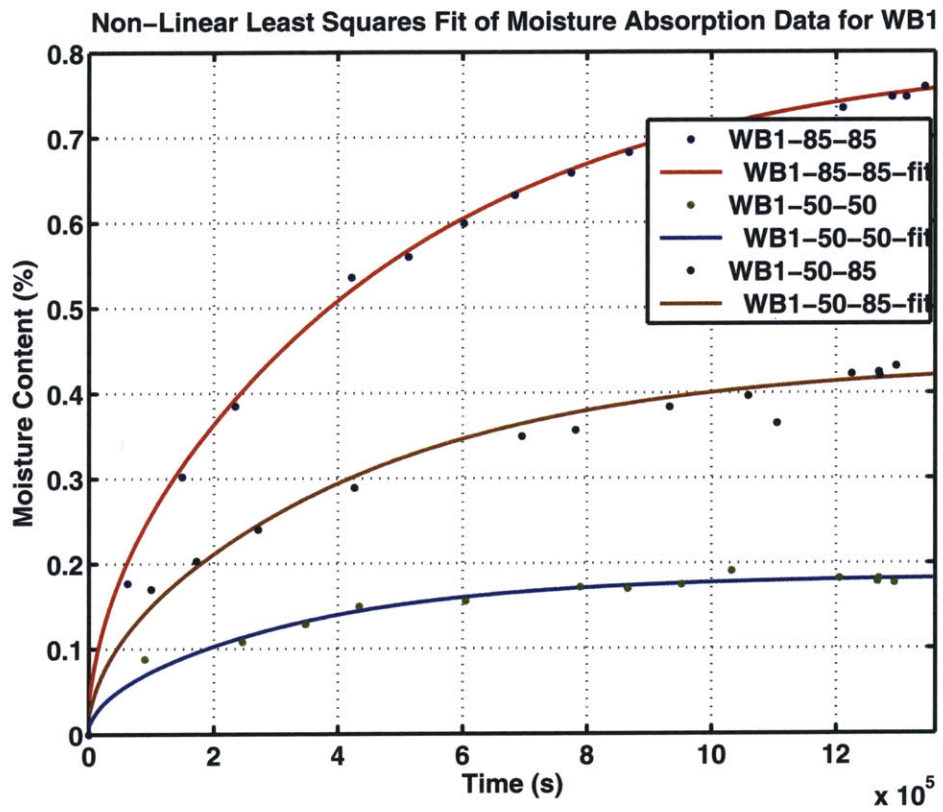


Figure 9.7: Non-Least Squares Fit of Moisture Absorption Data for WB1

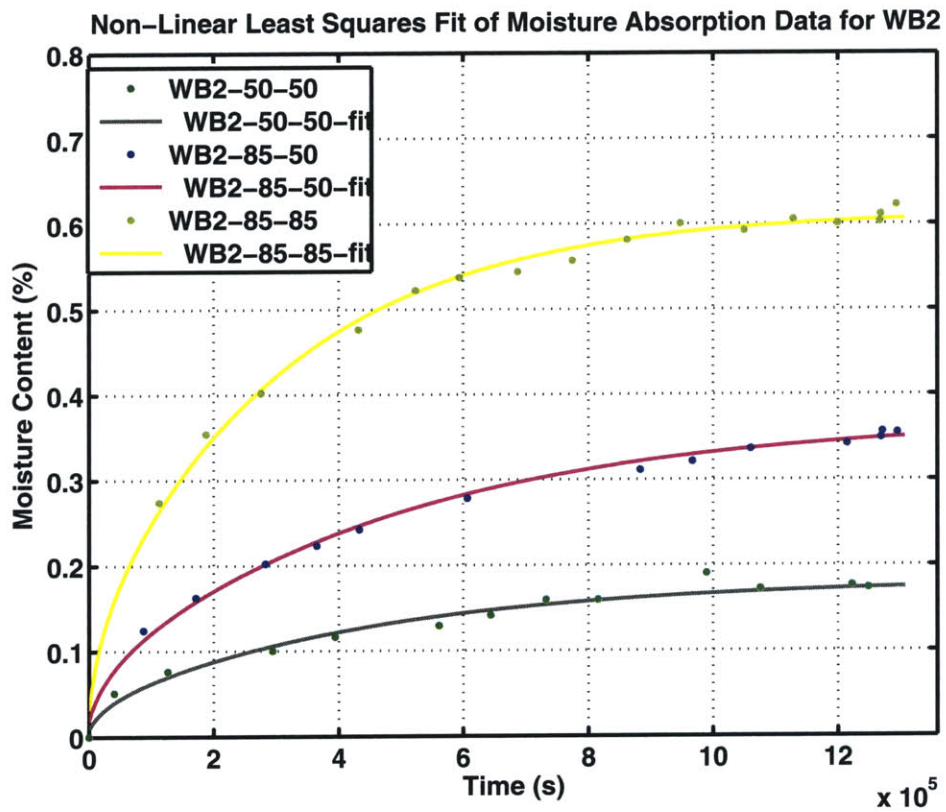


Figure 9.8: Non-Least Squares Fit of Moisture Absorption Data for WB2

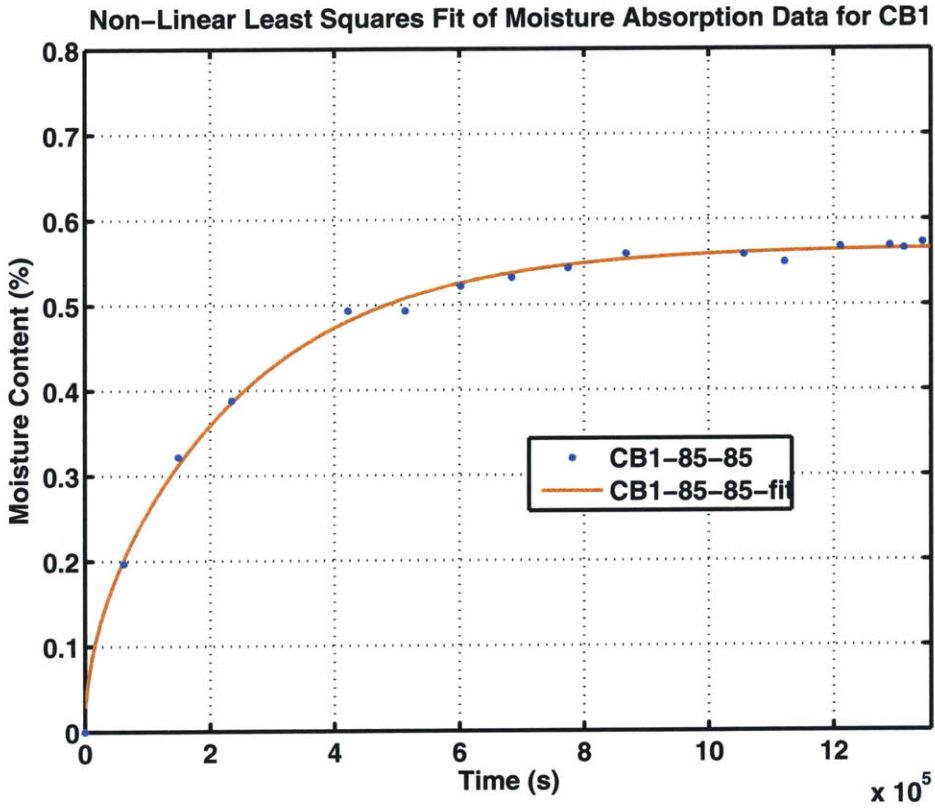


Figure 9.9: Non-Least Squares Fit of Moisture Absorption Data for CB1

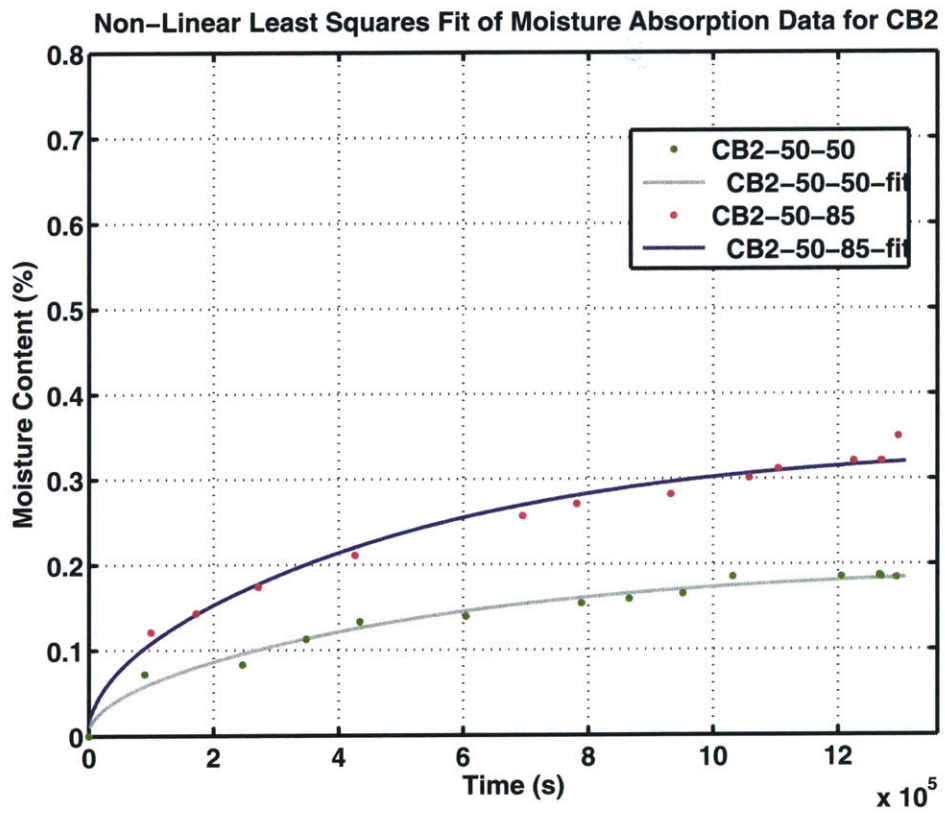


Figure 9.10: Non-Least Squares Fit of Moisture Absorption Data for CB2

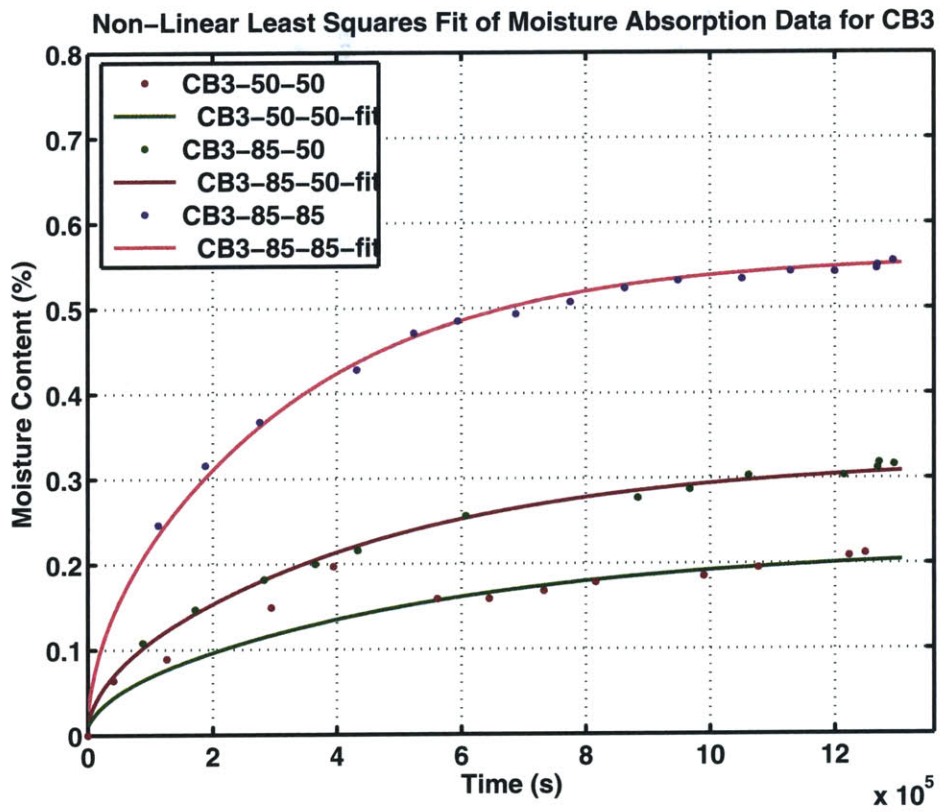


Figure 9.11: Non-Least Squares Fit of Moisture Absorption Data for CB3

9.5 Moisture Diffusion Characteristics

Board	Condition	Diffusion Coefficient, D, (cm^2/s)	Saturation Moisture Gain, M_{∞} , (%)
WB1	85/85	1.13×10^{-9}	0.7994
	50/50	1.7×10^{-9}	0.1851
	50/85	1.256×10^{-9}	0.439
WB2	50/50	1.256×10^{-9}	0.1826
	85/50	1.14×10^{-9}	0.3722
	85/85	1.785×10^{-9}	0.6146
CB1	85/85	2.223×10^{-9}	0.5685
CB2	50/50	1.024×10^{-9}	0.1997
	50/85	1.083×10^{-9}	0.3425
CB3	50/50	1.05×10^{-9}	0.22
	85/50	1.226×10^{-9}	0.324
	85/85	1.684×10^{-9}	0.5615

Table 9.3: Calculated Values of the Diffusion Coefficient and Saturation Moisture during Absorption

Except for WB1, the other boards displayed higher diffusion coefficients at higher temperatures and higher humidity conditions. WB1's anomalous behavior can once again be attributed to the 85°C/85% RH stress at the beginning of the hygrothermal test series.

Board	Vacuum Sequence	Diffusion Coefficient, D , (cm^2/s)	Saturation Moisture Loss, M_{∞} , (%)
WB1	1	1.25×10^{-9}	0.135
	2	0.9069×10^{-9}	0.404
	3	0.8941×10^{-9}	0.2903
	4	0.804×10^{-9}	0.4344
WB2	1	1.5×10^{-9}	0.112
	2	1.397×10^{-9}	0.1527
	3	1.216×10^{-9}	0.195
CB1	1	1.5×10^{-9}	0.06005
CB2	1	0.7064×10^{-9}	0.1087
	2	1.202×10^{-9}	0.1608
	3	0.8112×10^{-9}	0.3179
CB3	1	1.535×10^{-8}	0.04568
	2	1.505×10^{-9}	0.132
	3	1.124×10^{-9}	0.1725

Table 9.4: Calculated Values of the Diffusion Coefficient and Saturation Moisture during Desorption

9.5.2 Theoretical Concentration-Distance Estimates

With these calculated values of diffusion coefficients, we can begin to make estimates as to the depth of penetration of water with respect to time. We have to be very cautious here and it is important to emphasize that we might be falsely assuming uniform diffusion all across the board. In fact our calculation of the diffusion coefficient was based on the integral shown in Equation 3.5 which is an accurate integral. However, in the direction orthogonal to our assumed 1-dimensional diffusion, we assume that concentration is independent of dimensions transverse to the board thickness. Also, in fitting the moisture absorption and desorption data we have used Equation 3.6 which corresponds to the solutions that are computed for long times given by Equation 3.3. Since we do not have sufficient data corresponding to short times, the diffusion coefficient may not be completely accurate in this small time regime. However, in the following discussion we will be making estimates for long times (days and weeks) as well as short times (minutes and hours). Therefore, we will also use the short time Laplace solution given by Equation 3.4 with the diffusion coefficient determined from the long time equations.

To determine the value of the diffusion coefficient, we will take average values for all the conduction boards at a particular hygrothermal condition. We choose the conduction boards because the depth of penetration as a function of time might give us an indication of the impact of moisture (present just below the surface) on surface conductivity. We assume the thickness to remain constant for simplicity and take that value to equal 1.5 mm. We will also assume that initially the board was at zero concentration ($C_0 = 0$).

It is evident from Figures 9.12, 9.13, 9.14 and 9.15 that by about two weeks, the region just below the surface is fairly well saturated. There is also quite a difference between the amount of moisture that penetrates at 85°C/85% RH and at other conditions.

In the next few sections, we will set aside the study of moisture diffusion dynamics and focus on studying and modeling electrical conduction.

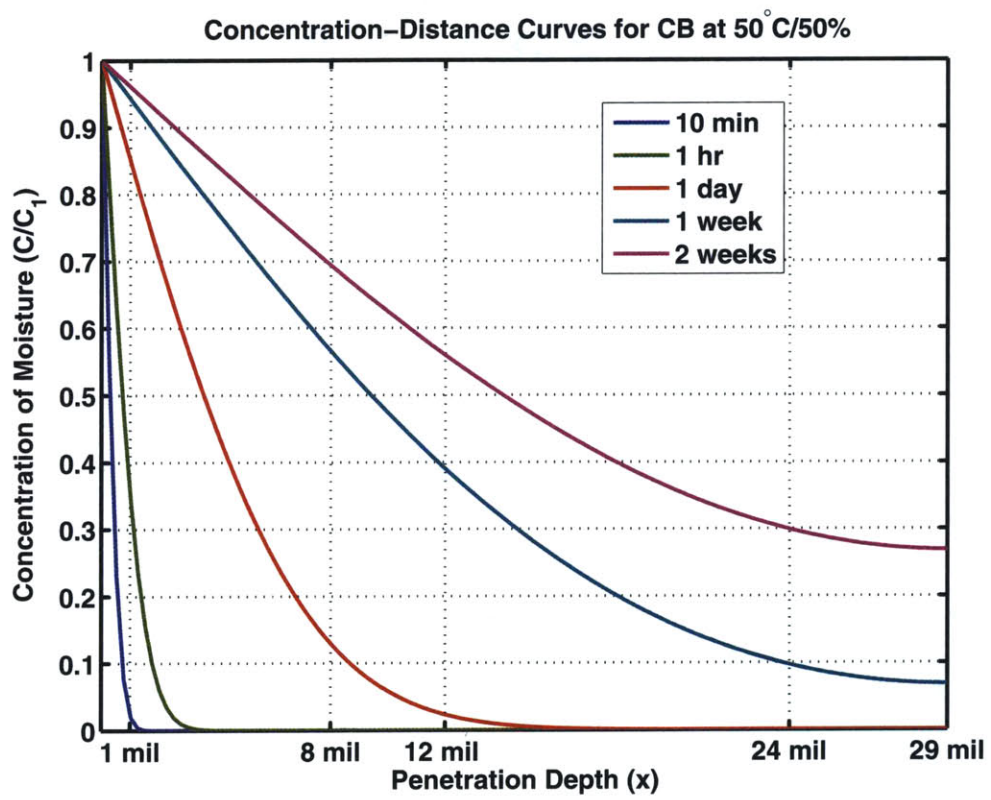


Figure 9.12: Concentration-Distance Curves at 50°C/50% RH

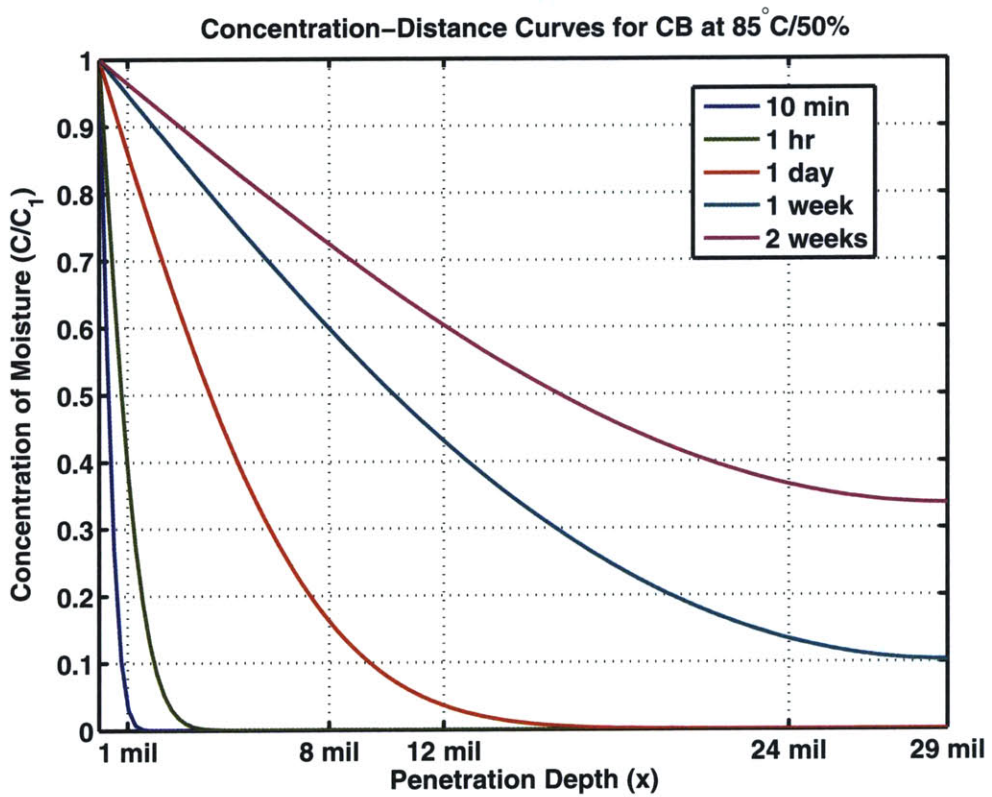


Figure 9.13: Concentration-Distance Curves at 85°C/50% RH

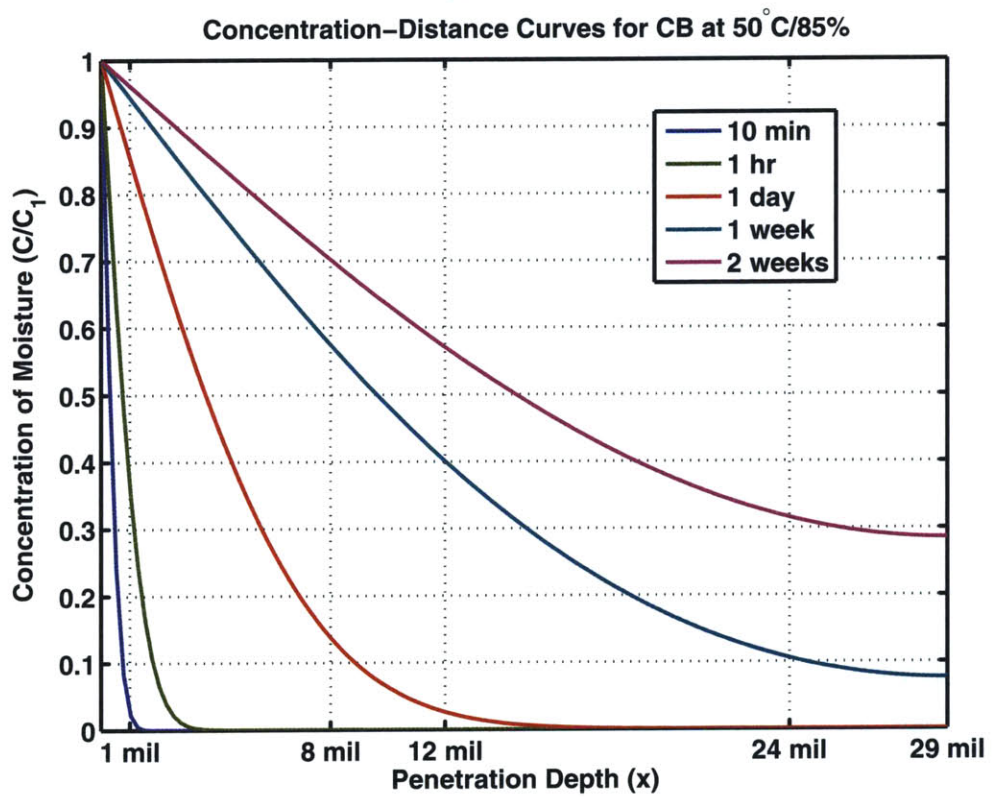


Figure 9.14: Concentration-Distance Curves at 50°C/85% RH

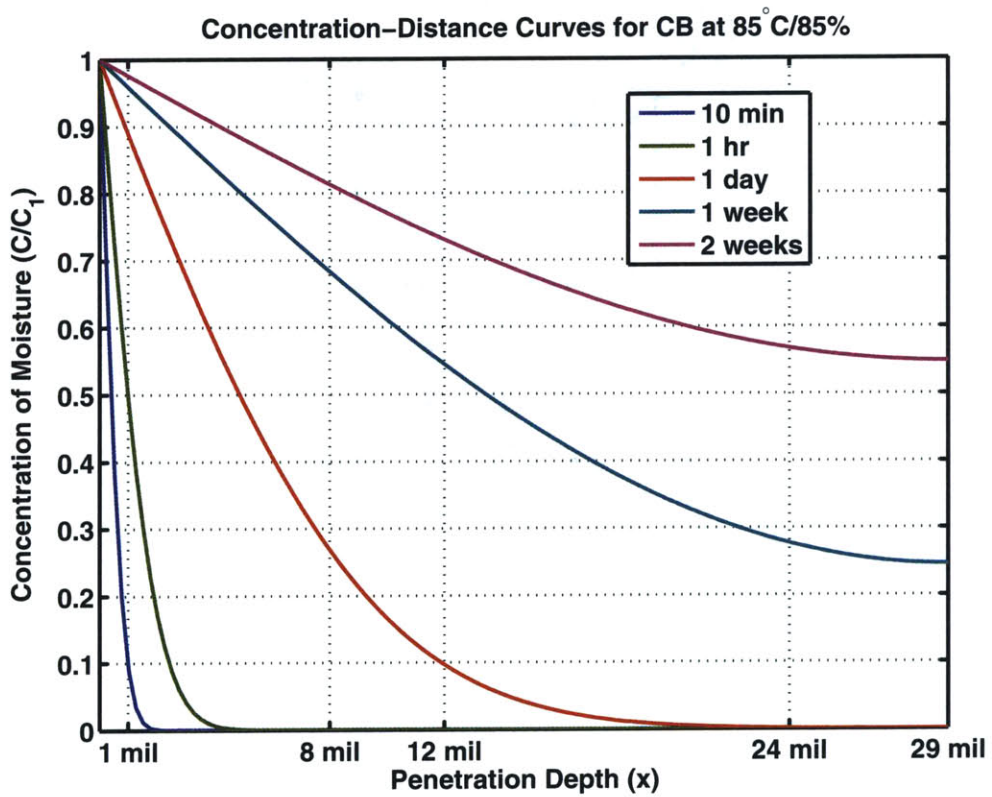


Figure 9.15: Concentration-Distance Curves at 85°C/85% RH

9.6 Electrical Steady State Conduction

9.6.1 General Observations

The leakage current and temperature data obtained during the modified conduction test through the Automated Data Acquisition System (ADAQ) was first converted into a convenient MATLAB data file which would then be used for post-processing and plotting. The “ADAQ Extractor” (given in Appendix D.1) converts the voltage outputs to corresponding current readings and then reformats the data for plotting convenience. Additionally, “Smoothing Data” (given in Appendix D.2) averages this data once again using the averaged downsampling technique presented in Section 7.3.1 so that the plots do not appear too cluttered with data points. In this second stage of averaging, we use a window size (described by Equation 7.1) of 30. Therefore, to summarize, the averaging technique yields 1 data point for every 30s of data. This is different from a moving average filter where we obtain 30 data points for 30s of data.

Shown below in Figures 9.16, 9.17 and 9.18 are the plots of the currents for each of the three conduction boards. It is important to note here that in the remainder of this document all the plots will have the same color scheme. Red refers to the small pattern, green refers to the large pattern and blue refers to the bulk volume pattern.

Looking at Figures 9.16, 9.17 and 9.18, we can make some general observations. Firstly, the leakage currents on all the patterns on all the three conduction boards displayed Arrhenius type relationships with temperature. The activation energies varied across patterns and conditions but were around 1eV. The magnitudes of the currents varied many orders of magnitude. Secondly, under certain conditions, the surface patterns displayed what appears to be two activation energies – one for each above and below $\sim 60^{\circ}\text{C}$. This dual-activation energy phenomena was not observed in the dry state and was also not observed in the volume pattern. Next, when the boards were in their driest states, the volume pattern displayed highest leakage currents. Additionally, the difference between the magnitudes of the volume and the surface pattern (at any temperature) in this dry state was quite small. In more humid conditions this difference increased by a fair amount. In fact, as the moisture levels are increased, the surface patterns begin to display higher and higher leakage currents growing (with moisture) much faster than the currents in the volume pattern. Eventually, at higher humidity and temperature conditions, the surface patterns are about an order of magnitude above the volume pattern. It was encouraging to see that the leakage currents in CB2 and CB3 at $50^{\circ}\text{C}/50\% \text{RH}$ were comparable as was the case with their weight gain at these same conditions.

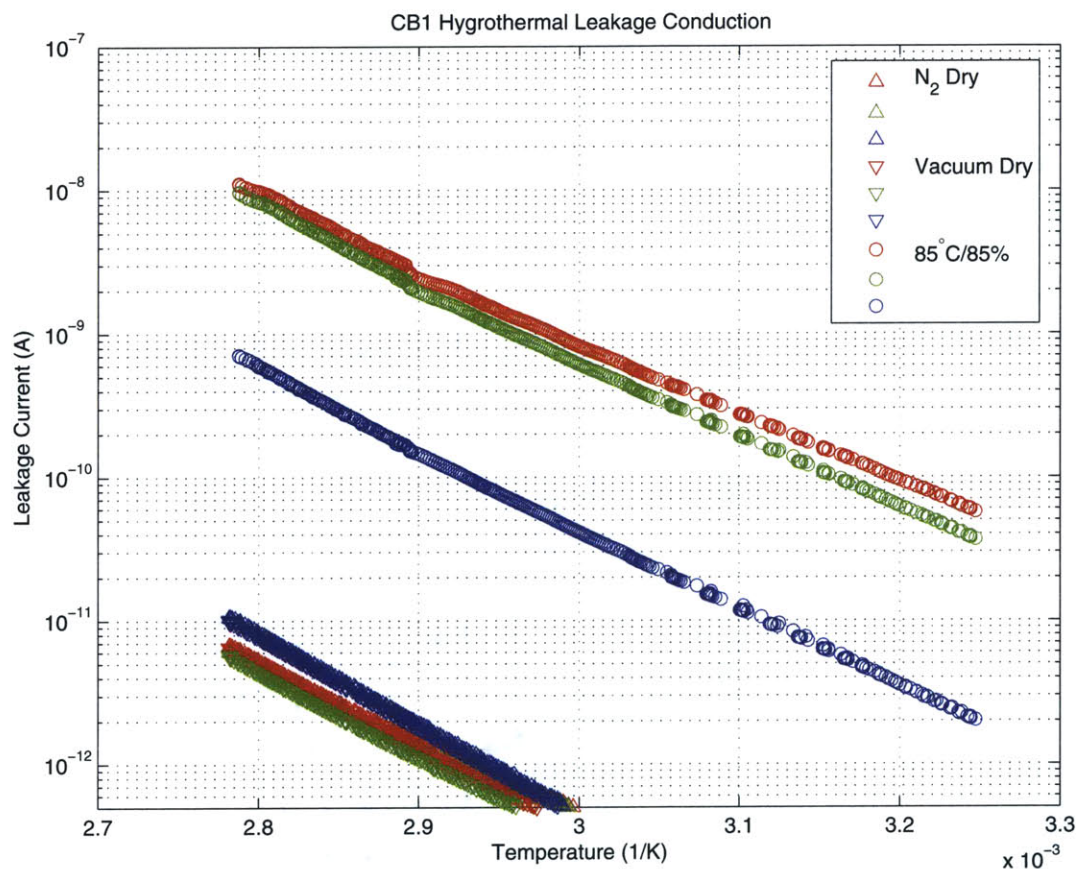


Figure 9.16: Hygrothermal Leakage Conduction in CB1

CB1 was first dried in a chamber at 50°C and purged with N_2 gas. After this initial drying, it was placed in a vacuum chamber and dried further. Figure 9.16 shows us that the leakage currents for all the patterns after N_2 treatment and after the vacuum drying treatment were identical. Figure 9.4 also showed us that there wasn't much of a weight difference between the two drying treatments either. CB1 was probably in its driest state given its age since the remaining water was purely bound and even an extended vacuum treatment was not able to remove it. Furthermore, comparing Figure 9.16 to Figures 9.17 and 9.18, we can see that the dry leakage currents of CB1 were much higher than CB2 or CB3. As a reminder, CB1 had already been treated to a variety of conditions prior to these tests as part of the preliminary experiments. Therefore, CB1 had already absorbed plenty of moisture and other impurities that can contribute to the higher values of leakage currents.

The simplified mathematical expression for conduction can be formulated from the Arrhe-

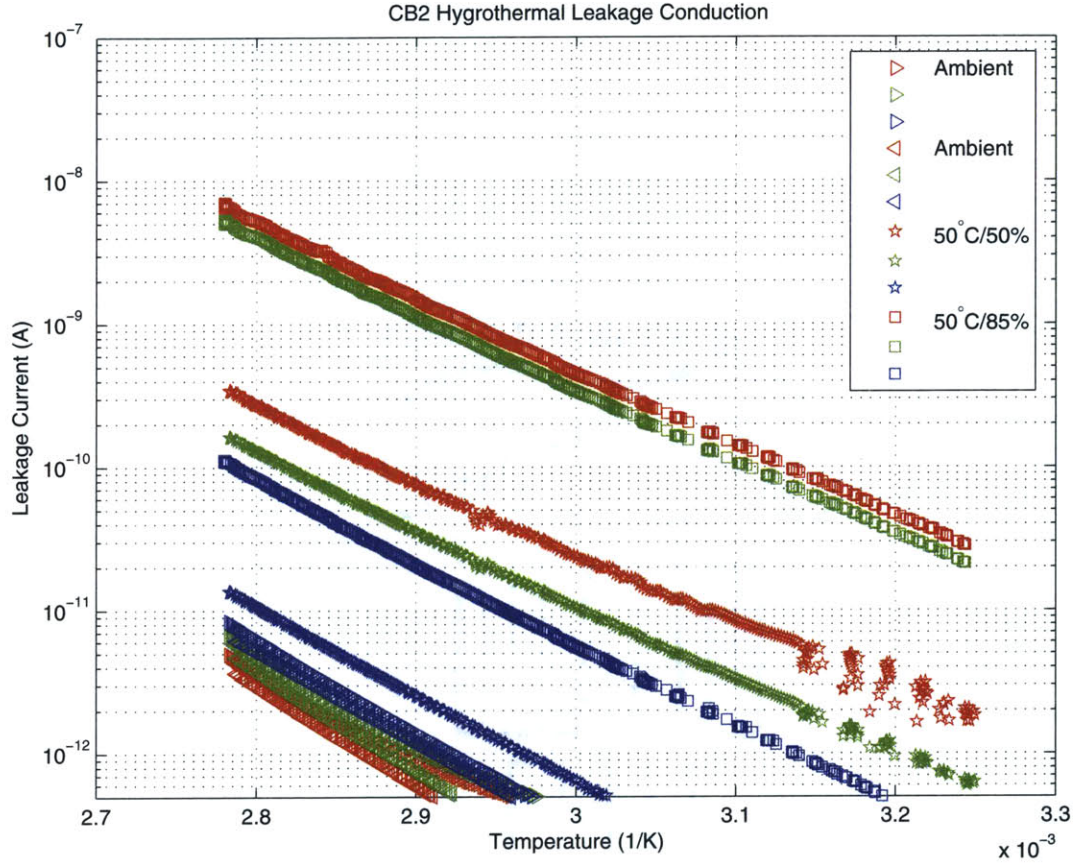


Figure 9.17: Hygrothermal Leakage Conduction in CB2

nius type law that applies to ionic conduction and fits Figures 9.16, 9.17 and 9.18.

$$I \propto I_0 e^{-\frac{E_A}{k_B T}} \quad (9.1)$$

where I is the leakage current, T is the temperature in absolute scale, I_0 is the current at infinitely high temperature, E_A is the activation energy for conduction and k_B is the Boltzmann's constant.

Next, we will analyze each component of this equation more closely and eventually derive a more descriptive equation.

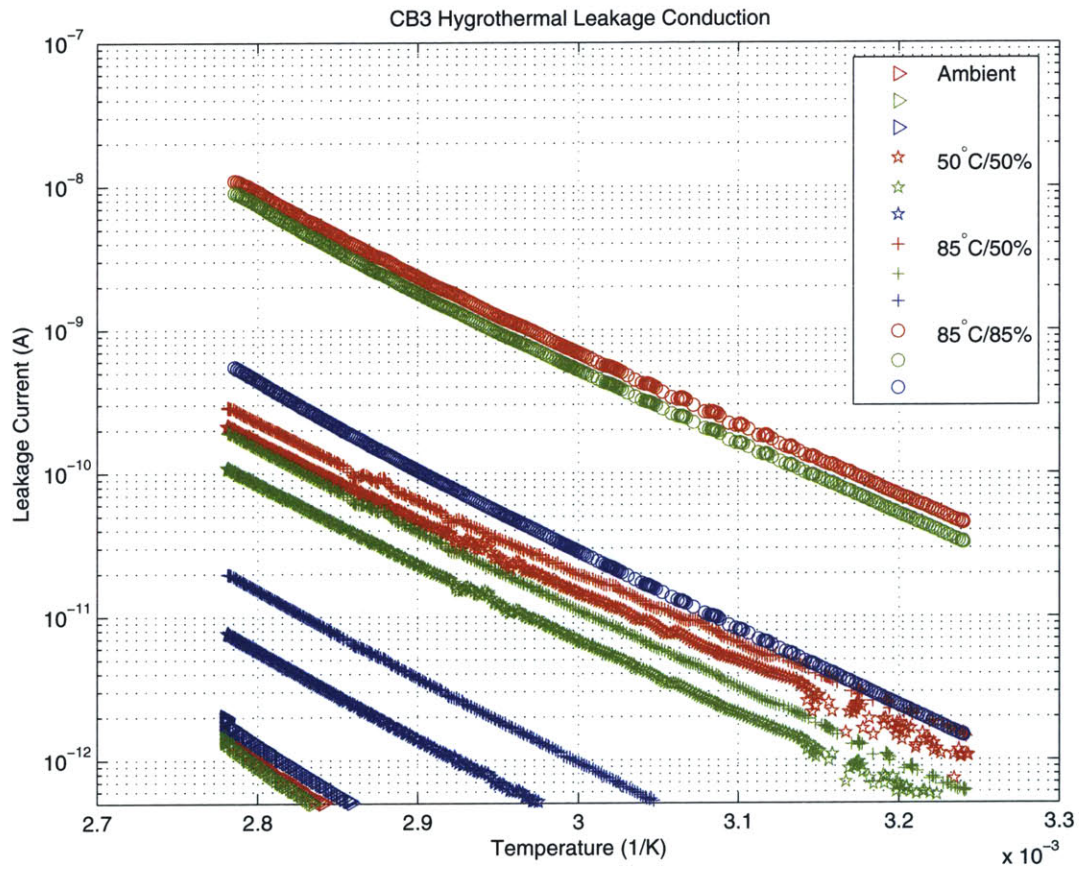


Figure 9.18: Hygrothermal Leakage Conduction in CB3

9.6.2 Quasi-Steady State Currents

The current, I_0 , at infinitely high temperature in the Arrhenius equation, is not very intuitive and instead, we will study the current at 85°C. We will shift the temperature axis and modify the Arrhenius equation as follows:

$$I = I_{85} e^{-\frac{E_A}{k_B} \left[\frac{1}{T} - \frac{1}{358} \right]} \quad (9.2)$$

where, I_{85} represents the current at 85°C and 358 is the Kelvin equivalent of 85°C.

It can be recalled from Section 9.2.1 that after the application of a step voltage at 85°C and either 50% or 85% RH depending on the test, the patterns are energized for about 1 hour before the temperature is gradually brought down from 85°C to 35°C. Therefore, the current, I_{85} is actually the current at a quasi-steady state. Therefore, we will rename the current at 85°C as the *Quasi-Steady State (QSS) current*.

The QSS current is in fact quasi-steady state because the leakage currents reach a visible steady state in this 1 hour time frame. Therefore, a more formal definition of QSS current is that current just prior to the start of the temperature down-ramp in the modified conduction testing scheme after a one hour stabilization at 85°C.

The Modified Arrhenius Equation now becomes:

$$I = I_{QSS} e^{-\frac{E_A}{k_B} \left[\frac{1}{T} - \frac{1}{358} \right]} \quad (9.3)$$

Shown below in Table 9.5 are the calculated values of all the QSS currents for all the boards in all the different conditions based on least squares global curve fit on each board, each pattern and each condition.

9.6.2.1 The Exponential Dependence of I_{QSS} on Moisture

To better understand and interpret the values of this data, we will plot it against both the environmental moisture and the state of the board. The environmental condition that the boards were subjected to prior to the modified conduction test is given by a temperature and relative humidity. We are also interested in moisture and its role in conduction and, therefore, we will additionally use the metric of actual water vapor density or absolute

9.6 Electrical Steady State Conduction

Board	Condition	Small	Large	Volume
CB1	Dry	6.529×10^{-12}	5.763×10^{-12}	10.154×10^{-12}
	85/85	11.132×10^{-9}	9.719×10^{-9}	0.711×10^{-9}
CB2	Dry	3.661×10^{-12}	4.719×10^{-12}	6.181×10^{-12}
	50/50	0.344×10^{-9}	0.163×10^{-9}	0.0136×10^{-9}
	50/85	7.037×10^{-9}	5.369×10^{-9}	0.1132×10^{-9}
CB3	Dry	1.561×10^{-12}	1.515×10^{-12}	2.028×10^{-12}
	50/50	0.2097×10^{-9}	0.1069×10^{-9}	7.632×10^{-12}
	85/50	0.2841×10^{-9}	0.1887×10^{-9}	0.0195×10^{-9}
	85/85	10.932×10^{-9}	9.002×10^{-9}	0.549×10^{-9}

Table 9.5: Calculated Values of Quasi-Steady State (QSS) Current (A)

humidity.

The amount of water that a cubic meter of air can hold is a function of temperature and is given by the empirical fit for saturation vapor density¹ in g/m^3 .

$$V_{sat} = 5.018 + (0.32321) \times T + (8.1847e - 3) \times T^2 + (3.1243e - 4) \times T^3 \quad (9.4)$$

where T is the temperature in degrees Celsius.

The relative humidity, R , is then determined as the percent of this saturation vapor density that is actually present in the environment (V_d).

$$R = \frac{V_d}{V_{sat}} \times 100 \quad (9.5)$$

Therefore, the actual vapor density (V_d) becomes

$$V_d = \frac{R \times V_{sat}}{100} \quad (9.6)$$

The actual water vapor density is, in some sense, a driving force that determines the amount of moisture in the boards. We can now, plot the QSS current versus the actual water vapor density as shown in Figure 9.19. The colors represent the different patterns as before with red for the small pattern, green for the large and blue for the volume.

¹Hyperphysics: <http://hyperphysics.phy-astr.gsu.edu>

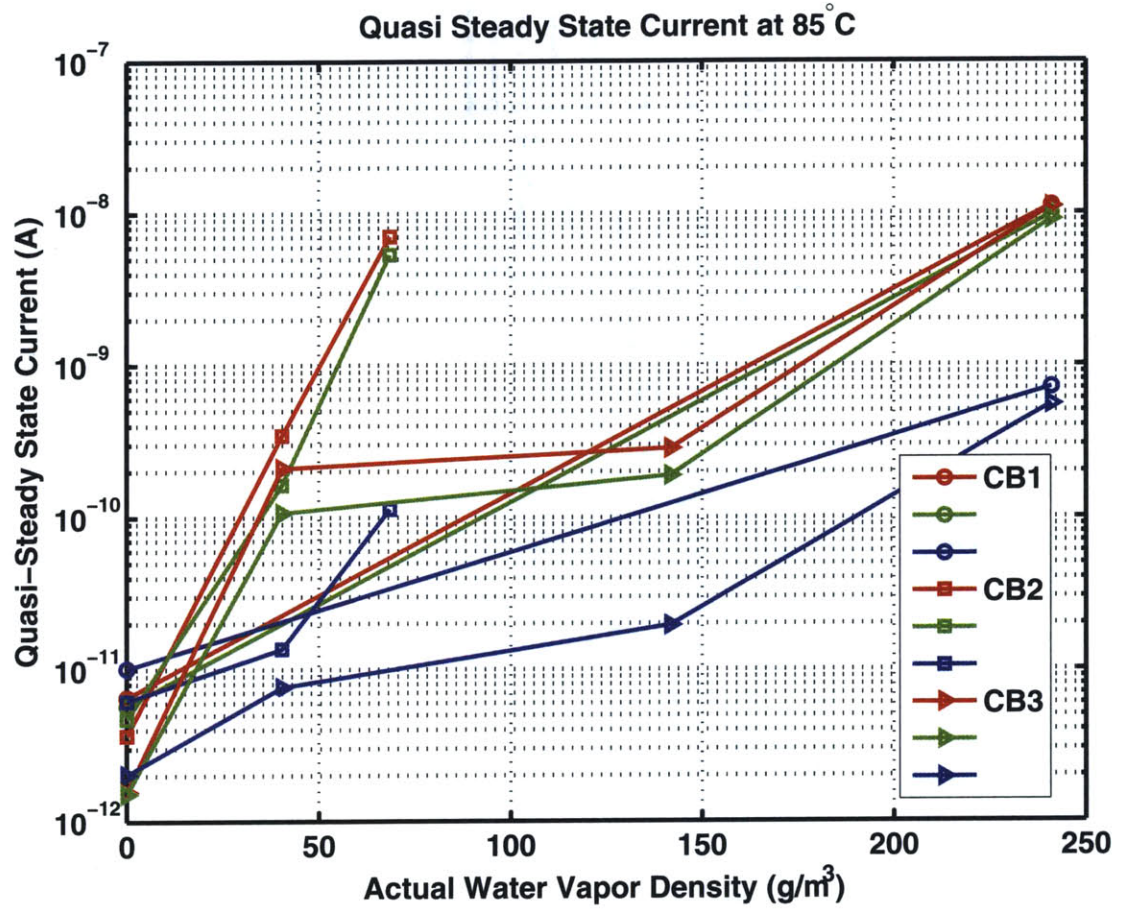


Figure 9.19: Quasi-Steady State Currents measured at 85°C plotted versus actual water vapor density

Even though we have very few data points, it is fairly evident that with an increase in actual water vapor density of the environment, there is an increase in QSS currents and in fact, the range of measured currents span a range of four orders of magnitude. Also, plotted in Figure 9.20 is the variation of the QSS current with the relative humidity.

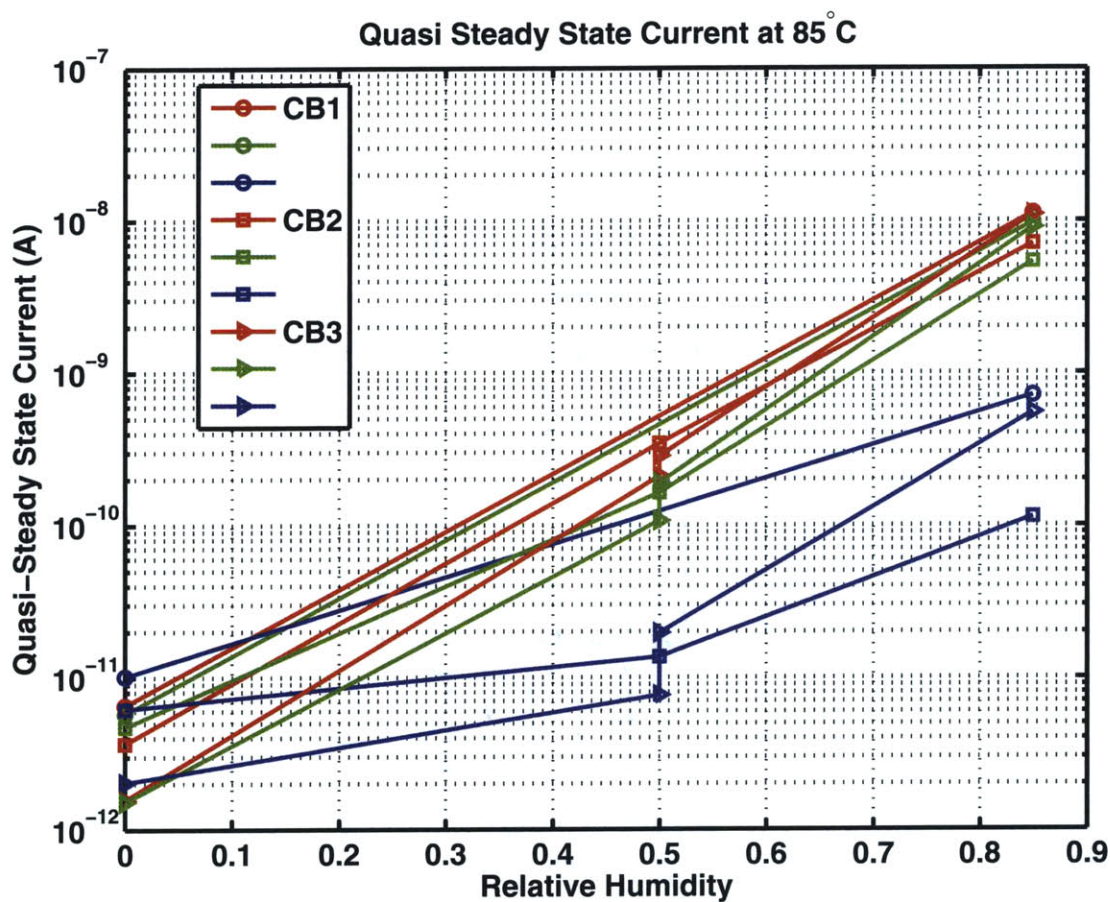


Figure 9.20: Quasi-Steady State Currents measured at 85°C plotted versus relative humidity

Besides the actual water vapor density and relative humidity, we can also study the QSS currents' variation with the weight gain of the boards. This might be more indicative of the effect of absorbed moisture on leakage currents. Shown below in Figure 9.21 is the QSS current plotted against the net weight gain given in Table 9.1.

From Figures 9.19, 9.20 and 9.21 it is clear that there is some kind of an exponential dependency with respect to both the environmental moisture as well as the absorbed moisture quantified as a weight gain percentage. We will soon study the mathematical expressions used to describe these dependencies.

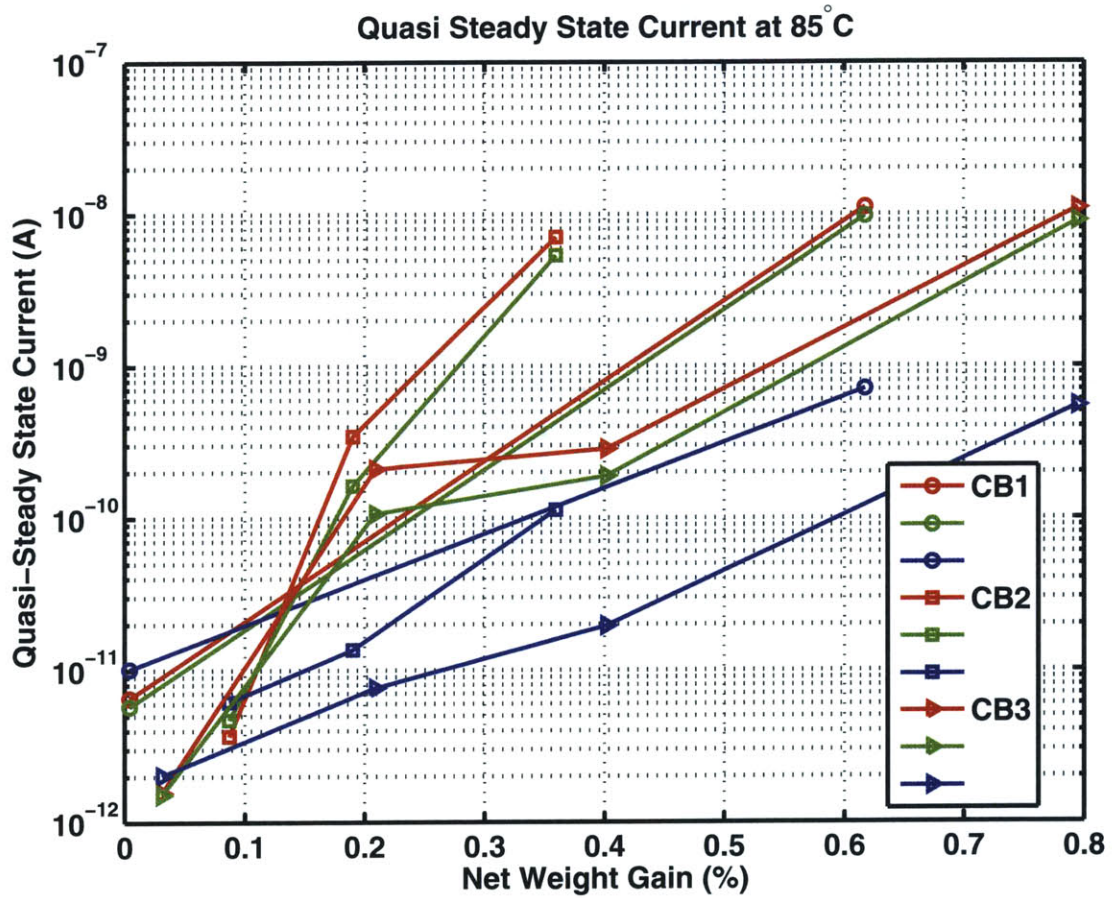


Figure 9.21: Quasi-Steady State Currents measured at 85°C plotted versus net weight gain

9.6.3 Activation Energy

Once again, the modified Arrhenius equation is given as:

$$I = I_{QSS} e^{-\frac{E_A}{k_B} \left[\frac{1}{T} - \frac{1}{353} \right]} \quad (9.7)$$

The other very important quantity in the Arrhenius relationship besides the QSS current is activation energy or potential energy barrier to be overcome to facilitate conduction, E_A . The ion hopping model presented in Section 4.4.3 introduced the concept of activation barrier for ionic conduction and percolation theory later expanded the fundamental meaning of this activation energy in Section 4.4.4. Here we will look at the measured values of the activation energy and understand its variability with moisture content.

It was shown in Figures 9.16, 9.17 and 9.18 that some of the surface patterns seemed display multiple activation energies. Table 9.6 includes all the calculated values of this activation energy for all the patterns when the conduction data was fit to the modified Arrhenius equation using a least squares algorithm.

Board	Condition	Small (60°C)	Small (60°C)	Large (60°C)	Large (60°C)	Volume (60°C)	Volume (60°C)
CB1	Dry	1.241	1.241	1.205	1.205	1.241	1.241
	85/85	0.897	1.166	0.951	1.191	1.159	1.159
CB2	Dry	1.425	1.425	1.391	1.391	1.241	1.241
	50/50	0.906	0.977	0.997	1.068	1.127	1.127
	50/85	1.005	1.054	1.038	1.091	1.117	1.117
CB3	Dry	1.469	1.469	1.446	1.446	1.352	1.352
	50/50	0.9935	0.9935	1.0611	1.0611	1.2074	1.2074
	85/50	0.9747	0.9626	1.077	1.1265	1.2	1.2
	85/85	1.0026	1.207	1.038	1.24	1.0782	1.264

Table 9.6: Calculated Values of the Activation Energy (eV)

9.6.3.1 The Dependence of E_A on Moisture

Just as we did with the QSS current, we can plot the activation energy against the actual vapor density. We will, however, average the high temperature ($> 60^\circ\text{C}$) and the low temperature ($< 60^\circ\text{C}$) activation energies for each pattern.

Figure 9.22 shows this averaged activation energy for all the patterns on all the boards. The colors, as usual, represent the patterns and the markers represent the boards.

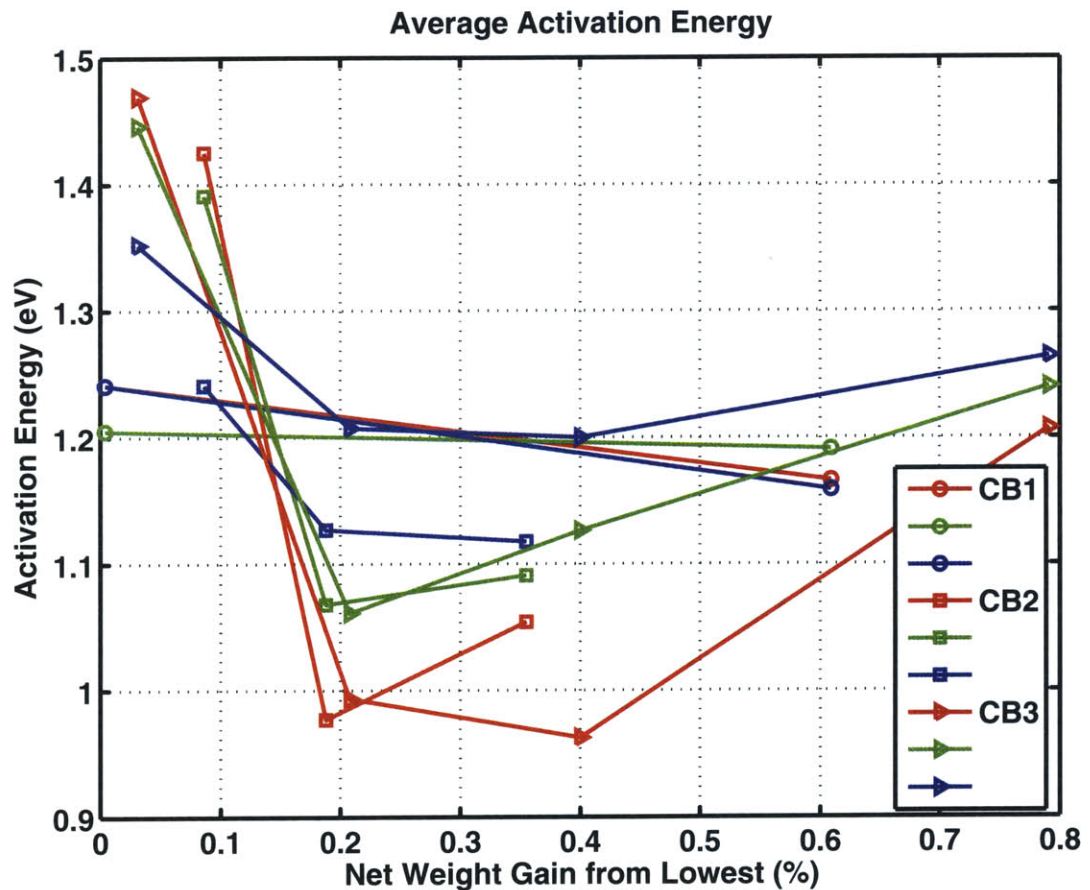


Figure 9.22: Activation Energies measured in eV plotted versus net weight gain

We will use these values to build the mathematical model.

9.7 Mathematical Model for Steady State Conduction

In general we have seen that the conduction plots display a near Arrhenius relationship. The QSS current (intercept) and the activation energy (slope) are influenced by both the atmospheric moisture as well as the absorbed moisture through diffusion.

Before we begin to model the currents, we will clearly define some quantities that will be used in the model.

9.7.1 Absorbed Moisture Density $\tilde{\rho}$

The net weight gain of the sample is in some sense a measure of the amount of moisture absorbed by the sample.

Let w be the measured weight of the sample in grams, g . Then, w_{dry} is the driest measured weight and w_{wet} is the measured weight at a certain time during moisture absorption. Therefore $w_{wet} > w_{dry}$.

We can now define *absorbed moisture density*, $\tilde{\rho}$ (g/mm^3), as follows:

$$\tilde{\rho} = \frac{w_{wet} - w_{dry}}{\bar{V}} \quad (9.8)$$

where \bar{V} is the total volume of the sample in mm^3 .

9.7.2 Exposure Rate \tilde{r}

The next variable we will consider is what we will call here as the *exposure rate*, \tilde{r} . This variable primarily controls surface effects. In our tests we attempt to maintain the relative humidity fairly constant throughout the duration of the test. So, in fact, the exposure rate is simply the relative humidity given by:

$$\tilde{r} = \frac{R}{100} \quad (9.9)$$

where R is the relative humidity in percent.

The relative humidity can be thought of as an exposure rate because it is indicative of molecules of water striking the surface and forming mono-layers.

9.7.3 Simplified First-Order Models

The exponential dependence of QSS currents on the absorbed as well as environmental moisture was discussed earlier. In addition, we also noted the behavior of activation energy with moisture.

We will first model both these effects in two separate schemes and then compare them later.

9.7.3.1 Mass-Based Model (MBM)

The *absorbed moisture density*, $\tilde{\rho}$, is a measure of the mass of water gained by the sample over the course of a fixed period of time.

The QSS current in the *Mass-Based Model* is mathematically expressed as:

$$I_{QSS}^{\tilde{\rho}} = I_{dry} e^{\alpha_{\tilde{\rho}} \tilde{\rho}} \quad (9.10)$$

where I_{dry} is the current when the board is considered to be completely dry.

It was seen in Section 9.6.3 and particularly in Figure 9.22 that as we increase the moisture level, there is an initial drop in activation energy that reaches a steady state once a desired moisture level is crossed.

Therefore, we will analyze this change from the driest state to a moist state. Additionally, from a least squares fit of the data to the Arrhenius type relationship, we will approximate the two activation energies displayed by some surface patterns to one value (Table 9.6).

Mathematically,

$$E_A^{\tilde{\rho}} = -\delta + E_{A,dry} \quad (9.11)$$

where $E_{A,dry}$ is the activation energy when the board is completely dry and δ is the change

(decrease) in activation energy in moist conditions.

9.7.3.2 Exposure-Based Model (EBM)

The moisture conditions that the samples were exposed to is measured by the relative humidity or the previously defined term – Exposure Rate, \tilde{r} .

We can define relationships for the QSS current and the activation energy for this model in much the same way as we did with the MBM.

Therefore the QSS current is given as:

$$I_{QSS}^{\tilde{r}} = I_{dry} e^{\alpha \tilde{r}} \quad (9.12)$$

where I_{dry} is the current when the test environment has very low relative humidity.

The activation energy is once again given as:

$$E_A^{\tilde{r}} = -\delta + E_{A,dry} \quad (9.13)$$

where $E_{A,dry}$ is the activation energy when the test environment has very low relative humidity and δ is the change (decrease) in activation energy in moist environments.

9.7.4 Arrhenius Fit and Parameter Estimation

We can fit the equations from both the MBM and EBM to the QSS currents and the activation energies obtained from the least squares Arrhenius fit. The idea is to obtain one value of α and δ that can be used to characterize our sample boards.

To meet this end, we will first obtain α and δ values for each of the models, for each pattern on each board and at each condition. Then, we will analyze the behavior of α and δ across all the conditions and boards and determine the best choice α and δ for our boards. We will finally, compare our model with observed data for one specific board.

Figures 9.23 – 9.28 show the data and the corresponding least squares fits of each of the

samples at each hygrothermal condition. It should be note that in many of the plots, the data coincides very well with the fitted model thereby obscuring the latter.

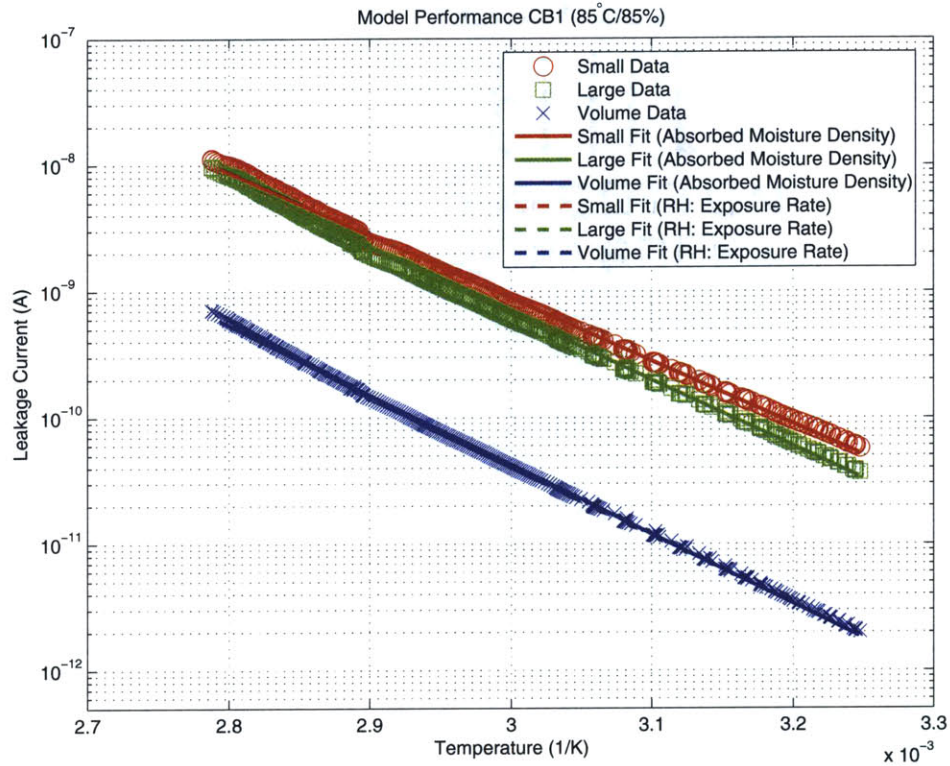


Figure 9.23: CB1 (85°C/85% RH))

Using these curve fits, we calculate the values of QSS current and activation energy.

It is evident that in all the curve fits, both the absorbed moisture density fits and the exposure rate fits coincide. For each hygrothermal test condition, we can calculate the α and δ parameters from the corresponding QSS current and activation energy.

9.7 Mathematical Model for Steady State Conduction

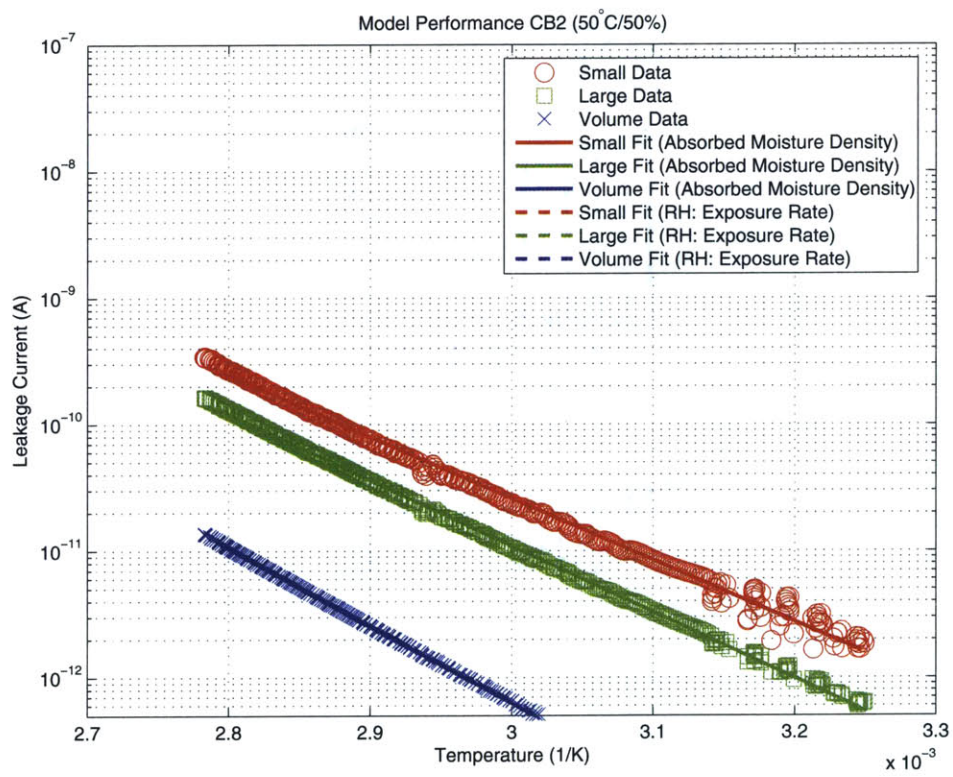


Figure 9.24: CB2 (50°C/50% RH))

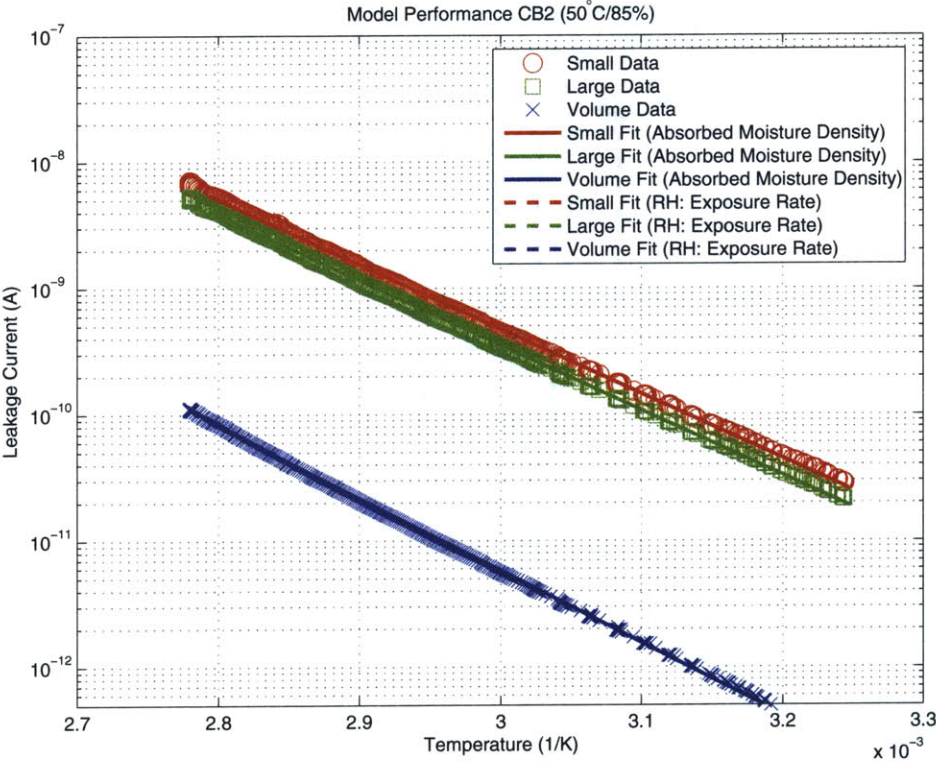


Figure 9.25: CB2 (50°C/85% RH)

9.7 Mathematical Model for Steady State Conduction

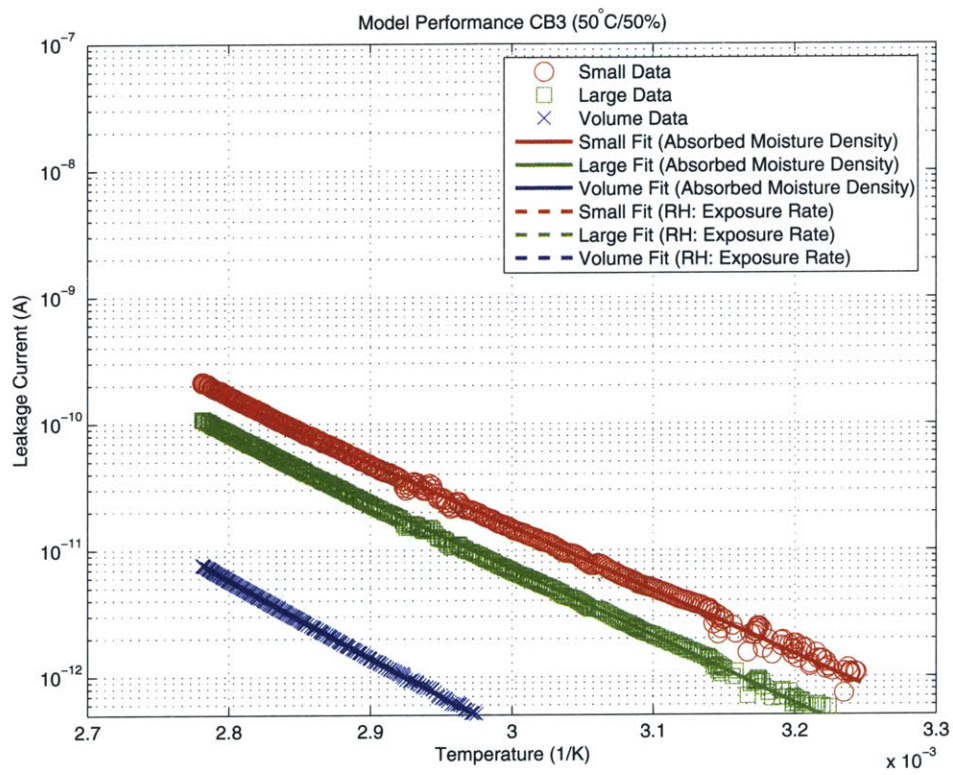


Figure 9.26: CB3 (50°C/50% RH)

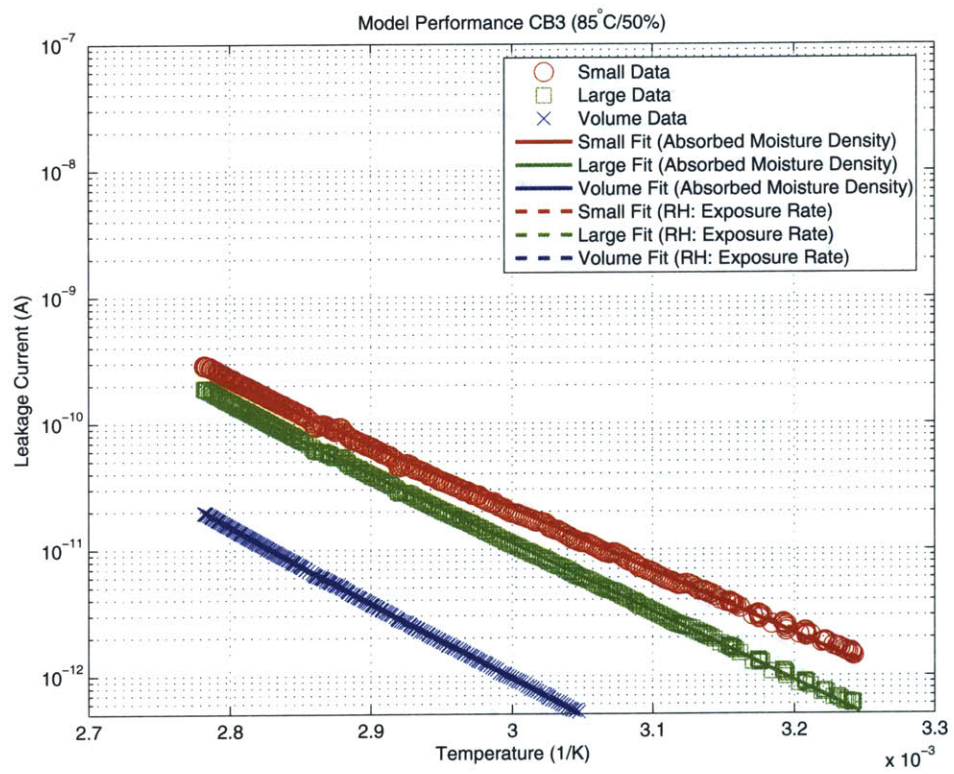


Figure 9.27: CB3 (85°C/50% RH))

9.7 Mathematical Model for Steady State Conduction

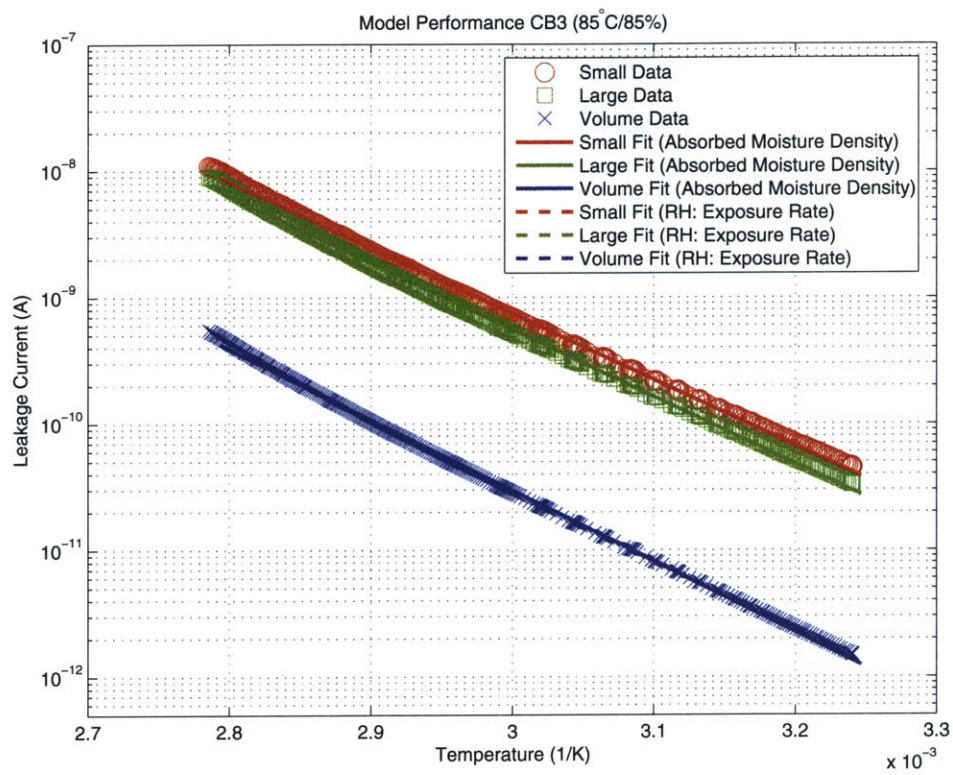


Figure 9.28: CB3 (85°C/85% RH)

9.7.4.1 Estimated α Values for the Exposure-Based Model

Tables 9.7 – 9.9 show the estimated values for α based on the exposure-based model for each board, each pattern and each hygrothermal condition.

	50°C/50%	85°C/50%	50°C/85%	85°C/85%
CB1				8.744
CB2	8.853		8.748	
CB3	9.993	10.69		10.55

Table 9.7: Calculated Values of $\alpha_{\bar{r}}$ for the Small Pattern

	50°C/50%	85°C/50%	50°C/85%	85°C/85%
CB1				8.752
CB2	6.962		8.153	
CB3	8.811	9.892		10.31

Table 9.8: Calculated Values of $\alpha_{\bar{r}}$ for the Large Pattern

	50°C/50%	85°C/50%	50°C/85%	85°C/85%
CB1				4.995
CB2	1.437		3.247	
CB3	2.852	4.764		6.635

Table 9.9: Calculated Values of $\alpha_{\bar{r}}$ for the Volume Pattern

To be able to determine the more suitable model for a specific pattern, the α values have to be fairly constant across all hygrothermal conditions. We can see in Tables 9.7 – 9.9 that there is some variation across conditions as well as across boards. To illustrate this variation, Figure 9.29 shows α from both CB2 and CB3 through all the hygrothermal conditions.

It can be seen in Figure 9.29 that there is comparatively less variation in the small and the large pattern than in the volume pattern. There seems to be a general decrease in value as we move from small to large to volume. Furthermore, the averaged CB2 and CB3 plots are quite parallel indicating that the variation between boards seems fairly constant through all the patterns.

9.7 Mathematical Model for Steady State Conduction

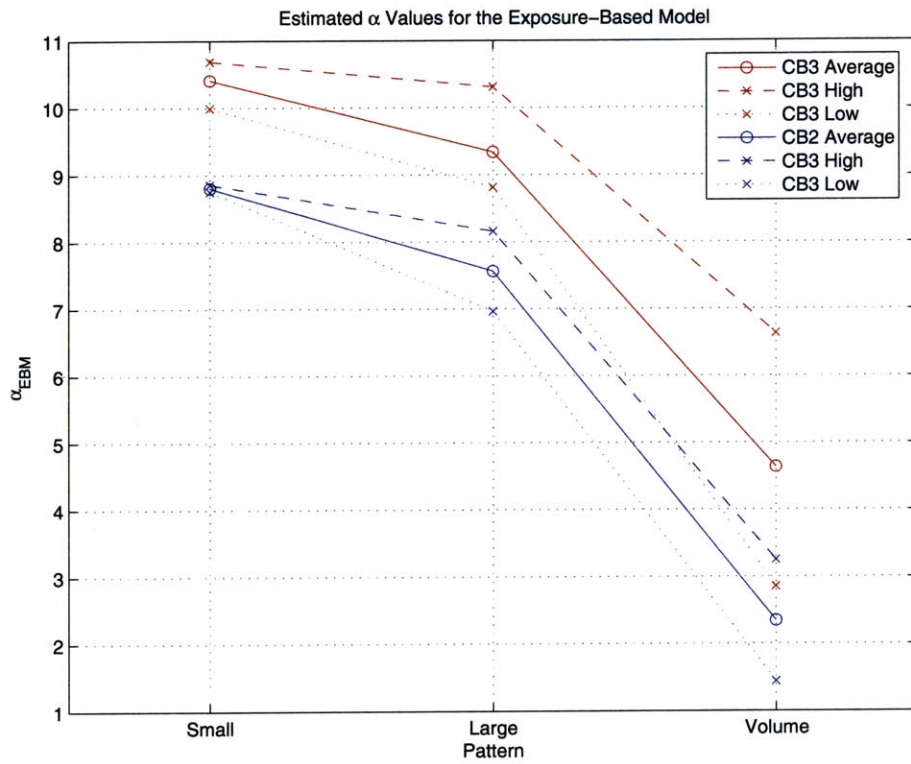


Figure 9.29: Estimated α Values for the Exposure-Based Model

9.7.4.2 Estimated α Values for the Mass-Based Model

Tables 9.10 – 9.12 show the estimated values for α based on the mass-based model for each board, each pattern and each hygrothermal condition.

	50°C/50%	85°C/50%	50°C/85%	85°C/85%
CB1				531000
CB2	1024000		911300	
CB3	1045000	576900		493200

Table 9.10: Calculated Values of $\alpha_{\bar{\rho}}$ for the Small Pattern (mm³/g)

	50°C/50%	85°C/50%	50°C/85%	85°C/85%
CB1				531400
CB2	805500		849300	
CB3	921500	538000		482200

Table 9.11: Calculated Values of $\alpha_{\bar{\rho}}$ for the Large Pattern (mm³/g)

	50°C/50%	85°C/50%	50°C/85%	85°C/85%
CB1				303300
CB2	166300		338300	
CB3	298300	259100		310200

Table 9.12: Calculated Values of $\alpha_{\bar{\rho}}$ for the Volume Pattern (mm³/g)

The α values in the MBM seem to show a wider degree of variation than that of the EBM. We can compare CB2 and CB3 by plotting the averaged values of α . Shown in Figure 9.30 is the plot of α against the pattern for both CB2 and CB3.

In general, we observe a decrease in variation as we move from the small pattern to the large to the volume in CB3. The large pattern in CB2, however, shows a slightly anomalous behavior with a tighter range than the volume.

9.7 Mathematical Model for Steady State Conduction

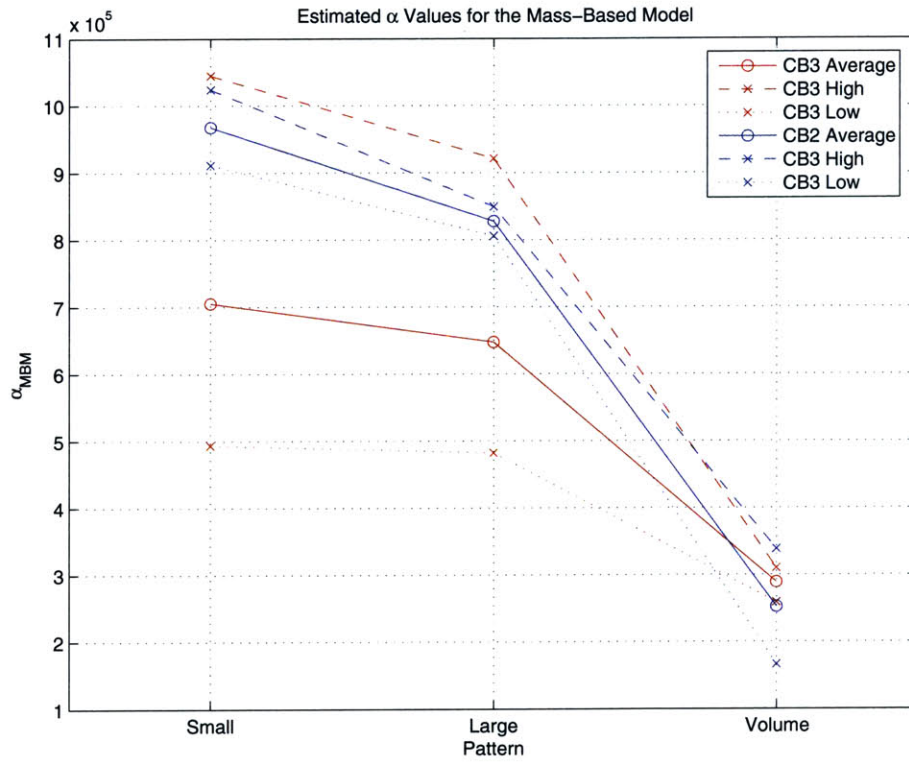


Figure 9.30: Estimated α Values for the Mass-Based Model

9.7.4.3 Estimated δ Values for Either Model

Tables 9.13 – 9.15 show the estimated values for δ for each board, each pattern and each hygrothermal condition. Also shown in these tables are the dry state activation energy, $E_{A,dry}$

	$E_{A,dry}$	50°C/50%	85°C/50%	50°C/85%	85°C/85%
CB1	1.166				0.178
CB2	1.378	0.409		0.361	
CB3	1.559	0.559	0.572		0.523

Table 9.13: Calculated Values of δ for the Small Pattern (eV) along with $E_{A,dry}$

	$E_{A,dry}$	50°C/50%	85°C/50%	50°C/85%	85°C/85%
CB1	1.181				0.141
CB2	1.387	0.350		0.363	
CB3	1.677	0.623	0.594		0.623

Table 9.14: Calculated Values of δ for the Large Pattern (eV) along with $E_{A,dry}$

	$E_{A,dry}$	50°C/50%	85°C/50%	50°C/85%	85°C/85%
CB1	1.255				0.165
CB2	1.260	0.047		0.126	
CB3	1.471	0.256	0.283		0.359

Table 9.15: Calculated Values of δ for the Volume Pattern (eV) along with $E_{A,dry}$

As described earlier, there is a substantial difference between the dry state activation energy and any other hygrothermal state. However, it becomes evident from Tables 9.13 – 9.15 that for a specific board, δ remains fairly constant across all the hygrothermal conditions. This is very useful when we are trying to show the applicability of the model.

9.7.4.4 Summary of α and δ Observations

It was generally observed that the α values based on the EBM for the small and the large patterns had less variations (across the different hygrothermal conditions) than those based on the MBM. However, for the volume pattern there seemed to be less variation in the α obtained using the MBM. There also seemed to be a general decreasing trend from the small pattern to the large pattern to the volume pattern.

The small pattern is largely a surface pattern and is much more influenced by the exposure and environmental conditions because the penetration of the current through the bulk of

9.7 Mathematical Model for Steady State Conduction

material in this pattern is quite small and therefore surface effects dominate. Therefore, it is better modeled with EBM.

Additionally, the relationship between the thickness of the adsorbed layer of water on the surface and the relative humidity is understood with the Brunauer Emmett - Teller (BET) model of adsorption of vapors [57]. In the BET model the first layer of water is bound to the surface with energy E_0 . Subsequent layers of water molecules bind to the underlying molecules with the energy E which is identical to the energy of evaporation.

A relationship for the average number of monolayers can be derived and is shown below in Equation 9.14.

$$N = \frac{\tilde{r} e^{(E_0-E)/k_B T}}{(1 - \tilde{r}) [1 + \tilde{r}(e^{(E_0-E)/k_B T} - 1)]} \quad (9.14)$$

However, for many moderately absorbing surfaces like FR4, the water adsorption energy is close to that of heat of water condensation and $E_0 = E$. Therefore, Equation 9.14 simplifies to a relation that is independent of temperature given by Equation 9.15.

$$N = \frac{\tilde{r}}{1 - \tilde{r}} \quad (9.15)$$

Therefore, the observed relationship between surface currents and relative humidity could in fact be linked to the formation of monolayers of water on the surface.

On the other hand, the volume pattern is better modeled with the MBM because current flowing through the interior portions of the material are more influenced by absorbed moisture than the surrounding atmosphere especially since moisture diffusion itself is a slow and time-consuming process. The large pattern falls in between the small and the volume in that even though there is a strong dependence on the environmental conditions and exposure rate, it is also impacted by the absorbed moisture. Consequently, even though the EBM might be the better model, the MBM might also be important. This became clear with the anomalous behavior observed in the α value of the large pattern in CB2 in Figure 9.30.

Therefore, it might be possible to postulate here that the α from the small pattern might be suitable reference values for the EBM. While, on the other hand, the α from the volume pattern might be a suitable reference value for the MBM.

An average can be taken on a per board, per pattern basis and is shown below in Table

The Hygrothermal Test Plan

	Small (EBM)	Large (EBM)	Volume (MBM)
CB1	8.744	8.752	303300
CB2	8.800	7.558	252300
CB3	10.411	9.671	289200

Table 9.16: Average Values of α for Each Pattern

We can now also calculate the average values for δ for each pattern on each board. This is shown in Table 9.17.

	Small	Large	Volume
CB1	0.178	0.141	0.165
CB2	0.385	0.357	0.086
CB3	0.551	0.613	0.299

Table 9.17: Average Values of δ for Each Pattern

We can see that moisture has an effect in reducing the activation barrier height. This was evident from the decrease in activation energy from the driest state to any of the other more moist conditions. This reduction of barrier height comes at moderate amount of moisture and then there is no further change even if more moisture is added to the system. In a certain sense moisture behaves a catalyst in reducing activation energy, however, increasing the quantity of the catalyst does not keep decreasing this activation barrier height

9.7.5 Performance of First-Order Model

We will now look compare the First-Order Model with the actual data for one of the boards to evaluate its performance.

The model we will be using for the surface patterns (small and the large) is the First-Order Exposure-Based Model which is mathematically given by,

$$I = I_{dry} \exp\{-\alpha\tilde{r}\} \exp\left\{-\frac{(-\delta + E_{A,dry})}{K_B} \left[\frac{1}{T} - \frac{1}{358}\right]\right\} \quad (9.16)$$

where α and δ values are specified for the small and the large pattern separately in Table 9.16 and 9.17.

Also, the model we will use for the volume pattern is the First-Order Mass-Based Model which is given mathematically as,

9.7 Mathematical Model for Steady State Conduction

$$I = I_{dry} \exp\{-\alpha\tilde{\rho}\} \exp\left\{-\frac{(-\delta + E_{A,dry})}{K_B} \left[\frac{1}{T} - \frac{1}{358}\right]\right\} \quad (9.17)$$

where α and δ values are specified for the volume pattern in Table 9.16 and 9.17.

We will be only considering CB3 and therefore, we will use it's corresponding average values for α and δ .

Figures 9.31 – 9.33 show the performance of the first-order model with data.

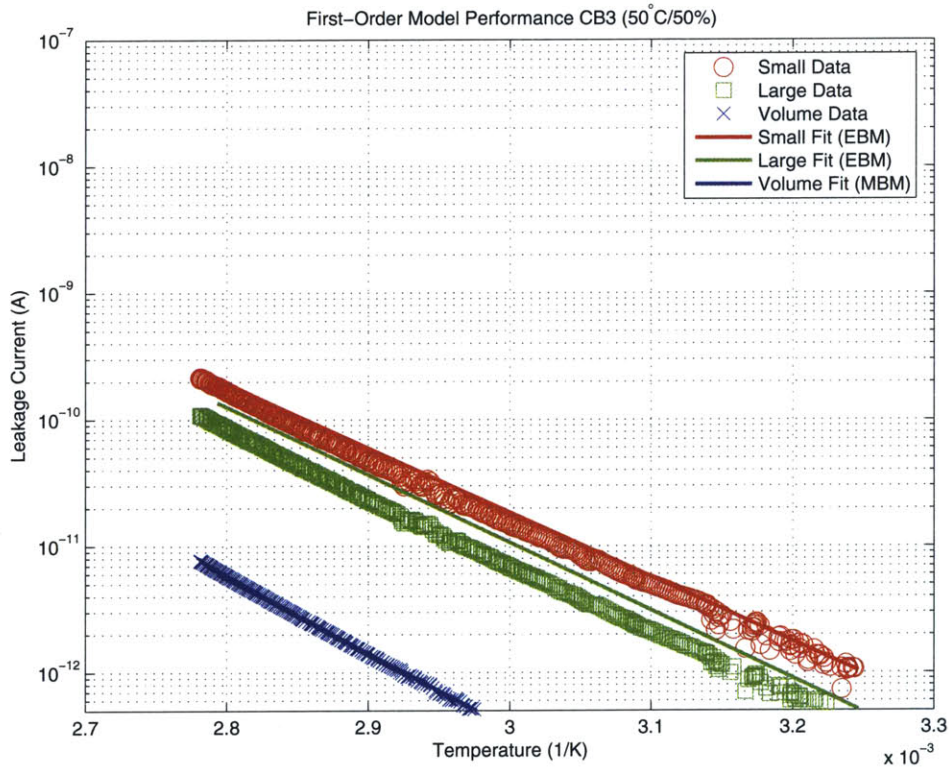


Figure 9.31: Performance of the First-Order Model on CB3 (50°C/50%)

Overall, the fits seemed to be quite acceptable. The exposure-based model seemed to fit well with the small pattern in all the moisture conditions. The mass-based model seemed to also work well with the volume pattern. There was, however, some observed deviation in the large pattern. This deviation could be due to the fact that the exposure-based model is probably not sufficient in estimating currents in the large pattern. The large pattern may additionally be influenced by absorbed moisture and therefore a mass based model may also

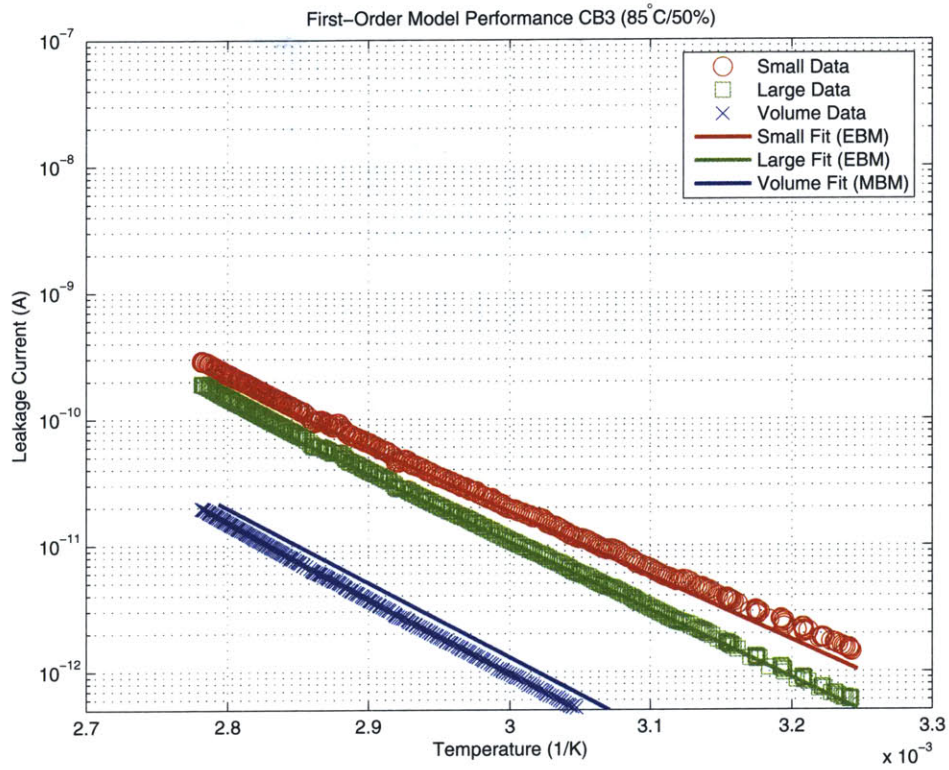


Figure 9.32: Performance of the First-Order Model on CB3 (85°C/50%)

be needed. This observation was also touched upon in Section 9.7.4.4.

9.7 Mathematical Model for Steady State Conduction

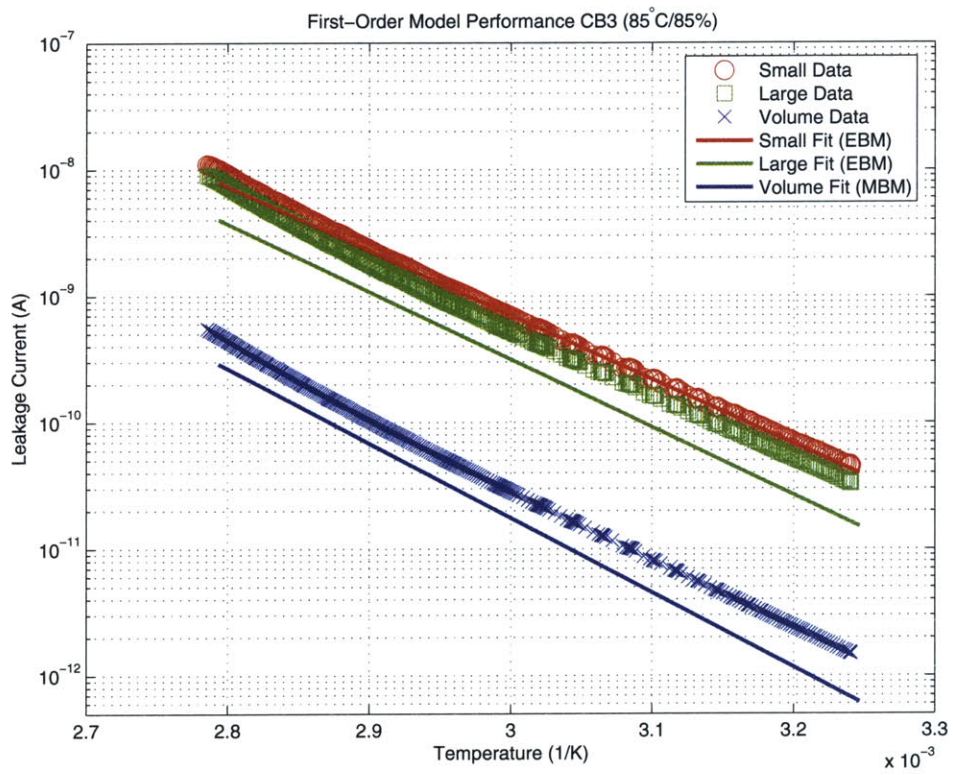


Figure 9.33: Performance of the First-Order Model on CB3 (85°C/85%)

9.7.6 Adjustments for Geometric Scaling

We will now attempt to quantify the differences observed in conduction between the small and the large surface pattern. We have seen that the currents in both the surface patterns seem to show similar moisture dependencies. This might open up the possibility for using one parametric value to represent the geometry that could then be used to appropriately scale the current data for different surface patterns.

Shown below are the geometric variables for both the surface comb patterns. In parentheses are the variable names used in Section 5.2.1 and Appendix A to describe the pattern geometry.

Surface Comb Patterns:

g (X_1)	Dielectric gap
n (N)	Number of fingers
l_f (L_f)	Active length per finger
c (X_2)	Conductor trace width per finger
ϵ	Depth of penetration of current
a_{cross}	Total cross section area of pattern

We can now derive some simple quantities:

Total cross section area:

$$a_{cross} = (n - 1)l_f\epsilon \quad (9.18)$$

We know that that typically the electrical conductance, G , is directly proportional to the cross-sectional area, a_{cross} and inversely proportional to the distance between the conductors through which current flows, s .

$$G \propto \frac{a_{cross}}{s} \quad (9.19)$$

$$G = \sigma \frac{a_{cross}}{s} \quad (9.20)$$

where σ is the conductivity of the material.

For the comb patterns, we can derive a simple equation for conductance based on the above relations.

$$G = \sigma \frac{l_f \epsilon}{g + c} (n - 1) \quad (9.21)$$

This relation is illustrated in Figure 9.34 where the length between the conductors ($s = g + c$).

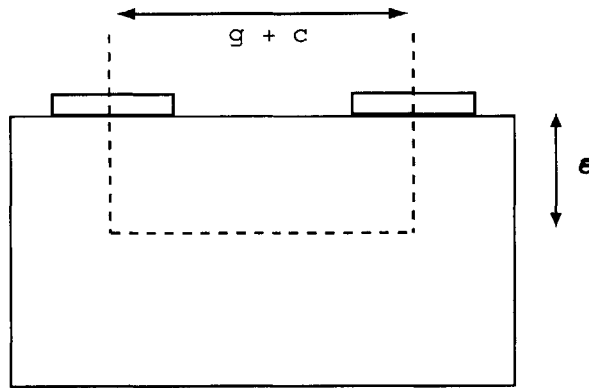


Figure 9.34: Cross Section of the Test Sample with Marked Dimensions

9.7.6.1 Depth of Penetration Estimate Based on Dielectric Gap

If we let the penetration depth, ϵ , equal the dielectric gap, then:

$$G = \sigma \frac{l_f g}{g + c} (n - 1) \quad (9.22)$$

Since we are assuming a consistent ohmic relationship to exist, we can say that the current is given by,

$$I = VG \quad (9.23)$$

$$I = V\sigma \frac{l_f g}{g + c} (n - 1) \quad (9.24)$$

The Hygrothermal Test Plan

Shown in Table 9.18 are the dimensions of the small and large patterns (also given in Section 5.3) along with the calculated value of the geometric parameter.

	Small Pattern	Large Pattern
g	0.008" (0.2032 mm)	0.024" (0.6096 mm)
c	0.008" (0.2032 mm)	0.012" (0.3048 mm)
ϵ	0.008" (0.2032 mm)	0.024" (0.6096 mm)
n	35	35
l_f	0.652" (16.561 mm)	0.652" (16.561 mm)
G/σ	11.084" (281.537 mm)	14.778" (375.378 mm)

Table 9.18: Pattern Dimensions with the $\epsilon = g$

If we take the ratio of the small and the large currents, we can see that:

$$\frac{I_S}{I_L} = \frac{\sigma \frac{l_f c_S}{g_S + c_S} (n-1)}{\sigma \frac{l_f c_L}{g_L + c_L} (n-1)} \quad (9.25)$$

Here, the subscripts S and L are used to refer to the small and the large pattern respectively.

Simplifying and calculating for our test samples based on the values from Table 9.18,

$$\frac{I_S}{I_L} = \frac{g_S(g_L + c_L)}{g_L(g_S + c_S)} = 0.75 \quad (9.26)$$

This ratio clearly contradicts our observed data for almost all the hygrothermal conditions for all the boards. It was observed that in almost all cases, the currents in the small pattern were greater than the currents in the large pattern. However, our estimates based on the above calculations seem to indicate otherwise.

9.7.6.2 Depth of Penetration Estimate Based on Conductor Trace Width

Due to the inability of the dielectric gap based geometric scaling model to predict surface currents, we revised the model to instead let the penetration depth, ϵ equal the conductor trace width. Therefore,

9.7 Mathematical Model for Steady State Conduction

$$G = \sigma \frac{l_f c}{g + c} (n - 1) \quad (9.27)$$

and,

$$I = V\sigma \frac{l_f c}{g + c} (n - 1) \quad (9.28)$$

Shown in Table 9.19 are the dimensions of the small and large patterns (also given in Section 5.3) along with the calculated value of the geometric parameter.

	Small Pattern	Large Pattern
g	0.008" (0.2032 mm)	0.024" (0.6096 mm)
c	0.008" (0.2032 mm)	0.012" (0.3048 mm)
ϵ	0.008" (0.2032 mm)	0.012" (0.3048 mm)
n	35	35
l_f	0.652" (16.561 mm)	0.652" (16.561 mm)
G/σ	11.084" (281.537 mm)	7.389" (187.691 mm)

Table 9.19: Pattern Dimensions

If we take the ratio of the small and the large currents, we can see that:

$$\frac{I_S}{I_L} = \frac{\sigma \frac{l_f c_S}{g_S + c_S} (n - 1)}{\sigma \frac{l_f c_L}{g_L + c_L} (n - 1)} \quad (9.29)$$

Here, the subscripts S and L are used to refer to the small and the large pattern respectively.

Simplifying and calculating for our test samples based on the values from Table 9.19,

$$\frac{I_S}{I_L} = \frac{c_S(g_L + c_L)}{c_L(g_S + c_S)} = 1.5 \quad (9.30)$$

This model seems to predict the observed higher currents in the small pattern. Now we can look at the ratio of the QSS currents in the small pattern to that of the large pattern in our experiments. Table 9.20 shows these values for all the boards at all the different test conditions.

The Hygrothermal Test Plan

	Dry	50°C/50%	85°C/50%	50°C/85%	85°C/85%	Average Value
CB1	1.177				1.169	1.173
CB2	0.794	2.044		1.317		1.385
CB3	1.048	1.892	1.499		1.280	1.430

Table 9.20: Ratio of Small QSS Current to Large QSS Current

It seems that based on the average values in Table 9.20 that the suggested model for geometric scaling specified by Equation 9.28 is quite close to the observed data across all the hygrothermal conditions.

It is clear that the depth of penetration seems to play an important role in modeling surface geometry and therefore more investigations are required before this variable can be understood.

9.7.6.3 Geometric Scaling for the Volume Pattern

A similar relationship can be derived for the volume pattern. However, we currently do not have enough data to test this model.

Bulk Circular Disc Pattern:

d	Thickness of the sample
r	Radius of the conducting plate
a_{cross}	Total cross section area

$$a_{cross} = \pi r^2 \tag{9.31}$$

and,

$$G = \sigma \frac{\pi r^2}{d} \tag{9.32}$$

Therefore,

$$I = V \sigma \frac{\pi r^2}{d} \tag{9.33}$$

9.7.7 Universal Scaled First-Order Model for Surface and Bulk Conduction

9.7.7.1 Surface Conduction

Combining the Arrhenius temperature relation with the exposure-based model and the corresponding surface geometric scaling (Equation 9.28), we get:

$$I = \sigma_{0,dry} V \frac{l_f c}{g + c} (n - 1) \exp\{-\alpha \bar{r}\} \exp\left\{-\frac{(-\delta + E_{A,dry})}{k_B} \left[\frac{1}{T} - \frac{1}{358}\right]\right\} \quad (9.34)$$

where $\sigma_{0,dry}$ is the dry state surface conductivity and α and δ values are specified for the small and the large pattern separately in Table 9.16 and 9.17.

9.7.7.2 Volume (Bulk) Conduction

We will combine the Arrhenius temperature relation with the mass-based model and the corresponding geometric scaling (Equation 9.33) to get,

$$I = \sigma_{0,dry} V \frac{\pi r^2}{d} \exp\{-\alpha \bar{\rho}\} \exp\left\{-\frac{(-\delta + E_{A,dry})}{k_B} \left[\frac{1}{T} - \frac{1}{358}\right]\right\} \quad (9.35)$$

where $\sigma_{0,dry}$ is the dry state bulk conductivity and α and δ values are specified for the small and the large pattern separately in Table 9.16 and 9.17.

9.7.8 Effects of Aging

We will now look at CB1 which had undergone extensive previous aging of over 100 days at different conditions of temperature and humidity and was therefore more aged than CB2 or CB3.

We will first use the average α and δ values obtained from CB3 (Tables 9.16 and 9.17) to model the performance of CB1 at 85°C/85% conditions. We choose CB3 as our model basis because firstly we have obtained more data points from it compared to CB2. Additionally, both CB3 and CB1 were exposed to the 85°C/85% condition.

Also, when discussing the variation of activation energy with moisture and relative humidity, we hypothesized that beyond a certain threshold, these activation energies are assumed to be constant. Therefore, we can test this hypothesis on CB1 and assume that it has been exposed to sufficient moisture conditions to cross this threshold and therefore, $\delta \approx 0$. In effect, even in the so-called vacuum dry state of CB1 there is more moisture than the dry states of CB2 and CB3.

Figure 9.35 shows the original CB1 data for all the three patterns at 85°C/85% along with both the averaged CB3 model as well as the CB3 model with $\delta = 0$ for all the patterns.

It is evident that the model derived from CB3 in dotted lines predicts higher currents than what is actually observed for both the surface patterns on CB1. On the other hand, this model did well in predicting the currents for the volume pattern. However, there was quite a discrepancy between the predicted activation energies and the observed data.

When δ was set to zero, this deviation in activation energy was corrected, to a large extent, in both surface patterns as indicated by the solid lines. This shows that our initial hypothesis of constant activation energies above a certain moisture level might in fact be a good one and that CB1 has crossed this threshold state resulting in no change in activation energy ($\delta = 0$) between the presumed dry condition and 85°C/85%. The activation energy on the volume pattern also appears to have changed towards the data.

9.7.9 Limitations of the First-Order Model

The model described thus far has helped shed some light on the basic differences between the surface and bulk conduction mechanisms. We could also see some subtle difference between the small and large pattern that could possibly be due to geometric scaling factor.

9.7 Mathematical Model for Steady State Conduction

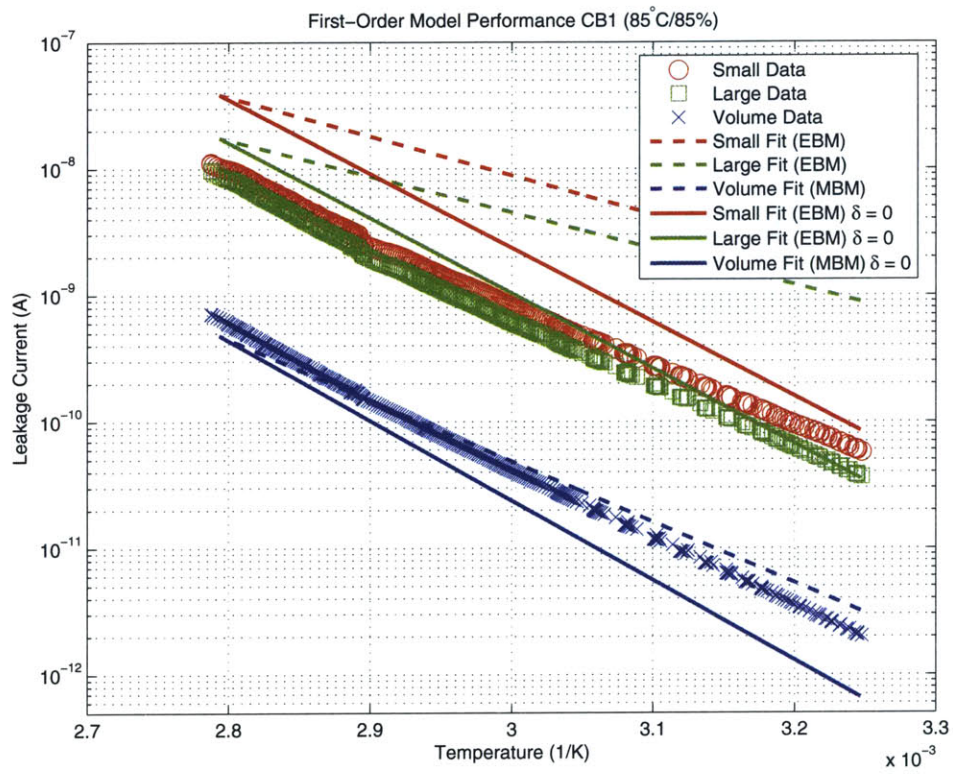


Figure 9.35: Performance of Model on CB1 (85°C/85% RH))

The Hygrothermal Test Plan

However, it is only a first-order approximation and clearly has many limitations. Firstly, the conduction is not perfectly Arrhenius. There was experimental evidence for dual activation energies under certain conditions. Therefore, there could be some second order effects that are ignored for simplicity. In this first-order model, we have separately modeled the effects of an environmental exposure and absorbed moisture. However, the performance of the model against the large pattern indicated that both the environmental exposure and the absorbed moisture can jointly impact conduction. In summary, the first-order model provides a good starting point for understanding conduction in insulators, however, further refinements and extensions are required to increase its usefulness.

9.8 Electrical Transient Conduction

Having studied steady state currents, we will now look at the transient responses. Both dipole orientation and charge hopping mechanisms were described in Section 4.5 as means to explain what happens at the instant a step voltage is turned on. We were able to measure this transient response for the boards on the application of the 100V DC voltage as per the modified conduction test shown in Figure 9.2.

Shown below in Figure 9.36 are the responses of the leakage current to a step voltage at various different environmental conditions. The data is plotted on a log-log scale to emphasize the universal power law response.

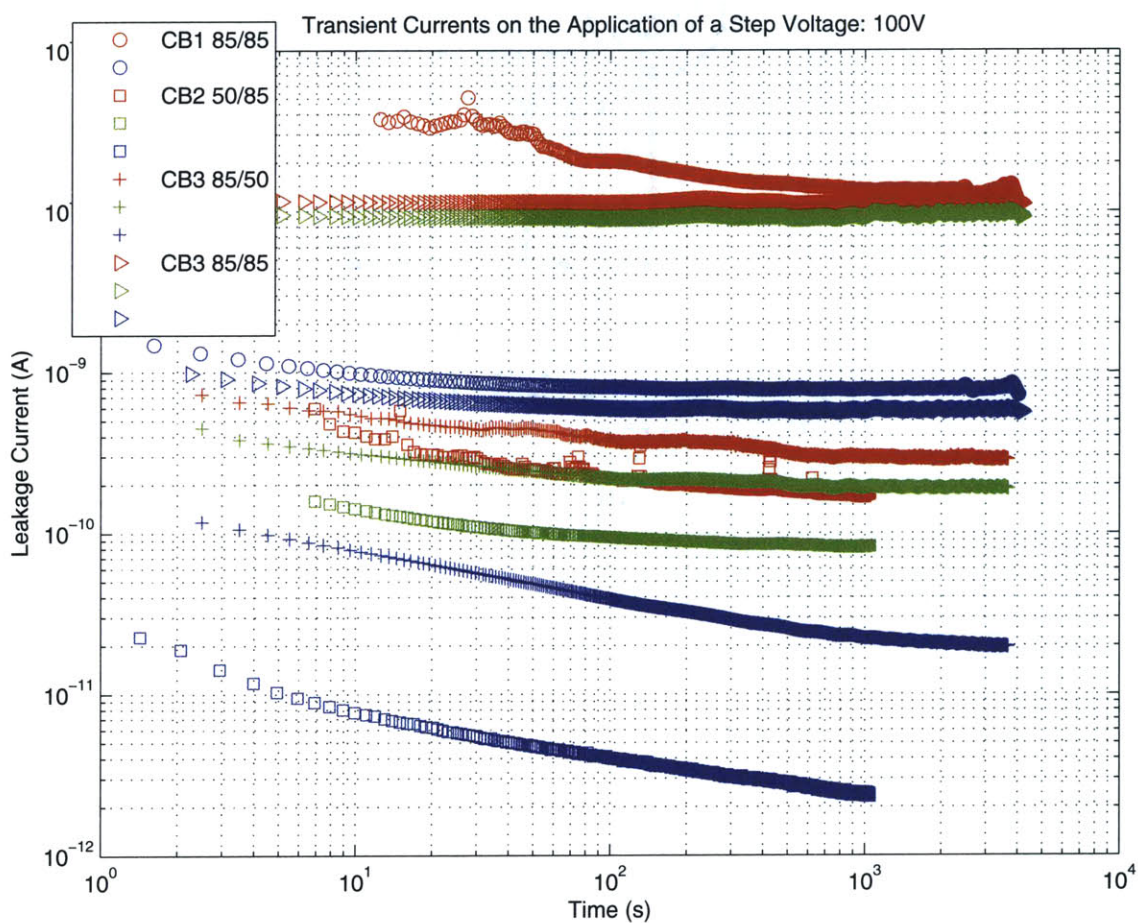


Figure 9.36: Transient (Absorption) Currents when a step voltage of 100V is applied

The Hygrothermal Test Plan

In Section 4.5 it was pointed out that at very small times, there is a universal power law response which makes it quite impossible to differentiate dipole orientation from charge transport. However, after a certain length of time the magnitude of the exponent in the power law changes. If dipole orientation was the only mechanism present, then the magnitude of the exponent would increase and cause the current to fall towards zero (total charge will converge). This is physically intuitive because once the dipole have re-aligned in the direction of the electric field then there is no more measured current. However, if a charge transport mechanism also existed, then at long times the magnitude of the power in the power law expression would in fact decrease. This was explained by Jonscher as the Low frequency dispersion phenomena. This is also physically intuitive because as long as there are mobile charges present, conduction will go on ad infinitum and the integral of the current will diverge.

From just looking at Figure 9.36, it is very obvious that a dual-power law relationship exists where for short times it is given by the Curie-Von Schweidler Power Law whereas for long times, it is explained by the Jonscher Low Frequency Dispersion (LFD) (Discussed in Section 4.5). Table 9.21 lists all the exponents and the time constant for LFD at various hygrothermal conditions.

Board	Pattern	n_1 : Universal Power Law	n_2 : Low Frequency Dispersion	$\tau(s)$
CB1 85/85	Small	0.280	0.114	300
	Volume	0.240	0.009	15
CB2 50/85	Small	0.437	0.111	50
	Large	0.309	0.042	50
	Volume	0.638	0.236	10
CB3 85/50	Small	0.188	0.033	250
	Large	0.161	0.006	200
	Volume	0.298	0.086	500
CB3 85/85	Volume	0.207	0.024	30

Table 9.21: The Least Squares Fitted Parameters for the Universal Curie-Von Schweidler Power Law and the Jonscher Low Frequency Dispersion Power Law

9.9 Visual Observations about Second Generation Test Samples

In this final section we will look at the photographs of all the five test samples. The copper on CB3 (shown in Figure 9.41) was the least oxidized indicating that it might have been exposed to the mildest conditions. It can be inferred that the 85°C/85% RH condition was able to produce the most damage in terms of copper oxidation which is clearly evident from all the samples that were subjected to the 85°C/85% RH condition.

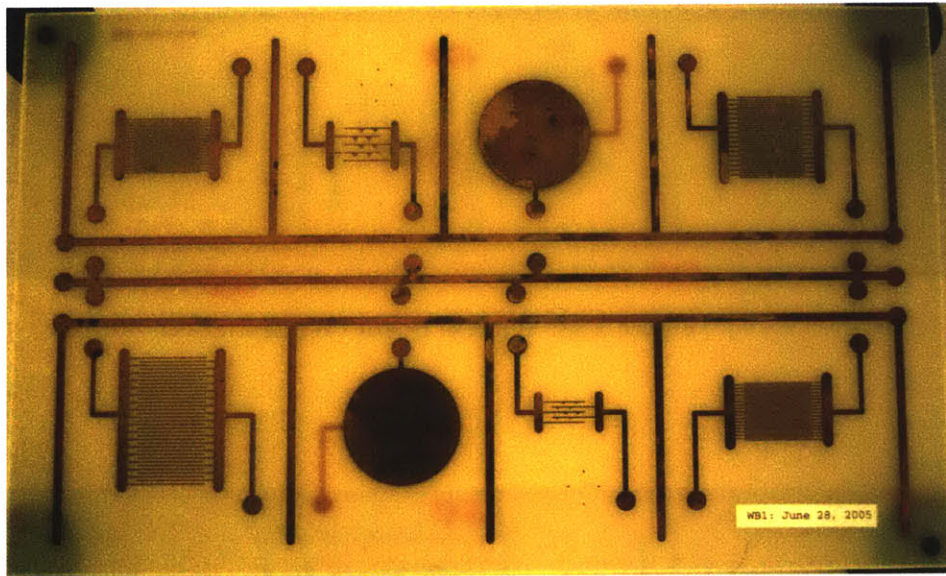


Figure 9.37: Witness Board (WB1)

This concludes the analysis of all the experimental results from both the first and second generation samples

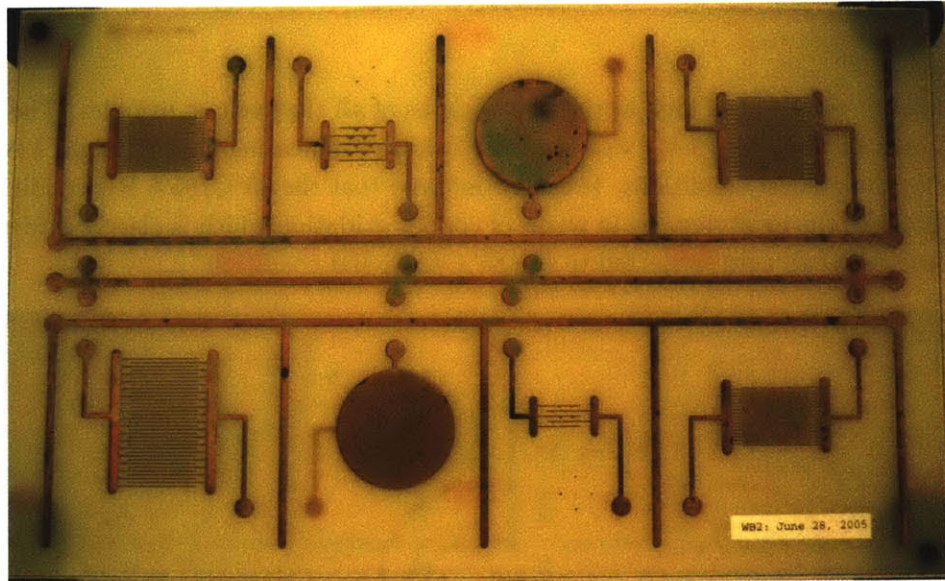


Figure 9.38: Witness Board (WB2)

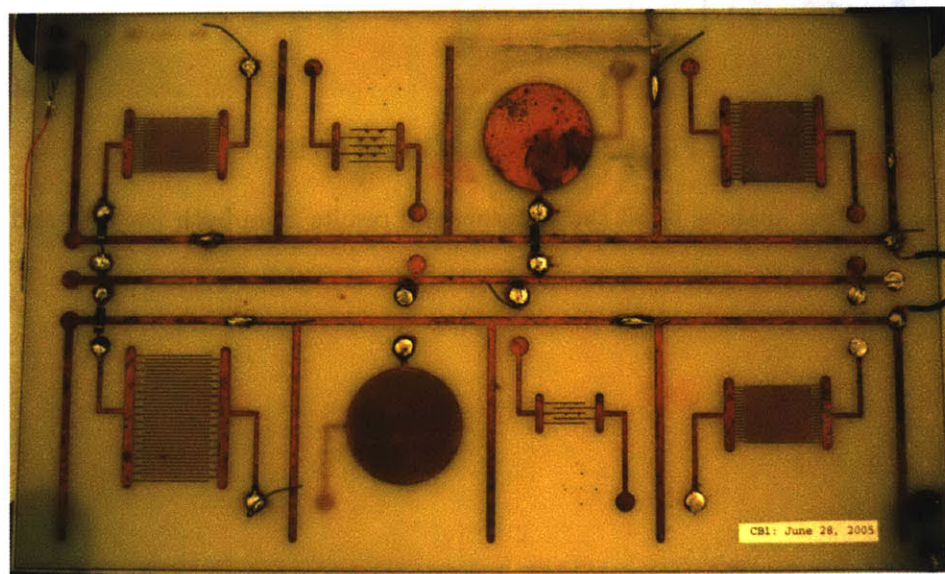


Figure 9.39: Conduction Board (CB1)

9.9 Visual Observations about Second Generation Test Samples

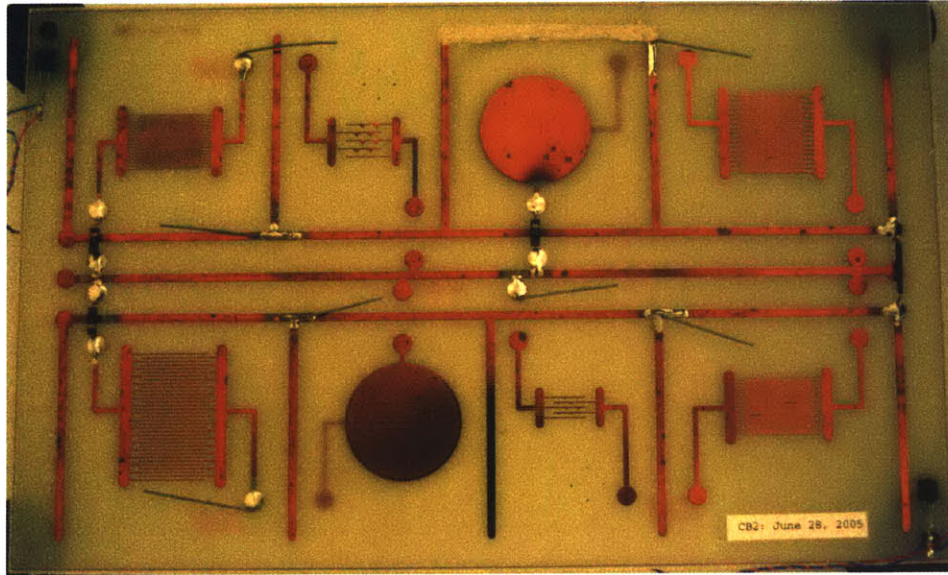


Figure 9.40: Conduction Board (CB2)

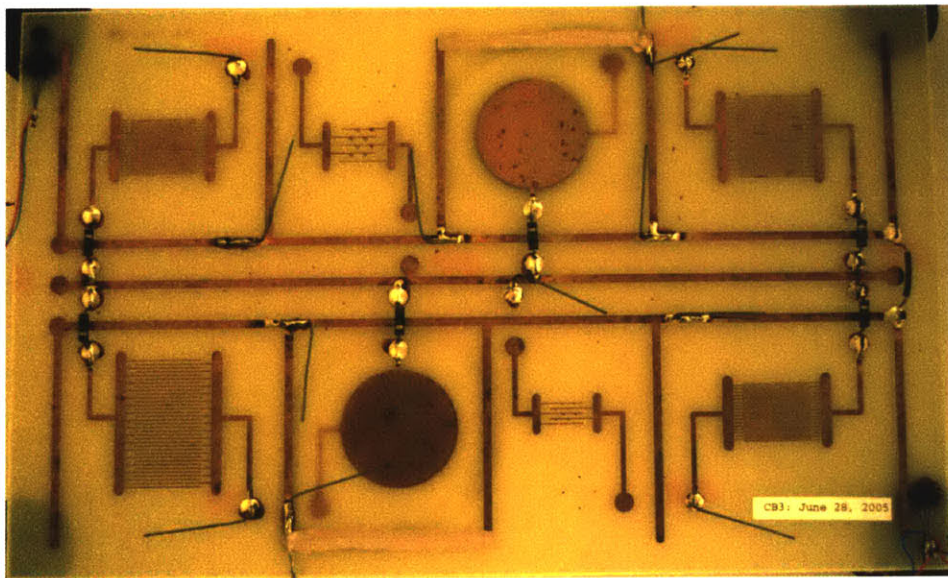


Figure 9.41: Conduction Board (CB3)

Conclusions

THIS chapter presents a brief summary of all the findings and major conclusions. In addition, the thesis objectives are evaluated to measure completion. Some original contributions are also emphasized.

10.1 Introduction

The main motivation for this research came from the need to develop well designed accelerated tests to predict in-service reliability of automotive electrical and electronic systems. In particular, there was need to be able to predict the level of degradation of electrical insulation through suitable acceleration. The development of such a test requires a solid understanding of the physics of the insulation in question which is the primary goal of this work. We chose the printed circuit board insulation as a suitable first case and attempted to further our understanding of electrical leakage conduction.

10.2 Summary and Major Conclusions

The following points in regard to FR4 (fiberglass reinforced epoxy) circuit board material with copper traces are the major conclusions from this thesis:

- Fick's law is adequate to describe moisture absorption and desorption in PCBs in the 50°C to 85°C temperature range.
- Electrical conduction displays a temperature dependance consistent with Arrhenius type activation processes.
- Conduction current magnitudes depend exponentially on moisture content.
- Ionic conduction processes are consistent with the results, but are not proven to occur.

Conclusions

- An exposure-based model of current was found more suitable for the surface patterns (small and large) than for the bulk pattern.
- A mass-based model of current was found more suitable for the volume (bulk) pattern than for the surface patterns.
- An essentially constant activation energy was exhibited for all hygrothermal conditions after sample exposure to 50% RH or more.
- Electrical conduction current scales with the geometric size of the test pattern.
- Moisture absorption and electrical conduction in PCBs are shown to exhibit memory of previous tests.
- Present-day accelerated testing schemes such as adopted by IPC are shown to have some drawbacks.

In Chapter 2, we presented a big picture view of the entire field of insulation research in the light of accelerated testing. It was made clear both in Chapter 1 and 2 that current standardized and non-standardized accelerated testing schemes leave a lot to desire. Our experiments on moisture absorption (Section 9.5) showed that even two weeks of soaking a sample at 85°C/85% RH does not ensure it to reach an equilibrium. This means that all the tests that measure insulation resistance after a week of conditioning at 85°C/85% RH are actually measuring some intermediate transient that cannot be consistently measured. It became evident that aging and memory are very important factors since the boards seemed to retain a fair amount of moisture even after being vacuum dried for two weeks. In fact, after an 85°C/85% RH conditioning, it was shown (Chapter 9) that even multiple cycles of vacuum drying did not completely remove all the excess moisture.

Another aspect of current accelerated tests that hasn't received much attention is the concept of polarization and transient currents. Published literature has been very arbitrary in defining the wait time before making an insulation resistance measurement. Our transient current data indicate that sometimes the wait time can be in the order of minutes or longer.

Even though much of the published literature on polymer moisture absorption alludes to the fact that we should expect non-Fickian behavior, our experimental results concluded that for the time frame of two weeks, Fickian approximations are adequate to characterize both moisture absorption and desorption in FR4.

In our regime of testing, the observed conduction seems to be consistent with ionic transport. All test boards exhibited very low currents with an Arrhenius relationship with temperature which can occur with ionic conduction. Additionally, the conduction is ohmic and scales

with voltage and pattern length. The hygrothermal experimental scheme indicated that steady currents at fixed conditions in all the conduction boards were exponentially dependent on the amount of absorbed moisture and the relative humidity. This not only helps to strengthen the argument for ionic conduction but also sheds light on the importance and role of water in electrical conduction. Dry samples displayed high activation energies and wet samples had lower activation energies. However, it was observed that the activation energy remained constant once a certain moisture threshold was crossed for the samples.

Similar to moisture absorption measurements, memory of previous conditions was also observed in electrical conduction measurements. In Section 9.7.8, we observed that activation energies for the dry state and the wet state in the most aged sample was almost the same.

We developed simple mathematical relationships to describe the dependence of both the environmental and absorbed moisture on steady-state current as well as the general behavior of activation energy with moisture. We also developed a physically based model to scale the geometries of the surface patterns. We observed that bulk conduction depends more on absorbed moisture while surface conduction seemed to depend more on relative humidity of the surrounding environment. The ionic transport mechanism is hypothesized to operate through a hopping mechanism as described in Section 4.4.3.

10.3 Evaluation of Thesis Objectives and Contributions

The stated goals of building and automating an experimental setup, building a test sample, designing and running experiments and identifying a likely model to explain conduction were completed and exceeded.

We built a completely automated data acquisition system capable of measuring very low currents even in the sub-pico ampere range (Chapter 6). The system can take measurements from multiple channels simultaneously and reduce the effects of various extraneous disturbances (Chapter 7). We designed and built two generations of test samples with certain testing patterns to differentiate surface and bulk conduction phenomena (Chapter 5). With the aid of results obtained from experiments performed (Chapters 8 and 9), we contended that the dominant conduction mechanism is ionic and we were able to build a simple first-order model to describe these currents.

Through this work, we have made some original contributions to the fields of insulation research and accelerated testing. Procedural contributions include the development and implementation of a new hygrothermal testing scheme including the simultaneous study of

moisture diffusion and electrical leakage in PCB insulation. We were able to suggest that ionic conduction was the dominant transport mechanism in PCBs and that moisture has an important role to play. We also built a novel first-order physically grounded mathematical model to describe electrical leakage conduction as a function of not only temperature, voltage and geometry, but also absorbed and environmental moisture. It is hoped that this initial work will provide a good launching pad for future work in understanding in-service insulation degradation and developing accelerated tests.

10.4 Future Work

The model presented in Section 9.7 clearly has a number of limitations. One of the most important objection was the general lack of data. Plenty of work still remains in acquiring more data so as to verify the model and refine the parameters. Therefore, a natural extension to strengthen our understanding of electrical leakage conduction, is to perform tests at many more hygrothermal conditions to add more data points and verify the fits for current. It is also important to perform similar tests on thicker and thinner boards, try other patterns, energize with different voltages and even attempt to vary the pressure. However, to be able to do this, we will need to expand the automated data acquisition system so that we can read more channels simultaneously.

We have thus far developed a basic understanding of electrical leakage conduction and more specifically we have focussed on the impact of moisture on it. It is only natural that we now perform the standard IPC testing schemes on our samples. Some of these tests were outlined in Section 1.4. In conjunction with this standardized test, the weight gain and thickness of the samples must also be monitored. A modified conduction test could also be performed at the end of the test to compare with our existing data.

We are also interested in proving that the conduction mechanism in PCB insulation is ionic. To be able to unambiguously prove ionic transport, we have to show mass transfer. Initial microscopy (not presented in this thesis) on samples indicated some changes in electrode boundaries, however, there was no conclusive evidence for mass transfer. Some time should be spent in chemically analyzing the electrodes and interfaces for signs of ionic mass transfer.

An area that has been gaining some steam is the fundamental understanding of conduction mechanisms in disordered material. The interpretation of activation energy was briefly introduced in Section 4.4.4. Some work has been undertaken in modeling the dynamics of ion hopping over barriers in a random energy landscape. These random energy landscapes are usually assumed to be static and therefore easier to model than dynamically changing

systems. However, there is possibility of using such concepts as stochastic resonance, dynamic random graphs and elements of chaos theory to model even dynamic systems. The significance of such a study not only helps in determining potential barrier distributions but also in defining the activation energy as a metric for material disorder. A good metric for material disorder can aid in monitoring general material aging since as polymeric materials get older, they tend to lose their degree of disorder and show decreased cross-linking through local degradation mechanisms and polymeric bond breaking.

Part IV

Appendices

Geometric Calculations of Test Samples

A.1 Geometric Considerations and Active Area Calculations

This section outlines some definitions that combine certain geometrical characteristics of the patterns. Some of these characteristics might later be useful to normalize data.

Figures A.1, A.2 and A.3 show the dimensioning of the different patterns.

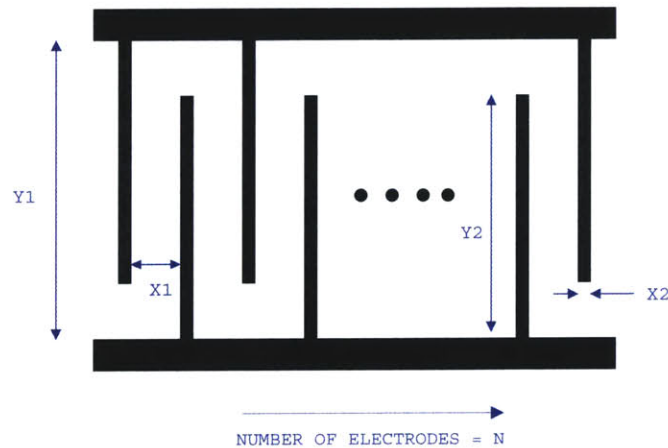


Figure A.1: Dimensions of the Comb Pattern

A.1.1 Comb Pattern

- **Active Length per Finger (L_f):** This is defined as that portion of one electrode finger length that is used in the calculation of the uniform electric field between the applied voltage and the ground.

$$L_f = Y2 - (Y1 - Y2) \quad (A.1)$$

- **Total Active Electrode Length (L_T):** This is defined as being the active length for the entire pattern. It is given by the L_f times the number of active fingers.

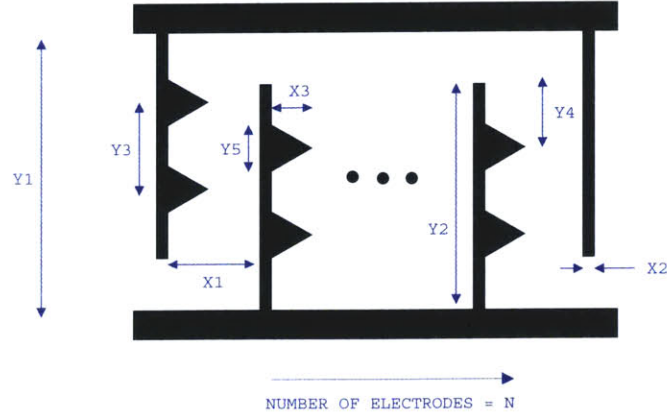


Figure A.2: Dimensions of the Comb Pattern with Triangular Dimples

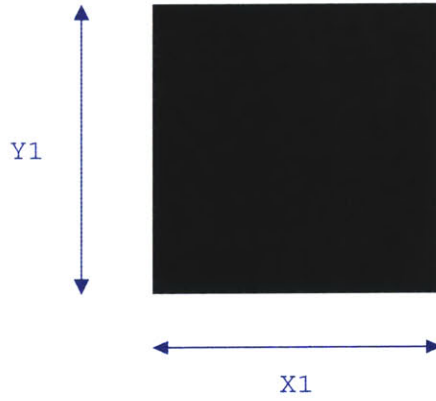


Figure A.3: Dimensions of the Filled Square Pattern

$$L_T = (N - 1)L_f \quad (\text{A.2})$$

$$L_T = (N - 1)[2(Y_2) - Y_1] \quad (\text{A.3})$$

- **Total Active Dielectric Surface Area (A_D):** The dielectric area in between the active lengths of 2 fingers is given by

$$a_D = L_f X_1 \quad (\text{A.4})$$

The total active dielectric surface area in the pattern.

$$A_D = a_D(N - 1) \quad (\text{A.5})$$

$$A_D = X_1 * (2 * Y_2 - Y_1) * (N - 1) \quad (\text{A.6})$$

A.1 Geometric Considerations and Active Area Calculations

- **Total Active Conductor Area (A_C):** The total active area occupied by all the conductors in a pattern.

$$A_C = (N - 1)L_f X_2 \quad (\text{A.7})$$

$$A_C = (N - 1)[2(Y_2) - Y_1]X_2 \quad (\text{A.8})$$

- **Total Active Area (A):** This is defined as the sum of the total active conductor area and the total active dielectric surface area.

$$A = A_D + A_C \quad (\text{A.9})$$

$$A = (N - 1)[2(Y_2) - Y_1](X_1 + X_2) \quad (\text{A.10})$$

A.1.2 Comb Pattern with Dimples

The definitions for this pattern are a little bit more complicated and are discussed below. Also, the formulas derived here are for comb patterns with 2 dimples per finger.

- **Active Length per Finger (L_f):** Once again this is defined as that portion of one electrode finger length that is used in the calculation of the uniform electric field between the bias voltage and the ground. Notice, dimples are not taken into account in this definition.

$$L_f = Y_2 - (Y_1 - Y_2) \quad (\text{A.11})$$

$$L_f = 2(Y_2) - Y_1 \quad (\text{A.12})$$

- **Total Active Electrode Length (L_T):** This is defined as being the active length for the entire pattern. It is given by the L_f times the number of active fingers.

$$L_T = (N - 1)L_f \quad (\text{A.13})$$

$$L_T = (N - 1)[2(Y_2) - Y_1] \quad (\text{A.14})$$

- **Dimple parameters:**

Dimple height: $h_{dp} = X_3$

Dimple base: $w_{dp} = Y_5$

Dimple Area: $a_{dp} = \frac{1}{2}X_3Y_5$

- **Total Active Dielectric Surface Area (A_D):** The dielectric area in between the active lengths of 2 fingers. Depending on the position and the size of the dimples this will vary.

Geometric Calculations of Test Samples

If $(Y3 + Y4 + \frac{1}{2}w_{dp}) \leq L_f$ (When both dimples lie within the active surface area):

$$a_{D1} = L_f X1 - 2a_{dp} \quad (\text{A.15})$$

If $(Y3 + Y4 + \frac{1}{2}w_{dp}) > L_f$ (When one dimple is partially outside the active area):

$$a_{D2} = L_f X1 - 2a_{dp} + \frac{1}{2}[(Y3 + Y4 + \frac{w_{dp}}{2}) - L_f][((Y3 + Y4 + \frac{w_{dp}}{2}) - L_f) \frac{2h_{pd}}{w_{pd}}] \quad (\text{A.16})$$

$$a_{D2} = L_f X1 - 2a_{dp} + \frac{1}{2}[(Y3 + Y4 + \frac{w_{dp}}{2}) - L_f]^2 \frac{2h_{pd}}{w_{pd}} \quad (\text{A.17})$$

The total active dielectric surface area in the pattern.

$$A_D = a_D(N - 1) \quad (\text{A.18})$$

$$A_{D1} = (N - 1)\{L_f X1 - 2a_{dp}\} \quad (\text{A.19})$$

$$A_{D2} = (N - 1)\{L_f X1 - 2a_{dp} + \frac{1}{2}[(Y3 + Y4 + \frac{w_{dp}}{2}) - L_f]^2 \frac{2h_{pd}}{w_{pd}}\} \quad (\text{A.20})$$

- **Total Active Conductor Area (A_C):** The total active area occupied by all the conductors in a pattern. Here also, depending on the position and size of the dimples, active conductor area will vary.

$$A_{C1} = (N - 1)\{L_f X2 + 2a_{dp}\} \quad (\text{A.21})$$

$$A_{C2} = (N - 1)\{L_f X2 + 2a_{dp} - \frac{1}{2}[(Y3 + Y4 + \frac{w_{dp}}{2}) - L_f]^2 \frac{2h_{pd}}{w_{pd}}\} \quad (\text{A.22})$$

- **Total Active Area (A):** This is defined as the sum of the total active conductor area and the total active dielectric surface area.

$$A = A_D + A_C \quad (\text{A.23})$$

$$A = (N - 1)L_f(X1 + X2) \quad (\text{A.24})$$

A.1.3 Square Pattern (First generation boards)

This pattern has an active volume associated with it.

- **Active Conductor Surface Area (A_C):** The total area of the top and bottom square plates.

$$A_C = 2(X1)(Y1) \quad (\text{A.25})$$

A.1 Geometric Considerations and Active Area Calculations

- Active Dielectric Volume (V_D): The total volume of the dielectric in between the two plates.

Let the thickness of the dielectric be d . Then,

$$V_D = (X1)(Y1)d \quad (\text{A.26})$$

A.1.4 Circular Disc Pattern (Second generation boards)

This pattern also has an active volume associated with it.

- Active Conductor Surface Area (A_C): The total area of the top and bottom square plates.

$$A_C = \frac{\pi(X1)^2}{2} \quad (\text{A.27})$$

where $X1$ is the diameter of the circular disc.

- Active Dielectric Volume (V_D): The total volume of the dielectric in between the two plates.

Let the thickness of the dielectric be d . Then,

$$V_D = \frac{d\pi(X1)^2}{4} \quad (\text{A.28})$$

A.1.5 Active Areas of all the Patterns

Shown in Table A.1 are all the active areas of all the patterns on the first generation samples. Similarly, Table A.2 shows the area and volume calculations for the second generation board.

Type	Size	$L_f(\text{mils})$	$L_T(\text{mils})$	$A_D(\text{mil}^2)$	$A_C(\text{mil}^2)$	$A(\text{mil}^2)$	$V_D(\text{mil}^3)$
Comb	Small	700	28000	224000	224000	448000	
	Medium	689	27560	325208	325208	650416	
	Large	689	27560	975624	325208	1300832	
Dimple	Small	319.6	1278.4	55629.2	21586.1	77215.4	
	Large	267	1068	64303.1	21243.7	85546.8	
Square					1.2×10^6		3.6×10^7

Table A.1: Active Lengths and Active Areas of all the Patterns on the First Generation Sample

Geometric Calculations of Test Samples

Type	Size	$L_f(mils)$	$L_T(mils)$	$A_D(mil^2)$	$A_C(mil^2)$	$A(mil^2)$	$V_D(mil^3)$
Comb	Small	652	22168	177344	177344	354688	
	Medium	652	22168	177344	266016	443360	
	Large	652	22168	532032	266016	798048	
Dimple	Small	312	1248	43632	16272	59904	
	Large	364	1456	95184	27120	122304	
Circular Disc					1.87×10^6		5.6×10^7

Table A.2: Active Lengths and Active Areas of all the Patterns on the Second Generation Sample

Appendix B

Solutions to Fick's Law

B.1 Method of Reflection and Superposition

A solution to the Equation 3.2 can be of the form:

$$C = \frac{A}{t^{1/2}} e^{-x^2/4Dt} \quad (\text{B.1})$$

Equation B.1 is symmetrical with respect to $x = 0$ and tends to zero as x approaches infinity.

We know that the total amount of substance diffusing, M , can be given by:

$$M = \int_{-\infty}^{\infty} C dx \quad (\text{B.2})$$

Solving this integral and substituting the value of A in Equation B.1, we obtain:

$$C = \frac{M}{2(\pi Dt)^{1/2}} e^{-x^2/4Dt} \quad (\text{B.3})$$

Equation B.3 is symmetric about $x = 0$ and therefore diffusion occurs in both the positive and negative x directions.

For a semi-infinite medium, where diffusion occurs only in the positive x direction, the following boundary condition will have to be satisfied:

$$\partial C / \partial x = 0, \quad x = 0 \quad (\text{B.4})$$

This is the mathematical condition for zero flow across a boundary. Also, since all the

diffusion occurs in one direction, Equation B.3 can be doubled:

$$C = \frac{M}{(\pi Dt)^{1/2}} e^{-x^2/4Dt} \quad (\text{B.5})$$

As a reminder, Equation B.5 represents diffusion of a fixed amount of diffusing substance located initially on the plane of $x = 0$. Shown in Figure B.1 is the plot of Equation B.5 for different values of Dt . The MATLAB code used to generate this plot is given in Section D.5.

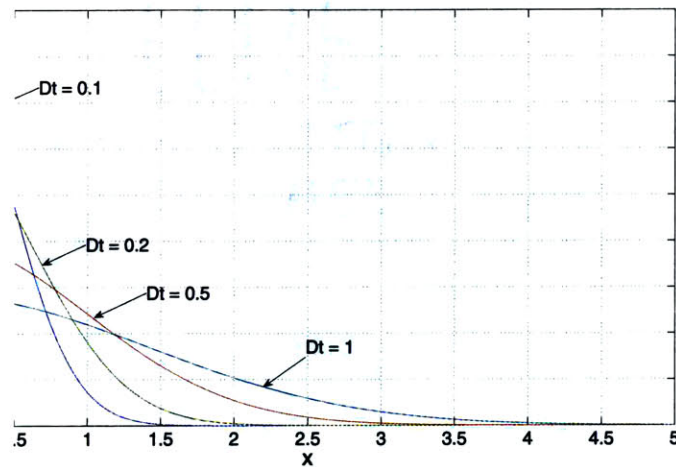


Figure B.1: Concentration-distance curves for an instantaneous plane source

B.2 Method of Separation of Variables

Equation 3.2 can be solved using the method of separation of variables as shown in the analysis below:

$$C = X(x)T(t) \quad (\text{B.6})$$

where X and T are functions of x and t respectively.

Therefore,

B.2 Method of Separation of Variables

$$X \frac{dT}{dt} = D_x T \frac{d^2 X}{dx^2} \quad (\text{B.7})$$

$$\frac{1}{T} \frac{dT}{dt} = \frac{D_x}{X} \frac{d^2 X}{dx^2} \quad (\text{B.8})$$

Each side of the equation now depends only on one variable x or t . Both sides must therefore equal the same constant ($-\lambda^2 D_x$). We now have two ordinary differential equations:

$$\frac{1}{T} \frac{dT}{dt} = -\lambda^2 D_x \quad (\text{B.9})$$

$$\frac{1}{X} \frac{d^2 X}{dx^2} = -\lambda^2 \quad (\text{B.10})$$

Solving,

$$T = e^{-\lambda^2 D_x t} \quad (\text{B.11})$$

$$X = A \sin(\lambda x) + B \cos(\lambda x) \quad (\text{B.12})$$

Combining the two separate variables X and T , we get:

$$C = (A \sin(\lambda x) + B \cos(\lambda x)) e^{-\lambda^2 D_x t} \quad (\text{B.13})$$

The most general solution is obtained by summing solutions of the above type to get:

$$C = \sum_{m=1}^{\infty} (A_m \sin(\lambda_m x) + B_m \cos(\lambda_m x)) e^{-\lambda_m^2 D_x t} \quad (\text{B.14})$$

where A_m , B_m and λ_m are determined by initial and boundary conditions for any problem. For e.g., consider that we are interested in diffusion out of a plane sheet of thickness l , through which the diffusing substance is uniformly distributed and the surfaces of which are kept at zero concentration. Solving for this case,

Solutions to Fick's Law

$$C = \frac{4C_0}{\pi} \sum_{n=0}^{\infty} \frac{1}{2n+1} e^{-D_x(2n+1)^2\pi^2t/l^2} \sin \frac{(2n+1)\pi x}{l} \quad (\text{B.15})$$

B.3 The Laplace Transform

Application of the Laplace transformation to the diffusion equation (Equation 3.2), removes the time variable, leaving an ordinary differential equation the solution of which yields the transform of the concentration as function of x .

The definition of the Laplace transform is given by:

$$\bar{f}(p) = \int_0^{\infty} e^{-pt} f(t) dt \quad (\text{B.16})$$

Where p is sufficiently large to make the integral converge.

Assuming a semi-infinite medium, with boundary conditions:

$$C = C_0, \quad x = 0, \quad t > 0 \quad (\text{B.17})$$

and initial condition:

$$C = 0, \quad x > 0, \quad t = 0 \quad (\text{B.18})$$

Multiplying Equation 3.2 by e^{-pt} and integrating and then simplifying, we get:

$$D \frac{\partial^2 \bar{C}}{\partial x^2} = p \bar{C} \quad (\text{B.19})$$

Applying boundary conditions, we get the solution:

$$\bar{C} = \frac{C_0}{p} e^{-qx} \quad (\text{B.20})$$

where $q^2 = p/D$.

The transform yields:

$$C = C_0 \operatorname{erfc} \frac{x}{2\sqrt{Dt}} \quad (\text{B.21})$$

B.3.1 Plane Sheet of Finite Thickness

So far we have looked at a semi-infinite medium. However, a more important problem is diffusion into a plane sheet of thickness $2l$, whose surfaces are maintained at constant concentration, C_0 , and with zero concentration of the diffusion substance throughout the sheet initially.

Using the relations of symmetry, we can solve for half the thickness of the sheet. The boundary conditions are:

$$C = C_0, \quad x = l, \quad t \geq 0 \quad (\text{B.22})$$

$$\partial C / \partial x = 0, \quad x = 0, \quad t \geq 0 \quad (\text{B.23})$$

Solving the Equation B.19 for the given boundary conditions, we get a solution:

$$\bar{C} = \frac{C_0 \cosh qx}{p \cosh ql} \quad (\text{B.24})$$

Expressing Equation B.24 in terms of negative exponentials and expanding in a series by the binomial theorem,

$$\bar{C} = \frac{C_0}{p} \sum_{n=0}^{\infty} (-1)^n e^{-q\{(2n+1)l-x\}} + \frac{C_0}{p} \sum_{n=0}^{\infty} (-1)^n e^{-q\{(2n+1)l+x\}} \quad (\text{B.25})$$

The transform of this function is given by:

$$C = C_0 \sum_{n=0}^{\infty} (-1)^n \operatorname{erfc} \frac{(2n+1)l-x}{2\sqrt{Dt}} + C_0 \sum_{n=0}^{\infty} (-1)^n \operatorname{erfc} \frac{(2n+1)l+x}{2\sqrt{Dt}} \quad (\text{B.26})$$

Equation B.26 is plotted below in Figure B.2. The number of terms chosen for the summation was 4 and the half-thickness of the sheet was $l = 2$. The MATLAB code used to generate this plot is presented in Section D.5.

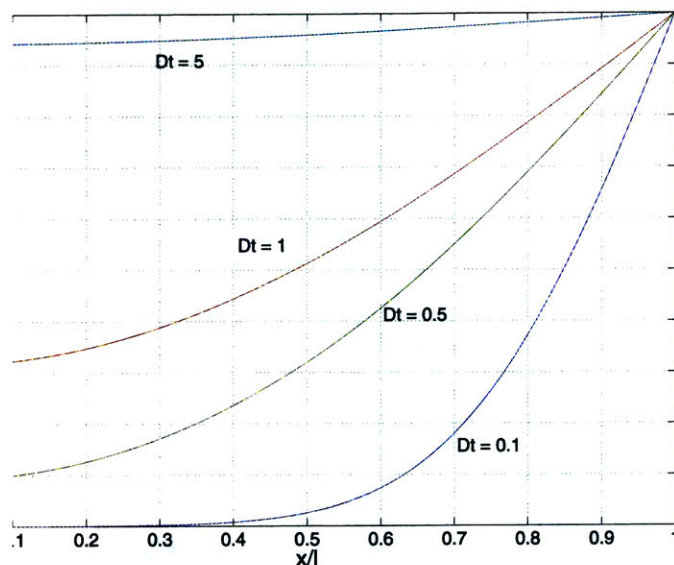


Figure B.2: Concentration-distance curves for a plane sheet of initial surface concentration C_0 at $x = l$

B.4 Other Solutions

Consider a semi-infinite medium with initial concentration throughout, C_0 and surface concentration is maintained constant at C_1 . Then the solution becomes:

$$\frac{C - C_1}{C_0 - C_1} = \operatorname{erf} \frac{x}{2\sqrt{Dt}} \quad (\text{B.27})$$

If the surface concentration were zero, then the rate of loss of the diffusing substance from the semi-infinite medium can be given by:

$$\left(D \frac{\partial C}{\partial x}\right)_{x=0} = \frac{DC_0}{\sqrt{\pi Dt}} \quad (\text{B.28})$$

The total amount of the diffusing substance, M_t , which has left the medium at time t is given by integrating the above equation with respect to t .

$$M_t = 2C_0 \left(\frac{Dt}{\pi}\right)^{1/2} \quad (\text{B.29})$$

C_0 in this expression can be replaced by C_1 to get diffusion into the medium with zero initial concentration, $C_1 = 0$.

B.4.1 Surface Evaporation

An interesting case is one where the boundary condition relates to the transfer of diffusing substance across the surface of a dry solid. In this case the solid takes up moisture and the rate of exchange at any instant depends on the relative humidity of the air and the moisture concentration in the surface of the solid.

A simple assumption is that the rate of exchange is directly proportional to the difference between the actual concentration in the surface (C_s) at any time and the concentration which would be in equilibrium (C_0) with the vapor pressure in the atmosphere remote from the surface. Mathematically,

$$-D \frac{\partial C}{\partial x} = \alpha(C_0 - C_s), \quad x = 0 \quad (\text{B.30})$$

where α is the constant of proportionality. If the concentration in a semi-infinite medium is initially C_2 throughout, and the surface exchange is determined by the above boundary condition, the solution is,

$$\frac{C - C_2}{C_0 - C_2} = \text{erfc} \frac{x}{2\sqrt{Dt}} - e^{hx+h^2Dt} \text{erfc} \left\{ \frac{x}{2\sqrt{Dt}} + h\sqrt{Dt} \right\} \quad (\text{B.31})$$

where $h = \alpha/D$. The special cases of zero concentration in the medium initially ($C_2 = 0$) and evaporation into the atmosphere of zero relative humidity ($C_0 = 0$) are clear. The rate at which the total amount of moisture, M_t , per unit cross sectional area changes is given by:

$$\frac{dM_t}{dt} = -\left(D \frac{\partial C}{\partial x}\right)_{x=0} = \alpha(C_0 - C_s) \quad (\text{B.32})$$

Solving,

$$M_t = \left(\frac{C_0 - C_2}{h}\right) \left\{ e^{h^2Dt} \text{erfc} h\sqrt{Dt} - 1 + \frac{2}{\pi^{1/2}} h\sqrt{Dt} \right\} \quad (\text{B.33})$$

If C_0 is greater than C_2 , then this amount is taken up by the medium.

Appendix C
Additional Plots

C.1 Moisture Desorption Data

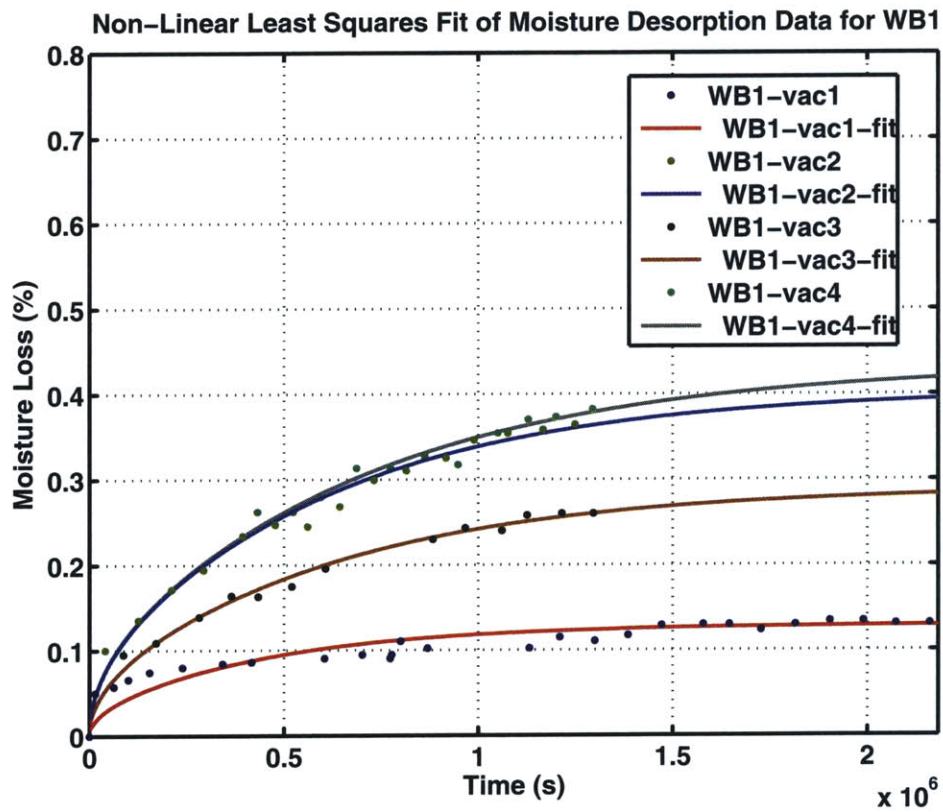


Figure C.1: Non-Linear Least Squares Fit of Moisture Desorption Data for WB1

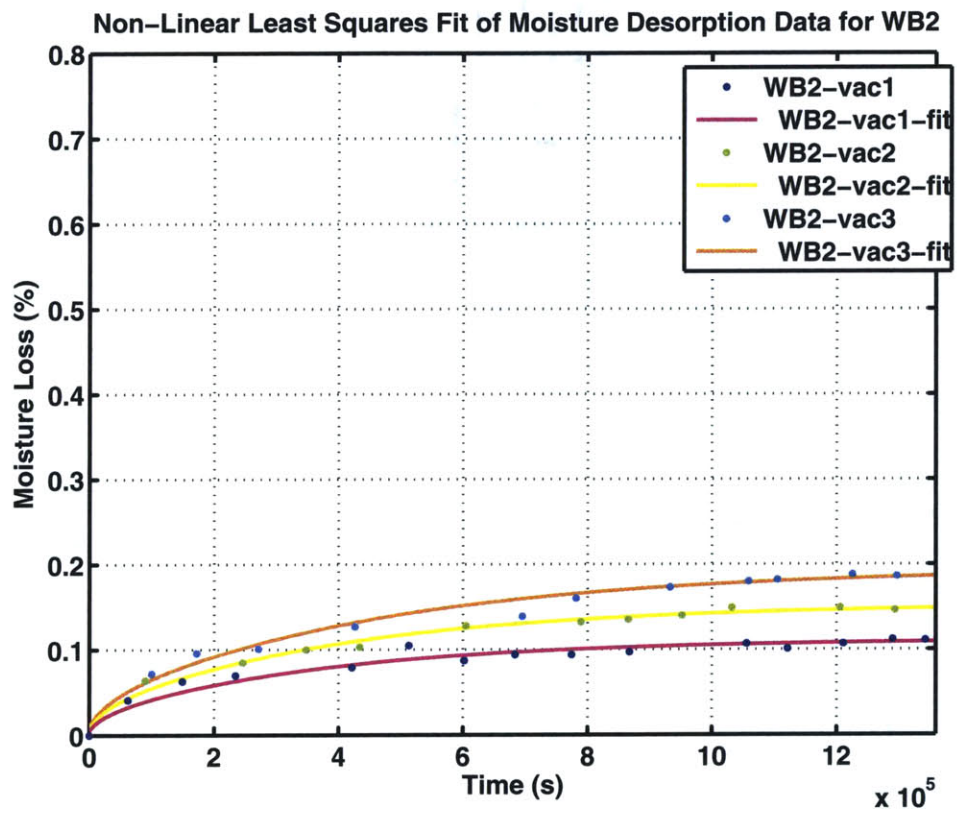


Figure C.2: Non-Least Squares Fit of Moisture Desorption Data for WB2

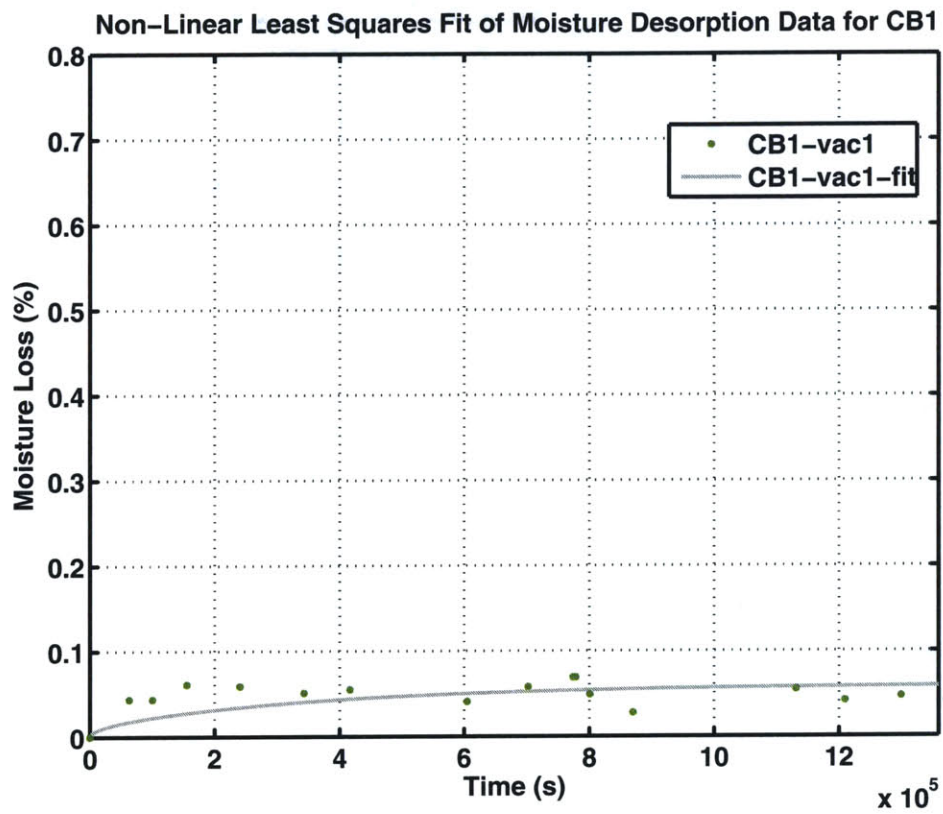


Figure C.3: Non-Least Squares Fit of Moisture Desorption Data for CB1

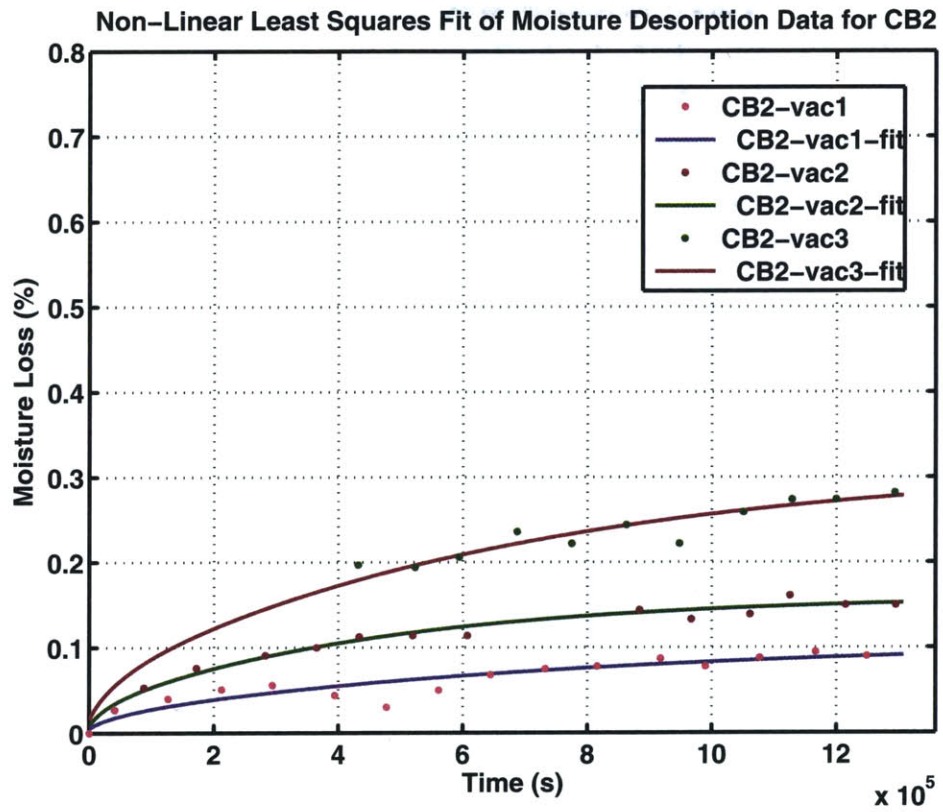


Figure C.4: Non-Least Squares Fit of Moisture Desorption Data for CB2

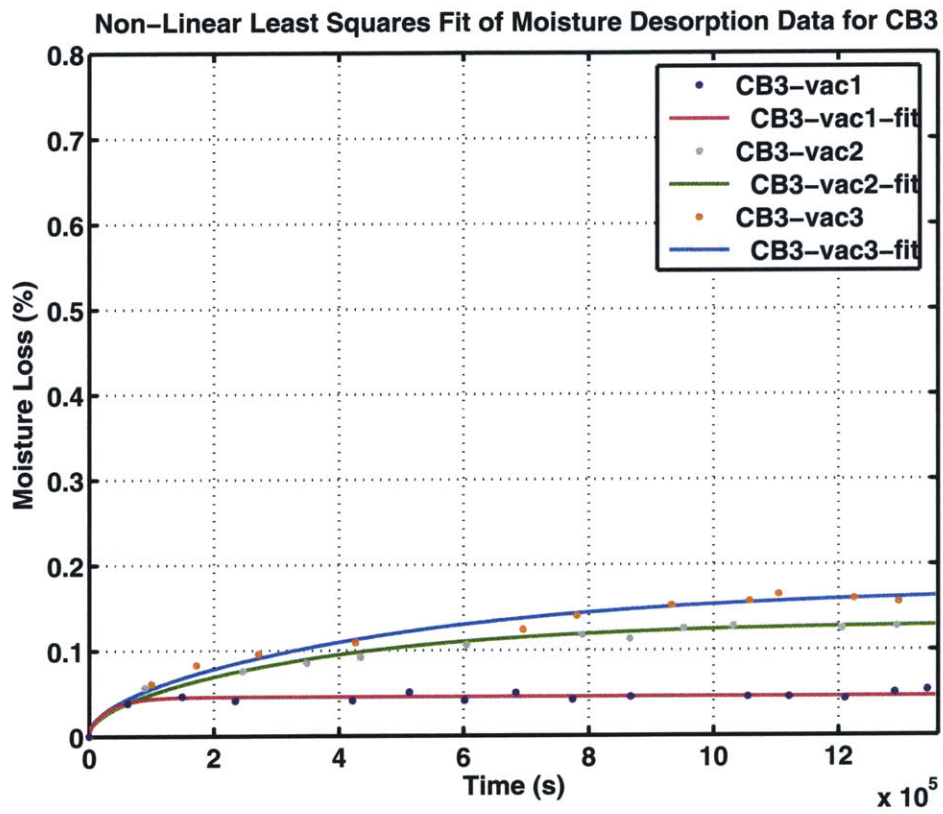


Figure C.5: Non-Least Squares Fit of Moisture Desorption Data for CB3

Appendix D

MATLAB Code

D.1 ADAQ Data Extracter

```
% ADAQ DATA EXTRACTER
% Author: Vasanth Sarathy
% Date: January 2005

% This script extracts all the data from the typical file output of the MIT
% Surface Corrosion and Tracking Automated Data Acquisition System (ADAQ).
% It assumes Channel 1 and Channel 2 are leakage currents read from the home
% built logarithmic amplifiers

% Channel 8 is the relative humidity.

clear all clc

% Load and pre-process the output data

% --- Load data from the text files created by the ADAQ LABVIEW based system
Keithley = load('Keithley_test_data.txt'); % Keithley output
Raw_ADR = load('raw_adr_data.txt'); % Raw output
Avg_ADR = load('test_data.txt'); % Averaged output
Temperature = load('temperature_data.txt'); % Temperature output from sensors

% --- Reformat Keithley data appropriately
Keithley_Time = Keithley(:,2); Keithley_Current =
Keithley(:,1).*1e-12;

% --- Read the raw A/D Converter (ADR) output into local arrays
% --- Make voltage corrections for the two logamps
Channel_1_Raw = Raw_ADR(:,1)-0.005; % Correction for logamp 1
Channel_2_Raw = Raw_ADR(:,2)+0.011; % Correction for logamp 2
Channel_3_Raw = Raw_ADR(:,3); Channel_4_Raw = Raw_ADR(:,4);
Channel_5_Raw = Raw_ADR(:,5); Channel_6_Raw = Raw_ADR(:,6);
```

MATLAB Code

```
Channel_7_Raw = Raw_ADR(:,7); Channel_8_Raw = Raw_ADR(:,8);

% --- Read raw time data
Time_Raw = Raw_ADR(:,9);

% --- Read the averaged A/D Converter (ADR) output into local arrays
% --- Make voltage corrections for the two logamps
Channel_1_Avg = Avg_ADR(:,1)-0.005; Channel_2_Avg =
Avg_ADR(:,2)+0.011; Channel_3_Avg = Avg_ADR(:,3); Channel_4_Avg =
Avg_ADR(:,4); Channel_5_Avg = Avg_ADR(:,5); Channel_6_Avg =
Avg_ADR(:,6); Channel_7_Avg = Avg_ADR(:,7); Channel_8_Avg =
Avg_ADR(:,8);

% --- Read averaged time data
Time_Avg = Avg_ADR(:,9);

%--- Read temperature output and corresponding time array
T_1 = Temperature(:,1); T_2 = Temperature(:,2); T_Time =
Temperature(:,3);

% Conversion of output voltages to leakage current

%--- Generate reference currents
I_ref = 6.2/660e6; % logamp reference current
I1_zero = 5.2473e-12; % logamp 1 offset
I2_zero = 5.0744e-12; % logamp 2 offset

%--- Calculate raw currents from channels 1 and 2
I_1_Raw = I_ref*10.^(Channel_1_Raw.*2) - I1_zero; I_2_Raw =
I_ref*10.^(Channel_2_Raw.*2) - I2_zero;

%--- Calculate average currents from channels 1 and 2
I_1_Avg = I_ref*10.^(Channel_1_Avg.*2) - I1_zero; I_2_Avg =
I_ref*10.^(Channel_2_Avg.*2) - I2_zero;

%--- Calculate current from Keithley
I_Keithley = Keithley_Current;

% Conversion of voltage to Relative Humidity
```


D.2 Data Interpolation and Smoothing

```
%--- Calculate the Relative Humidity from voltages
RH_Raw = (Channel_8_Raw - 0.896)./0.0317; RH_Avg = (Channel_8_Avg -
0.896)./0.0317;

% Interpolate data to have the same time stamp fixed to Keithley time

%--- Keithley time
xi = Keithley_Time;

%--- Interpolate the average logamp currents and relative humidity
I_1_Avg_int = interp1(Time_Avg,I_1_Avg,xi,'cubic'); I_2_Avg_int =
interp1(Time_Avg,I_2_Avg,xi,'cubic'); RH_Avg_int =
interp1(Time_Avg,RH_Avg,xi,'cubic');

%--- Interpolate temperature output
T_1_int = interp1(T_Time,T_1,xi,'cubic'); T_2_int =
interp1(T_Time,T_2,xi,'cubic');

% Renaming variables for storing convenience

Time = Keithley_Time; T1 = T_1_int; T2 = T_2_int; I1 = I_1_Avg_int;
I2 = I_2_Avg_int; IK = I_Keithley; RH = RH_Avg_int;

% Saving the processed output and clearing

save measurements Time T1 T2 I1 I2 IK RH clear all clc
```

D.2 Data Interpolation and Smoothing

```
% SMOOTHING DATA
% Author: Vasanth Sarathy
% Date: January 2005

function [I1_smooth, I2_smooth, IK_smooth, T1_smooth, T2_smooth,
```

MATLAB Code

```
Time_smooth] = smoothing_data(filename, window)

%SMOOTHING_DATA can read the output file generated by the ADAQ_EXTRACTER
%and averages the values determined by the chosen window size using the the
%Averaged Downsampling technique. A good window size is 30.

%This is designed especially for extracting data obtained from the
%hygrothermal conduction testing scheme.

%--- Loads file given by "filename"
load(filename)

%--- Averaged downsampling window size (default is 30)
window = 30; % Averaged Downsampling Window

%--- Reading data output from after stabilization (~1 hour)
I1 = I1(3300:end); I2 = I2(3300:end); IK = IK(3300:end); T1 =
T1(3300:end); T2 = T2(3300:end); Time = Time(3300:end);

%--- Alternative output for certain anomalous data files (can be ignored)
% I1 = I1(1:12500);
% I2 = I2(1:12500);
% IK = IK(1:12500);
% T1 = T1(1:12500);
% T2 = T2(1:12500);
% Time = Time(1:12500);

%--- Setting up index counter
j=0; i=1;

%--- Averaged Downsampling Operation
for i = 1:length(Time)
    if mod(i,window) == 0
        j = j+1;
        I1_smooth(j) = sum(I1(i-(window-1):i))./window;
        I2_smooth(j) = sum(I2(i-(window-1):i))./window;
        IK_smooth(j) = sum(IK(i-(window-1):i))./window;
        T1_smooth(j) = sum(T1(i-(window-1):i))./window;
        T2_smooth(j) = sum(T2(i-(window-1):i))./window;
        Time_smooth(j) = Time(i-(window/2));
    end
end
end
```

D.3 Moisture Absorption Curve Fitting

% Author: Vasanth Sarathy

% Date: June 2005

function

Moisture_Diffusion_Curve_Fitting(x1,y1,x2,y2,x3,y3,x4,y4,x5,y5,...

x6,y6,x7,y7,x8,y8,x9,y9,x10,y10,x11,y11,x12,y12)

%MOISTURE_DIFFUSION_CURVE_FITTING Create plot of datasets and fits

% MOISTURE_DIFFUSION_CURVE_FITTING(X1,Y1,X2,Y2,X3,Y3,X4,Y4,X5,Y5,...

% X6,Y6,X7,Y7,X8,Y8,X9,Y9,X10,Y10,X11,Y11,X12,Y12)

% Creates a plot, similar to the plot in the main curve fitting

% window, using the data that you provide as input.

% Number of datasets: 12

% Number of fits: 12

% Data from dataset "WB1-85-85":

% X = x1:

% Y = y1:

% Unweighted

% Data from dataset "WB1-50-50":

% X = x2:

% Y = y2:

% Unweighted

% Data from dataset "WB1-50-85":

% X = x3:

% Y = y3:

% Unweighted

% Data from dataset "WB2-50-50":

% X = x4:

% Y = y4:

% Unweighted

% Data from dataset "WB2-85-50":

% X = x5:

% Y = y5:

MATLAB Code

```
% Unweighted

% Data from dataset "WB2-85-85":
% X = x6:
% Y = y6:
% Unweighted

% Data from dataset "CB1-85-85":
% X = x7:
% Y = y7:
% Unweighted

% Data from dataset "CB2-50-50":
% X = x8:
% Y = y8:
% Unweighted

% Data from dataset "CB2-50-85":
% X = x9:
% Y = y9:
% Unweighted

% Data from dataset "CB3-50-50":
% X = x10:
% Y = y10:
% Unweighted

% Data from dataset "CB3-85-50":
% X = x11:
% Y = y11:
% Unweighted

% Data from dataset "CB3-85-85":
% X = x12:
% Y = y12:
% Unweighted
%

% Set up figure to receive datasets and fits
f_ = clf; figure(f_);
leg_h_ = []; leg_t_ = {}; % handles and text for legend
xlim_ = [-Inf -Inf]; % limits of x axis
ax_ = subplot(1,1,1); set(ax_,'Box','on'); grid(ax_,'on');
axes(ax_); hold on;
```

D.3 Moisture Absorption Curve Fitting

```
% REPEAT THE FOLLOWING PROCEDURE FOR EACH DATASET

% --- Plot data originally in dataset "WB1-85-85"
x1 = x1(:); y1 = y1(:); h_ =
line(x1,y1,'Parent',ax_,'Color',[0.333333 0 0.666667],...
      'LineStyle','none', 'LineWidth',1,...
      'Marker','.', 'MarkerSize',12);
xlim_(1) = min(xlim_(1),min(x1)); xlim_(2) = max(xlim_(2),max(x1));
legh_(end+1) = h_; legt_{end+1} = 'WB1-85-85';

% Nudge axis limits beyond data limits
if all(isfinite(xlim_))
    xlim_ = xlim_ + [-1 1] * 0.01 * diff(xlim_);
    set(ax_,'XLim',xlim_)
end

% --- Create fit "WB1-85-85-fit"
fo_ = fitoptions('method','NonlinearLeastSquares','Lower',[1.13e-009
0.7994 ],'Upper',[2e-009 0.811 ]); st_ = [0.1756414513994 0.5 ];
set(fo_,'Startpoint',st_); ft_ = fittype('1
-(8/pi^2)*exp(-D*pi^2*x/.0746^2) -
(8/(9*pi^2))*exp(-9*D*pi^2*x/.0746^2) -
(8/(25*pi^2))*exp(-25*D*pi^2*x/.0746^2) -
(8/(49*pi^2))*exp(-49*D*pi^2*x/.0746^2))*Minf' ,...
      'dependent',{'y'},'independent',{'x'},...
      'coefficients',{'D', 'Minf'});

% Fit this model using new data
cf_ = fit(x1,y1,ft_ ,fo_);

% Or use coefficients from the original fit:
if 0
    cv_ = {1.130076626541e-009, 0.7994006774491};
    cf_ = cfit(ft_,cv_{:});
end

% Plot this fit
h_ = plot(cf_,'fit',0.95);
legend off; % turn off legend from plot method call
set(h_(1),'Color',[1 0 0],...
      'LineStyle','-','LineWidth',2,...
      'Marker','none','MarkerSize',6);
```

MATLAB Code

```
legh_(end+1) = h_(1); legt_{end+1} = 'WB1-85-85-fit';  
  
hold off; legend(ax_,legh_, legt_);
```

D.4 Moisture Desorption Curve Fitting

```
% Author: Vasanth Sarathy  
% Date: June 2005  
  
function  
Moisture_Diffusion_Curve_Fitting_vac(p1,q1,p2,q2,p3,q3,p4,q4,p5,q5,...  
p6,q6,p7,q7,p8,q8,p9,q9,p10,q10,p11,q11,p12,q12,p13,q13,p14,q14)  
%MOISTURE_DIFFUSION_CURVE_FITTING_VAC Create plot of datasets and fits  
% MOISTURE_DIFFUSION_CURVE_FITTING_VAC(P1,Q1,P2,Q2,P3,Q3,P4,Q4,P5,Q5,...  
% P6,Q6,P7,Q7,P8,Q8,P9,Q9,P10,Q10,P11,Q11,P12,Q12,P13,Q13,P14,Q14)  
% Creates a plot, similar to the plot in the main curve fitting  
% window, using the data that you provide as input.  
% Number of datasets: 14  
% Number of fits: 14  
  
% Data from dataset "WB1-vac1":  
% X = p1:  
% Y = q1:  
% Unweighted  
  
% Data from dataset "WB1-vac2":  
% X = p2:  
% Y = q2:  
% Unweighted  
  
% Data from dataset "WB1-vac3":  
% X = p3:  
% Y = q3:  
% Unweighted  
  
% Data from dataset "WB1-vac4":  
% X = p4:  
% Y = q4:  
% Unweighted
```

D.4 Moisture Desorption Curve Fitting

```
% Data from dataset "WB2-vac1":
%   X = p5:
%   Y = q5:
%   Unweighted

% Data from dataset "WB2-vac2":
%   X = p6:
%   Y = q6:
%   Unweighted

% Data from dataset "WB2-vac3":
%   X = p7:
%   Y = q7:
%   Unweighted

% Data from dataset "CB1-vac1":
%   X = p8:
%   Y = q8:
%   Unweighted

% Data from dataset "CB2-vac1":
%   X = p9:
%   Y = q9:
%   Unweighted

% Data from dataset "CB2-vac2":
%   X = p10:
%   Y = q10:
%   Unweighted

% Data from dataset "CB2-vac3":
%   X = p11:
%   Y = q11:
%   Unweighted

% Data from dataset "CB3-vac1":
%   X = p12:
%   Y = q12:
%   Unweighted

% Data from dataset "CB3-vac2":
%   X = p13:
%   Y = q13:
%   Unweighted
```

MATLAB Code

```
% Data from dataset "CB3-vac3":
%   X = p14:
%   Y = q14:
%   Unweighted
%

% Set up figure to receive datasets and fits
f_ = clf; figure(f_);
xlim_ = [Inf -Inf];      % limits of x axis
ax_ = subplot(1,1,1); set(ax_,'Box','on'); axes(ax_); hold on;

% REPEAT THE FOLLOWING PROCEDURE FOR EACH DATASET

% --- Plot data originally in dataset "WB1-vac1"
p1 = p1(:); q1 = q1(:); h_ =
line(p1,q1,'Parent',ax_,'Color',[0.333333 0 0.666667],...
     'LineStyle','none', 'LineWidth',1,...
     'Marker','.', 'MarkerSize',12);
xlim_(1) = min(xlim_(1),min(p1)); xlim_(2) = max(xlim_(2),max(p1));

% Nudge axis limits beyond data limits
if all(isfinite(xlim_))
    xlim_ = xlim_ + [-1 1] * 0.01 * diff(xlim_);
    set(ax_,'XLim',xlim_)
end

% --- Create fit "WB1-vac1-fit"
fo_ = fitoptions('method','NonlinearLeastSquares','Lower',[5e-010
0.12 ],'Upper',[2e-009 0.14 ]); st_ = [0.8985308127813
0.8589957890599 ]; set(fo_,'Startpoint',st_); ft_ = fitttype('(1
-(8/pi^2)*exp(-D*pi^2*x/.0746^2) -
(8/(9*pi^2))*exp(-9*D*pi^2*x/.0746^2) -
(8/(25*pi^2))*exp(-25*D*pi^2*x/.0746^2) -
(8/(49*pi^2))*exp(-49*D*pi^2*x/.0746^2))*Minf' ,...
     'dependent',{'y'},'independent',{'x'},...
     'coefficients',{'D', 'Minf'});

% Fit this model using new data
cf_ = fit(p1,q1,ft_ ,fo_);
```


D.5 Solution to Fick's Diffusion Law

```
% Or use coefficients from the original fit:
if 0
    cv_ = {1.25e-009, 0.13};
    cf_ = cfit(ft_,cv_{:});
end

% Plot this fit
h_ = plot(cf_,'fit',0.95);
legend off; % turn off legend from plot method call
set(h_(1),'Color',[1 0 0],...
    'LineStyle','-','LineWidth',2,...
    'Marker','none','MarkerSize',6);

hold off;
```

D.5 Solution to Fick's Diffusion Law

```
% SOLUTIONS TO FICK'S LAW
% Author: Vasanth Sarathy
% Date: February 2005

% This code implements the analytically derived solutions to Fick's Law of
% diffusion and plots the concentration at different time intervals against
% the distance.

% --- Solution using the Method of Reflection and Superposition
clear all
x = 0:0.001:5; %Distance
Dt = 0.1:1:5; %D: Diffusion Coefficient, t: Time
h = 1; i = 1; j=1; for i = 1:length(Dt)
    for j = 1:length(x)
        C_by_M(j,i) = exp(-(x(j).^2)./(4.*Dt(i)))./(pi.*Dt(i)).^(1/2));
    end
end

figure
% Plots for Dt = 0.1, 0.5, 1 and 5
plot(x,C_by_M(:,1),x,C_by_M(:,2),x,C_by_M(:,5),x,C_by_M(:,10)) grid
xlabel('x') ylabel('C/M') legend('Dt = 0.1','Dt = 0.5','Dt = 1','Dt
= 5')

% --- Solution using the Method of the Lapace Transform
```

MATLAB Code

```
clear all l =2; x = 0:0.005:1; Dt = 0.1:.1:5; i = 1; j = 1; for i =
1:length(Dt)
    for j = 1:length(x)
        for n = 0:3
            C_old_by_C0 = (-1)^n.*erfc((((2.*n+1).*1) -x(j))./...
(2.*sqrt(Dt(i)))) + (-1)^n.*erfc((((2.*n+1).*1) +...
x(j))./(2.*sqrt(Dt(i)))));
            if n==0
                C_new = C_old_by_C0;
            else
                C_new = C_new + C_old_by_C0;
            end
        end
        C(j,i) = C_new;
    end
end

figure
% Plots for Dt = 0.1, 0.5, 1 and 5
plot(x./l,C(:,1),x./l,C(:,5),x./l,C(:,10),x./l,C(:,50)) grid
xlabel('x/l') ylabel('C/C_0') legend('Dt = 0.1','Dt = 0.5','Dt =
1','Dt = 5')
```

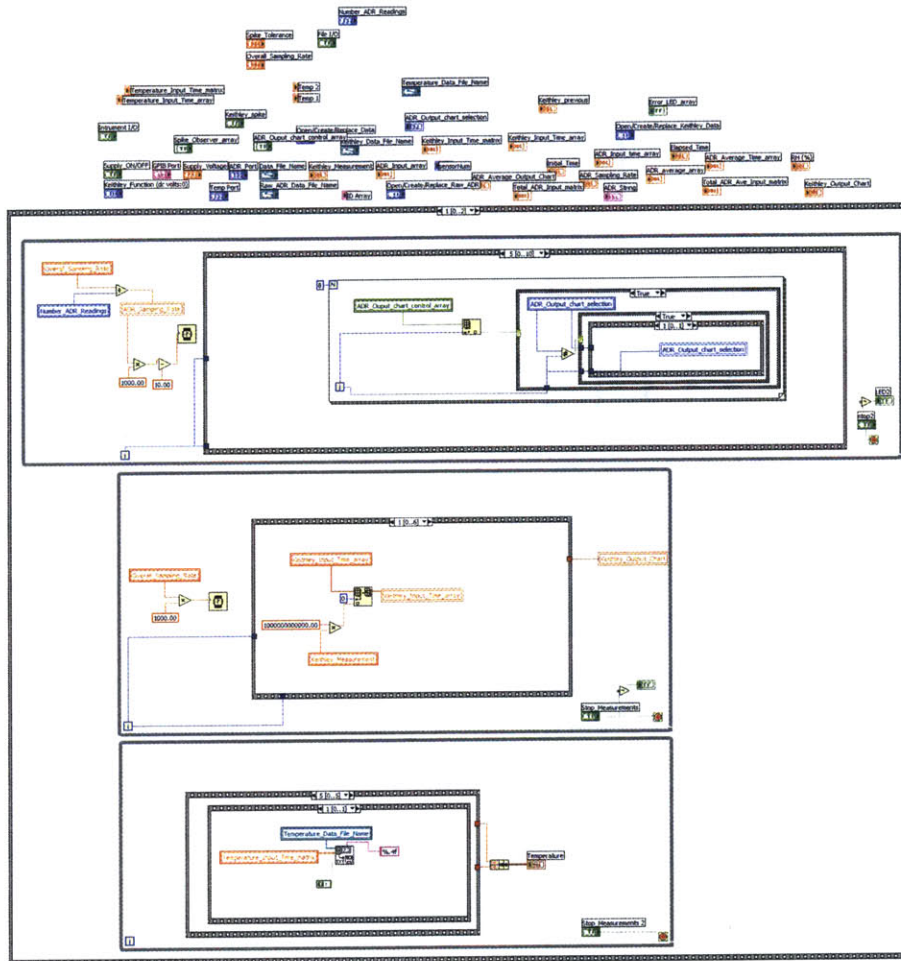
Appendix E
LABVIEW Code

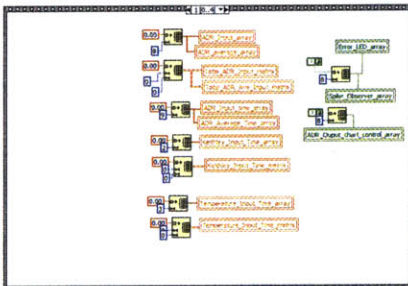
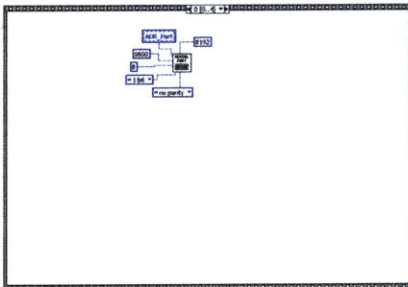
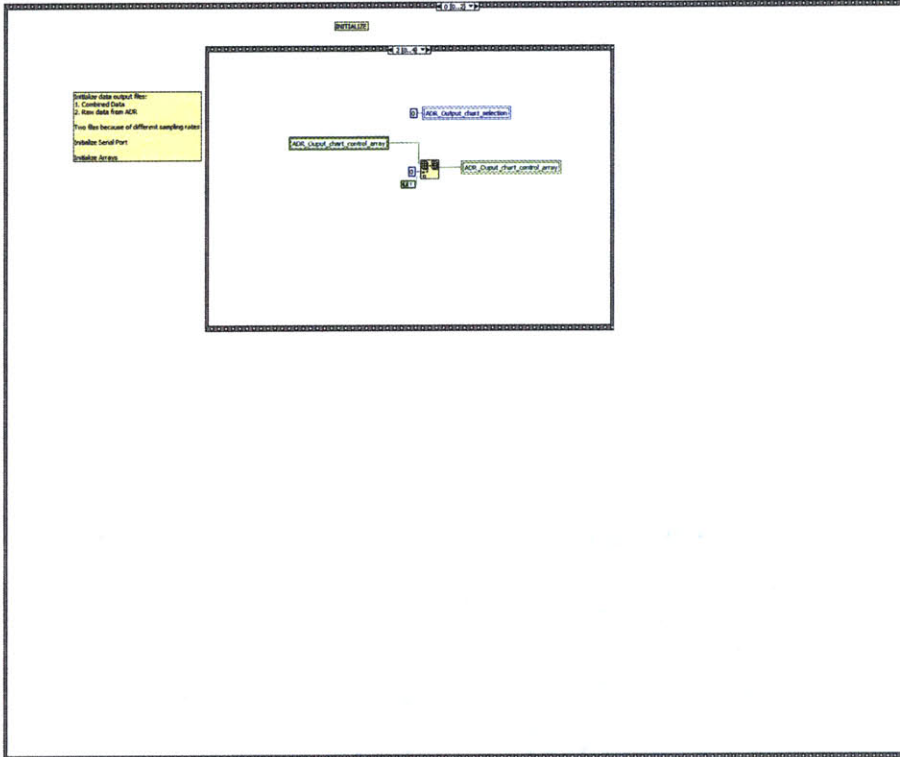
LABVIEW Code

MIT_ADAQ.vi
MIT_ADAQ.vi

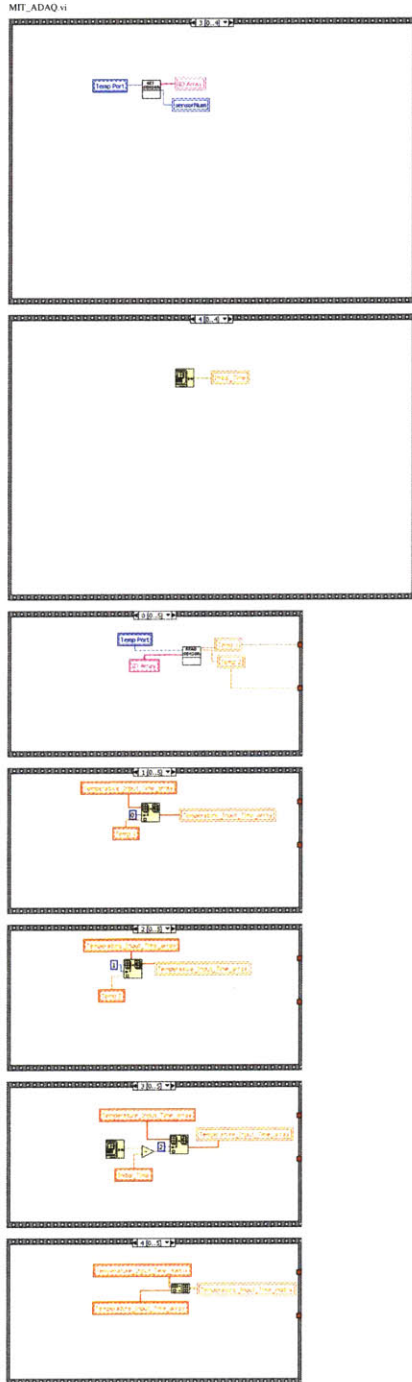
Page 1 of 12

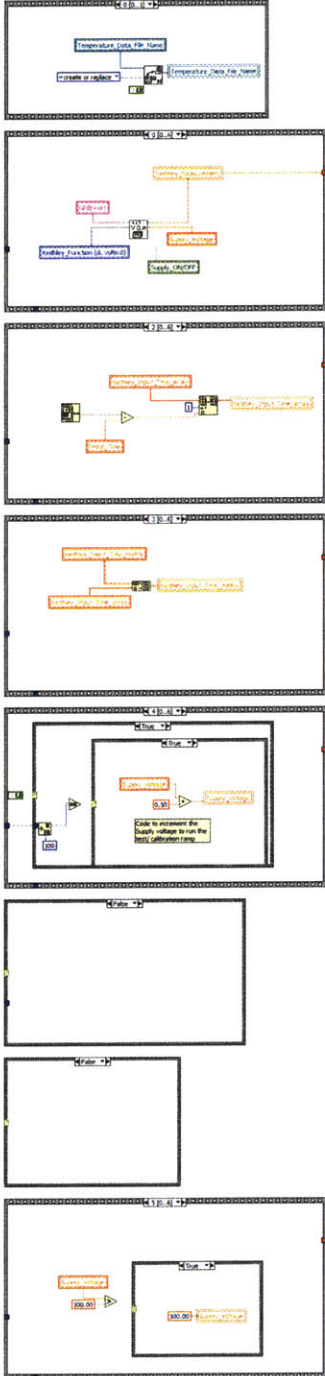
Block Diagram



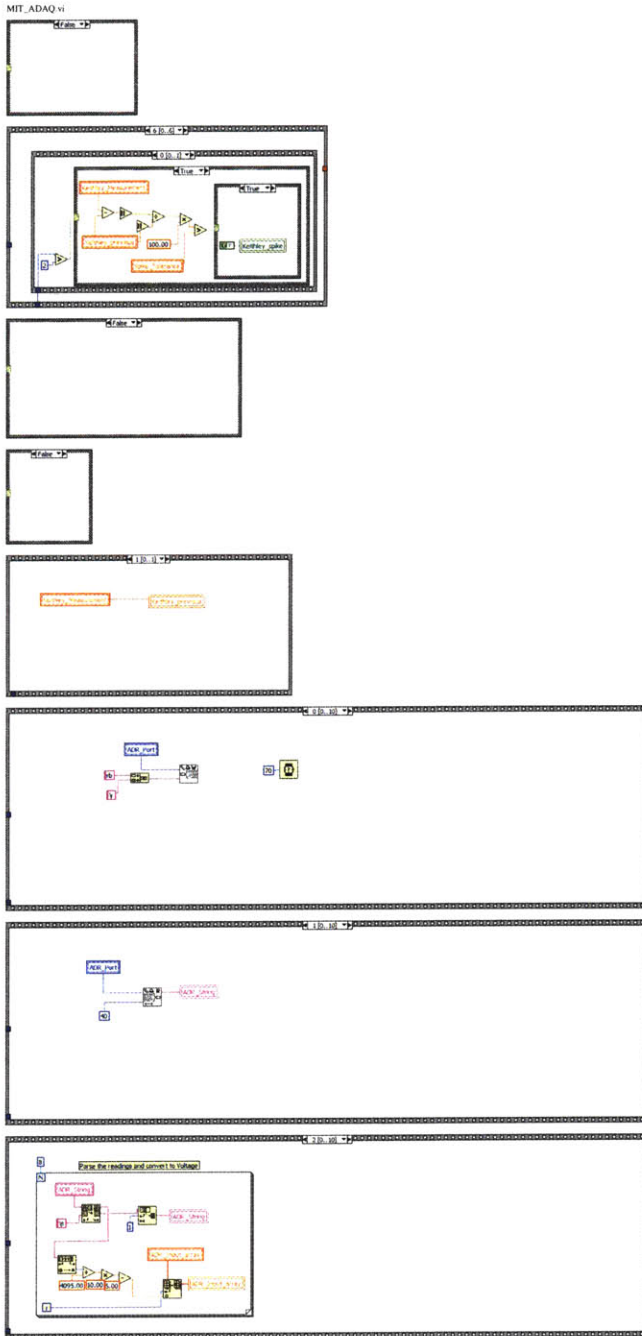


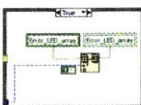
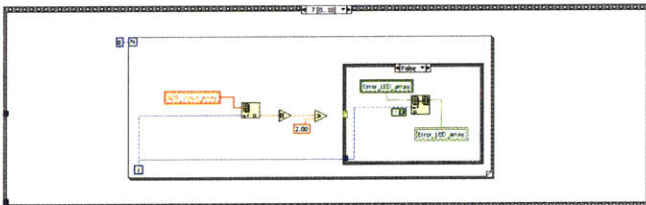
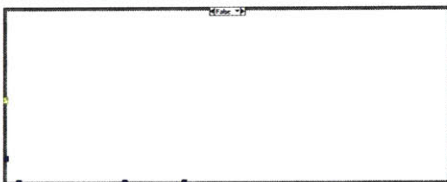
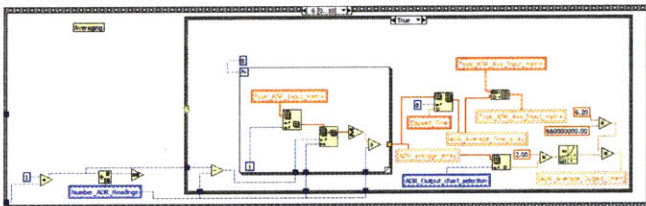
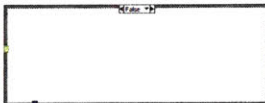
LABVIEW Code





LABVIEW Code

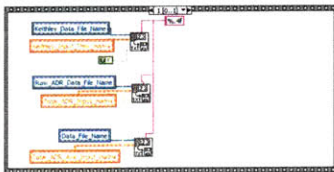
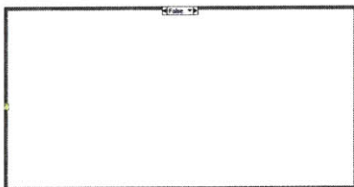
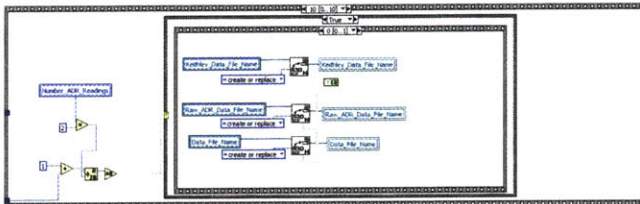
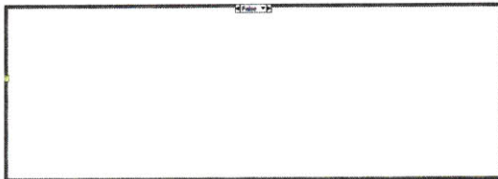
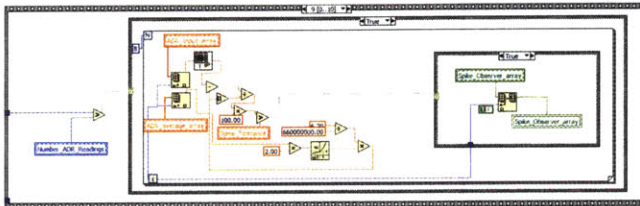
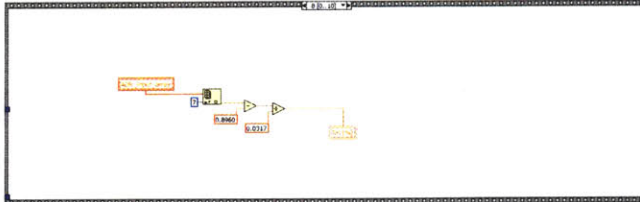


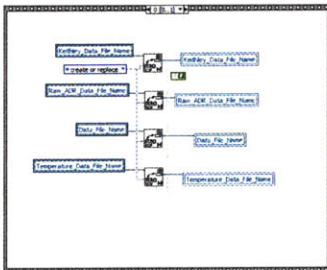
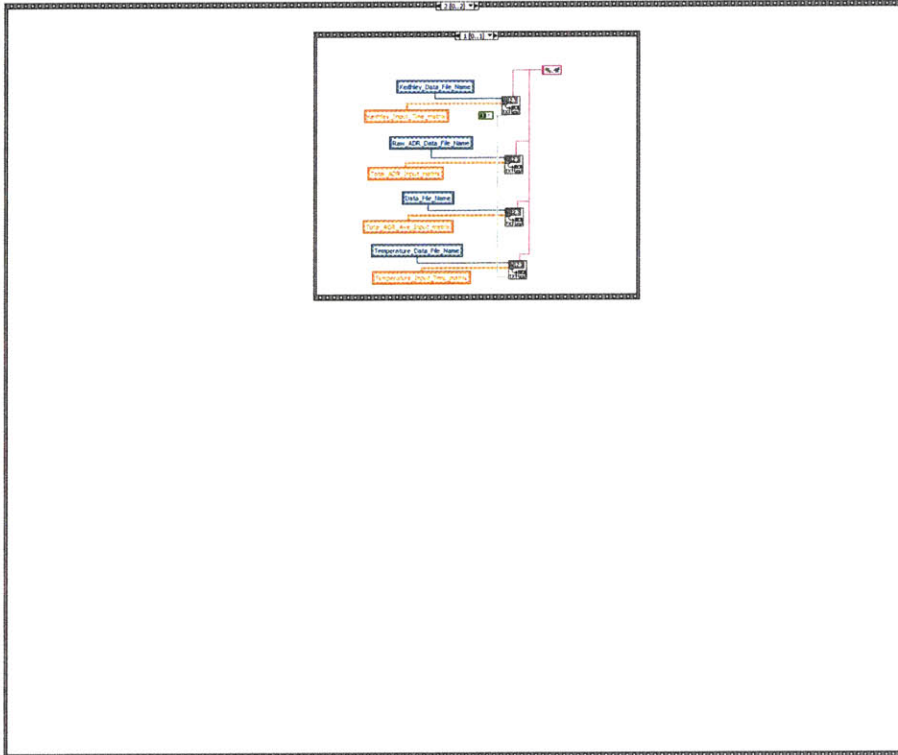


LABVIEW Code

MIT_ADAQ.vi

Page 7 of 12





List of SubVIs

Icon	SubVI Name	Path
Open/Create/Replace File	Open/Create/Replace File.vi	C:\Program Files\National Instruments\LabVIEW 6.1\vi.lib\Utility\file.lib\Open/Create/Replace File.vi
Serial Port Init	Serial Port Init.vi	C:\Program Files\National Instruments\LabVIEW 6.1\vi.lib\Instr\Serial IB\Serial Port Init.vi
Serial Port Write	Serial Port Write.vi	C:\Program Files\National Instruments\LabVIEW 6.1\vi.lib\Instr\Serial IB\Serial Port Write.vi
Serial Port Read	Serial Port Read.vi	C:\Program Files\National Instruments\LabVIEW 6.1\vi.lib\Instr\Serial IB\Serial Port Read.vi
Keithley 617	Keithley 617.vi	C:\Program Files\National Instruments\LabVIEW 6.1\Instr\ib\kei617\ib\Keithley 617.vi
Write To Spreadsheet File	Write To Spreadsheet File.vi	C:\Program Files\National Instruments\LabVIEW 6.1\vi.lib\Utility\file.lib\Write To Spreadsheet File.vi
Voltage_to_Current	Voltage_to_Current.vi	C:\SCAT\Labview VIs\Voltage_to_Current.vi
Get_Temp_Sensors	Get_Temp_Sensors.vi	C:\SCAT\Labview VIs\Get_Temp_Sensors.vi
Read_Temp_Sensors	Read_Temp_Sensors.vi	C:\SCAT\Labview VIs\Read_Temp_Sensors.vi
Read_Temp_Sensors	Read_Temp_Sensors.vi	C:\SCAT\Labview VIs\Read_Temp_Sensors.vi

Position in Hierarchy

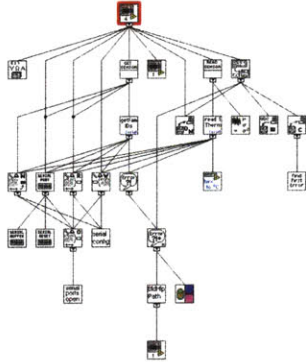
file:///C:/Documents%20and%20Settings/Vasanth/20Sarathy/Desktop/auug17/MIT_ADAQ.html

8/17/2005

LABVIEW Code

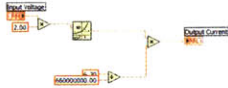
MIT_ADAQ.vi

Page 9 of 12



Voltage_to_Current.vi

Block Diagram



List of Sub VIs

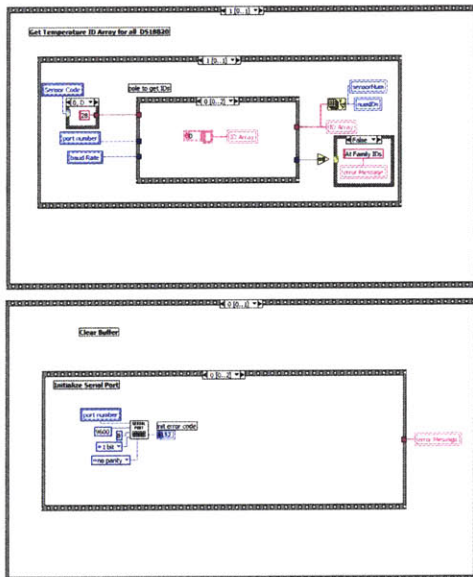
Position in Hierarchy



Get_Temp_Sensors.vi

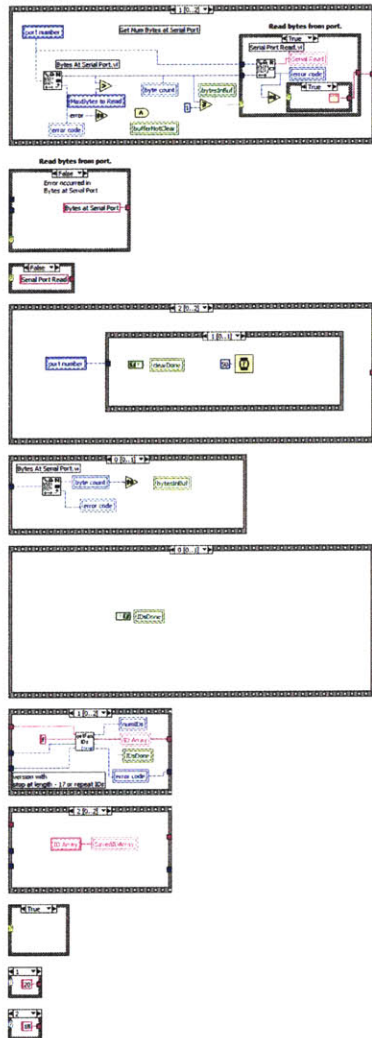
Block Diagram

File Edit View Help Run Debug Run Error Sensor Code I/O Control Panel Properties Help







file:///C:/Documents%20and%20Settings/Vasanth%20Saranya/Desktop/au17/MIT_ADAQ.html

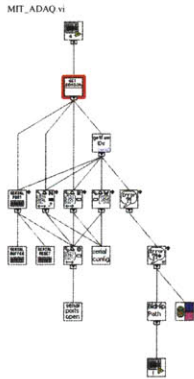
8/17/2005



List of SubVIs

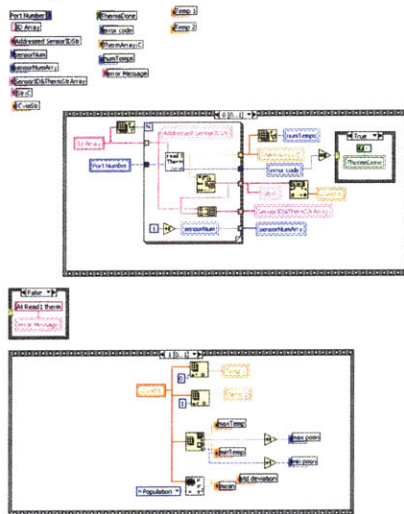
-  **Serial Port Init.vi**
C:\Program Files\National Instruments\LabVIEW 6.1\vi.lib\Inst\Serial.IB\Serial Port Init.vi
-  **Serial Port Read.vi**
C:\Program Files\National Instruments\LabVIEW 6.1\vi.lib\Inst\Serial.IB\Serial Port Read.vi
-  **Bytes At Serial Port.vi**
C:\Program Files\National Instruments\LabVIEW 6.1\vi.lib\Inst\Serial.IB\Bytes At Serial Port.vi
-  **1W.getFamilyIDs.vi**
C:\SCAT\Labview V\vi\Templ\W_ThermPot00\G4.IB\1W.getFamilyIDs.vi

Position in Hierarchy



Read_Temp_Sensors.vi

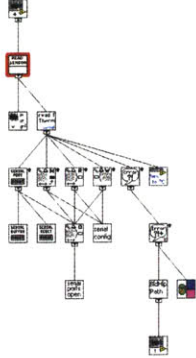
Block Diagram



List of SubVIs

- 1W.read1ThermG4.vi
C:\SCATM\labview_Vis\Temp\1W_Therm\Plot008G4_1B\1W.read1ThermG4.vi
- Std Deviation and Variance.vi
C:\Program Files\National Instruments\LabVIEW 6.1\vislib\analysis\baselny\libStd Deviation and Variance.vi

Position in Hierarchy



Bibliography

- [1] *IPC-6012A - Qualification and Performance Specification for Rigid Printed Circuit Boards.*
- [2] *IPC-9201 - Surface Insulation Handbook.*
- [3] *IPC-TM-650 - Test Methods Manual.*
- [4] *IPC-TR-476A - Electrochemical Migration:Electrically Induced Failures in Printed Wiring Assemblies.*
- [5] V. Adamec and J. H. Calderwood. Electrical-conduction and polarization phenomena in polymeric dielectrics at low fields. *Journal of Physics D-Applied Physics*, 11(6):781–800, 1978.
- [6] N. Agmon. The grotthuss mechanism. *Abstracts of Papers of the American Chemical Society*, 210:328–Phys, 1995.
- [7] Tarun Amla. Conductive anodic filament growth failure. In *IPC Printed Circuits Expo 2002*, 2002.
- [8] H. Ardebili, C. Hillman, M. A. E. Natishan, P. McCluskey, M. G. Pecht, and D. Peterson. A comparison of the theory of moisture diffusion in plastic encapsulated microelectronics with moisture sensor chip and weight-gain measurements. *IEEE Transactions on Components and Packaging Technologies*, 25(1):132–139, 2002.
- [9] S. D. Bhakta, S. Lundberg, and G. Mortensen. Accelerated tests to simulate metal migration in hybrid circuits. *Annual Reliability and Maintainability Symposium, 2002 Proceedings*, pages 319–324, 2002.
- [10] H. Anthony Chan. Surface insulation resistance methodology for today’s manufacturing technology. *IEEE Transactions on Components and Packaging Technologies*, 19(4), 1996.
- [11] Clyde F. Coombs. *Printed Circuits Handbook*. McGraw-Hill handbooks. McGraw-Hill, New York, 5th edition, 2001.
- [12] H. Cordes and S. D. Baranovskii. On the conduction mechanism in ionic glasses. *Physica Status Solidi B-Basic Research*, 218(1):133–138, 2000.
- [13] John Crank. *The Mathematics of Diffusion*. Oxford science publications. Clarendon Press, Oxford, Eng, 2d edition, 1979.

BIBLIOGRAPHY

- [14] John Crank and Graham Stuart Park. *Diffusion in Polymers*. Academic Press, London, New York,, 1968.
- [15] D. K. Das-Gupta. Dielectric and related molecular processes in polymers. *IEEE Transactions on Dielectrics and Electrical Insulation*, 8(1):6–14, 2001.
- [16] G. Digiacomio. Current-leakage kinetics across tinned cr/cu lands having epoxy overlay. *IEEE Transactions on Components Hybrids and Manufacturing Technology*, 8(4):440–445, 1985.
- [17] L. A. Dissado. Understanding electrical trees in solids: From experiment to theory. *IEEE Transactions on Dielectrics and Electrical Insulation*, 9(4):483–497, 2002.
- [18] L. A. Dissado and J. C. Fothergill. *Electrical Degradation and Breakdown in Polymers*. P. Peregrinus, London, 1992.
- [19] J. C. Dyre. The random free-energy barrier model for ac conduction in disordered solids. *Journal of Applied Physics*, 64(5):2456–2468, 1988.
- [20] J. C. Dyre. Some remarks on ac conduction in disordered solids. *Journal of Non-Crystalline Solids*, 135(2-3):219–226, 1991.
- [21] J. C. Dyre. Studies of ac hopping conduction at low-temperatures. *Physical Review B*, 49(17):11709–11720, 1994.
- [22] J. C. Dyre and T. B. Schroder. Effective one-dimensionality of universal ac hopping conduction in the extreme disorder limit. *Physical Review B*, 54(21):14884–14887, 1996.
- [23] J. C. Dyre and T. B. Schroder. Universality of ac conduction in disordered solids. *Reviews of Modern Physics*, 72(3):873–892, 2000.
- [24] H. El-Kishky. Electric field and energy computation on wet insulating surfaces. *IEEE Transactions on Dielectrics and Electrical Insulation*, 3(4), 1996.
- [25] M. Fernandez-Garcia and M. Y. M. Chiang. Effect of hygrothermal aging history on sorption process, swelling, and glass transition temperature in a particle-filled epoxy-based adhesive. *Journal of Applied Polymer Science*, 84(8):1581–1591, 2002.
- [26] G. Harsanyi. Electrochemical processes resulting in migrated short failures in microcircuits. *IEEE Transactions on Components Packaging and Manufacturing Technology Part A*, 18(3):602–610, 1995.
- [27] J. A. Jachim, G. B. Freeman, and L. J. Turbini. Use of surface insulation resistance and contact angle measurements to characterize the interactions of three water soluble fluxes with fr-4 substrates. *IEEE Transactions on Components Packaging and Manufacturing Technology Part B-Advanced Packaging*, 20(4):443–451, 1997.
- [28] A. K. Jonscher. The universal dielectric response and its physical significance. *IEEE Transactions on Electrical Insulation*, 27(3):407–423, 1992.

- [29] A. K. Jonscher. "universal" response of hopping carriers. *Journal of Materials Science Letters*, 17(23):1975–1977, 1998.
- [30] A. K. Jonscher. Dielectric relaxation in solids. *Journal of Physics D-Applied Physics*, 32(14):R57–R70, 1999.
- [31] K. C. Kao and D. M. Tu. Hole injection initiated by ionic conduction in electrically stressed insulating polymers. *Journal of Applied Polymer Science*, 90(7):1864–1867, 2003.
- [32] Phil Kinner. The principle of surface insulation resistance (sir) testing and its role in establishing the electrochemical reliability of a printed circuit board. In *IEEE International Conference on Business of Electronic Product Reliability and Liability*, Hong Kong, China, 2004.
- [33] S. J. Krumbein. Metallic electromigration phenomena. *IEEE Transactions on Components Hybrids and Manufacturing Technology*, 11(1):5–15, 1988.
- [34] S. J. Krumbein. Tutorial - electrolytic models for metallic electromigration failure mechanisms. *IEEE Transactions on Reliability*, 44(4):539–549, 1995.
- [35] Michael Lindsey. Amber tcu project sir test report. Technical report, Ricardo, 2003.
- [36] J. Lowell. Absorption and conduction currents in polymers - a unified model. *Journal of Physics D-Applied Physics*, 23(2):205–210, 1990.
- [37] L. L. Marsh, R. Lasky, D. P. Seraphim, and G. S. Springer. Moisture solubility and diffusion in epoxy and epoxy-glass composites. *IBM Journal of Research and Development*, 28(6):655–661, 1984.
- [38] L. L. Marsh, D. C. Vanhart, and S. M. Kotkiewicz. A dielectric loss investigation of moisture in epoxy-glass composites. *IBM Journal of Research and Development*, 29(1):18–26, 1985.
- [39] N. F. Mott and Ronald W. Gurney. *Electronic Processes in Ionic Crystals*. Dover Publications, New York,, 2d edition, 1964.
- [40] T. J. Mouthaan and V. Petrescu. The modeling of resistance changes in the early phase of electromigration. *Microelectronics and Reliability*, 38(1):99–105, 1998.
- [41] Bruce A. Myers. Cooling issues for automotive electronics, 2003.
- [42] Clarissa Navarro. Standardizing a test method for conductive anodic filament growth failure. In *IPC Printed Circuits Expo 2001*, 2001.
- [43] J. W. Park, D. G. Harlow, and H. F. Nied. Characterization of interfacial adhesion damage induced by accelerated life testing. *IEEE Transactions on Advanced Packaging*, 23(1):100–107, 2000.

BIBLIOGRAPHY

- [44] N. Pavlenko. Proton wires in an electric field: The impact of the grotthuss mechanism on charge translocation. *Journal of Physics-Condensed Matter*, 15(2):291–307, 2003.
- [45] M. G. Pecht, H. Ardebili, A. A. Shukla, J. K. Hagge, and D. Jennings. Moisture ingress into organic laminates. *IEEE Transactions on Components and Packaging Technologies*, 22(1):104–110, 1999.
- [46] W. J. Ready, L. J. Turbini, R. Nickel, and J. Fischer. A novel test circuit for automatically detecting electrochemical migration and conductive anodic filament formation. *Journal of Electronic Materials*, 28(11):1158–1163, 1999.
- [47] J. Reinisch and A. Heuer. Simple lattice models of ion conduction: Counter ion model versus random energy model. *Physical Review B*, 66(6), 2002.
- [48] G. Sarkar. A study of the factors affecting surface insulation resistance measurements. *Journal of Materials Science Letters*, 17, 1998.
- [49] N. L. Sbar and R. P. Kozakiewicz. New acceleration factors for temperature, humidity, bias testing. *IEEE Transactions on Electron Devices*, 26(1):56–71, 1979.
- [50] Donald A. Seanor. *Electrical Properties of Polymers*. Academic Press, New York, 1982.
- [51] Y. X. Shao and S. Kouadi. Durability of fiberglass composite sheet piles in water. *Journal of Composites for Construction*, 6(4):280–287, 2002.
- [52] C. L. Soles, F. T. Chang, B. A. Bolan, H. A. Hristov, D. W. Gidley, and A. F. Yee. Contributions of the nanovoid structure to the moisture absorption properties of epoxy resins. *Journal of Polymer Science Part B-Polymer Physics*, 36(17):3035–3048, 1998.
- [53] C. L. Soles, F. T. Chang, D. W. Gidley, and A. F. Yee. Contributions of the nanovoid structure to the kinetics of moisture transport in epoxy resins. *Journal of Polymer Science Part B-Polymer Physics*, 38(5):776–791, 2000.
- [54] Dietrich Stauffer and Amnon Aharony. *Introduction to Percolation Theory*. Taylor & Francis, London, Washington, DC, 2nd edition, 1992.
- [55] S. M. Sze. *Semiconductor Devices, Physics and Technology*. Wiley, New York, 2nd edition, 2002.
- [56] K. M. Takahashi. Conduction paths and mechanisms in fr-4 epoxy glass composite printed wiring boards. *Journal of the Electrochemical Society*, 138(6):1587–1593, 1991.
- [57] Michal Tencer and John Seaborn Moss. Humidity management of outdoor electronic equipment: Methods, pitfalls, and recommendations. *IEEE Transactions on Components and Packaging Technologies*, 25(1):66–72, 2002.
- [58] M. R. Vanlandingham, R. F. Eduljee, and J. W. Gillespie. Moisture diffusion in epoxy systems. *Journal of Applied Polymer Science*, 71(5):787–798, 1999.

BIBLIOGRAPHY

- [59] H. J. Wintle. Charge motion and trapping in insulators - surface and bulk effects. *IEEE Transactions on Dielectrics and Electrical Insulation*, 6(1):1–10, 1999.
- [60] D. Young and A. Christou. Failure-mechanism models for electromigration. *IEEE Transactions on Reliability*, 43(2):186–192, 1994.
- [61] M. Zahn. Drift-dominated conduction within an ohmic medium. *Journal of Applied Physics*, 47(7):3122–3126, 1976.
- [62] Markus Zahn. *Electromagnetic Field Theory : A Problem Solving Approach*. Krieger Pub. Co., Malabar, Fla., reprint edition, 2003.

5460-73